Study on the impact of atmospheric pollution on eco-environment changes using satellite remote sensing technique

（衛星リモートセンシングを用いた生態環境変化への
大気汚染の影響に関する研究）

北海道大学　大学院農学院
共生基盤学専攻　博士後期課程

鐘　国盛

Contents

Abstract

Atmospheric aerosol is a liquid and solid particles suspended in the atmosphere with diameters ranging from 10^{-3} to 10^{2} micrometers. Most atmospheric aerosols are produced by natural processes and some are from human industrial and agricultural activities. The aerosol particles that are directly emitted into the atmosphere including: sea spray aerosol, dust, biomass or fossil fuel burning aerosol, volcanic ash, primary organic aerosol, in addition, there are some aerosol particles can be produced from precursor gases (e.g., sulfates, nitrates, ammonium salts, secondary organic aerosol).

Atmospheric aerosol has a significant influence on the radiative balance of the Earth and global climate change by both direct and indirect ways. On the one hand, the atmospheric aerosols can directly reflect and absorb the incoming solar and terrestrial radiation. On the other hand, the atmospheric aerosols can affect the incoming radiation indirectly through modifying cloud formation and the microphysical properties of clouds.

Recently, air pollution has become a matter of global concern. Atmospheric aerosols play very crucial role in air quality. Ground-level aerosols, also known as particulate matter (PM), are associated with human health and as such are regulated as a priority air quality pollutant.

The studies of atmospheric aerosols properties are therefore significant to understanding Earth system dynamics and atmospheric environment. Satellites are increasingly contributing to obtain information on aerosol properties (e.g., the aerosol optical depth (AOD), the columnar concentration of particles, their sizes). In addition, the atmospheric aerosol is one of the largest uncertainties in surface observation from satellite-level, since aerosol distribution is often heterogeneous. Therefore, the remote sensing of the Earth’s surface results are effected by atmospheric gases (e.g. water vapor and ozone) and aerosol particles scattering and absorption.

The main objectives of this research are to develop an aerosol retrieval algorithm in order to retrieve aerosol properties from satellite observations, and to develop an atmospheric correction method for high-precision surface monitoring. To achieve these aims, three main tasks have been undertaken:

First, the surface contribution at satellite-level was determined. The signal obtained by the spaceborne sensor measures the radiance at the top of the Earth's atmosphere (TOA), which consists of two basic components: the radiance scattered by atmosphere and the radiance reflected by the surface. Therefore, to derive the aerosol information,

the surface contribution should be separated from the atmosphere contribution. Secondly, an aerosol retrieval algorithm was established. Thirdly, a self-correction method for minimizing the atmospheric influences in spectral bands according to predicted aerosol information was developed.

The main contents of this thesis include 5 parts:

1. I created a new algorithm for retrieving AOD over land, from the Cloud and Aerosol Imager (CAI), which is one of the instruments on the Greenhouse gases Observing SATellite (GOSAT) for detecting and correcting cloud and aerosol interference. I used the GOSAT and AErosol RObotic NETwork (AERONET) collocated data from different regions over the globe to analyze the relationship between the TOA reflectance in the shortwave infrared (SWIR) 1.6 μm band and the surface reflectance in the red (0.67 μm) band. Our results confirmed that the relationships between the surface reflectance at 0.67 μm and TOA reflectance at 1.6 μm are not constant for different surface conditions. Under low AOD conditions (AOD at 0.55 μm < 0.1), a Normalized Difference Vegetation Index (NDVI) based regression function for estimating the surface reflectance of 0.67 μm band from the 1.6 μm band was summarized, and it achieved good performance, proving that the reflectance relations of the 0.67 μm and 1.6 μm bands are typically vegetation dependent. Since the NDVI itself is easily affected by aerosols, I combined the advantages of the Aerosol FRee vegetation Index (AFRI), which is aerosol resistant and highly correlated with regular NDVI, with our regression function, which can preserve the various correlations of 0.67 μm and 1.6 μm bands for different surface types, and developed a new surface reflectance and aerosol-free NDVI estimation algorithm, which I named the Modified AFRI1.6 algorithm. This algorithm was applied to AOD retrieval, and the validation results for our algorithm show that the retrieved AOD has a consistent relationship with AERONET measurements, with a correlation coefficient of 0.912, and approximately 67.7% of the AOD retrieved data were within the expected error range (± 0.1 ± $15\%AOD_{AERONET}$).

2. I evaluated the performances of Atmospherically Resistant Vegetation Index (ARVI), Enhanced Vegetation Index (EVI), two-band-based EVI (EVI2), Visible Atmospherically Resistant Index (VARI) and AFRI for vegetation detection and monitoring with various AOD levels using the Moderate Resolution Imaging Spectroradiometer (MODIS) and AERONET data. Vegetation indices (VIs) calculated from satellite observations in the visible and infrared bands have been widely used for the assessment of vegetation cover and conditions. The NDVI is a commonly used VI for the retrieval of the biophysical properties of the vegetation canopy. However, due to the significant disadvantages of NDVI, including that it is sensitive to atmospheric

influences, there is a considerable reduction in the precision of the detection of vegetation dynamics at the satellite level. Therefore, several modified spectral vegetation indices have been developed to remove or minimize atmospheric disturbances. The ARVI and EVI utilize the reflectance measurements in the blue wavelengths to conduct a self-correction process to correct the atmospheric scattering effects in the red bands. The VARI is designed to emphasize vegetation and to mitigate atmospheric influences by using three color (blue, green and red) bands. The AFRI was developed using the SWIR 1.6 μm and 2.1 μm bands, which are more sensitive to differences in vegetation and less affected by atmospheric influences due to their longer wavelengths. The objective of this part was to evaluate the performances of ARVI, EVI, VARI, AFRI, and their variants for different AOD values. For the validation analysis, I used the spatially and temporally matched MODIS and AERONET collocated data. The TOA reflectance provided by the MODIS/Terra calibrated radiances (MOD02HKM) data were used to calculate the TOA VI values (not atmospherically corrected), and the surface VIs (atmospherically corrected) were calculated using the reflectance data from the MODIS surface reflectance product (MOD09HKM). The experimental results revealed that the TOA ARVI and TOA EVI are highly correlated with the surface NDVI for different levels of AODs. However, their TOA VI values were somewhat different from the corresponding surface VI values. AFRIs outperform other VIs due to the smaller differences in their TOA and surface VI values. Compared with ARVI, EVI, and AFRI, the EVI2 and VARI were more easily affected by atmospheric aerosols.

3. A self-corrected method to minimize the atmospheric influences on vegetation indices was developed. Based on the linear relationship between the surface reflectance relationship in the 0.6-μm red and 2.1-μm SWIR bands, the surface reflectance in the red band can be estimated. Under a median assumption in viewing geometry, we can derive a predicted AOD according to the top-of-atmosphere reflectance and estimated surface reflectance. The predicted AOD value can be considered as prior knowledge of the atmospheric conditions to actualize the self-corrected procedure. Based on simulation results from a radiative transfer model, I summarized two empirical functions to correct for the aerosol influences in near-infrared (NIR) and red bands. Consequently, the corrected NIR band could be singly utilized to improve the measurement accuracy of SWIR-based vegetation indices. The corrected NIR and red band pair could also be directly used in the construction of vegetation indices, which would have the capability to assess vegetation and even aerosols that are present in the atmosphere. This method was applied in the construction of the corrected NIR-derived $AFRI_{2.1}$ and the corrected NDVI, the performances of which were investigated under different aerosol loading conditions. The results revealed that under different AOD values, the corrected NIR-derived $AFRI_{2.1}$ was generally closer to the atmospherically

corrected NDVI than the original $AFRI_{2.1}$. Compared with the uncorrected NDVI, the NDVI corrected by our method exhibited an obviously better performance under aerosol loading conditions; the atmospheric influences on the NIR and red bands were largely removed, generating near-theoretical values.

4. A SWIR 2.1-μm-based self-correction method has been developed for the correction of the atmospheric influences in the red and NIR bands. However, there are many sensors that only provide observations in the 1.6-μm SWIR band, and it is difficult to apply this correction method to the sensors without 2.1-μm bands. To overcome this issue, I analyzed the reflectance relationship between the 1.6 μm and 2.1 μm bands using the MODIS surface reflectance product, and attempted to adapt the 2.1-μm-based self-correction method to the 1.6-μm-based sensors, according to the reflectance relationship between the 1.6 μm and 2.1 μm bands. The analyzed results revealed that the reflectance relationship between the 1.6 μm and 2.1 μm bands is typically dependent on vegetation conditions and that the reflectance at 2.1 μm can be parameterized as a function of the 1.6 μm reflectance and the VI. Based on our experimental results, an $AFRI_{2.1}$-based regression function connecting the 1.6 μm and 2.1 μm bands was summarized. Under light aerosol loading (AOD at 0.55 μm < 0.1), the 2.1 μm reflectance derived by our method has an extremely high correlation with the true 2.1 μm reflectance (r-value = 0.928). Using the relationship between the 1.6 μm and 2.1 μm bands, the adaption of the correction method has been successfully accomplished. The performance of the 1.6-μm-based correction method has been tested with different levels of AOD by a comparison of the atmospherically corrected VIs. The results showed that the atmospheric influences in the red and NIR bands were effectively corrected using the 1.6-μm-based correction method, and the corrected red and NIR band derived VIs have obvious improvements in accuracy. The development of the 1.6-μm-based correction method offers the potential for 1.6-μm sensors to detect the vegetation dynamics in the presence of aerosols. The corrected red and NIR bands can be directly used in the construction of VIs (e.g., NDVI, Ratio Vegetation Index (RVI)); the single corrected band, such as the corrected NIR band, can also be used alone in aerosol resist VIs (e.g., the AFRI, $NDVI_{MIR}$) to improve their accuracies.

5. I developed a Dark Target (DT) AOD retrieval algorithm for GOSAT CAI based on the strategy of MODIS DT algorithm. When retrieving AOD from satellite platforms, the determination of surface contributions is a major challenge. In the MODIS DT algorithm, surface signals in the visible wavelengths are estimated based on the relationships between visible channels and SWIR near the 2.1-μm channel. However, the CAI only has the 1.6-μm band to cover SWIR wavelengths. To resolve the difficulties in determining surface reflectance caused by the lack of 2.1-μm band data, the relationship between reflectance at 1.6 μm and at 2.1 μm summarized in Chapter 5

were used. Similar to the MODIS DT algorithms (Collection 5 and Collection 6), a Thermal and Near-infrared Sensor for Carbon Observation-Cloud and Aerosol Imager (TANSO-CAI)-applicable approach that uses $AFRI_{2.1}$ and the scattering angle to account for the visible surface signals was proposed. It was then applied to the CAI sensor for AOD retrieval; the retrievals were validated by comparisons with ground-level measurements from AERONET sites. Validations show that retrievals from the CAI have high agreement with the AERONET measurements, with an r-value of 0.922, and 69.2% of the AOD retrieved data falling within the expected error envelope of $\pm (0.1 + 15\% AOD_{AERONET})$.

This thesis introduced two new algorithms for retrieval AOD over land from GOSAT TANSO-CAI. They can extend the function of GOSAT TANSO-CAI to the AOD observations to provide one-platform combination data (including carbon dioxide, methane and AOD) for future studies on the relationship between greenhouse gases and aerosols. In addition, a 2.1-μm band based self-correction method for minimizing the atmospheric influences in red and NIR bands was proposed. Based on the reflectance relationship between 2.1-μm and 1.6-μm bands, the self-correction method has been successfully adapted to the sensors that only provide observation near the 1.6-μm spectral band.

Chapter 1 General introduction

1.1 Introduction

The main objectives of this research are to develop aerosol retrieval algorithm and retrieve aerosol properties from satellite observations, and to develop atmospheric correction method for high-precision surface monitoring. This chapter introduces the thesis structure: (1) the research background; (2) the methods applied in this thesis and (3) the outline of the chapters.

1.2 Background

1.2.1 Impact of aerosols on the Earth's environment

The word aerosol is an analogy of the term hydrosol and is defined as the liquid and solid particles suspended in the atmosphere with diameters ranging from a few nanometers to 100 micrometers (μm) [1,2]. Several phenomena, such as dust, fumes, smoke, mist, fog, haze, and smog, are essentially types of aerosols [3]. Aerosols can be natural or anthropogenic; although most atmospheric aerosols are produced by natural processes, some are from human industrial and agricultural activities [4]. On a global scale, natural aerosols are much more common than anthropogenic ones, by a factor of approximately 4 to 5. However, due to human activities, regional aerosols may considerably increase, particularly in developing and industrialized regions [5]. The primary particles are emitted directly from a wide variety of natural and anthropogenic sources as aerosol particles, such as sea spray aerosols, dust, biomass- or fossil fuel-burning aerosols, volcanic ash, and primary organic aerosols, which can be emitted directly into the atmosphere. Secondary aerosol particles can be produced from precursor gases (e.g., sulfates, nitrates, ammonium salts, secondary organic aerosols) [6].

Atmospheric aerosols are important components of the climate system and strongly impact the Earth's radiation balance, hydrological cycle, and climate. Aerosol effects in the climate system can be roughly classified as "direct effects" and "indirect effects". Aerosols scatter and absorb the thermal radiation that is emitted from the Earth's surface and atmosphere as well as solar radiation (known as the direct aerosol effects) and modify the fractional cloud cover and the microphysical properties of clouds (known as the indirect aerosol effects) [7–10]. Compared to the anthropogenic greenhouse gases that cause the retention of heat, aerosol particles are much harder to

characterize. The direct effects (the scattering or absorption of solar radiation) are dependent on the physical and chemical properties of the atmospheric aerosols, such as the particle size, hygroscopicity, and complex refractive index. The scattering of incoming solar radiation back to space results in a net decrease in the solar energy at the Earth's surface, whereas absorbing aerosol particles (such as black carbon) warm the atmosphere through the efficient absorption of solar and thermal radiation [6]. Aerosols have short lifetimes, so their concentrations, compositions, and size distributions are temporally and spatially highly variable, depending on the aerosol type and meteorology [11,12].

Over the past decades, anthropogenic emissions of atmospheric aerosol and their precursors have dramatically increased [13]. Ground-level aerosols, also known as particulate matter (PM), are highly associated with human health and as such are regulated as a priority air quality pollutant [14,15]. Air pollution has become a matter of global concern. Aerosol particles of 0.1 to 1 μm can cause a degradation of visibility. Suspended particle matter of less than 2.5 μm in diameter (PM2.5) can penetrate the lungs and be incorporated into the blood, leading to diseases [16].

1.2.2 Observation of atmospheric aerosols

Aerosol monitoring contributes significantly to the understanding of the Earth's environmental systems. Satellites are increasingly being used to monitor the spatial and temporal distribution of aerosols from the local to global scale, and to study their physical and chemical properties [17]. Spectral aerosol optical depth (AOD) is the most frequently used aerosol optical property, because it is directly related to PM loading. AOD derived from satellite observations has thus been used as a proxy for surface PM [15,18]. AOD is a dimensionless measure of aerosol abundance and the amount of solar light extinction (scattering and absorption) caused by aerosol particles passing through a column of the atmosphere [18,19]. The satellite sensor receives a reflectance containing contributions from both the land surface and the atmosphere (especially aerosols). The main challenge of aerosol retrieval over land is to remove the surface contributions from the integrated reflectance signal at the satellite level [20–22].

Several algorithms have been developed based on different physical principles to separate the surface and atmospheric contributions for different sensors [23]. For instance, Moderate Resolution Imaging Spectroradiometer (MODIS), as typical single-view sensors, use the shortwave infrared (SWIR) channel to determine surface reflectance in the visible channels based on stable relationship between the visible and SWIR channels [24,25]. Multi-angle Imaging SpectroRadiometer (MISR) and Advanced Along Track Scanning Radiometer (AATSR) are multiangular sensors that

make it possible to accurately account for directional surface scattering [26,27]. The Polarization and Directionality of Earth's Reflectance (POLDER) instrumentation on the Advanced Earth Observing Satellite 1 (ADEOS-1) can achieve polarization measurement, which allows ground contributions to be determined based on the fact that atmospheric scattering is much more polarized than surface reflection [22,28]. Dark Target (DT) is a classic and popular technique for surface reflectance estimation and has been successfully applied to MODIS [29,30], Landsat Thematic Mapper [21], Advanced Very High Resolution Radiometer (AVHRR) [31,32], as well as several other sensors [7,33,34]. The DT approach assumes that aerosols over "dark" surfaces (such as vegetated land and dark oceans) will brighten the scene, and the aerosol signal is a major component of the top-of-atmosphere (TOA) signal in this case [7,35]. Thus, low surface reflectance values favor good discrimination between the surface and atmospheric contributions. In the MODIS DT algorithm, the influence of aerosols on the SWIR 2.1-μm channel is negligible (except for heavy aerosol or dusts), so the correlations of reflectance in the 0.47, 0.67 and 2.1 μm channels are used to estimate surface reflectance. Although highly accurate estimations can be made over low reflectance areas, the DT algorithm is limited by surface conditions and cannot be used over bright-reflection regions such as cites, desert or semi desert regions; this is because the surface reflectance signals over these regions are too large, which makes it difficult to discriminate aerosol contributions from satellite level TOA signals [2,36,37].

1.2.3 Atmospheric effects on the remote sensing of surface reflectance

Solar radiation reflected by the Earth's surface undergoes significant interactions with the atmosphere before it reaches satellite sensors. Satellite images of the Earth's surface and the reflected solar spectrum do not represent the true ground-leaving radiance. Part of the observed brightness is from the reflected solar radiance at the surface, and the remainder is derived from the brightness of the atmosphere [38].

The radiance of light reflected by the Earth-atmosphere system for a cloudless sky consists of three components:

$$L = L_o + L_s + L_d \quad (1)$$

where L is the radiance of the light reflected from the (cloudless) Earth-atmosphere system, L_o is the radiance of the light scattered by the direct sunbeam in the sensor's field of view from the atmosphere which is not reflected by the surface; L_s is the radiance of the light reflected by the surface and directly transmitted through the atmosphere; and L_d is the radiance of the light reflected by the surface and then scattered by the atmosphere to the sensor [39].

The atmospheric effects on the remote sensing of the surface reflectance by molecular scattering and absorption and aerosol scattering. The absorption depends on the amount of absorbing gases, mainly ozone and oxygen, and the molecular scattering depends on atmospheric pressure. Because the molecular scattering and absorption depend on ozone and oxygen, which have relatively stable atmospheric concentrations [40–44], molecular scattering and absorption can be accounted for satisfactorily. However, aerosols are a major unknown atmospheric component and their effects on remote sensing depend on the characteristics of the particular atmospheric aerosols, such as the particle size distributions, shapes, chemical compositions and refractive indices of the different components [39].

When using multispectral satellite data for monitoring surface conditions, atmospheric effects can lead to a darkening if the surface is bright (sand, vegetation) in the near-infrared (NIR) band, and brightening if the surface is dark (water, vegetation) in the visible part of the spectrum [39,44,45]. This problem is especially significant for monitoring purposes, such as for agricultural or land use studies [38].

1.2.4 Atmospheric effects on vegetation indices

Vegetation is a key component of global ecosystems and represents an active surface interacting with solar radiation and transforming it. Understanding the changes in Earth's vegetation cover is highly associated with understanding land-atmosphere interactions and their effects on climate [46,47]. Since the first remote sensing satellite was launched and began taken the advantage of the satellite data that can provide spatially and periodically comprehensive views of land vegetation cover, considerable efforts have been made to monitor and characterize the dynamics of the Earth's vegetation from space [46–49]. During the past few decades, several vegetation indices (VIs) were developed and used for terrestrial science applications. VIs are mathematical combinations of spectral bands that accentuate the spectral properties of vegetation (such as the optical characteristics of leaf chlorophyll, leaf area, canopy cover, and canopy architecture) and distinguishes vegetation from other terrestrial features [50–53]. Although VIs are not intrinsic physical quantities, they are widely used for vegetation-related remote sensing and the assessment of biophysical and biochemical variables (such as the canopy chlorophyll content, leaf area index, green vegetation fraction, gross primary productivity, and fraction of photosynthetically active radiation absorbed by vegetation) [53,54].

The Normalized Difference Vegetation Index (NDVI) is the most representative VI, and its usefulness in monitoring and assessing global vegetation coverage and condition has been well demonstrated [55]. NDVI is calculated based on the behavior of the vegetation spectra, wherein chlorophyll pigments absorb light in the red region,

and the cellular structures of leaves reflect large portions of the light in the NIR wavelengths. Such differences in the reflected red and NIR bands are typical due to vegetation and do not show over other ground types. NDVI generally ranges from -1 to 1 with vegetation; a 0 or negative value means no vegetation (such as areas with cloud or snow cover), a value between 0.1 and 0.4 is indicative of urban areas, while a value between 0.4 and 1 indicates the higher possible densities of green leaves [56].

It is well known that NDVI is sensitive to atmospheric absorption and scattering caused by highly variable aerosols [51,53]. Atmospheric molecules and aerosols create "atmosphere path radiance" through the scattering of solar radiant flux, which becomes an added flux component observed by satellite sensors. Conversely, the atmosphere absorbs ground-reflected radiance fluxes, resulting in a loss of the transmitted radiant energy. These coupled effects lead to variations in satellite-sensor-observed reflectances in the NIR and red bands and cause the apparent NDVI values to be lower than the true NDVI values [55]. Thus, a certain number of vegetation indices such as Atmospherically Resistant Vegetation Index (ARVI), Enhanced Vegetation Index (EVI) and Aerosol FRee vegetation Index (AFRI), have been developed with similar vegetation index functions as well as eliminating or at least reducing the atmosphere influences. However, they basically addressed the issue that atmospheric effects on the red band, and only very few studies focus on the atmospheric effects on the NIR band. Under heavy aerosol loading conditions, the errors in NIR exert considerable influence on computation of vegetation indices.

1.3 Aims and approaches

The main objectives of this research are to develop an aerosol retrieval algorithm in order to retrieve aerosol properties from satellite observations, and to develop an atmospheric correction method for high-precision surface monitoring. The more specific objectives are outlined below:

(1) To analyze relationship between surface reflectance in the visible and SWIR bands of Greenhouse gases Observing SATellite Thermal and Near-infrared Sensor for Carbon Observation-Cloud and Aerosol Imager (GOSAT TANSO-CAI), and to develop surface reflectance estimation methods.

(2) To develop aerosol retrieval algorithms for GOSAT TANSO-CAI sensor.

(3) To develop a self-correction method for minimizing the atmospheric influences in spectral bands according to predicted aerosol information.

The main remote sensing data used in this thesis contain MODIS data, GOSAT

TANSO-CAI data, and Aerosol Robotic Network (AERONET) AOD data.

1.4 Thesis contents

This thesis consists of seven chapters, covering five main topics. The schematic framework for this research is shown in Figure 1.1.

In Chapter 2, I used the GOSAT and AERONET collocated data from different regions over the globe to analyze the relationship between the TOA reflectance in the SWIR (1.6 μm) band and the surface reflectance in the red (0.67 μm) band. This information was used to develop an AOD retrieval algorithm for GOSAT TANSO-CAI. The retrieval results have been validated through a comparison with ground-level measurements from AERONET.

In Chapter 3, the performances of different vegetation indices, including the ARVI, EVI, two-band-based EVI (EVI2), Visible Atmospherically Resistant Index (VARI), and AFRI for vegetation detection and monitoring were evaluated using the MODIS and AERONET data, given various AOD levels.

In Chapter 4, a SWIR 2.1-μm-based self-corrected method to minimize the atmospheric influences in the red and NIR bands was introduced. This method has been applied in the construction of a corrected NIR-derived $AFRI_{2.1}$ and a corrected NDVI, the performances of which have been investigated under different aerosol loading conditions by comparing their results with the atmospherically corrected VIs.

In Chapter 5, the reflectance relationship between the 1.6 μm and 2.1 μm bands was analyzed using the MODIS surface reflectance product, and an attempt to adapt the 2.1-μm-band-based self-correction method to the 1.6-μm-based sensors was made, using the reflectance relationship between the 1.6 μm and 2.1 μm bands. The performance of the 1.6-μm-based correction method has been tested under different levels of AODs by a comparison with the atmospherically corrected VIs.

In Chapter 6, a DT aerosol retrieval algorithm for GOSAT CAI, based on the Moderate Resolution Imaging Spectroradiometer (MODIS) DT algorithm, was introduced. The TANSO-CAI-applicable DT approach uses $AFRI_{2.1}$ and the scattering angle to account for the visible surface signals, and the observed AOD was validated by comparisons with the ground-level measurements from AERONET sites.

Chapter 7 presents a summary of the important findings and overall conclusions of this study. The limitations of the approaches and methods used in this and future works are discussed.

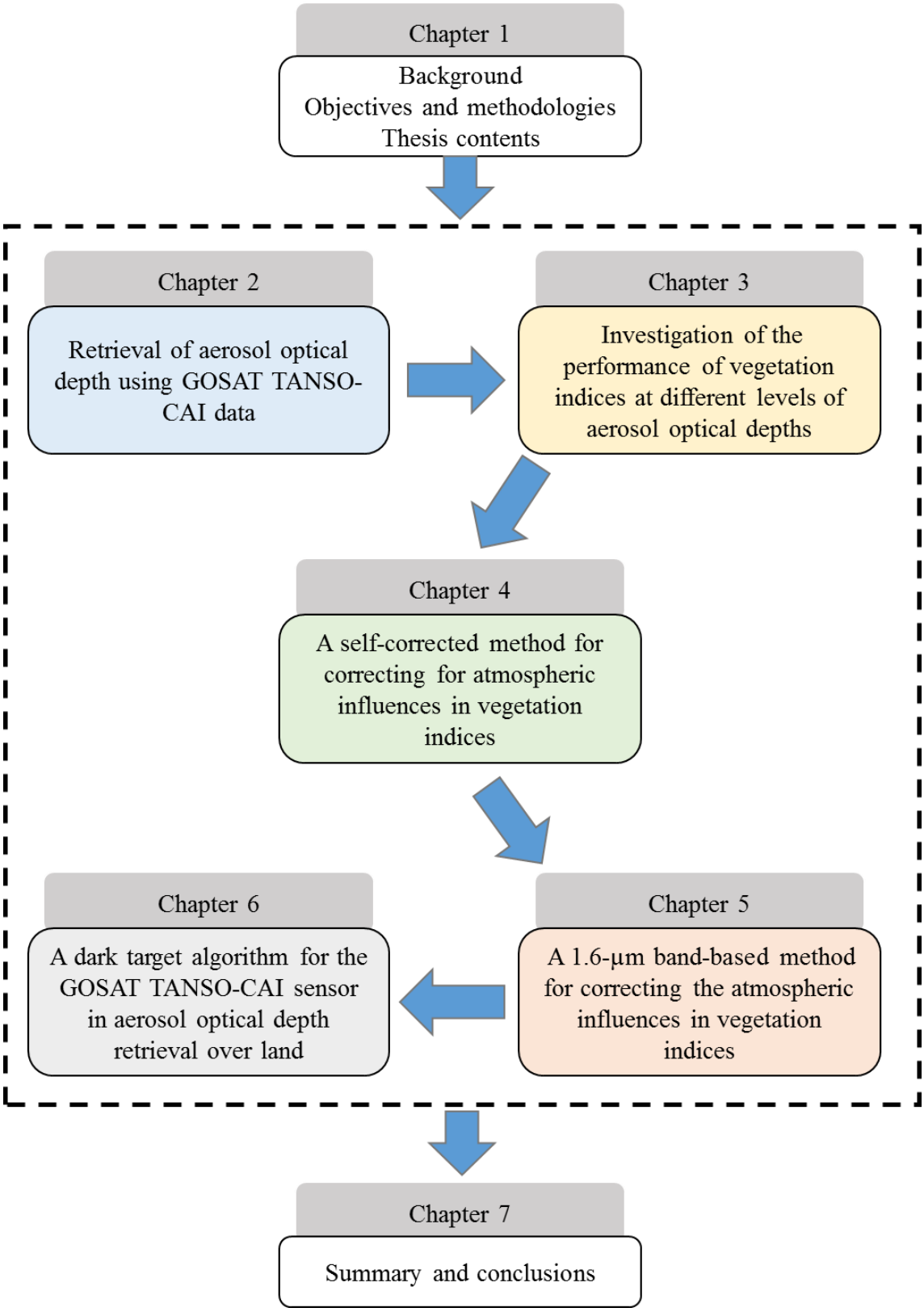

Figure 1.1 A schematic flow of the research organization.

References

1. Hinds, W.C. Aerosol technology: Properties, behavior, and measurement of airborne particles. John Wiley & Sons: **2012**.
2. Sun, L.; Wei, J.; Bilal, M.; Tian, X.; Jia, C.; Guo, Y.; Mi, X. Aerosol Optical Depth Retrieval over Bright Areas Using Landsat 8 OLI Images. *Remote Sens-Basel* **2015**, *8*, 23.
3. Sinclair, D. A new photometer for aerosol particle size analysis. *Journal of the Air Pollution Control Association* **1967**, *17*, 105-108.
4. Fuzzi, S.; Baltensperger, U.; Carslaw, K.; Decesari, S.; Denier Van Der Gon, H.; Facchini, M.; Fowler, D.; Koren, I.; Langford, B.; Lohmann, U. Particulate matter, air quality and climate: Lessons learned and future needs. *Atmospheric Chemistry and Physics* **2015**, *15*, 8217-8299.
5. Barry, R.G.; Chorley, R.J. Atmosphere, weather and climate. CUP Archive: **1992**.
6. Kokhanovsky, A.A.; Leeuw, G. Satellite aerosol remote sensing over land. Springer: **2009**.
7. Levy, R.; Munchak, L.; Mattoo, S.; Patadia, F.; Remer, L.; Holz, R. Towards a long-term global aerosol optical depth record: Applying a consistent aerosol retrieval algorithm to modis and viirs-observed reflectance. *Atmospheric Measurement Techniques* **2015**, *8*, 4083.
8. Forster, P.; Ramaswamy, V.; Artaxo, P.; Berntsen, T.; Betts, R.; Fahey, D.W.; Haywood, J.; Lean, J.; Lowe, D.C.; Myhre, G. Changes in atmospheric constituents and in radiative forcing. Chapter 2. In Climate change 2007. *The physical science basis*, **2007**.
9. Kaufman, Y.J.; Tanré, D.; Boucher, O. A satellite view of aerosols in the climate system. *Nature* **2002**, *419*, 215-223.
10. Ramanathan, V.; Crutzen, P.; Kiehl, J.; Rosenfeld, D. Aerosols, climate, and the hydrological cycle. *Science* **2001**, *294*, 2119-2124.
11. Choudhry, P.; Misra, A.; Tripathi, S. In Study of modis derived aod at three different locations in the indo gangetic plain: Kanpur, gandhi college and nainital, Annales Geophysicae, **2012**; Copernicus GmbH: pp 1479-1493.
12. Pöschl, U. Atmospheric aerosols: Composition, transformation, climate and health effects. Angewandte Chemie International Edition **2005**, 44, 7520-7540.
13. Finlayson-Pitts, B.J.; Hemminger, J.C. Physical chemistry of airborne sea salt particles and their components. *The Journal of Physical Chemistry* A **2000**, *104*, 11463-11477.
14. Jiang, X.; Liu, Y.; Yu, B.; Jiang, M. Comparison of MISR aerosol optical thickness with AERONET measurements in Beijing metropolitan area. *Remote Sensing of Environment* **2007**, *107*, 45-53.

15. Zhang, H.; Hoff, R.; Kondragunta, S.; Laszlo, I.; Lyapustin, A. Aerosol optical depth (AOD) retrieval using simultaneous GOES-East and GOES-West reflected radiances over the western United States. *Atmospheric Measurement Techniques* **2013**, *6*, 471-486.
16. Xing, Y.-F.; Xu, Y.-H.; Shi, M.-H.; Lian, Y.-X. The impact of PM2.5 on the human respiratory system. *Journal of thoracic disease* **2016**, *8*, E69.
17. Riffler, M.; Popp, C.; Hauser, A.; Fontana, F.; Wunderle, S. Validation of a modified AVHRR aerosol optical depth retrieval algorithm over Central Europe. *Atmospheric Measurement Techniques* **2010**, *3*, 1255-1270.
18. Liu, Y.; Park, R.J.; Jacob, D.J.; Li, Q.; Kilaru, V.; Sarnat, J.A. Mapping annual mean ground‐level PM2.5 concentrations using Multiangle Imaging Spectroradiometer aerosol optical thickness over the contiguous United States. *Journal of Geophysical Research: Atmospheres* **2004**, *109*.
19. NOAA Earth System Research Laboratory Global Monitoring Division Global Radiation Group. Available online: https://www.esrl.noaa.gov/gmd/grad/surfrad/aod/ (accessed on 8 January 2017).
20. Kaufman, Y.; Tanré, D.; Gordon, H.; Nakajima, T.; Lenoble, J.; Frouin, R.; Grassl, H.; Herman, B.; King, M.; Teillet, P. Passive remote sensing of tropospheric aerosol and atmospheric correction for the aerosol effect. *Journal of Geophysical Research: Atmospheres* **1997**, *102*, 16815-16830.
21. Kaufman, Y.; Tanré, D.; Remer, L.A.; Vermote, E.; Chu, A.; Holben, B. Operational remote sensing of tropospheric aerosol over land from EOS moderate resolution imaging spectroradiometer. *Journal of Geophysical Research: Atmospheres* **1997**, *102*, 17051-17067.
22. Kokhanovsky, A.; Breon, F.-M.; Cacciari, A.; Carboni, E.; Diner, D.; Di Nicolantonio, W.; Grainger, R.; Grey, W.; Höller, R.; Lee, K.-H. Aerosol remote sensing over land: A comparison of satellite retrievals using different algorithms and instruments. *Atmospheric Research* **2007**, *85*, 372-394.
23. de Leeuw, G.; Holzer-Popp, T.; Bevan, S.; Davies, W.H.; Descloitres, J.; Grainger, R.G.; Griesfeller, J.; Heckel, A.; Kinne, S.; Klüser, L. Evaluation of seven European aerosol optical depth retrieval algorithms for climate analysis. *Remote Sensing of Environment* **2015**, *162*, 295-315.
24. Kaufman, Y.J.; Wald, A.E.; Remer, L.A.; Gao, B.-C.; Li, R.-R.; Flynn, L. The MODIS 2.1-μm channel-correlation with visible reflectance for use in remote sensing of aerosol. *IEEE transactions on Geoscience and Remote Sensing* **1997**, *35*, 1286-1298.
25. Remer, L.A.; Kaufman, Y.; Tanré, D.; Mattoo, S.; Chu, D.; Martins, J.V.; Li, R.-R.; Ichoku, C.; Levy, R.; Kleidman, R. The MODIS aerosol algorithm, products, and validation. *Journal of the atmospheric sciences* **2005**, *62*, 947-973.

26. Diner, D.J.; Martonchik, J.V.; Kahn, R.A.; Pinty, B.; Gobron, N.; Nelson, D.L.; Holben, B.N. Using angular and spectral shape similarity constraints to improve MISR aerosol and surface retrievals over land. *Remote Sensing of Environment* **2005**, *94*, 155-171.
27. Grey, W.M.; North, P.R.; Los, S.O.; Mitchell, R.M. Aerosol optical depth and land surface reflectance from multiangle AATSR measurements: Global validation and intersensor comparisons. *IEEE Transactions on Geoscience and Remote Sensing* **2006**, *44*, 2184-2197.
28. Deuzé, J.; Bréon, F.; Devaux, C.; Goloub, P.; Herman, M.; Lafrance, B.; Maignan, F.; Marchand, A.; Nadal, F.; Perry, G. Remote sensing of aerosols over land surfaces from POLDER‐ADEOS‐1 polarized measurements. *Journal of Geophysical Research: Atmospheres* **2001**, *106*, 4913-4926.
29. Levy, R.C.; Remer, L.A.; Mattoo, S.; Vermote, E.F.; Kaufman, Y.J. Second‐generation operational algorithm: Retrieval of aerosol properties over land from inversion of Moderate Resolution Imaging Spectroradiometer spectral reflectance. *Journal of Geophysical Research: Atmospheres* **2007**, *112*.
30. Levy, R.; Mattoo, S.; Munchak, L.; Remer, L.; Sayer, A.; Patadia, F.; Hsu, N. The Collection 6 MODIS aerosol products over land and ocean. *Atmospheric Measurement Techniques* **2013**, *6*, 2989.
31. Soufflet, V.; Tanré, D.; Royer, A.; O'Neil, N. Remote sensing of aerosols over boreal forest and lake water from AVHRR data. *Remote Sensing of Environment* **1997**, *60*, 22-34.
32. Mei, L.; Xue, Y.; Kokhanovsky, A.; von Hoyningen-Huene, W.; de Leeuw, G.; Burrows, J. Retrieval of aerosol optical depth over land surfaces from AVHRR data. *Atmospheric Measurement Techniques Discussions* **2013**, *6*, 2227-2251.
33. Holzer-Popp, T.; Schroedter-Homscheidt, M.; Breitkreuz, H.; Martynenko, D.; Klüser, L. Improvements of synergetic aerosol retrieval for ENVISAT. *Atmospheric Chemistry and Physics* **2008**, *8*, 7651-7672.
34. Xie, D.; Cheng, T.; Zhang, W.; Yu, J.; Li, X.; Gong, H. Aerosol type over east Asian retrieval using total and polarized remote sensing. *Journal of Quantitative Spectroscopy and Radiative Transfer* **2013**, *129*, 15-30.
35. Dark Target (MODIS Aerosol Retrieval Algorithm), About the Algorithm. Available online: https://darktarget.gsfc.nasa.gov/algorithm (accessed on 26 December 2016).
36. Dark Target (MODIS Aerosol Retrieval Algorithm). Available online: http://darktarget.gsfc.nasa.gov/content/what-difference-between-dark-target-and-deep-blue (accessed on 28 December 2016).
37. Hsu, N.; Jeong, M.J.; Bettenhausen, C.; Sayer, A.; Hansell, R.; Seftor, C.; Huang, J.; Tsay, S.C. Enhanced deep blue aerosol retrieval algorithm: The second

generation. *Journal of Geophysical Research: Atmospheres* **2013**, *118*, 9296-9315.
38. Hadjimitsis, D.G.; Papadavid, G.; Agapiou, A.; Themistocleous, K.; Hadjimitsis, M.; Retalis, A.; Michaelides, S.; Chrysoulakis, N.; Toulios, L.; Clayton, C. Atmospheric correction for satellite remotely sensed data intended for agricultural applications: Impact on vegetation indices. *Natural Hazards and Earth System Sciences* **2010**, *10*, 89-95.
39. Kaufman, Y.J.; Sendra, C. Algorithm for automatic atmospheric corrections to visible and near-ir satellite imagery. *International Journal of Remote Sensing* **1988**, *9*, 1357-1381.
40. Vermote, E.F.; El Saleous, N.Z.; Justice, C.O. Atmospheric correction of MODIS data in the visible to middle infrared: First results. *Remote Sensing of Environment* **2002**, *83*, 97-111.
41. Vermote, E.F.; Kotchenova, S. Atmospheric correction for the monitoring of land surfaces. *Journal of Geophysical Research: Atmospheres* **2008**, *113*.
42. Fu, Q.; Min, X.; Sun, L.; Ma, S. Atmospheric correction of HJ-1 A/B CCD over land: Land surface reflectance calculation for geographical information product. *Journal of Geographical Sciences* **2014**, *24*, 1083-1094.
43. Liang, S.; Fang, H.; Chen, M. Atmospheric correction of LANDSAT ETM+ land surface imagery. I. Methods. *IEEE Transactions on Geoscience and Remote Sensing* **2001**, *39*, 2490-2498.
44. Herman, B.M.; Browning, S.R. The effect of aerosols on the earth-atmosphere albedo. *Journal of the Atmospheric Sciences* **1975**, *32*, 1430-1445.
45. Otterman, J.; Fraser, R. Earth-atmosphere system and surface reflectivities in arid regions from landsat mss data. *Remote Sensing of Environment* **1976**, *5*, 247-266.
46. Jiang, Z.; Huete, A.R.; Chen, J.; Chen, Y.; Li, J.; Yan, G.; Zhang, X. Analysis of ndvi and scaled difference vegetation index retrievals of vegetation fraction. *Remote sensing of environment* **2006**, *101*, 366-378.
47. Jorgensen, S.E.; Svirezhev, Y.M. Towards a thermodynamic theory for ecological systems. *Elsevier*: **2004**.
48. Myneni, R.B.; Keeling, C.; Tucker, C.J.; Asrar, G.; Nemani, R.R. Increased plant growth in the northern high latitudes from 1981 to 1991. *Nature* **1997**, *386*, 698.
49. Saleska, S.R.; Didan, K.; Huete, A.R.; Da Rocha, H.R. Amazon forests green-up during 2005 drought. *Science* **2007**, *318*, 612-612.
50. Huete, A.R. A soil-adjusted vegetation index (savi). *Remote sensing of environment* **1988**, *25*, 295-309.
51. Kaufman, Y.J.; Tanre, D. Atmospherically resistant vegetation index (arvi) for eos-modis. *IEEE transactions on Geoscience and Remote Sensing* **1992**, *30*, 261-270.
52. Liu, H.Q.; Huete, A. A feedback based modification of the ndvi to minimize

canopy background and atmospheric noise. *IEEE Transactions on Geoscience and Remote Sensing* **1995**, *33*, 457-465.

53. Jiang, Z.; Huete, A.R.; Didan, K.; Miura, T. Development of a two-band enhanced vegetation index without a blue band. *Remote Sensing of Environment* **2008**, *112*, 3833-3845.
54. Hanan, N.; Prince, S.; Hiernaux, P. Spectral modelling of multicomponent landscapes in the sahel. *International Journal of Remote Sensing* **1991**, *12*, 1243-4258.
55. Huete, A.R.; Liu, H.Q. An error and sensitivity analysis of the atmospheric-and soil-correcting variants of the ndvi for the modis-eos. *IEEE Transactions on Geoscience and Remote Sensing* **1994**, *32*, 897-905.
56. Liu, G.-R.; Liang, C.-K.; Kuo, T.-H.; Lin, T.-H.; Huang, S. Comparison of the ndvi, arvi and afri vegetation index, along with their relations with the aod using spot 4 vegetation dat. *Terrestrial Atmospheric and Oceanic Sciences* **2004**, *15*, 15-32.

Chapter 2 A modified aerosol free vegetation index algorithm for aerosol optical depth retrieval using GOSAT TANSO-CAI data

2.1 Introduction

Aerosols have a considerable influence on the radiative balance of the Earth and global climate change through the absorption and scattering of solar radiation [1–3]. Particularly, atmospheric aerosol particles are closely associated with public health and the environment (e.g., the tropospheric aerosols, also known as particulate matter, PM) [4–6]. One important aerosol optical property, aerosol optical depth (AOD), can reflect the characteristics of atmospheric turbidity and is the most frequently used monitoring parameter of atmospheric aerosols [7].

Satellite remote-sensing techniques are very effective for observing the spatial distributions and temporal variations of aerosol optical properties on a large scale [8]. Various satellite sensors have been applied to retrieve AOD [9–11], even though these sensors are not initially intended for aerosol monitoring [12]. The estimation of AOD has benefited from the development of algorithms for sensors with different wavelengths, viewing angles and polarizations [13,14].

Removal of the surface contribution has long been considered the primary task for estimating the optical properties of aerosols [14,15]. Due to the complexities of the land surface, aerosol retrieval over land is much more difficult compared to retrieval over ocean. Currently, several methods have been developed to remove the land surface contribution in satellite remote sensing. Among these, the Dark Target (DT) algorithm has been widely used for aerosol retrieval and has been successfully applied to different satellite sensors, such as Moderate-Resolution Imaging Spectroradiometer (MODIS) [16,17], Advanced Very High Resolution Radiometer (AVHRR) [18] and Visible infrared Imaging Radiometer (VIIRS) [19]. The DT algorithm is based on the assumption that aerosols will brighten the scene over “dark” surfaces (vegetated land and dark ocean). Generally, the dark surfaces have low surface reflectances in parts of the visible and shortwave infrared (SWIR) channels, and the low surface contribution benefits the determination of contribution of aerosols. The MODIS DT algorithm uses the linear relationships between the surface reflectance of the SWIR (2.1 μm) channel (negligibly affected by aerosols at this wavelength) and the red or blue channels to

account for the surface signal in the corresponding channel. This method works best over dark vegetated surfaces, but not over bright land surfaces. This is because the top-of-atmosphere (TOA) reflectances acquired by satellite sensors over bright land surfaces are overwhelmed by the surface contributions, making it very difficult to estimate the contribution of aerosols [20,21]. The development of the Deep Blue algorithm has made up the gap in aerosols retrieval over bright land surface; the Deep Blue algorithm successfully performed aerosols retrieval over bright targets as well as over most vegetated targets [21,22]. The precalculated surface reflectance database in the blue channels is the prerequisite of the Deep Blue algorithm, and it is a complicated task to develop a reflectance database for other sensors. Despite the MODIS DT algorithm having been proven to be a mature algorithm for AOD retrieving, sensors without a 2.1 μm channel onboard cannot rely on this algorithm to estimate the surface reflectance of red or blue channels. Therefore, different strategies were developed for the instruments that do not measure reflectance in the 2.1 μm channel. In the synergetic aerosol retrieval (SYNAER) method [14,23], Holzer-Popp et al. introduced a Normalized Difference Vegetation Index (NDVI) and scattering angle-involved iterative regression function for estimating the surface reflectance at 0.67 μm from the apparent reflectance of the 1.6 μm band [23,24]. This method was carried out with Advanced Along-Track Scanning Radiometer (AATSR) and Scanning Imaging Absorption Spectrometer for Atmospheric CHartographY (SCIAMACHY) sensors onboard Environmental Satellite (ENVISAT) used for AOD retrieval [23–25]. Similarly, Mei et al. derived an approach to estimate surface reflectance at 0.67 μm from the apparent reflectance at 3.75 μm from the AVHRR data based on NDVI. In their algorithms, the NDVI is used to determine the dark fields and tune the ratios and relationships between the 0.67 μm and the 1.6 μm or 3.75 μm bands under different surface conditions [26]. Nevertheless, aerosols easily influence NDVI, and increasing AOD would typically result in the decrease of NDVI values [27,28]. To eliminate the errors in NDVI caused by aerosols, an additional one-step iteration was performed to adjust the NDVI value [23–26,29]. Compared with non-iterative retrieval algorithms, the iteration step will increase the computational cost of retrieval. Therefore, replacing NDVI with the Aerosol FRee vegetation Index (AFRI) has the potential to simplify the retrieval process.

In our study, the data from Greenhouse gases Observing SATellite (GOSAT) were used for AOD retrieval. GOSAT is the world's first spacecraft to retrieve the concentrations of carbon dioxide and methane. Thermal and Near-infrared Sensor for carbon Observation Fourier Transform Spectrometer (TANSO-FTS) and Cloud & Aerosol Imager (TANSO-CAI) are the observation instruments on board the satellite. TANSO-FTS is used to measure the total columns of carbon dioxide and methane [30].

One of the important responsibilities or functions of TANSO-CAI is to provide information about aerosols by visualizing the atmosphere and the ground surface to detect cirrus clouds and aerosols, which are then used to correct the TANSO-FTS data [31,32]. Many studies show that inaccurate aerosol information can result in significant errors in the retrieved column-averaged dry-air mole fractions of CO_2 (XCO_2) results, and information on aerosol optical properties has been considered the most substantial factor affecting the XCO_2 retrieval algorithm [32,33]. However, since the TANSO-CAI does not have any definitive aerosol product, a priori information on aerosol as the input to the TANSO-FTS retrieval process is utilized from other platforms [34]. Because the atmosphere is constantly changing, different platforms will inevitably bring uncertainty due to their observation conditions and spatial-temporal differences. Therefore, as the onboard instruments use the same platform as TANSO-FTS, the development of the aerosol retrieval algorithm for TANSO-CAI can take full advantage of their spatial-temporal consistency and fulfill the requirement of obtaining more accurate aerosol information for the TANSO-FTS retrieval process. An AOD retrieval algorithm can extend the function of TANSO-CAI to the AOD observations to provide one-platform combination data (including carbon dioxide, methane and AOD) for future studies on the relationship between greenhouse gases and aerosols. Moreover, the AOD observations also play a key role for estimating ground-level PM2.5 concentrations [35]. The improvements of aerosol and chemical transport model have proliferated the assimilation of aerosol data, which can analyze and forecast dust storms and general air quality [36,37].

In this paper, I mainly describe a non-iterative AOD retrieval algorithm over land using the GOSAT TANSO-CAI red (0.67 μm), near-infrared (NIR, 0.87 μm) and SWIR (1.6 μm) bands. An important part of this work was the development of a surface reflectance estimation algorithm based on the analysis of TANSO-CAI and AErosol Robotic Network (AERONET) collocated data from different ground stations located in different global regions (described in Section 2.2.3). The AOD retrieval was based on a look-up table method that was established using a radiative transfer model, and the evaluation of the retrieval algorithm was conducted by comparing the retrieved AOD and AERONET AOD (described in Section 2.2.4).

2.2 General principle

For Lambertain surfaces under a cloud-free and vertically homogeneous atmosphere, the physical processes of reflection, scattering and absorption of solar radiation are described by Equation 1.

$$R_{TOA}(\lambda, \mu_0, \mu, \varphi) = R_{Path}(\lambda, \mu_0, \mu, \varphi) + \frac{R_{Surf}(\lambda) T_d(\lambda, \mu_0) T_u(\lambda, \mu)}{1 - R_{Surf}(\lambda) S(\lambda)} \quad (1)$$

where μ_0, μ and φ are the cosine of the solar zenith angle, the cosine of the satellite zenith angle and the relative azimuth angle between the sun and satellite, respectively; R_{TOA} is the TOA reflectance at a given wavelength λ; R_{Path} is the atmospheric "path reflectance", which includes the molecular and aerosol scattering; R_{surf} is the angular "surface reflectance"; S is the atmospheric hemispherical albedo; T_d is the atmospheric transmittance from TOA to surface; and T_u is the atmospheric transmission from the surface to TOA. From Equation 1, the TOA reflectance received by the satellite sensor can be regarded as the joint contribution of surface and atmosphere [20,38].

Three very important atmospheric parameters are $R_{Path,}$ T_dT_u and S, and they are functions of AOD. When the aerosol model is determined, multiple sets of $R_{Path,}$ T_dT_u and S values can be precomputed according to pre-defined combinations of AODs and geometrical conditions using the radiative transfer model. Then, a look-up table can be established for AOD retrieval [39–41].

When using the look-up table to retrieve AOD, the geometric parameters in the look-up table that are equal or closest to the geometric parameters of the satellite observations would be found. The selected geometric parameter set has multiple corresponding sets of atmospheric parameters: $R_{Path,}$ T_dT_u and S with different AOD values. Each set of atmospheric parameters $R_{Path,}$ T_dT_u and S, along with the estimated surface reflectance, is substituted into Equation 1 to calculate the theoretical apparent reflectance. The theoretical apparent reflectances for the different parameter sets are compared with the actual apparent reflectance; to find the one that is closest to the actual apparent reflectance; its corresponding AOD will be considered the retrieved AOD.

In Equation 1, we can see that the three atmospheric parameters and the surface reflectance are critical to the retrieval accuracy. Among these, the atmospheric parameters are provided by the radiative transfer model, which in turn is determined by the surface reflectance estimation algorithm.

2.3 Data and algorithm

2.3.1 GOSAT TANSO-CAI

The Greenhouse gases Observing SATellite, developed by the Japan Aerospace Exploration Agency (JAXA), the Ministry of the Environment of Japan (MOE) and the

National Institute for Environmental Studies (NIES) of Japan, was successfully launched on 23 January 2009 from Tanegashima Island, Japan [30,42]. GOSAT flies in a sun-synchronous orbit with a ground speed of 6.8 km/s at an altitude of 666 km and maintains an inclination angle of 98°. Its period of revolution is approximately 1 hour and 40 minutes, the local nadir overpass time is approximately 12:47 p.m., and it revisits the same point in space every three days with a total of 44 paths [42]. GOSAT carries two primary instruments, TANSO-FTS and the TANSO-CAI, to monitor the global distributions of carbon dioxide and methane and to detect clouds and aerosols [43].

The TANSO-CAI is a multichannel, narrow-band radiometer with ultraviolet (UV, band 1), visible (band 2), NIR (band 3) and SWIR (band 4) bands, used to capture daytime images of the atmosphere and ground. The center wavelengths of bands 1 to 4 are 0.38, 0.67, 0.87 and 1.6 μm, respectively. Bands 1, 2 and 3 all have 20 μm bandwidths, while band 4 has a 90 μm bandwidth. Bands 1 to 3 have a 500 m spatial resolution at the nadir and a 1000 km observation swath; band 4 has a 1.5 km spatial resolution and a 750 km scan swath [42–44].

TANSO-CAI provides different processing-level radiances, cloud flag, global radiance and reflectance distribution, along with NDVI products [30]. The satellite data used in this study are the CAI L1B+ radiance data, and the radiance of each band has to be converted to reflectance for AOD retrieval [45]. In CAI L1B+ product, radiometric and geometric corrections (such as orthorectification, band-to-band registration and resampling) have been performed [46,47]. The observation information includes important geometric parameters for retrieval, such as the solar zenith/azimuth angle and satellite zenith/azimuth angle, which are recorded and added into the product data [48].

2.3.2 AERONET AOD data

The AERONET [49] is a ground-based remote-sensing aerosol network with over 800 stations globally, providing long-term, continuous, standardized data on aerosol optical, microphysical and radiative properties. The AERONET obtains spectral AOD within the 0.34 to 1.02 μm wavelength range by direct Sun measurement with an accuracy of 0.01–0.02, and the AOD data are computed for three data quality levels: Level 1.0 (raw, unscreened), Level 1.5 (cloud-screened), and Level 2.0 (cloud-screened and quality-assured) [50,51]. In this study, extensive use of AERONET Level 2.0 AOD data was made for atmospheric correction and validation of satellite retrievals. Since the retrieved AOD is at the wavelength of 550 nm, comparing TANSO-CAI AOD with AERONET AOD at the same wavelength requires that all AERONET AOD at other wavelengths should first be interpolated into 0.55 μm using the Angstrom exponent,

which can be calculated as follows [52]:

$$\alpha = -\frac{\ln\left(\frac{\tau_\lambda}{\tau_{0.55}}\right)}{\ln\left(\frac{\lambda}{0.55}\right)} \quad (2)$$

where τ_λ is the AOD at a given wavelength λ, and α is the Angstrom exponent, the values of which are provided by AERONET measurement.

2.3.3 Atmospheric correction of collocated TANSO-CAI/AERONET data

To develop a surface reflectance (at 0.67 μm) estimation algorithm using the TOA reflectances at 1.6 μm, it is imperative to analyze the relationship between the satellite-measured reflectance and the surface reflectance by conducting accurate atmospheric correction.

Through atmospheric correction, I attempt to obtain information on atmospheric optical properties and then determine the real surface reflectance using the information from satellite observation [27]. Atmospheric correction primarily eliminates the impact of molecular and aerosol scattering and absorption by gases, such as water vapor, ozone, oxygen, and aerosols [53–56]. Molecular scattering and absorption by ozone and oxygen, which have relatively stable atmospheric concentrations, are not difficult to subtract. In addition, it is practical to correct the effects of water vapor by using climatology data or other satellite data. However, aerosols are the most difficult component to eliminate since their distributions are often heterogeneous [56].

Fortunately, the theoretical model of atmospheric radiative transfer can be used to account for the effects of the atmospheric components, including those mentioned above [57]. In this study, the 6S (Second Simulation of a Satellite Signal in the Solar Spectrum) radiative transfer model and the ground-measured AOD from AERONET were used to perform atmospheric correction on TANSO-CAI images. 6S is an advanced radiative transfer code developed specifically for satellite applications [58]. It offers two main working modalities: simulation and atmospheric correction [59]. To run this code, a number of parameters are required as input: geometric conditions, atmospheric model, aerosol model and AOD, spectral conditions, ground reflectance type, and TOA reflectance/radiance. The atmospherically corrected reflectance/radiance and the relevant correction coefficients are output as results [60]. The continental aerosol model was selected as it can broadly describe both the scattering and absorption properties [16,61]. The atmospheric correction was performed on the arranged spatially and temporally matched TANSO-CAI/AERONET collocated data. The selection of TANSO-CAI/AERONET collocation data are based

on the following criteria: GOSAT overpasses are within 15 minutes of the AERONET measurements and localized within a 30 km radius around the AERONET sites. To reduce the effect of multiple aerosol scattering, only the collocated data with low AOD are corrected atmospherically [61]. The TANSO-CAI/AERONET collocated data, selected in 2011, with $\tau_{0.55} < 0.1$, were obtained from nine global sites (Figure 2.1 and Table 2.1) [62]. After atmospheric correction, they were utilized to study the relation between 0.67 μm surface reflectance and 1.6 μm TOA reflectance.

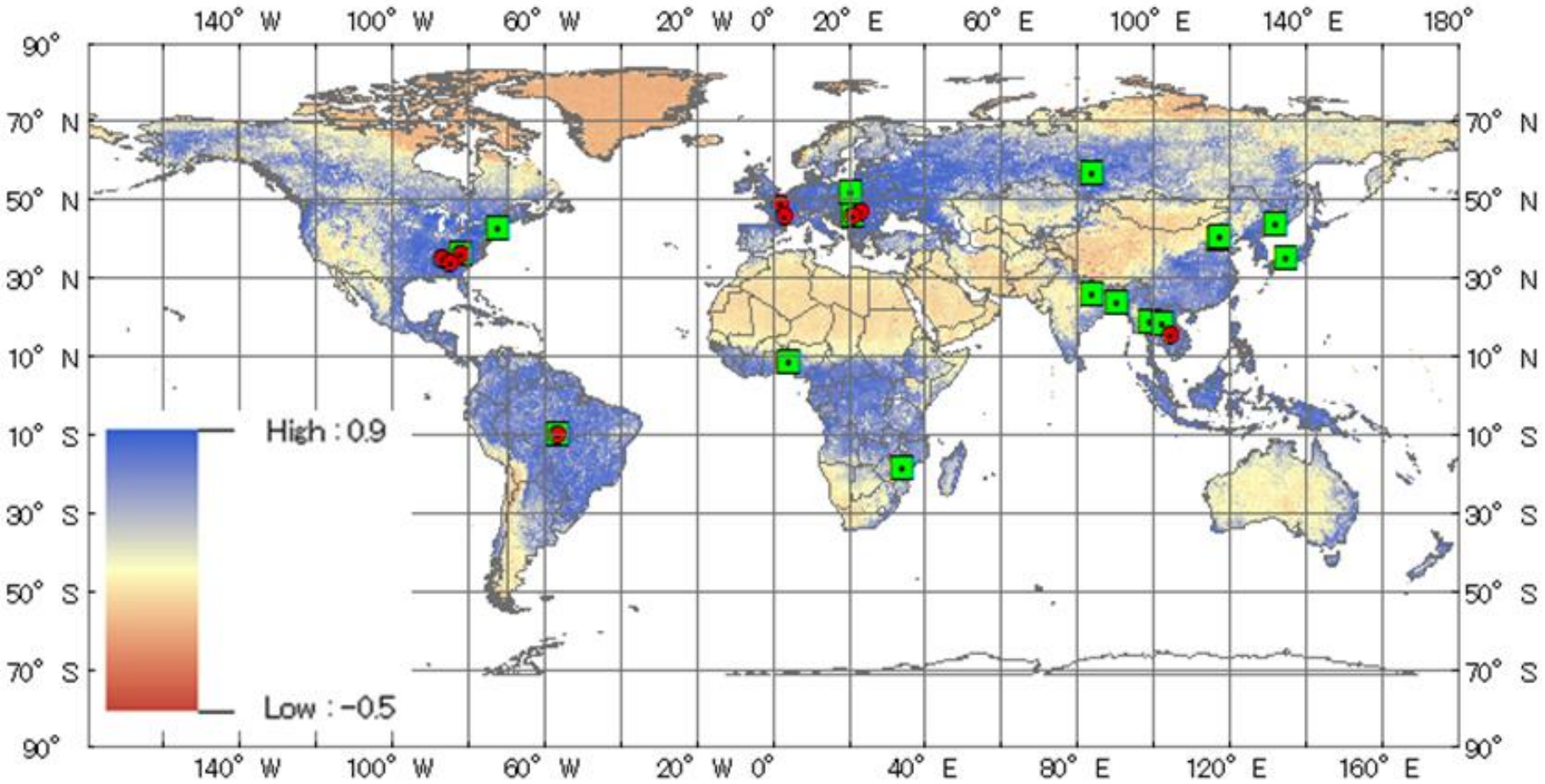

Figure 2.1 The geographical distribution of AErosol Robotic Network (AERONET) sites (red sites were used for studying reflectance relationships, and green sites were used for validating results) and global Normalized Difference Vegetation Index (NDVI, it ranges from −1 to 1, a 0 or negative value means no vegetation and close to 1 indicates the highest possible density of green leaves) from Thermal and Near-infrared Sensor for Carbon Observation-Cloud and Aerosol Imager (TANSO-CAI) on 29 June 2015.

Table 2.1 The geographical information of AERONET sites ([S] sites were used for studying reflectance relationships, [V] sites were used for validating results).

Site Name	Longitude (decimal_degrees)	Latitude (decimal_degrees)	Elevation (meters)
Alta_Floresta [S, V]	−56.10	−9.87	277
Appalachian_State [S, V]	−81.69	36.21	1080
Aubiere_LAMP [S]	3.11	45.76	423
Belsk [V]	20.79	51.84	190
Chiang_Mai_Met_Sta [V]	98.97	18.77	312
CLUJ_UBB [S]	23.55	46.77	405
Dhaka_University [V]	90.40	23.73	34
DRAGON_Mt_Rokko [V]	135.23	34.76	760
Gandhi_College [V]	84.13	25.87	60
Georgia_Tech [S]	−84.40	33.78	294
Gorongosa [V]	34.35	−18.98	30
Harvard_Forest [V]	−72.19	42.53	322
Ilorin [V]	4.34	8.32	350
Palaiseau [S]	2.21	48.70	156
Timisoara [S, V]	21.23	45.75	122
Tomsk_22 [V]	84.07	56.42	80
UAHuntsville [S]	−86.65	34.73	223
Ubon_Ratchathani [S]	104.87	15.25	120
Ussuriysk [V]	132.16	43.70	280
Vientiane [V]	102.57	17.99	170
XiangHe [V]	116.96	39.75	36
Xinglong [V]	117.58	40.40	970

2.3.4 Relationship between TOA reflectance at 1.6 μm and surface reflectance at 0.67 μm

Atmospheric correction resulted in surface reflectance at 0.67 μm (TANSO-CAI band 2), which was compared with the TOA reflectance at 1.6 μm; Figure 2.2a shows a plot of their match-ups and regression line, with the color scale indicating the data frequency. The correlation coefficient (r) value is 0.79, and the slope and offset are approximately 0.42 and −0.01. The regression exhibits large scatter and cannot satisfactorily ensure retrieval accuracy. For example, where the TOA reflectance at 1.6 μm is 0.2, the regression function would lead to a surface reflectance of 0.072 at 0.67 μm. The scatter plot shows the surface reflectance at 0.67 has a large variation, ranging from 0.020 to 0.185. This uncertainty could cause large deviations in AOD retrieval. Therefore, using this regression function to estimate surface reflectance at 0.67 μm is not advised.

Levy et al. (2007) and Thomas et al. (2008) suggest that the reflectance relationships between the red (0.67 μm) and SWIR bands (such as 1.6 and 2.1 μm) vary based on the surface type (vegetation condition/amount) [23,61,63]. Figure 2.2b shows the comparison of the surface reflectance at 0.67 μm and TOA reflectance at 1.6 μm, and the color of each point indicates the value of the NDVI, according to the given color scale. It is easy to see that this relationship of surface reflectance at 0.67 μm and TOA reflectance at 1.6 μm (0.67 vs. 1.6) is a function of NDVI, and an apparent change in regulation is that the higher NDVI data seem to have lower slope, and vice versa. Therefore, like Levy et al. (2007) and Thomas et al. (2008), I also attempted to use the NDVI to indicate the impact of surface variability on the reflectance relationships of the red and SWIR bands [23,61,63]. NDVI is a numerical indicator that has been widely applied to estimate the quantity, quality and development of vegetation. It uses the different absorption properties of vegetation toward the red and NIR wavelengths to measure the biomass amount. Sensors onboard satellites or aircrafts can calculate the NDVI value according to Equation 3 [64–66].

$$\mathrm{NDVI} = (\mathrm{R_{NIR}} - \mathrm{R_{red}})/(\mathrm{R_{NIR}} + \mathrm{R_{red}}) \quad (3)$$

where R_{NIR} and R_{red} are the reflectances in the NIR and red bands. Specifically, these bands are the TANSO-CAI band 3 (0.87 μm) and band 2 (0.67 μm), respectively. The NDVI values of these experimentally collocated data were calculated performing atmospheric correction on bands 2 and 3. The scatter plots in Figure 2.3 are the subsets of the total set of experimental data in Figure 2.2, they display the reflectance relationships at 1.6 μm and 0.67 μm, varying by intervals of 0.025 in NDVI. Each

scatter plot of Figure 2.3 has a specific 0.67 vs. 1.6 relationship and regression line for a given NDVI value. Almost all of them were found to show significantly higher r-values than the total set of experimental data. In Figure 2.4, the slopes and intercepts of 0.67 vs. 1.6 regressions (for the scatter plots in Figure 2.3) are plotted as functions of NDVI. The regression slopes of the scatter plots are highly correlated with NDVI ($r = -0.955$), and the slopes are decreasing as surface NDVI increases. In contrast, the regression intercepts have a very weak correlation ($r = -0.198$) with NDVI changes. Based on these results, an NDVI-dependent regression function for estimating the surface reflectance at 0.67 μm from the 1.6 μm band was established and is given in Equation 4.

$$
\begin{aligned}
&R_{0.67} = \mathrm{Slope}_{0.67/1.6} * R_{1.6} + \mathrm{Intercept}_{0.67/1.6},\\
&\text{with}\\
&\mathrm{Slope}_{0.67/1.6} = a_1 * \mathrm{NDVI} + b_1,\\
&\mathrm{Intercept}_{0.67/1.6} = a_2 * \mathrm{NDVI} + b_2,
\end{aligned}
\tag{4}
$$

where $R_{0.67}$ is the surface reflectance at 0.67 μm; $R_{1.6}$ is the TOA reflectance at 1.6 μm; and NDVI is calculated by atmospherically correcting the reflectances of the NIR and red bands. The coefficient values ($a_1 = -0.605$, $b_1 = 0.590$, and $a_2 = -0.009$, $b_2 = 0.023$) are based on the results in Figure 2.4.

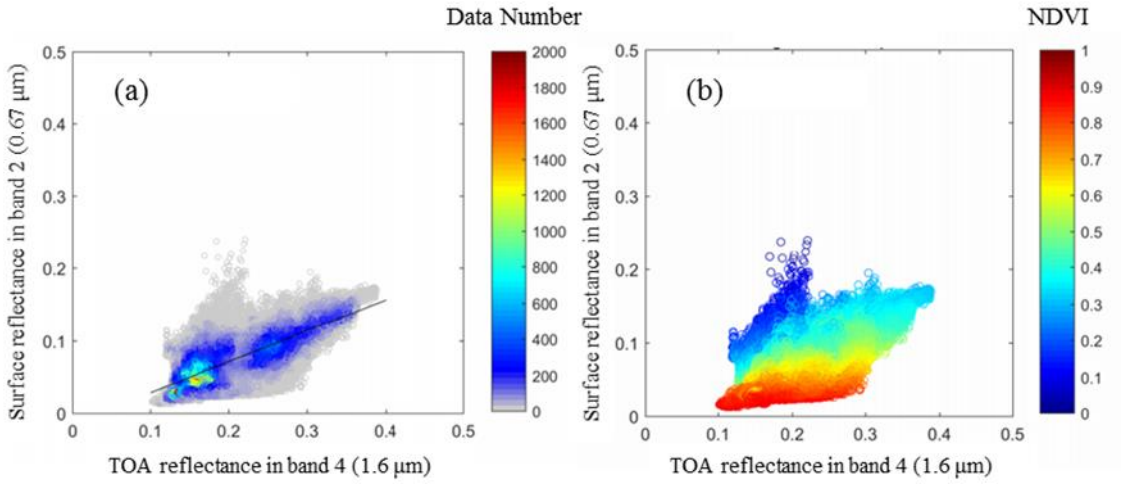

Figure 2.2 Scatter plots of top-of-atmosphere (TOA) reflectance at 1.6 μm and surface reflectance at 0.67 μm with: density data frequency (**a**); and NDVI (**b**). The results are from TANSO-CAI/AERONET collocated data (selected from the [s] marked AERONET sites in Table 2.1) in 2011 with AOD (at 0.55 μm) < 0.1.

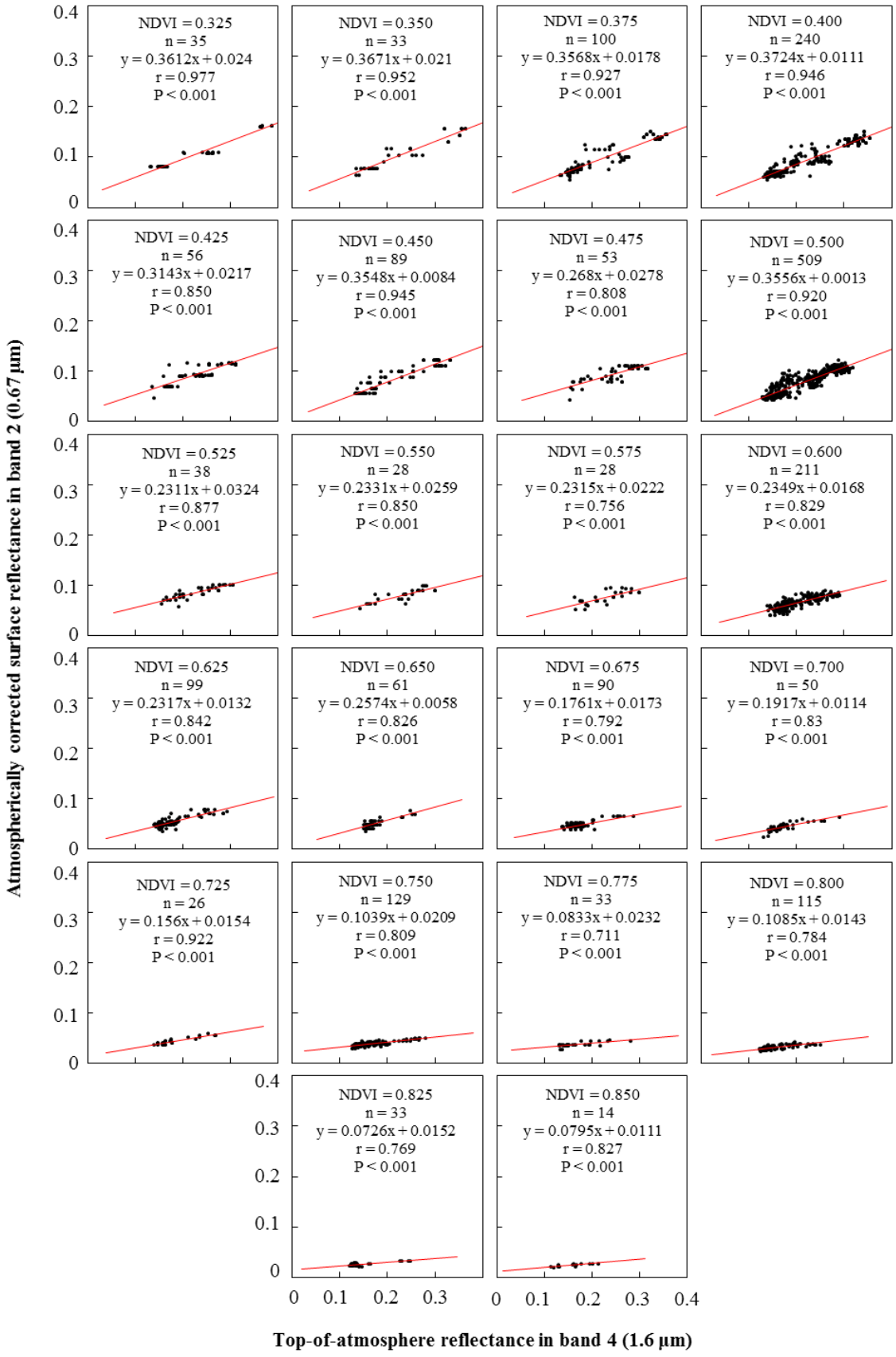

Figure 2.3 Relationship between TOA reflectances at 1.6 µm and surface reflectance at 0.67 µm varying with different NDVI values (All data points in each graph fall within NDVI value ± 0.0001).

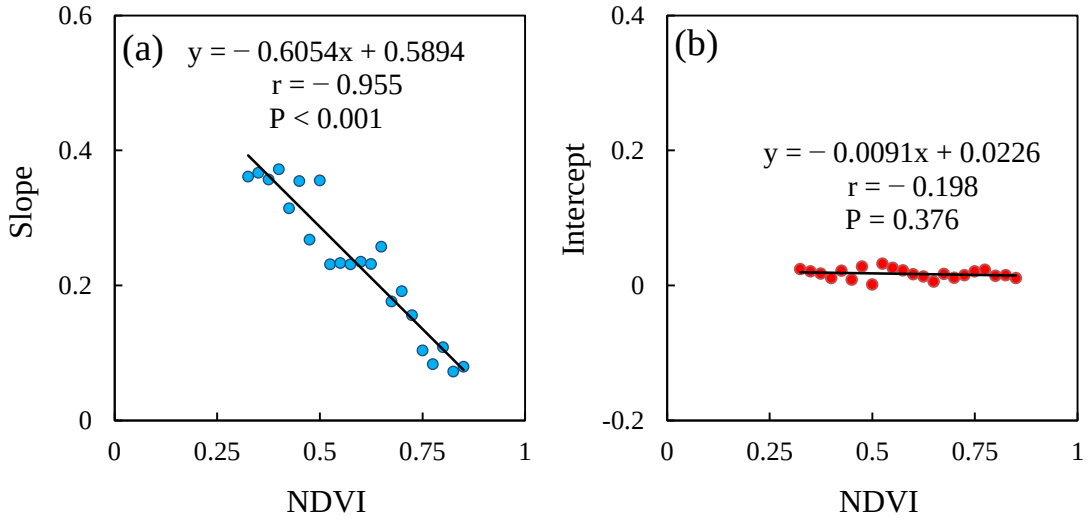

Figure 2.4 Relationship between TOA reflectances at 1.6 μm and surface reflectance at 0.67 μm as a function of NDVI: (**a**) slopes (for each scatter plot in Figure 3 with given NDVI values) as a function of NDVI; and (**b**) intercepts as a function of NDVI.

I tested this regression function by comparing the estimated results with the atmospherically corrected surface reflectance using the 6S radiative transfer code and AERONET measurements (Figure 2.5a). With an r-value of 0.959, the estimated surface reflectance has a very high consistency with the atmospherically corrected surface reflectance. In a biophysical context, as NIR light is reflected by spongy mesophyll cells [66], so it could be expected that higher-density vegetation land surface would show relatively higher reflectance at 0.87 μm than other surface types. Many studies suggest that the reflectances of red and SWIR have stronger correlation in dense dark vegetation areas [63]. Therefore, I also tested the data with surface reflectance values higher than 0.25 in band 3. As depicted in Figure 2.5b, the r-value increases to 0.980, and most of the overestimated points have been removed. The above results indicate that the relationship of 0.67 vs. 1.6 is dependent on the amount of vegetation and that NDVI can be used as a suitable tuner to interpret how the 0.67 vs. 1.6 ratio changes with different surface types.

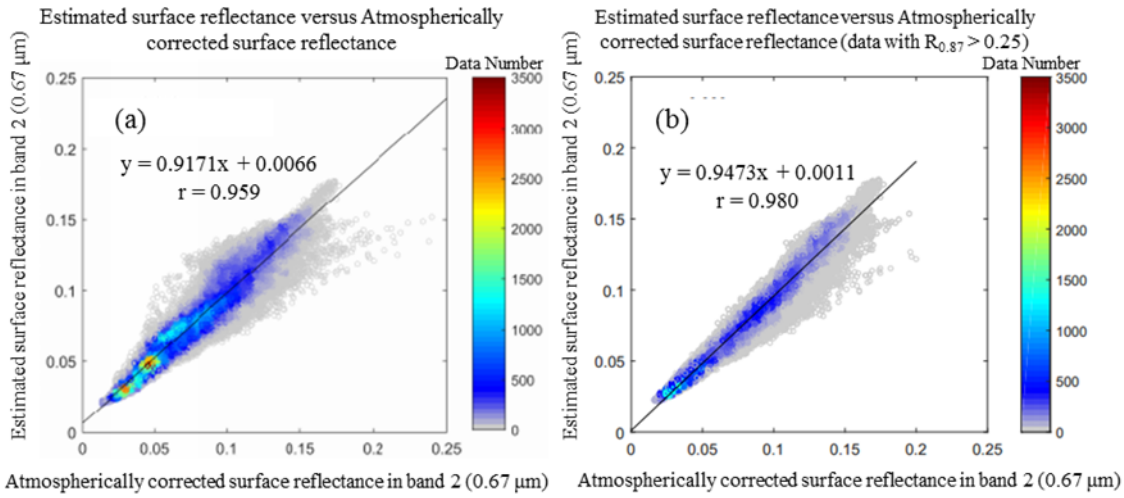

Figure 2.5 Comparison of estimated surface reflectances and atmospherically corrected surface reflectances at 0.67 μm: (**a**) experimental data; and (**b**) experimental data with reflectance of band 3 larger than 0.25.

2.3.5 The modified $AFRI_{1.6}$ algorithm

The NDVI-based regression function has great practicability for estimating surface reflectance under very low aerosol conditions. However, the sensitivity of NDVI to the influence of atmospheric aerosols [27,28] render it ill-suited for estimating reflectance under higher aerosol conditions. Typically, as the AOD increases, the satellite-measured NDVI values rapidly decrease [66,67]. In the MODIS retrieval algorithm Collection 5, $NDVI_{SWIR}$, a new vegetation index (VI) much less influenced by aerosols, is calculated from the 1.2 μm and 2.1 μm channels used for estimating the surface conditions [61,63]. Nevertheless, TANSO-CAI does not have the 1.2 μm and 2.1 μm wavelength bands on board. To overcome these difficulties, I developed a new algorithm based upon the idea of AFRI [68], which was first proposed by Karnieli et al. (2001). AFRI is calculated as function of reflectances of NIR and SWIR (1.6 or 2.1 μm) bands and described by the following equations.

$$AFRI_{2.1} = (R_{NIR} - 0.5 * R_{2.1})/(R_{NIR} + 0.5 * R_{2.1}) \quad (5)$$

$$AFRI_{1.6} = (R_{NIR} - 0.66 * R_{1.6})/(R_{NIR} + 0.66 * R_{1.6}) \quad (6)$$

where R_{NIR}, $R_{1.6}$ and $R_{2.1}$ are the surface reflectances of NIR, 1.6 and 2.1 μm bands, respectively, and the coefficients 0.5 and 0.66 are based on the empirical linear relationships between the red (0.67 μm) band and the SWIR (1.6 and 2.1 μm) bands that were found by aircraft measurements [68]. The difference between NDVI and AFRI is that the SWIR reflectance has replaced the red reflectance of NDVI, according

to these empirical linear relationships. Thus, it takes full advantage of the ability of SWIR to penetrate the atmospheric column containing aerosols with negligible influence; at the same time, it remains sensitive to vegetation and has the potential to become a capable alternative to NDVI for estimating surface status [68,69]. $AFRI_{1.6}$ and $AFRI_{2.1}$ were developed based on a single constant linear relationship between red and SWIR bands; however, the relationship of 0.67 vs. 1.6 is sensitive to changes in the surface type. Regarding this, it was already shown in Section 2.3.4 that the relationship of 0.67 vs. 1.6 is typically dependent on surface vegetation conditions (tested using TANSO-CAI bands). Therefore, a single constant linear relationship cannot represent the true correlation of 0.67 vs. 1.6 for ground with complicated surface conditions, because any error from a biased linear regression function would be inherited and applied in $AFRI_{1.6}$.

Combining the main strategies of the AFRI and the NDVI-based regression functions, I developed a new aerosol-free NDVI estimation method named the modified $AFRI_{1.6}$ algorithm. The modified $AFRI_{1.6}$ algorithm retains the original advantages of $AFRI_{1.6}$, which is less influenced by aerosols, but replaces the single constant relationship-based method with a method that takes the vegetation-dependent relationships of 0.67 vs. 1.6 into account. Equation 4 can be rewritten as Equation 7, in which, the surface reflectance at 0.67 μm is a function of both the NDVI and TOA surface reflectance at 1.6 μm. Equation 8 shows the NDVI calculated from the TANSO-CAI bands.

$$R_{0.67} = (a_1 * NDVI + b_1) * R_{1.6} + a_2 * NDVI + b_2 \quad (7)$$

$$NDVI = (R_{0.87} - R_{0.67})/(R_{0.87} + R_{0.67}) \quad (8)$$

where $R_{0.87}$ is the TOA reflectance of TANSO-CAI band 3; $R_{0.67}$ is the estimated surface reflectance of TANSO-CAI band 2; and NDVI is the aerosol-free NDVI, calculated by $R_{0.87}$ and $R_{0.67}$. By substituting Equation 7 into Equation 8, and then rearranging, I obtain Equation 9.

$$NDVI^2 * (a_1 * R_{1.6} + a_2) + NDVI * (R_{0.87} + (a_1 + b_1) * R_{1.6} + a_2 + b_2) + (b_1 * R_{1.6} + b_2 - R_{0.87}) = 0 \quad (9)$$

Equation 9 is a quadratic equation in NDVI, and the solutions of the equation are as follows:

$$\mathrm{NDVI} = \frac{-(R_{0.87} + (a_1 + b_1) * R_{1.6} + a_2 + b_2)}{2 * (a_1 * R_{1.6} + a_2)} \pm \frac{\sqrt{(R_{0.87} + (a_1 + b_1) * R_{1.6} + a_2 + b_2)^2 - 4 * (a_1 * R_{1.6} + a_2) * (b_1 * R_{1.6} + b_2 - R_{0.87})}}{2 * (a_1 * R_{1.6} + a_2)} \quad (10)$$

In Equations 7 to 10, the coefficient values are $a_1 = -0.605$, $b_1 = 0.590$, and $a_2 = 0$, $b_2 = 0.023$. Among these, a_2 was set to a value of 0 since the relationship of the intercepts with NDVI is considered very weak. As Equation 10 shows, this formula has two roots. In actual retrieval, only one reasonable root would be obtained because NDVI should be within the range of −1 to 1 and the other root exceeds this range. Using the estimated aerosol-free NDVI in Equation 7, the surface reflectance at 0.67 μm can be estimated and used to retrieve the AOD.

2.3.6 The look-up table

The AOD can be determined by solving the radiative transfer equation with the relevant atmospheric parameters. For faster processing, I created a look-up table using the 6S radiative transfer code that has been widely used in different remote-sensing applications and sensors; for example, it is used to calculate the look-up table for MODIS atmospheric correction algorithm [61,70]. This look-up table includes pre-computed atmospheric parameters ($R_{Path,}$ T_dT_u and S) with given combinations of aerosol models, geometrical conditions and AODs. By using the look-up table, the appropriate atmospheric parameter combinations for solving the radiative transfer equation, can be rapidly selected, thereby improving retrieval efficiency.

The 6S model is applicable for calculating atmospheric radiative transfer with a solar reflection range of 0.25 to 4.0 μm, and a 2.5 nm step used for spectral integration [61]. Before using the 6S model, the spectral condition of GOSAT TANSO-CAI was defined band by band with the interpolated TANSO-CAI Spectral Response Function. The look-up table was constructed using the following parameters: geometrical conditions, atmosphere model, aerosol models, AOD and atmospheric parameters ($R_{Path,}$ T_dT_u and S). The geometrical conditions include twenty-one solar zenith angles from 0° to 60° with a step of 3°, six satellite zenith angles from 0° to 60° with a step of 12°, eight relative azimuth angles from 0° to 168° with a step of 24°, and one relative azimuth angle at 180°. Three different atmosphere models, Tropical, Midlatitude Summer and Midlatitude Winter, were taken into account. Because the previous atmospheric correction was performed with the continental aerosol model, I selected the continental aerosol model as the aerosol model for the look-up table construction

[16,61]. AOD values in the look-up table were set: the smallest with a value of 0.001, and others in the range of 0.01 to 2.00 with an increment of 0.01.

2.3.7 AOD retrieval

In this paper I use the TANSO-CAI 1.6 μm band to estimate the surface reflectance of 0.67 μm band to retrieve the AOD. According to the observation geometry parameters (solar zenith angle, azimuth angle, satellite zenith angle, and azimuth angle) in the satellite data files, the relevant observation geometry parameters that are equal or closest to the values in the established look-up table can be selected. Corresponding to the selected geometric parameters, there are multiple sets of $R_{Path,}$ T_dT_u and S values with different AOD values. I input every parameter set and the surface reflectance into Equation 1 to calculate the theoretical apparent reflectance in the 0.67 μm band. Then I could obtain multiple sets of theoretical apparent reflectances. Comparing the apparent reflectance of the TANSO-CAI data with these theoretical apparent reflectances, the one closest to the actual apparent reflectance and its corresponding AOD was selected as the retrieved AOD of this pixel.

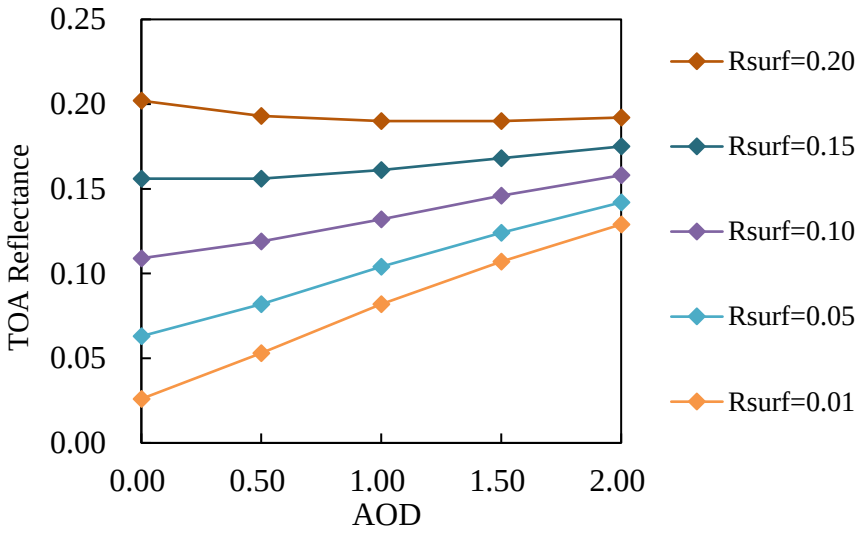

Figure 2.6 TOA reflectance as a function of AOD and surface reflectance at 0.67 μm. Simulation is performed under the observation geometric conditions with solar zenith angle = 45°, satellite zenith angle = 2° and relative azimuth angles = 45°.

However, due to the limitations of the instruments and algorithm, not all pixels can be used for retrieval. For example, when using the DT algorithm, the dark pixels should be preselected. I simulated the relationship between the TOA reflectance in the TANSO-CAI 0.67 μm band and the AOD for different surface reflectances using the 6S code. Figure 2.6 demonstrates that the higher surface reflectance has smaller TOA reflectance changes as AOD increases. Namely, the higher surface reflectance areas are not sensitive to the AOD changes. It is noted that when the surface reflectance increases from 0.01 to 0.1, the TOA reflectance still responds to the increase in the AOD. To reduce the simulation difference, even with other observed geometric conditions, the pixels with surface reflectance values that are higher than 0.085 should not be selected to perform AOD retrieval [23]. In addition, based on the results presented in Section 2.3.4, to ensure the AOD retrieval accuracy, the thresholds of TOA reflectance of red band and estimated aerosol-free NDVI were set, when the TOA reflectance of red band is lower than 0.225, or the estimated aerosol-free NDVI is out the range of 0.375 to 0.825, it should not be taken into account during the retrieval.

2.4 Results and discussion

2.4.1 Case study over South Asia

An example of the AOD retrieval over the South Asian region from TANSO-CAI using our algorithm is shown in Figure 2.7. Figure 2.7a,b shows the TANSO-CAI RGB composite images (shown in true color) of 4 and 7 November 2011, and their retrieved AOD distributions are shown in Figure 2.7c,d, respectively. The Southwestern part of China, Nepal and the Northern part of India are covered in this scene. The area between lines A and B is the North of Indo-Gangetic basin, one of the world's largest drainage basins [71]. It is bordered by the Himalayas, which are located on the border between Nepal and Tibet, China. Rapidly growing industrialization and expanding urbanization has led to high pollution in these regions, and as such it has become a regional aerosol hot spot [71,72]. Comparing Figure 2.7a,b, the air condition of Figure 2.7a in the region between lines A and B seems highly polluted. This could be attributed to the burning of biomass. I used MODIS Thermal Anomalies/Fire products (MOD14A1) [73] to detect the occurrence of fire. A large patch of clustered burning spots out of and near the scene was extracted on 4 November 2011, and burning spots were apparently decreased on 7 November 2011. As shown in Figure 2.7c,d, the relatively higher AOD dominates in the area between lines A and B; in contrast, very low AOD is distributed in the area between lines B and C. This is due to the unique topography (Figure 2.7e), with the mighty Himalayan peaks [74] of acting like a barrier and blocking the transfer of biomass-burning aerosols, causing the aerosols to

accumulate in the area between lines A and B surrounding the peaks. Our retrieval result successfully illustrated the contrast in AOD between areas of AB (line A to line B) and BC (line B to line C). Additionally, as the terrain gradually increases from the foot of a hill to the top (near the area of line B), the influx of aerosols decreases and becomes rare. Our results also reflected this detailed gradual change in AOD: over the area of the peak slope, there is a long and narrow zone with smoothly changing color. I can see that there is only a small retrieval result in the China area (the area north of line C). This is mainly because the surface over western China is relatively bright [26], and when the estimated surface reflectance is higher than 0.085, those pixels are not taken into account in the AOD retrieval. The absence of AOD retrieval in the area between lines A and B is also caused by the high estimated surface reflectance and the influence of cloud cover. The AERONET station Pokhara, located in the southeastern part of the image, provided the AOD measurements within ± 15 min of the satellite observation time, and the mean AOD on 4 and 7 November are 1.98 and 0.57, respectively. The results of our algorithm show that the retrieved AOD near the Pokhara station are 1.95 and 0.65 on corresponding date, very close to the AERONET measurements. The details of validation using ground-level measurements from global sites are shown in Section 2.4.2. As shown in this case study, one of the deficiencies as well as challenges in the retrieval performance is that there are some retrieved spots at the edges of clouds.

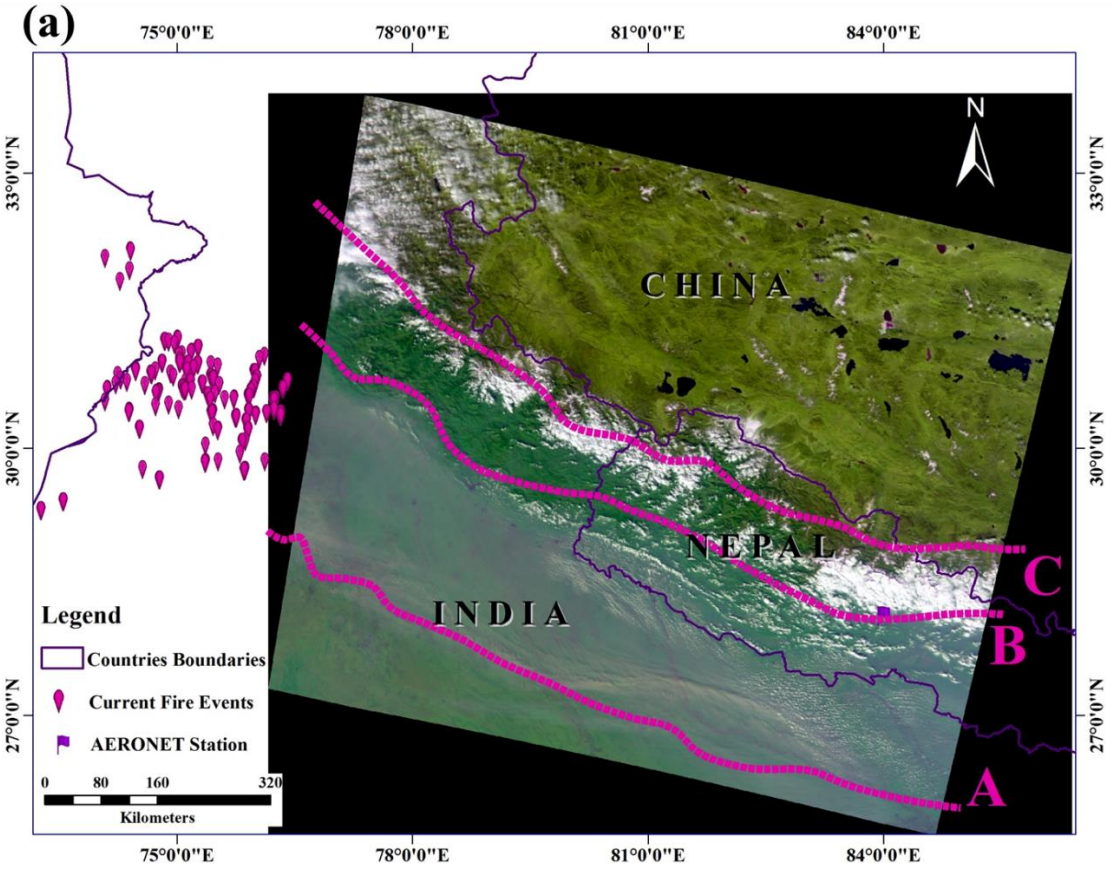
(a)
75°0'0"E
78°0'0"E
81°0'0"E
84°0'0"E
33°0'0"N
30°0'0"N
27°0'0"N
N
CHINA
NEPAL
INDIA
C
B
A
Legend
Countries Boundaries
Current Fire Events
AERONET Station
0 80 160 320
Kilometers

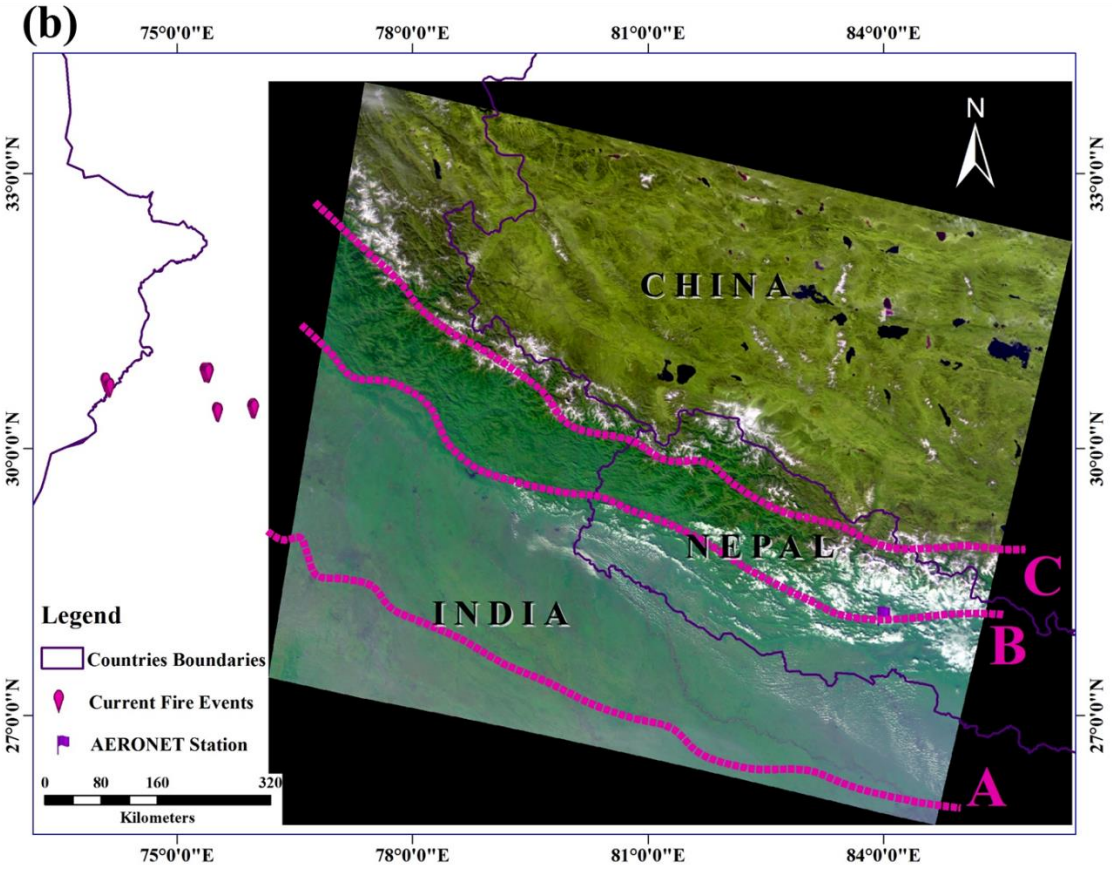
(b)
75°0'0"E
78°0'0"E
81°0'0"E
84°0'0"E
33°0'0"N
30°0'0"N
27°0'0"N
N
CHINA
NEPAL
INDIA
C
B
A
Legend
Countries Boundaries
Current Fire Events
AERONET Station
0 80 160 320
Kilometers

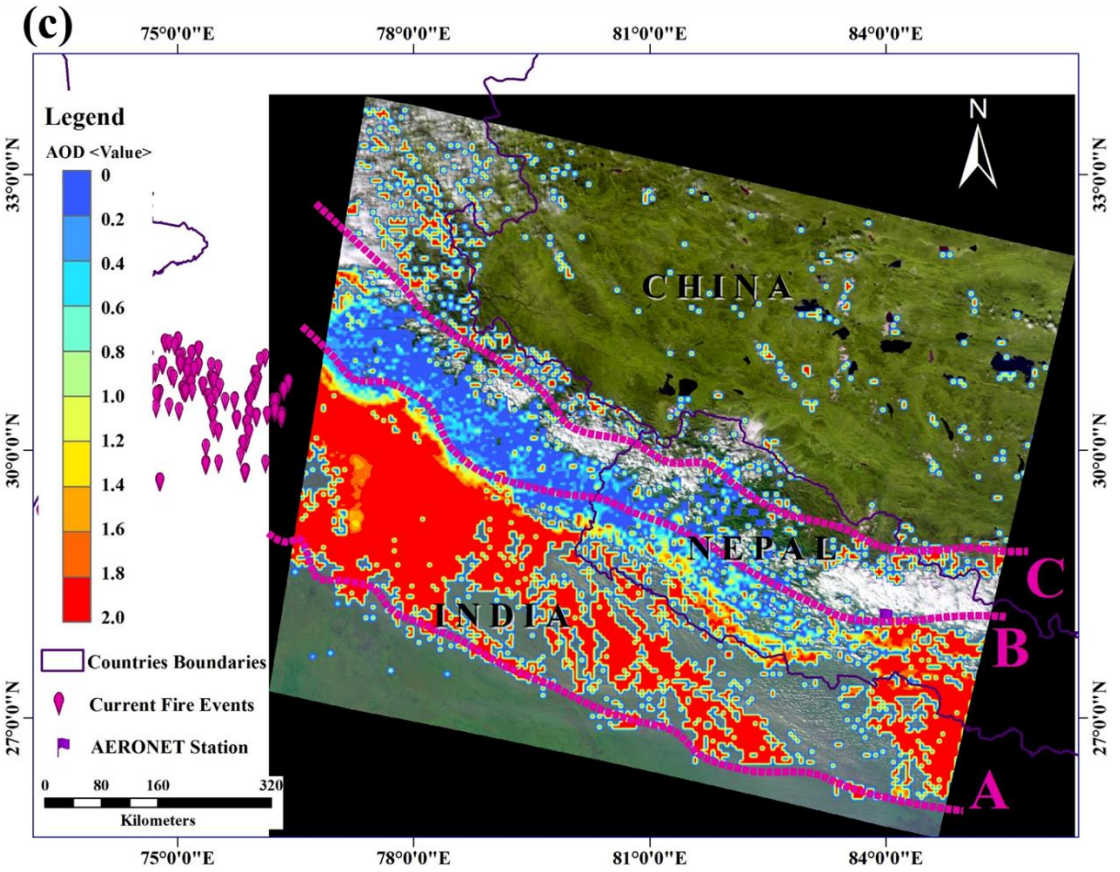
(c)
75°0'0"E
78°0'0"E
81°0'0"E
84°0'0"E
33°0'0"N
30°0'0"N
27°0'0"N
Legend
AOD <Value>
0
0.2
0.4
0.6
0.8
1.0
1.2
1.4
1.6
1.8
2.0
Countries Boundaries
Current Fire Events
AERONET Station
0 80 160 320
Kilometers
N
CHINA
NEPAL
INDIA
A
B
C

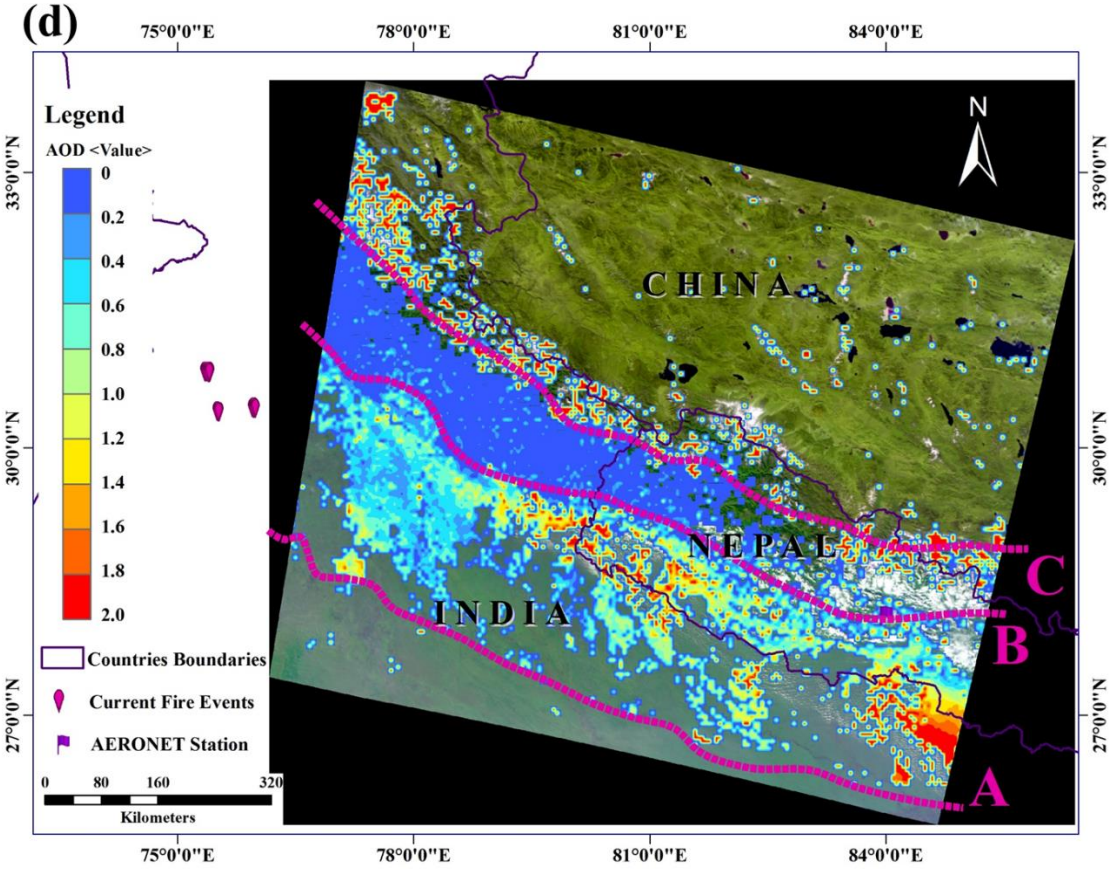
(d)
75°0'0"E
78°0'0"E
81°0'0"E
84°0'0"E
33°0'0"N
30°0'0"N
27°0'0"N
Legend
AOD <Value>
0
0.2
0.4
0.6
0.8
1.0
1.2
1.4
1.6
1.8
2.0
Countries Boundaries
Current Fire Events
AERONET Station
0 80 160 320
Kilometers
N
CHINA
NEPAL
INDIA
A
B
C

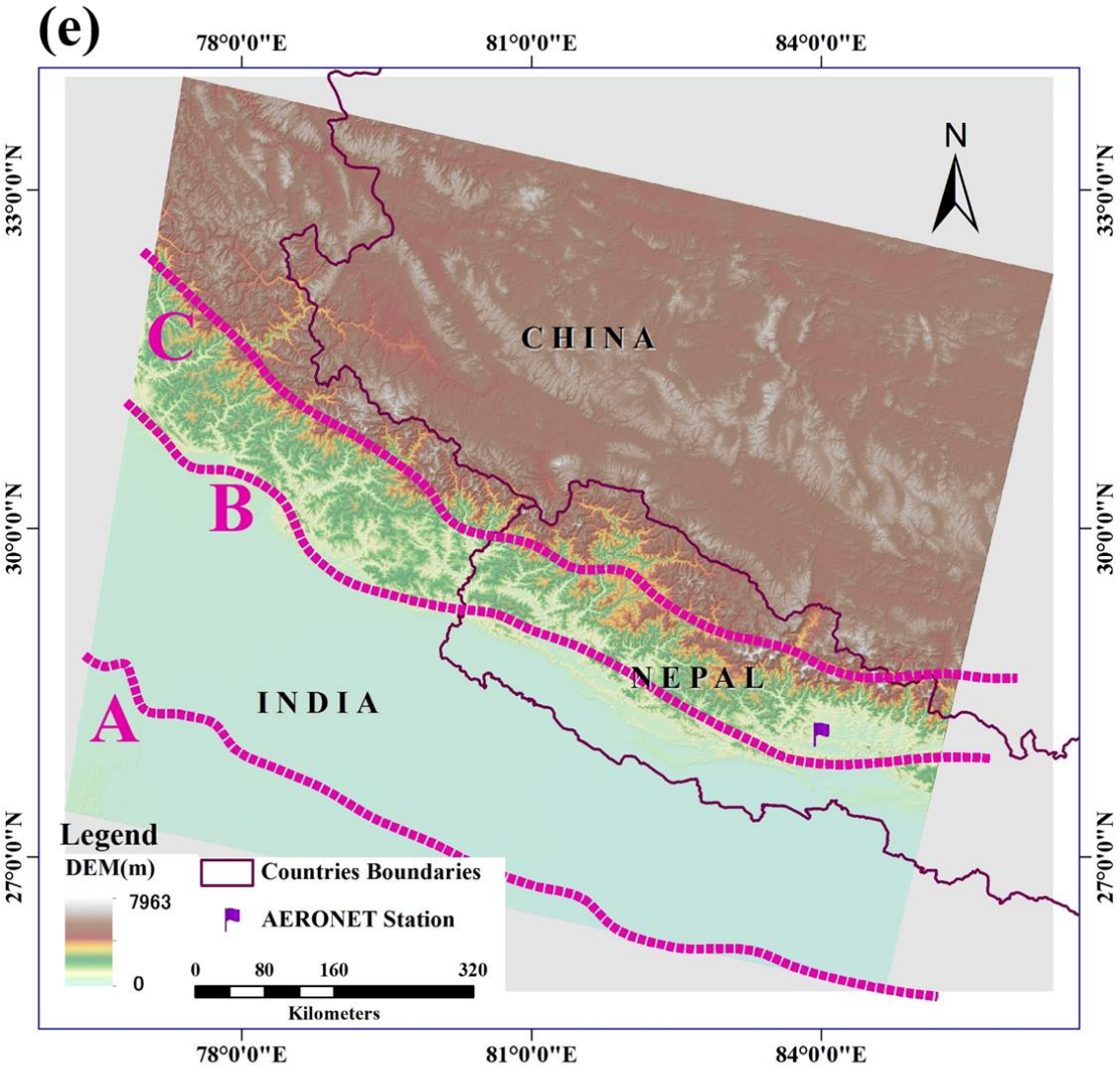

Figure 2.7 Examples of the AOD retrieval over South Asian region: (**a**) RGB image from TANSO-CAI on 4 November 2011; (**b**) RGB image from TANSO-CAI on 7 November 2011; (**c**) retrieved AOD at 550 nm on 4 November 2011; (**d**) retrieved AOD at 550 nm on 7 November 2011; and (**e**) topographic image.

2.4.2 Comparison of retrieved AOD with AERONET measurements

For quantitative validation, ground-based Sun photometer measurements are widely used to evaluate the accuracy of AOD satellite retrievals. All ground-based AOD measurements from AERONET that are within 15 minutes of the GOSAT observation are considered for validation. The TANSO-CAI/AERONET collocation criteria [75–77] for validation are more stringent in space. AOD results retrieved

within a radius of 7.5 km of the AERONET site are averaged and then evaluated by comparison with a total of 300 collocated data points, provided from 16 AERONET sites for the period from April 2009 to August 2014. The 16 AERONET sites are located in East Asia (XiangHe, DRAGON_Mt_Rokko and XiangHe), Southeast Asia (Chiang_Mai_Met_Sta, Vientiane and Gandhi_College), South Asia (Dhaka_University), North Asia (Tomsk_22 and Ussuriysk), South Africa (Gorongosa and Ilorin), Europe (Belsk and Timisoara), South America (Alta_Floresta) and North America (Appalachian_State and Harvard_Forest) (green points in Figure 2.1).

The scatter plots of TANSO-CAI versus AERONET AOD are shown in Figure 2.8. The linear regression analysis shows that the TANSO-CAI-retrieved AOD has high agreement on the AERONET AOD with an r-value of 0.91. The regression line lies close to the one-to-one line with a slope of 1.10 and an intercept of 0.02. In addition to the linear regression analysis, some additional statistical indicators, including root mean square error (RMSE), mean bias error (MBE) and expected error (EE), were used to evaluate this algorithm. The RMSE [50,78,79] is sensitive to systematic and random errors. It is an absolute criterion and is commonly used to determine differences between satellite-retrieved AODs and ground-measured AODs. The RMSE (Equation 11) is defined as follows.

$$\mathrm{RMSE} = \sqrt{\frac{1}{n}\sum_{i=1}^{n}(\mathrm{AOD}_{(\mathrm{TANSO-CAI})i} - \mathrm{AOD}_{(\mathrm{AERONET})i})^2}. \quad (11)$$

The MBE [80] (Equation 12) is used here to measure the mean error magnitude and calculated as

$$\mathrm{MBE} = \frac{1}{n}\sum_{i=1}^{n}(\mathrm{AOD}_{(\mathrm{TANSO-CAI})i} - \mathrm{AOD}_{(\mathrm{AERONET})i}). \quad (12)$$

EE [81] can denote the expected uncertainty of retrieval and is the major target of the validation studies. It is a confidence envelope that encompasses the sum of the absolute (dominating at low AOD) and relative (dominating at high AOD) AOD errors. The definition of EE (Equation 13) is based on a single criterion: at least 66% (approximately one standard deviation) of the collocated AOD match-ups fall within the corresponding envelope that is described as

$$\mathrm{AOD}_{(\mathrm{AERONET})} - |\mathrm{EE}| \le \mathrm{AOD}_{(\mathrm{TANSO-CAI})} \le \mathrm{AOD}_{(\mathrm{AERONET})} + |\mathrm{EE}|. \quad (13)$$

Many studies have estimated the uncertainties of satellite-retrieved AOD and

attempted to define EE to validate a related algorithm or product [81]. Prior to the Terra launch, Kaufman et al. (1997) estimated the EE ($\pm 0.05 \pm 0.2AOD_{(AERONET)}$) of MODIS-retrieved AOD by sensitivity studies [17]. After the launch of Terra (later renamed Aqua), Chu et al. (2002) estimated the MODIS-measured AOD with the EE ($\pm 0.05 \pm 0.2AOD_{(AERONET)}$) [82]. MODIS Collection 5 (C005) DT aerosol products is reported EE for land to $\pm 0.05 \pm 0.15AOD_{(AERONET)}$ [83]. In addition, Mei et al. (2014) defined EE with a different envelope of $\pm 0.1 \pm 0.15AOD_{(AERONET)}$ for an AVHRR retrieval algorithm [26]. I tried three different EEs (EE1: $\pm 0.05 \pm 0.15AOD_{(AERONET)}$, EE2: $\pm 0.05 \pm 0.2AOD_{(AERONET)}$, EE3: $\pm 0.10 \pm 0.15AOD_{(AERONET)}$) mentioned above to estimate AOD retrieval uncertainty. The analysis of the results of our algorithm (for total retrieval) shows that the RMSE and MBE between the TANSO-CAI and AERONET AOD are 0.196 and 0.052. The proportion of retrievals agreeing within EE1 of the AERONET measurements is 48.0%. For the relaxed criteria with EE3, there are 67.7% match-ups within the EE3.

Although a good level of agreement was found for the total set of retrieved AOD from the globally distributed sites, I had no idea how the algorithm would behave over different regions [84]. To study more detailed situations than the descriptions for the total data in Figure 2.8a, it is instructive to regionally compare the TANSO-CAI and AERONET according to the locations of the AERONET sites. Based on the previous analysis methods, the following statistics are shown in the Table 2.2: number of experimental points (N), regression line, correlation coefficient (r), RMSE (AOD unit), MBE and EEs (EE1, EE2 and EE3) for each region (East Asia, Southeast Asia, South Asia, North Asia, South Africa, Europe, South America and North America). The comparisons of TANSO-CAI versus AERONET AOD for each region are shown in Figure 2.8b to 2.8i. For all regions except South Asia, which has a high ground-truth AOD, the RMSE and the MBE are always below 0.22 and 0.12, respectively (in absolute terms). The TANSO-CAI AOD obtained very high r-value (more than 0.85) in East Asia, Southeast Asia, South Asia and North Asia. Among them, South Asia has the poorest RMSE and MBE in all regions. The proportions of the points within EEs are only with 35.5%, 54.8% and 51.6% for EE1, EE2 and EE3, respectively. This could be explained by the complicated surface-cover types around the Dhaka_University AERONET site, which lead to improper estimations of surface reflectance during certain seasons, because for two consecutive years I found that most of the outliers were obtained during the period from February to April. On the other hand, the high ground-truth AOD (with a mean value of 0.915) can also bring uncertainties due to the effect of multiple scattering. Contrary to South Asia, the results for North America show a low r-value of 0.377, but a large proportion of data within EEs. As shown in Figure 2.8i, the ground-truth AOD was very low (with a mean value of 0.102). The

retrieval errors and the insufficient observation of high AOD experimental data lead to the low statistical r-value; however, the low RMSE and MBE (in absolute terms), and the match-up rate of 66% within EE1 indicate that our algorithm achieved good performance in North America.

Although the mean ground-truth AOD in Southeast Asia were measured with a high value of 0.646, good retrieval is still observed over this region with low RMSE and MBE, high r-value, a large proportion of experimental data within EEs, and a regression line that is very close to the one-to-one line. This is not surprising as the Chiang_Mai_Met_Sta, Vientiane and Gandhi_College AERONET sites are typical rural vegetated sites, which have relatively lower surface reflectances and are ideal for AOD retrieval [85]. The experimental data for Europe are from the Belsk and Timisoara sites. The Belsk site is a vegetated rural site, and the Timisoara site is located in the center of one of the most developed towns in Romania [86]. It can clearly be seen in Figure 2.8g that the retrieved AOD for this region is easily overestimated, compared with the ground-level measured data. In the analysis, I found that almost all the outliers with large errors are from Timisoara. It is possible that uncertainty arises from the complicated reflectance relationship between the 0.67 vs. 1.6 over urban areas and high local emissions, such as aerosol pollution from roads and power plants [85,86], both of which pose a huge challenge to the satellite retrieval of aerosol properties.

The sites in North Asia, South Africa and North America all have negative MBE values (−0.073, −0.119 and −0.018, respectively). I found that the AERONET sites in these regions, which have very high vegetation backgrounds, tend to underestimate AOD in very light loading conditions. Similarly, the MODIS DT algorithm also tends to underestimate dark-target sites with small AOD [81,87]. This error may result from the systematic overestimation of the surface reflectance, since the parameters in the regression function for estimating surface reflectance are determined by the experimental data over the selected areas (in Section 2.3), and high-quality estimations are concentrated on a certain range of surface-type variation. When the algorithm is applied to an extremely highly vegetated or bare-surface area, the factual parameters for estimating surface reflectance would be biased toward the parameters presumed by these overall experimental data, and the biases would become intrinsic systematic errors [87].

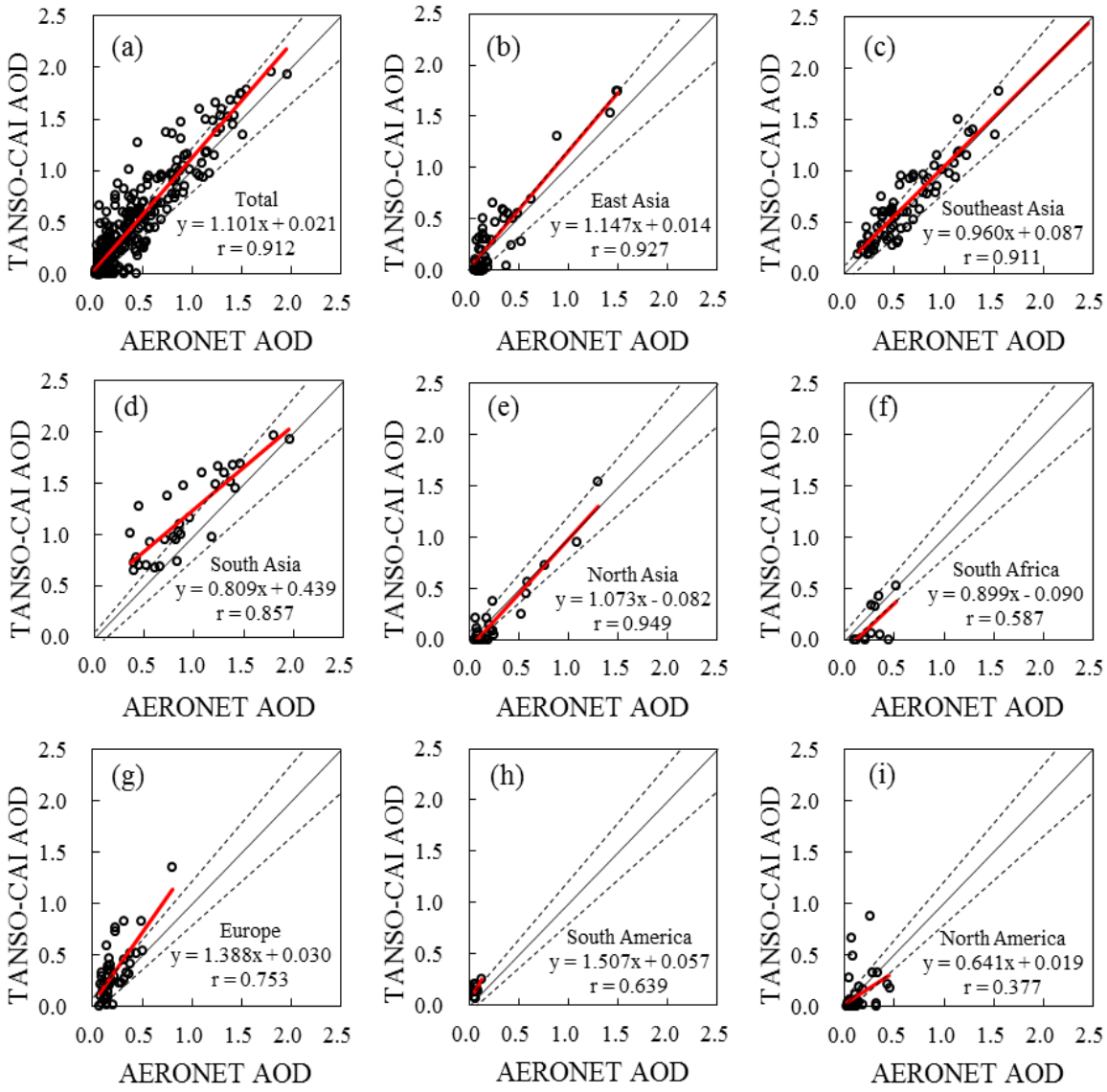

Figure 2.8 The comparison of retrieved AOD and AERONET measurements over different regions: (**a**) all regions; (**b**) East Asia; (**c**) Southeast Asia; (**d**) South Asia; (**e**) North Asia; (**f**) South Africa; (**g**) Europe; (**h**) South America; and (**i**) North America. The red solid, black solid and dashed lines are the regression line, one-to-one line and expected error (EE1) ($\pm 0.05 \pm 0.15AOD_{(AERONET)}$) envelope line, respectively.

Table 2.2 Summary statistics for the entire dataset and each individual region: number of samples (N), correlation coefficients (r), root mean square error (RMSE), mean bias error (MBE),and EEs.

Region	N	Mean AERONET AOD	r	RMSE	MBE	EE1	EE2	EE3
East Asia	49	0.282	0.927	0.178	0.055	36.7%	38.8%	59.2%
Southeast Asia	76	0.646	0.911	0.159	0.018	56.6%	65.8%	77.6%
South Asia	31	0.915	0.857	0.343	0.264	35.5%	54.8%	51.6%
North Asia	26	0.307	0.949	0.129	−0.073	38.5%	42.3%	61.5%
South Africa	11	0.283	0.578	0.167	−0.119	9.1%	36.4%	54.5%
Europe	45	0.217	0.753	0.213	0.114	46.7%	51.1%	60.0%
South America	9	0.067	0.639	0.102	0.091	33.3%	33.3%	66.7%
North America	53	0.102	0.377	0.164	−0.018	66.0%	71.7%	83.0%
Total	300	0.381	0.912	0.196	0.052	48.0%	55.0%	67.7%

Table 2.3 Proportions of match-ups below, within and above the EEs for AOD < 0.6 and > 0.6.

		EE1			EE2			EE3		
AODs	**N**	**Below**	**Within**	**Above**	**Below**	**Within**	**Above**	**Below**	**Within**	**Above**
AOD < 0.6	238	23.1%	44.5%	32.4%	21.0%	48.3%	30.7%	12.2%	64.7%	23.1%
AOD > 0.6	62	3.2%	61.3%	33.9%	0%	80.6%	19.4%	0%	79.0%	20.9%

Only two regions (Southeast Asia and North America) had more than 55% of match-ups fall in EE1. Even excluding the two regions (South Africa and South America) that have very small volumes of collocated data, only 35.5%~46.7% of match-ups fell in EE1 for the other regions. Obviously, EE1 is an overly strict criterion with which to evaluate the accuracy of the current algorithm. For the relaxed EEs, at least 51% of match-ups fell into EE3 for each region. Comparing the results for EE2 and EE3, more match-ups were virtually contained in EE3 for all regions (except for South Asia). The statistics in Table 2.3 show that the proportions of match-ups that fell well within EEs are higher for the observations with higher ground-truth AOD [16], and most of the match-ups that fell below the EEs were for lower aerosol loading conditions.

2.5 Conclusions

I introduced a new aerosol retrieval algorithm for land from the observation of the GOSAT TANSO-CAI sensor. Based upon the preliminary analysis from selected TANSO-CAI/AERONET collocations, we found that the relationship between surface reflectance in the red band and TOA reflectance in the SWIR 1.6 μm band varies with surface conditions. The NDVI was successfully utilized as a key factor to interpret the variety of 0.67 vs. 1.6 ratios with different surface properties. A regression function dependent on NDVI to estimate the surface reflectance of red band from the TOA reflectance of the 1.6 μm band for clear-sky conditions (AOD at 0.55 μm less than 0.1) was summarized. I compared the estimated surface reflectance against the atmospherically corrected surface reflectance, and the results show that the estimated surface reflectance has a very good agreement with the theoretical surface reflectance. The results also confirmed that the correlations between the 0.67 vs. 1.6 are vegetation dependent and proved that the regression function is practical and accurate for this application. The main problem in aerosol retrieval is that the NDVI itself can be affected by aerosols. Therefore, by combining the advantages of AFRI, which can resist the influences from atmospheric aerosols, with our regression function, which can preserve the correlations of 0.67 vs. 1.6 with different vegetation amounts, a modified $AFRI_{1.6}$ algorithm for estimating aerosol-free NDVI and surface reflectance of 0.67 μm was developed. This modified $AFRI_{1.6}$ algorithm-based AOD retrieval was tested by comparing its results with the collocated AERONET AOD from 16 AERONET sites located in different global regions. The results show that the retrieved AOD has very high consistency with the AERONET measurements, with an r-value of 0.912, and a regression line (with an equation of $y = 1.101x + 0.021$) that lies close to the one-to-one line. There are 67.7% experimental match-ups falling within the EE of ± 0.1 ±

$0.15AOD_{(AERONET)}$.

This algorithm demonstrates a new approach to retrieve AOD from an onboard satellite sensor that can only pick up the 1.6 μm and the NDVI (red and NIR) bands. In theory, this algorithm can be implemented for any satellite sensor if it provide reflectances in the appropriate bands.

References

1. Boucher, O.; Anderson, T.L. General circulation model assessment of the sensitivity of direct climate forcing by anthropogenic sulfate aerosols to aerosol size and chemistry. *Journal of Geophysical Research: Atmospheres* **1995**, *100*, 26117-26134.
2. Kaufman, Y.J.; Tanre, D.; Boucher, O. A satellite view of aerosols in the climate system. *Nature* **2002**, *419*, 215-223.
3. Charlson, R.J.; Schwartz, S.E.; Hales, J.M.; Cess, R.D.; Coakley, J.A.; Hansen, J.E.; Hofmann, D.J. Climate forcing by anthropogenic aerosols. *Science* **1992**, *255*, 423-430.
4. Kocifaj, M.; Horvath, H.; Jovanović, O.; Gangl, M. Optical properties of urban aerosols in the region Bratislava-Vienna I. methods and tests. *Atmospheric Environment* **2006**, *40*, 1922-1934.
5. World Health Organization. *Air Quality Guidelines for Europe*; WHO Regional Office for Europe: Copenhagen, Danmark, 2000.
6. Wang, Z.; Chen, L.; Tao, J.; Zhang, Y.; Su, L. Satellite-based estimation of regional particulate matter (PM) in Beijing using vertical-and-RH correcting method. *Remote sensing of environment* **2010**, *114*, 50-63.
7. Zhang, X.; Yang, L.; Yamaguchi, Y. Retrieval of aerosol optical depth over urban areas using Terra/MODIS data. *International Archives of the Photogrammetry, Remote Sensing and Spatial Information Science* **2010**, *38*, 374-379.
8. Higurashi, A.; Nakajima, T. Development of a two-channel aerosol retrieval algorithm on a global scale using NOAA AVHRR. *Journal of the Atmospheric Sciences* **1999**, *56*, 924-941.
9. Yu, H.; Kaufman, Y.; Chin, M.; Feingold, G.; Remer, L.; Anderson, T.; Balkanski, Y.; Bellouin, N.; Boucher, O.; Christopher, S. A review of measurement-based assessments of the aerosol direct radiative effect and forcing. *Atmospheric Chemistry and Physics* **2006**, *6*, 613-666.
10. Kokhanovsky, A.; Breon, F.-M.; Cacciari, A.; Carboni, E.; Diner, D.; Di Nicolantonio, W.; Grainger, R.; Grey, W.; Höller, R.; Lee, K.-H. Aerosol remote sensing over land: A comparison of satellite retrievals using different algorithms and instruments. *Atmospheric Research* **2007**, *85*, 372-394.

11. de Leeuw, G.; Holzer-Popp, T.; Bevan, S.; Davies, W.H.; Descloitres, J.; Grainger, R.G.; Griesfeller, J.; Heckel, A.; Kinne, S.; Klüser, L. Evaluation of seven European aerosol optical depth retrieval algorithms for climate analysis. *Remote Sensing of Environment* **2015**, *162*, 295-315.
12. Riffler, M.; Popp, C.; Hauser, A.; Fontana, F.; Wunderle, S. Validation of a modified AVHRR aerosol optical depth retrieval algorithm over Central Europe. *Atmospheric Measurement Techniques* **2010**, *3*, 1255-1270.
13. King, M.D.; Kaufman, Y.J.; Tanré, D.; Nakajima, T. Remote sensing of tropospheric aerosols from space: Past, present, and future. *Bulletin of the American Meteorological society* **1999**, *80*, 2229-2259.
14. Holzer‐Popp, T.; Schroedter, M.; Gesell, G. Retrieving aerosol optical depth and type in the boundary layer over land and ocean from simultaneous GOME spectrometer and ATSR‐2 radiometer measurements, 1, method description. *Journal of Geophysical Research: Atmospheres* **2002**, *107*, D21.
15. Wang, Z.; Li, Q.; Wang, Q.; Li, S.; Chen, L.; Zhou, C.; Zhang, L.; Xu, Y. HJ-1 terrestrial aerosol data retrieval using deep blue algorithm. *Journal of Remote Sensing* **2012**, *16*, 596-610. (In Chinese)
16. Kaufman, Y.J.; Wald, A.E.; Remer, L.A.; Gao, B.-C.; Li, R.-R.; Flynn, L. The MODIS 2.1-μm channel-correlation with visible reflectance for use in remote sensing of aerosol. *IEEE transactions on Geoscience and Remote Sensing* **1997**, *35*, 1286-1298.
17. Kaufman, Y.; Tanré, D.; Remer, L.A.; Vermote, E.; Chu, A.; Holben, B. Operational remote sensing of tropospheric aerosol over land from EOS moderate resolution imaging spectroradiometer. *Journal of Geophysical Research: Atmospheres* **1997**, *102*, 17051-17067.
18. Soufflet, V.; Tanré, D.; Royer, A.; O'Neil, N. Remote sensing of aerosols over boreal forest and lake water from AVHRR data. *Remote Sensing of Environment* **1997**, *60*, 22-34.
19. Dark Target (MODIS Aerosol Retrieval Algorithm): VIIRS. Available online: http://darktarget.gsfc.nasa.gov/platforms/viirs (accessed on 8 July 2016).
20. Sun, L.; Wei, J.; Bilal, M.; Tian, X.; Jia, C.; Guo, Y.; Mi, X. Aerosol optical depth retrieval over bright areas using Landsat 8 OLI images. *Remote Sensing* **2016**, *8*, 23.
21. Dark Target (MODIS Aerosol Retrieval Algorithm): What is the difference between dark target and deep blue? Available online: http://darktarget.gsfc.nasa.gov/content/what-difference-between-dark-target-and-deep-blue (accessed on 18 July 2016).
22. Hsu, N.; Jeong, M.J.; Bettenhausen, C.; Sayer, A.; Hansell, R.; Seftor, C.; Huang, J.; Tsay, S.C. Enhanced deep blue aerosol retrieval algorithm: The second

generation. *Journal of Geophysical Research: Atmospheres* **2013**, *118*, 9296-9315.
23. Holzer-Popp, T.; Schroedter-Homscheidt, M.; Breitkreuz, H.; Martynenko, D.; Klüser, L. Improvements of synergetic aerosol retrieval for ENVISAT. *Atmospheric Chemistry & Physics* **2008**, *8*, 7651-7672.
24. Holzer-Popp, T.; Schroedter-Homscheidt, M.; Breitkreuz, H.; Klüser, L.; Martynenko, D. Synergetic aerosol retrieval from SCIAMACHY and AATSR onboard ENVISAT. *Atmospheric Chemistry and Physics Discussions* **2008**, *8*, 1-49.
25. Holzer-Popp, T.; Schroedter-Homscheidt, M. Synergetic aerosol retrieval from ENVISAT. In Proceedings of ENVISAT & ERS Symposium, Salzburg, Austria, 6–10 September 2004.
26. Mei, L.; Xue, Y.; Kokhanovsky, A.; von Hoyningen-Huene, W.; de Leeuw, G.; Burrows, J. Retrieval of aerosol optical depth over land surfaces from AVHRR data. *Atmospheric Measurement Techniques* **2013**, *6*, 2227-2251.
27. Kaufman, Y.J.; Sendra, C. Algorithm for automatic atmospheric corrections to visible and near-IR satellite imagery. *International Journal of Remote Sensing* **1988**, *9*, 1357-1381.
28. Kaufman, Y.J.; Tanre, D. Atmospherically resistant vegetation index (ARVI) for EOS-MODIS. *IEEE transactions on Geoscience and Remote Sensing* **1992**, *30*, 261-270.
29. von Hoyningen‐Huene, W.; Freitag, M.; Burrows, J. Retrieval of aerosol optical thickness over land surfaces from top-of-atmosphere radiance. *Journal of Geophysical Research: Atmospheres* **2003**, *108*, D9.
30. Global Greenhouse Gas Observation by Satellite Project (7th Edition (July 2016)). Available online: http://www.gosat.nies.go.jp/eng/GOSAT_pamphlet_en.pdf (accessed on 18 May 2016).
31. Arai, K.; Sakashita, M. Evaluation of cirrus cloud detection accuracy of GOSAT/CAI and Landsat-8 with laser radar: Lidar and confirmation with Calipso data. *Evaluation.* **2016**, *5*, 12-21.
32. GOSAT/IBUKI Data Users Handbook 1st Edition. Available online: https://data.gosat.nies.go.jp/GosatUserInterfaceGateway/guig/doc/GOSAT_HB_E_1stEdition_for_HP.pdf (accessed on 12 May 2016).
33. Jung, Y.; Kim, J.; Kim, W.; Boesch, H.; Lee, H.; Cho, C.; Goo, T.-Y. Impact of aerosol property on the accuracy of a CO_2 retrieval algorithm from satellite remote sensing. *Remote Sensing* **2016**, *8*, 322.
34. Algorithm Theoretical Basis Document (ATBD) for CO_2 and CH_4 Columun Amounts Retrieval from GOSAT TANSO-FTS SWIR. Available online: http://data.gosat.nies.go.jp/GosatUserInterfaceGateway/guig/doc/documents/ATBD_FTSSWIRL2_V1.1_en.pdf (accessed on 22 May 2016).
35. Schaap, M.; Apituley, A.; Timmermans, R.; Koelemeijer, R.; de Leeuw, G.

Exploring the relation between aerosol optical depth and PM2.5 at Cabauw, The Netherlands. *Atmospheric Chemistry and Physics* **2009**, *9*, 909-925.

36. Liu, Z.; Liu, Q.; Lin, H.C.; Schwartz, C.S.; Lee, Y.H.; Wang, T. Three-dimensional variational assimilation of MODIS aerosol optical depth: Implementation and application to a dust storm over East Asia. *Journal of Geophysical Research: Atmospheres* **2011**, *116*, D23206.
37. Schwartz, C.S.; Liu, Z.; Lin, H.C.; Cetola, J.D. Assimilating aerosol observations with a "hybrid" variational‐ensemble data assimilation system. *Journal of Geophysical Research: Atmospheres* **2014**, *119*, 4043-4069.
38. Istomina, L.; von Hoyningen-Huene, W.; Kokhanovsky, A.; Schultz, E.; Burrows, J. Remote sensing of aerosols over snow using infrared AATSR observations. *Atmospheric Measurement Techniques* **2011**, *4*, 1133-1145.
39. Zhang, Y.; Li, Z.; Qie, L.; Zhang, Y.; Liu, Z.; Chen, X.; Hou, W.; Li, K.; Li, D.; Xu, H. Retrieval of aerosol fine-mode fraction from intensity and polarization measurements by PARASOL over East Asia. *Remote Sensing* **2016**, *8*, 417.
40. Wang, Z.; Gao, Z.; Li, Q.; Wang, W.; Chen, L.; Li, S. Urban aerosol monitoring over Ning-Bo from HJ-1. In Proceedings IEEE International Geoscience and Remote Sensing Symposium, Munich, Germany, 22-27 July 2012; pp. 2520-2523.
41. Wong, M.S.; Lee, K.-H.; Nichol, J.E.; Li, Z. Retrieval of aerosol optical thickness using MODIS, a study in Hong Kong and the Pearl River Delta Region. *IEEE Transactions on Geoscience and Remote Sensing* **2010**, *48*, 3318-3327.
42. Kuze, A.; O'Brien, D.M.; Taylor, T.E.; Day, J.O.; O'Dell, C.W.; Kataoka, F.; Yoshida, M.; Mitomi, Y.; Bruegge, C.J.; Pollock, H. Vicarious calibration of the GOSAT sensors using the railroad valley desert playa. *IEEE Transactions on Geoscience and Remote Sensing* **2011**, *49*, 1781-1795.
43. Huo, J.; Zhang, W.; Zeng, X.; Lü, D.; Liu, Y. Examination of the quality of GOSAT/CAI cloud flag data over Beijing using ground-based cloud data. *Advances in Atmospheric Sciences* **2013**, *30*, 1526-1534.
44. Fukuda, S.; Nakajima, T.; Takenaka, H.; Higurashi, A.; Kikuchi, N.; Nakajima, T.Y.; Ishida, H. New approaches to removing cloud shadows and evaluating the 380 nm surface reflectance for improved aerosol optical thickness retrievals from the GOSAT/TANSO‐cloud and aerosol imager. *Journal of Geophysical Research: Atmospheres* **2013**, *118*, 13520-13531.
45. Algorithm Theoretical Basis Document (ATBD) on the Processing of GOSAT TANSO-CAI L3 Global Reflectance Products. Available online: https://data.gosat.nies.go.jp/GosatWebDds/productorder/distribution/user/ATBD_CAIL3REF_V1.0_en.pdf (accessed on 29 May 2016).
46. Algorithm theoretical basis document for TANSO-CAI L1B processing. Available online:

https://data.gosat.nies.go.jp/GosatWebDds/productorder/distribution/user/ATBD_CAIL1B_V1.0_en.pdf (accessed on 23 May 2016).
47. Algorithm theoretical basis document for TANSO-CAI L1B+ processing. Available online: https://data.gosat.nies.go.jp/GosatWebDds/productorder/distribution/user/ATBD_CAIL1BP_V1.01_en.pdf (accessed on 26 May 2016).
48. NIES GOSAT Product Format Descriptions. Available online: https://data.gosat.nies.go.jp/GosatWebDds/productorder/distribution/user/GOSAT_ProductDescription_V1.50_en.pdf (accessed on 17 May 2015).
49. Holben, B.N.; Eck, T.; Slutsker, I.; Tanre, D.; Buis, J.; Setzer, A.; Vermote, E.; Reagan, J.A.; Kaufman, Y.; Nakajima, T. AERONET-A federated instrument network and data archive for aerosol characterization. *Remote sensing of environment* **1998**, *66*, 1-16.
50. Chen, H.; Cheng, T.; Gu, X.; Li, Z.; Wu, Y. Evaluation of polarized remote sensing of aerosol optical thickness retrieval over China. *Remote Sensing* **2015**, *7*, 13711-13728.
51. Homepage of AEROSOL ROBOTIC NETWORK. Available online: http://aeronet.gsfc.nasa.gov/new_web/index.html (accessed on 11 May 2016).
52. Ångström, A. The parameters of atmospheric turbidity. *Tellus* **1964**, *16*, 64-75.
53. Vermote, E.F.; El Saleous, N.Z.; Justice, C.O. Atmospheric correction of MODIS data in the visible to middle infrared: First results. *Remote sensing of environment* **2002**, *83*, 97-111.
54. Vermote, E.F.; Kotchenova, S. Atmospheric correction for the monitoring of land surfaces. *Journal of Geophysical Research: Atmospheres* **2008**, *113*.
55. Fu, Q.; Min, X.; Sun, L.; Ma, S. Atmospheric correction of HJ-1 A/B CCD over land: Land surface reflectance calculation for geographical information product. *Journal of Geographical Sciences* **2014**, *24*, 1083-1094.
56. Liang, S.; Fang, H.; Chen, M. Atmospheric correction of LANDSAT ETM+ land surface imagery. I. Methods. *IEEE Transactions on Geoscience and Remote Sensing* **2001**, *39*, 2490-2498.
57. Vermote, E.F.; Tanré, D.; Deuze, J.L.; Herman, M.; Morcette, J.-J. Second simulation of the satellite signal in the solar spectrum, 6S: An overview. *IEEE Transactions on Geoscience and Remote Sensing* **1997**, *35*, 675-686.
58. Kotchenova, S.Y.; Vermote, E.F.; Levy, R.; Lyapustin, A. Radiative transfer codes for atmospheric correction and aerosol retrieval: Intercomparison study. *Applied Optics* **2008**, *47*, 2215-2226.
59. Callieco, F.; Dell'Acqua, F. A comparison between two radiative transfer models for atmospheric correction over a wide range of wavelengths. *International journal of remote sensing* **2011**, *32*, 1357-1370.

60. Vermote, E.; Tanré, D.; Deuzé, J.; Herman, M.; Morcrette, J.; Kotchenova, S. Second simulation of a satellite signal in the solar spectrum-vector (6sv). *6S User Guide Version* **2006**, *3*, 1-55.
61. Levy, R.C.; Remer, L.A.; Mattoo, S.; Vermote, E.F.; Kaufman, Y.J. Second‐generation operational algorithm: Retrieval of aerosol properties over land from inversion of moderate resolution imaging spectroradiometer spectral reflectance. *Journal of Geophysical Research: Atmospheres* **2007**, *112*, D13211.
62. Homepage of NASA Earth Observatory. Available online: http://earthobservatory.nasa.gov/Features/MeasuringVegetation/measuring_vegetation_2.php (accessed on 23 October 2016).
63. Algorithm for Remote Sensing of Tropospheric Aerosol from MODIS: Collection 5. Available online: http://modis.gsfc.nasa.gov/data/atbd/atbd_mod02.pdf (accessed on 20 May 2015).
64. Rouse, J.W.; Haas, R.H.; Deering, D.W.; Sehell, J.A. *Monitoring the Vernal Advancement and Retrogradation (Green Wave Effect) of Natural Vegetation.* Remote Sensing Center: Texas A&M University, College Station, TX, USA, 1974.
65. Ogutu, B.O.; Dash, J. An algorithm to derive the fraction of photosynthetically active radiation absorbed by photosynthetic elements of the canopy (FAPARps) from eddy covariance flux tower data. *New Phytologist* **2013**, *197*, 511-523.
66. Liu, G.-R.; Liang, C.-K.; Kuo, T.-H.; Lin, T.-H.; Huang, S. Comparison of the NDVI, ARVI and AFRI vegetation index, along with their relations with the AOD using SPOT 4 vegetation dat. *Terrestrial Atmospheric and Oceanic Sciences* **2004**, *15*, 15-32.
67. Zhou, L.; Kaufmann, R.; Tian, Y.; Myneni, R.; Tucker, C. Relation between interannual variations in satellite measures of northern forest greenness and climate between 1982 and 1999. *Journal of Geophysical Research: Atmospheres* **2003**, *108*, D1.
68. Karnieli, A.; Kaufman, Y.J.; Remer, L.; Wald, A. AFRI—Aerosol free vegetation index. *Remote Sensing of Environment* **2001**, *77*, 10-21.
69. Ben‐Ze'ev, E.; Karnieli, A.; Agam, N.; Kaufman, Y.; Holben, B. Assessing vegetation condition in the presence of biomass burning smoke by applying the aerosol‐free vegetation index (AFRI) on MODIS images. *International Journal of Remote Sensing* **2006**, *27*, 3203-3221.
70. Vermote, E.; Vermeulen, A. Atmospheric correction algorithm: Spectral reflectances (MOD09), ATBD version 4.0, April 1999. Available online: http://modis.gsfc.nasa.gov/data/atbd/atbd_mod08.pdf (accessed on 5 May 2016).
71. Tripathi, S.; Dey, S.; Chandel, A.; Srivastava, S.; Singh, R.P.; Holben, B. Comparison of MODIS and AERONET derived aerosol optical depth over the Ganga Basin, India. *Annales Geophysicae* **2005**, *23*, 1093-1101.

72. Tiwari, S.; Singh, A. Variability of aerosol parameters derived from ground and satellite measurements over Varanasi located in the Indo-Gangetic Basin. *Aerosol and Air Quality Research* **2013**, *13*, 627-638.
73. Giglio, L. MODIS collection 5 active fire product user's guide version 2.4. 2010. Available online: http://www.fao.org/fileadmin/templates/gfims/docs/MODIS_Fire_Users_Guide_2.4.pdf (accessed on 22 May 2016).
74. Khatiwada, K.R.; Panthi, J.; Shrestha, M.L.; Nepal, S. Hydro-climatic variability in the Karnali River Basin of Nepal Himalaya. *Climate* **2016**, *4*, 17.
75. Witek, M.L.; Garay, M.J.; Diner, D.J.; Smirnov, A. Aerosol optical depths over oceans: A view from MISR retrievals and collocated MAN and AERONET in situ observations. *Journal of Geophysical Research: Atmospheres* **2013**, *118*, 12620-12633.
76. Petrenko, M.; Ichoku, C.; Leptoukh, G. Multi-sensor aerosol products sampling system (MAPSS). *Atmospheric Measurement Techniques* **2012**, *5*, 913-926.
77. More, S.; Pradeep Kumar, P.; Gupta, P.; Devara, P.; Aher, G. Comparison of aerosol products retrieved from AERONET, MICROTOPS and MODIS over a tropical urban city, Pune, India. *Aerosol and Air Quality Research* **2013**, *13*, 107-121.
78. Shi, Y.; Zhang, J.; Reid, J.; Holben, B.; Hyer, E.; Curtis, C. An analysis of the collection 5 MODIS over-ocean aerosol optical depth product for its implication in aerosol assimilation. *Atmospheric Chemistry and Physics* **2011**, *11*, 557-565.
79. Shi, Y.; Zhang, J.; Reid, J.; Hyer, E.; Hsu, N. Critical evaluation of the MODIS deep blue aerosol optical depth product for data assimilation over North Africa. *Atmospheric Measurement Techniques* **2013**, *6*, 949-969.
80. Willmott, C.J.; Matsuura, K. Advantages of the mean absolute error (MAE) over the root mean square error (RMSE) in assessing average model performance. *Climate research* **2005**, *30*, 79-82.
81. Levy, R.C.; Remer, L.A.; Kleidman, R.G.; Mattoo, S.; Ichoku, C.; Kahn, R.; Eck, T. Global evaluation of the collection 5 MODIS dark-target aerosol products over land. *Atmospheric Chemistry and Physics* **2010**, *10*, 10399-10420.
82. Chu, D.; Kaufman, Y.; Ichoku, C.; Remer, L.; Tanré, D.; Holben, B. Validation of MODIS aerosol optical depth retrieval over land. *Geophysical research letters* **2002**, *29*, 12.
83. Remer, L.A.; Kaufman, Y.; Tanré, D.; Mattoo, S.; Chu, D.; Martins, J.V.; Li, R.-R.; Ichoku, C.; Levy, R.; Kleidman, R. The MODIS aerosol algorithm, products, and validation. *Journal of the atmospheric sciences* **2005**, *62*, 947-973.
84. Ruiz-Arias, J.; Dudhia, J.; Gueymard, C.; Pozo-Vázquez, D. Assessment of the level-3 MODIS daily aerosol optical depth in the context of surface solar radiation and numerical weather modeling. *Atmospheric Chemistry and Physics* **2013**, *13*,

675-692.
85. Nichol, J.E.; Bilal, M. Validation of modis 3 km resolution aerosol optical depth retrievals over Asia. *Remote Sensing* **2016**, *8*, 328.
86. Calinoiu, D.; Ionel, I.; Triftordai, G. Analysis of aerosol optical thickness in timisoara from aeronet global network observations. *Strojarstvo* **2011**, *53*, 353-358.
87. Xie, Y.; Zhang, Y.; Xiong, X.; Qu, J.J.; Che, H. Validation of MODIS aerosol optical depth product over China using CARSNET measurements. *Atmospheric environment* **2011**, *45*, 5970-5978.

Chapter 3 Investigation of the performance of vegetation indices at different levels of aerosol optical depths

3.1 Introduction

Vegetation is a key component of global ecosystems and represents an active surface interacting with solar radiation and transforming it. Understanding the changes in Earth's vegetation cover is highly associated with understanding land-atmosphere interactions and their effects on climate [1,2]. During the past few decades, several vegetation indices (VIs) were developed and used for terrestrial science applications [3–6]. The Normalized Difference Vegetation Index (NDVI) [7,8] is the most representative VI, and it is formulated as follows (Equation 1):

$$\mathrm{NDVI} = (\mathrm{R_{NIR}} - \mathrm{R_{red}})/(\mathrm{R_{NIR}} + \mathrm{R_{red}}) \quad (1)$$

where R_{red} and R_{NIR} are the surface reflectances over the NIR and visible regions of the spectrum, respectively. NDVI is calculated based on the behavior of the vegetation spectra, wherein chlorophyll pigments absorb light in the red region, and the cellular structures of leaves reflect large portions of the light in the NIR wavelengths. Such differences in the reflected red and NIR bands are typical due to vegetation and do not show over other ground types. It is well known that NDVI is sensitive to atmospheric absorption and scattering caused by highly variable aerosols [4,6]. Thus, a certain number of vegetation indices have been developed with similar vegetation index functions with the aim of eliminating, or at least reducing, the atmospheric influences.

One such approach is the Atmospherically Resistant Vegetation Index (ARVI), which was first proposed and used for the remote sensing of vegetation from the Earth Observing System (EOS) Moderate Resolution Imaging Spectroradiometer (MODIS). ARVI takes advantage of the presence of the blue band (0.47 μm) in addition to that of the red and NIR bands included in NDVI. The self-correction of ARVI works by using the differences in the radiances measured in the blue and the red bands to conduct a correction of the atmospheric influences on the red band [4]. ARVI can be written as follows (Equations 2):

$$\mathrm{ARVI} = (\mathrm{R^*_{NIR}} - \mathrm{R^*_{rb}})/(\mathrm{R^*_{NIR}} + \mathrm{R^*_{rb}}) \quad (2a)$$

where

$$R^*_{rb} = R^*_{red} - \gamma(R^*_{blue} - R^*_{red}) \quad (2b)$$

in which is the subscript rb denotes the red and blue bands, R^* stands for the atmospherically corrected or partially atmospherically corrected (Rayleigh and ozone absorptions) surface reflectances, and γ has a recommended value of 1.

The Enhanced Vegetation Index (EVI) is an advanced VI that was developed to improve the sensitivity of the index to high biomass regions and enhance its vegetation monitoring capability. Through a decoupling of the canopy background signal and a reduction of the atmospheric influences, a feedback-based approach that takes both the background adjustment and atmospheric resistance concepts into consideration is established in EVI. Currently, the MODIS provided standard VI products include the NDVI and EVI data generated from the Terra and Aqua instruments. EVI is defined as follows (Equation 3) [9,10]:

$$EVI = G(R^*_{NIR} - R^*_{red})/(R^*_{NIR} + C_1R^*_{red} - C_2R^*_{blue} + L) \quad (3)$$

where G is the gain or scaling factor; C_1 and C_2 are the coefficients of the aerosol resistance terms, which use the blue band to correct for the aerosol influences in the red band; and L is the canopy background adjustment for correcting the nonlinear, differential NIR and red wavelength transfers through a canopy. The coefficients adopted in the MODIS EVI algorithm are L=1, C_1=6, C_2=7.5, and G=2.5 [11].

EVI is a 3-band VI and is limited to sensor systems that include the blue, red and NIR bands, making it more difficult to generate the long-term EVI time series than their NDVI counterparts [6]. Moreover, due to the inability of the (saturated) blue band to convey any useful atmospheric information, EVI exhibits extremely high values over bright targets (heavy clouds, and snow/ice). To address this issue, a modified 2-band EVI (EVI2), which is the most similar to the 3-band EVI, was designed without the blue band. In addition, starting with the collection 5.0 of the MODIS VI products, the standard 3-band EVI was replaced by EVI2 over high-reflectance surfaces, such as clouds, snow and ice. By simply assuming the relationship between the red and blue bands, the EVI equation can be reduced to the 2-band EVI2 as follows (Equation 4):

$$EVI2 = 2.5 * (R^*_{NIR} - R^*_{red})/(R^*_{NIR} + 2.4 * R^*_{red} + 1) \quad (4)$$

The studies of Jiang et al. (2008) have shown that EVI and EVI2 have similarly good consistencies for areas with insignificant atmospheric effects. However, when aerosols or residual clouds are present, EVI has larger values than EVI2 [11].

The aforementioned VIs are calculated by transforming the spectral bands in the visible and NIR regions. The Visible Atmospherically Resistant Index (VARI) [12], which is based entirely on the visible part of the spectrum, is minimally sensitive to

atmospheric effects and was developed to estimate the green vegetation fraction [13]. In addition, VARI was utilized in monitoring the chaparral moisture content [14]. To reduce atmospheric effects, ARVI [4] was introduced in VARI, which is calculated as (Equation 5)

$$\mathrm{VARI} = \left(\mathrm{R_{green}} - \mathrm{R_{red}}\right)/\left(\mathrm{R_{green}} + \mathrm{R_{red}} - \mathrm{R_{blue}}\right) \quad (5)$$

where R_{green} stands for the surface reflectance in the green band (0.56 μm). Compared with NDVI, which is sensitive to changes in small vegetation fractions and insensitive to changes in moderate and high vegetation fractions, VARI performs well in the estimation of the vegetation fraction from the visible range of the spectrum and shows a linear response to vegetation fraction [13].

In addition to the NIR and visible band derived atmospherically resistant VIs, the shortwave infrared (SWIR) wavelength bands have also been used in VIs. The SWIR bands (1.6 or 2.1 μm) are sensitive to changes in vegetation and can penetrate the atmospheric column even in the presence of aerosols, such as smoke or sulfates, due to their longer-than-visible-band wavelengths, which are considered to be much larger than the radius of most aerosols (expect for dust particles) [15]. Making full of these advantages, Miura et al. (1998) used the SWIR bands in place of the red band in NDVI, and analyzed their ability to minimize atmospheric "smoke" contamination [16]. Afterwards, Karnieli et al. (2001) found that, under clear sky conditions, there are very high correlation coefficient between the red and the SWIR spectral bands at approximately 2.1 and 1.6 μm, and their empirical linear relationships were summarized as follows (Equations 6a and 6b):

$$\mathrm{R_{red}} = 0.5 * \mathrm{R_{2.1}} \quad (6a)$$

$$\mathrm{R_{red}} = 0.66 * \mathrm{R_{1.6}} \quad (6b)$$

where $R_{2.1}$ and $R_{1.6}$ are the reflectances at 2.1 and 1.6 μm, respectively. The linear relationship between the 1.6-μm and red bands can be improved by applying a curvilinear relationship to produce slight higher correlation coefficients, as in Equation 6c [17]:

$$\mathrm{R_{red}} = 0.01 + 0.14 * \mathrm{R_{1.6}} + 0.72 * \mathrm{R_{1.6}}^2 \quad (6c)$$

Based on the above relationships, the SWIR bands can be included in a new VI, in which the 2.1 μm or 1.6 μm bands can replace the red band. Thus, a new VI called the Aerosol FRee vegetation Index (AFRI) has been developed. AFRI has three versions ($AFRI_{2.1}$, $AFRI_{1.6}$-1 (based on Equation 6b), and $AFRI_{1.6}$-2 (based on Equation 6c)), computed as follows (Equations 7a to 7c) [17]:

$$AFRI_{2.1} = (R_{NIR} - 0.5 * R_{2.1})/(R_{NIR} + 0.5 * R_{2.1}) \quad (7a)$$

$$AFRI_{1.6}\text{-}1 = (R_{NIR} - 0.66 * R_{1.6})/(R_{NIR} + 0.66 * R_{1.6}) \quad (7b)$$

$$AFRI_{1.6}\text{-}2 = \frac{(R_{NIR} - 0.01 - 0.14 * R_{1.6} - 0.72 * R_{1.6}^{2})}{(R_{NIR} + 0.01 + 0.14 * R_{1.6} + 0.72 * R_{1.6}^{2})} \quad (7c)$$

Although these self-corrected, atmospherically resistant, and SWIR-derived VIs were developed based on their theoretical resistances to atmospheric influences, some of their performances have been tested for different applications. However, variations introduced by atmospheric effects, absorption and scattering can considerably reduce the precision of the subsequent detections of the vegetation dynamics over the Earth's surface [18], and very few studies have investigated the performances of VIs across different aerosol optical depth (AOD) levels. Therefore, in this study, I quantitatively compared the performances of these self-corrected, atmospherically resistant, and SWIR-derived VIs for different AOD over different AErosol Robotic Network (AERONET) sites.

3.2 Data sources and methods

3.2.1 Satellite and AERONET data

The MODIS instrument onboard the EOS Terra satellite has 36 spectral bands, ranging in wavelength from the visible to the thermal-IR (0.4 to 14.4 μm); the red (0.65 μm) and NIR (0.86 μm) bands that are used in NDVI have nominal resolutions of 250 m at nadir, and the other bands used in the VIs (Equations 2 to 7), including the blue (0.47 μm), green (0.56 μm), 1.6-μm SWIR, and 2.1-μm SWIR bands, have resolutions of 500 m [19].

MODIS completes a global survey every one to two days and provides 44 standard data products of various global changes. The MODIS/Terra Calibrated Radiances (MOD02HKM) provides the calibrated and geolocated at-aperture radiances for the 7 bands located in the 0.45 to 2.20 μm range, with a spatial resolution of 500 m. The MOD02HKM are not atmospherically corrected and were used as the TOA reflectance data [20].

MODIS also provides the Surface Reflectance Product (MOD09HKM), which is an estimation of the surface reflectance in the same 7 bands of the MOD02HKM. Through correcting the effects of atmospheric scattering and absorption due to atmospheric gases, aerosols, and thin cirrus clouds, the adjusted reflectance of MOD09 has been verified as highly accurate and similar to that measured at ground level [21].

Thus, the MODIS Surface Reflectance Product is used to calculate the surface VIs in this study.

To evaluate the performance of the above VIs with different levels of AOD, the AERONET measurements were used to understand the VIs measurements at the corresponding aerosol loadings. AERONET [22] is a worldwide remote sensing aerosol network that provides information on various aerosol properties from direct ground-level measurements. It has been validated that the ground-level measurements have higher accuracies than the current satellite-based measurements, and the uncertainties of the visible and NIR wavelengths are very low, with a value of 0.01 [22,23].

To ensure the accuracy of the data sources, the new version of the MODIS products (collection 6) and the AERONET level 2.0 (cloud screened and quality-assured) data were used in our analysis.

3.2.2 Selection of experimental data

In this study, I utilized the spatially and temporally matched MODIS/AERONET collocated data as the experimental data. The selection of the MODIS/AERONET collocated data was based on the following criterion: The cloud-free MODIS data (both MOD02HKM and MOD09HKM) should by located within a 10-km radius of the AERONET sites, and the corresponding AOD provided by AERONET should be within 30 minutes of the MODIS pass.

According to these selection criterion, several MODIS/AERONET matches with AOD values ranging from 0.1 to 1.2 were found among the AERONET sites: those at Ubon Ratchathani, Ussuriysk, and Gandhi College. The geographical and landcover information from the three sites includes the location, dominant landcover type and fraction of dominant landcover type within the radii of 5 km and 10 km, as shown in Table 3.1.

Table 3.1 The geographical and land cover information about the AErosol Robotic Network (AERONET) Ubon_Ratchathani, Ussuriysk, and Gandhi College sites.

Site Name	Longitude (decimal_ degrees)	Latitude (decimal_ degrees)	Elevation (meters)	Dominant landcover (Radius: 5 km)		Dominant landcover (Radius: 10 km)	
				Type	Fraction	Type	Fraction
Ubon_Ratchathani	104.87	15.25	120	Urban area	60%	Cropland, irrigated or post-flooded	81%
Ussuriysk	132.16	43.70	280	Tree cover, broadleaved, deciduous	94%	Tree cover, broadleaved, deciduous	84%
Gandhi_College	84.13	25.87	60	Cropland, rainfed	60%	Cropland, irrigated or post-flooded	86%

3.3 Results and discussion

3.3.1 Comparison of NDVI with other vegetation indices

For the selected spatially and temporally matched MODIS/AERONET collocated data, the pairs of top-of-atmosphere (TOA) and top-of-canopy (TOC) VIs were calculated using the MODIS TOA reflectance and the surface reflectance data, respectively. Their performances for different AOD levels were analyzed through comparisons of the TOA and TOC VIs. It should be noted that, although some of the mentioned VIs (such as ARVI, EVI) were originally calculated using partially atmospherically corrected (Rayleigh and ozone absorption) reflectances, to maintain consistency with the other VIs, all the TOA VIs were calculated using the uncorrected TOA reflectances.

I first compared all the TOA VIs against the TOC NDVI, and the comparison results for the three AERONET sites are shown as the graphs (a to h) in Figures 3.1 to 3.12. The statistical root mean square error (RMSE) and mean bias error (MBE) were used to assess the overall errors, and the results for each experimental site are shown in Tables 3.2 to 3.7. The TOA ARVI showed a high consistency with the TOC NDVI, and the linear correlation of R^2 was approximately 0.5 to 0.9. The uncorrected TOA reflectance-derived ARVIs all displayed higher values than the TOC NDVI.

The TOA EVI also agrees well with the TOC NDVI; however, it was found that, under light aerosol loading conditions, two lower correlation cases (graph (c) in Figures 3.5 and 3.7) were observed over the densely vegetated Ussuriysk site. This is mainly due to the saturation of the NDVI in the dense vegetation area. In addition, this phenomenon suggests that the differences between EVI and NDVI caused by the saturation of NDVI over highly vegetated areas were smaller under higher AOD conditions. The two band-based TOA EVI2 showed considerable differences from the values of the EVI. For all the experimental cases, the TOA EVI was generally larger than the TOC NDVI, while EVI2 was lower than the TOC NDVI. This is because the aerosol resistant property of EVI was not retained in EVI2. For the TOA VARI, there was a weak consistency with the TOC NDVI.

The three SWIR-derived AFRIs can be considered as modified NDVIs. Generally, the TOA $AFRI_{2.1}$ showed a higher correlation with the TOC NDVI than did the TOA $AFRI_{1.6}$. This may be the reason that the reflectance relationship between the 2.1-μm and red bands is stronger than that of the 1.6-μm and red bands. A comparison of $AFRI_{1.6}$-1 with $AFRI_{1.6}$-2 shows that their statistical RMSE and MBE values imply that TOA $AFRI_{1.6}$-2 is much closer to the TOC NDVI; it may be possible that the curvilinear relationships in Equation 6c better describe the reflectance relationship

between the 1.6-μm and red bands. In addition, I noted that the TOA AFRIs closely resemble the TOC NDVI and showed considerably less scatter over the Ussuriysk site; in contrast, the AFRIs exhibit erratic behavior over the Gandhi College site. This is mostly due to reflectance relationships between the red and SWIR (1.6 μm or 2.1 μm) bands, which are independent of the vegetation fraction, and the rules of $R_{0.6} = 0.5R_{2.1}$ and $R_{0.6} = 0.66R_{1.6}$ were summarized over a vegetated area. Therefore, AFRIs perform well over the highly vegetated Ussuriysk site, while abnormally high AFRI values were observed for the low-vegetation areas (with NDVI < 0.4) over the Gandhi College site.

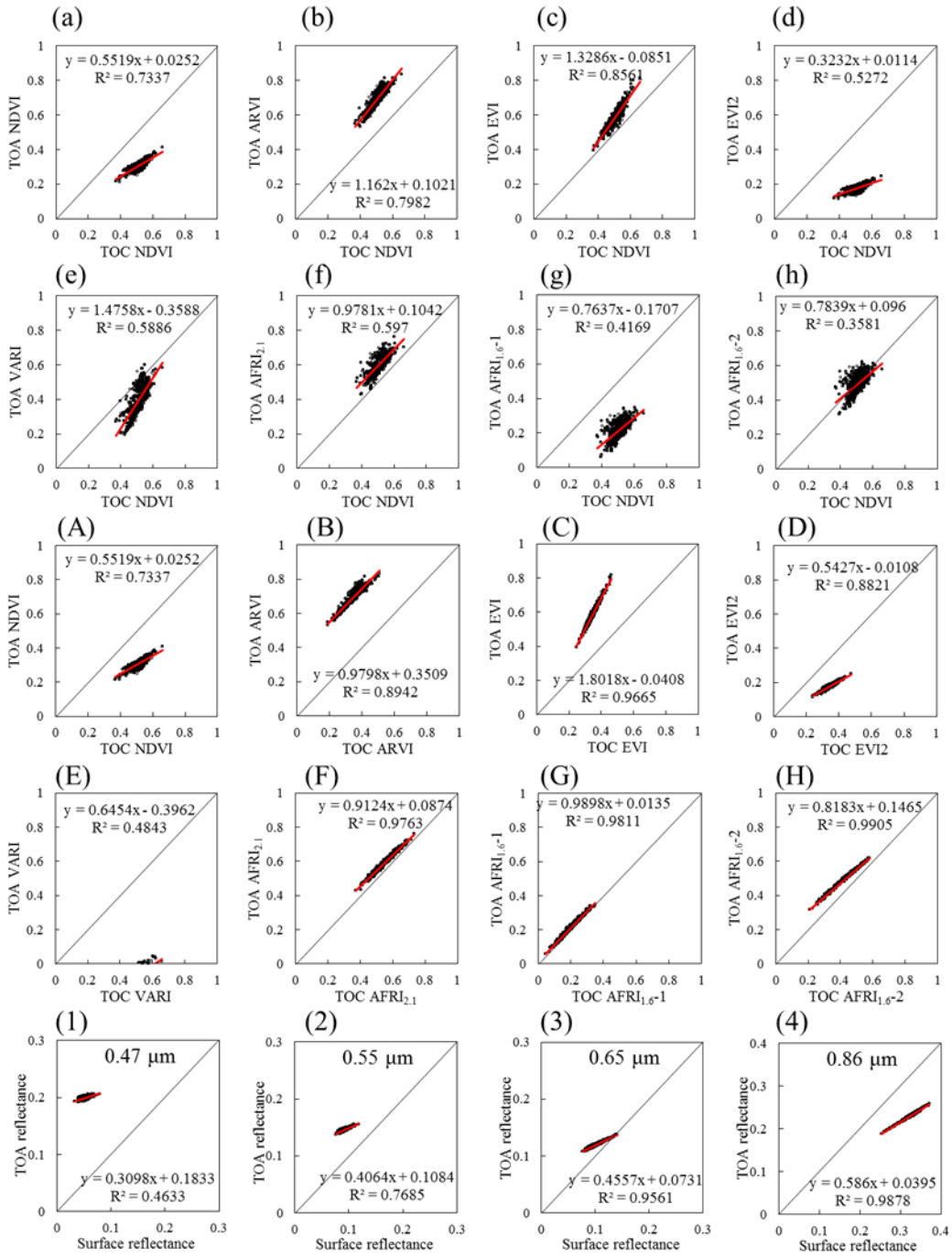

Figure 3.1 Experimental results for the Ubon_Ratchathani site (Julian calendar day 047 in 2010) with an AOD at 0.55 µm of 0.59). (**a**) Top-of-atmosphere (TOA) Normalized Difference Vegetation Index (NDVI), (**b**) TOA Atmospherically Resistant Vegetation Index (ARVI), (**c**) TOA Enhanced Vegetation Index (EVI), (**d**) TOA modified 2-band EVI (EVI2), (**e**) TOA Visible Atmospherically Resistant Index (VARI), (**f**) TOA Aerosol FRee vegetation Index ($AFRI_{2.1}$), (**g**) TOA $AFRI_{1.6}$-1 and (**h**) TOA $AFRI_{1.6}$-2 plotted against the top-of-canopy NDVI (TOC NDVI); (**A**) TOA NDVI, (**B**) TOA ARVI, (**C**) TOA EVI, (**D**) TOA EVI2, (**E**) TOA VARI, (**F**) TOA $AFRI_{2.1}$, (**G**) TOA $AFRI_{1.6}$-1 and (**H**) TOA $AFRI_{1.6}$-2 plotted against their TOC index values, respectively; (**1**) TOA reflectance in blue (0.47 µm), (**2**) TOA reflectance in green (0.55 µm), (**3**) TOA reflectance in red (0.65µm) and (**4**) TOA reflectance in near-infrared (NIR, 0.86 µm) plotted against their surface reflectance values, respectively.

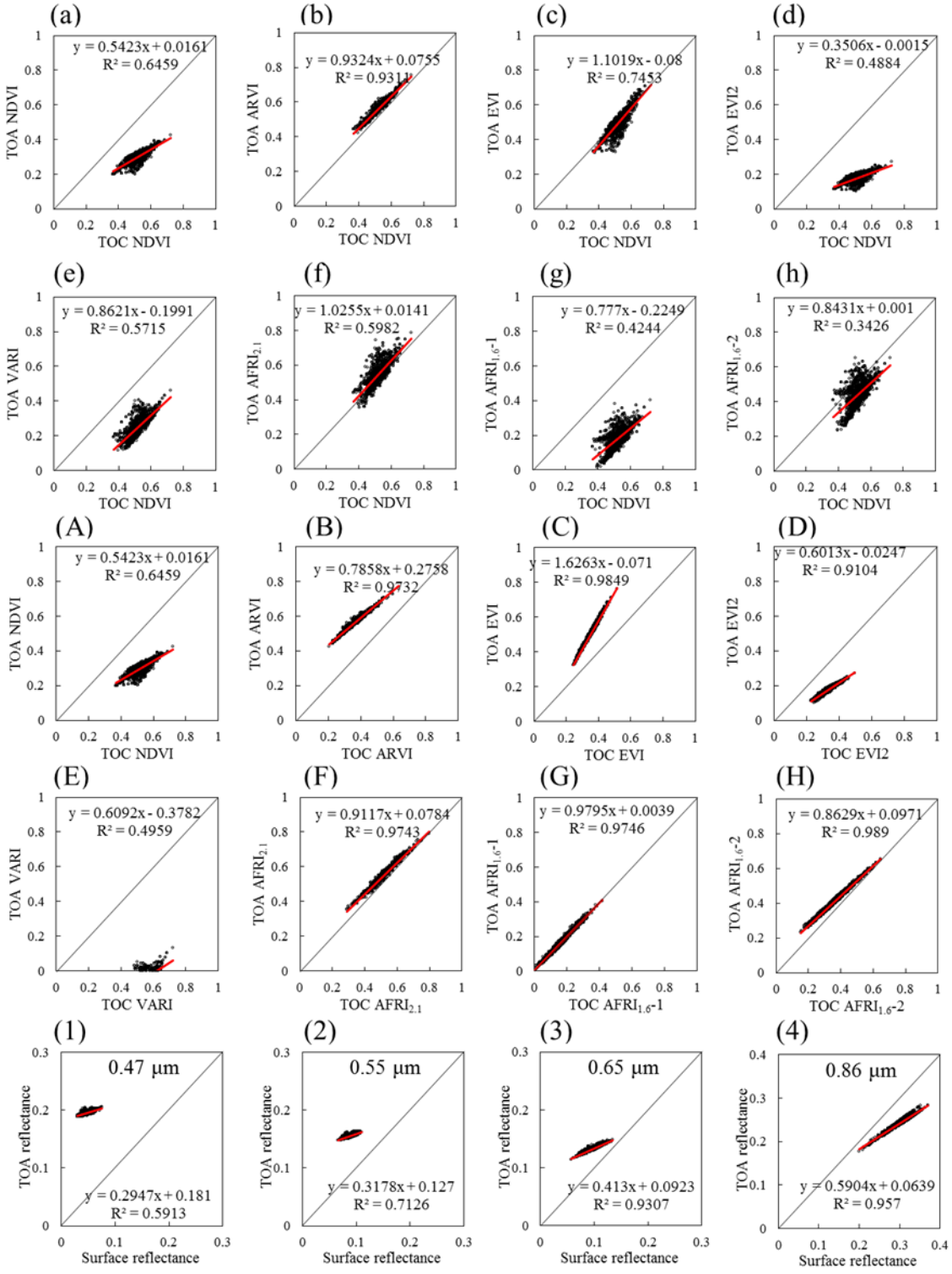

Figure 3.2 Experimental results for the Ubon_Ratchathani site (Julian calendar day 068 in 2010) with an AOD at 0.55 µm of 1.21). (**a**) TOA NDVI, (**b**) TOA ARVI, (**c**) TOA EVI, (**d**) TOA EVI2, (**e**) TOA VARI, (**f**) TOA $AFRI_{2.1}$, (**g**) TOA $AFRI_{1.6}$-1 and (**h**) TOA $AFRI_{1.6}$-2 plotted against the TOC NDVI; (**A**) TOA NDVI, (**B**) TOA ARVI, (**C**) TOA EVI, (**D**) TOA EVI2, (**E**) TOA VARI, (**F**) TOA $AFRI_{2.1}$, (**G**) TOA $AFRI_{1.6}$-1 and (**H**) TOA $AFRI_{1.6}$-2 plotted against their TOC index values, respectively; (**1**) TOA reflectance in blue (0.47 µm), (**2**) TOA reflectance in green (0.55 µm), (**3**) TOA reflectance in red (0.65 µm) and (**4**) TOA reflectance in NIR (0.86 µm) plotted against their surface reflectance values, respectively.

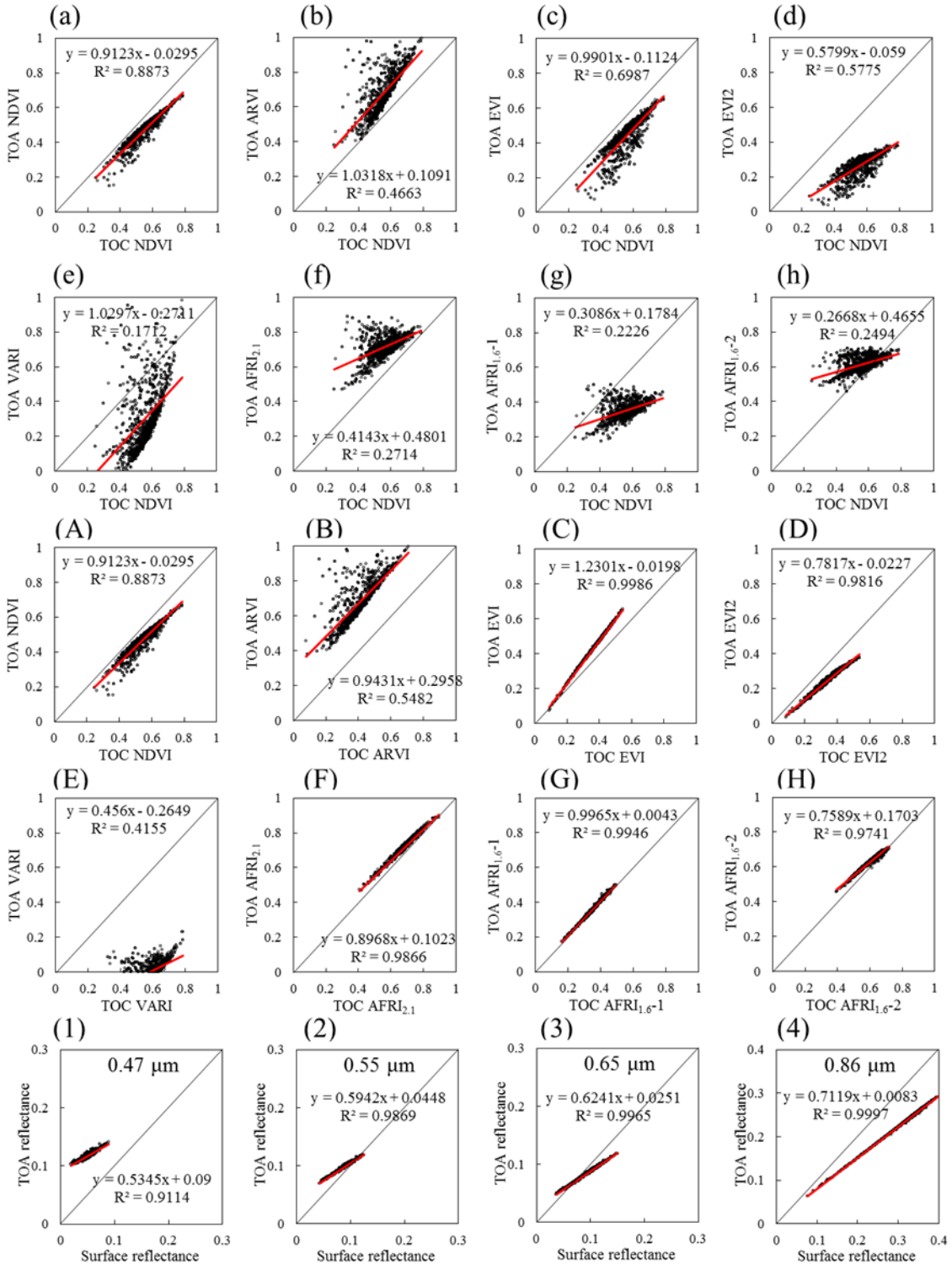

Figure 3.3 Experimental results for the Ubon_Ratchathani site (Julian calendar day 324 in 2010) with an AOD at 0.55 µm of 0.12). (**a**) TOA NDVI, (**b**) TOA ARVI, (**c**) TOA EVI, (**d**) TOA EVI2, (**e**) TOA VARI, (**f**) TOA $AFRI_{2.1}$, (**g**) TOA $AFRI_{1.6}$-1 and (**h**) TOA $AFRI_{1.6}$-2 plotted against the TOC NDVI; (**A**) TOA NDVI, (**B**) TOA ARVI, (**C**) TOA EVI, (**D**) TOA EVI2, (**E**) TOA VARI, (**F**) TOA $AFRI_{2.1}$, (**G**) TOA $AFRI_{1.6}$-1 and (**H**) TOA $AFRI_{1.6}$-2 plotted against their TOC index values, respectively; (**1**) TOA reflectance in blue (0.47 µm), (**2**) TOA reflectance in green (0.55 µm), (**3**) TOA reflectance in red (0.65 µm) and (**4**) TOA reflectance in NIR (0.86 µm) plotted against their surface reflectance values, respectively.

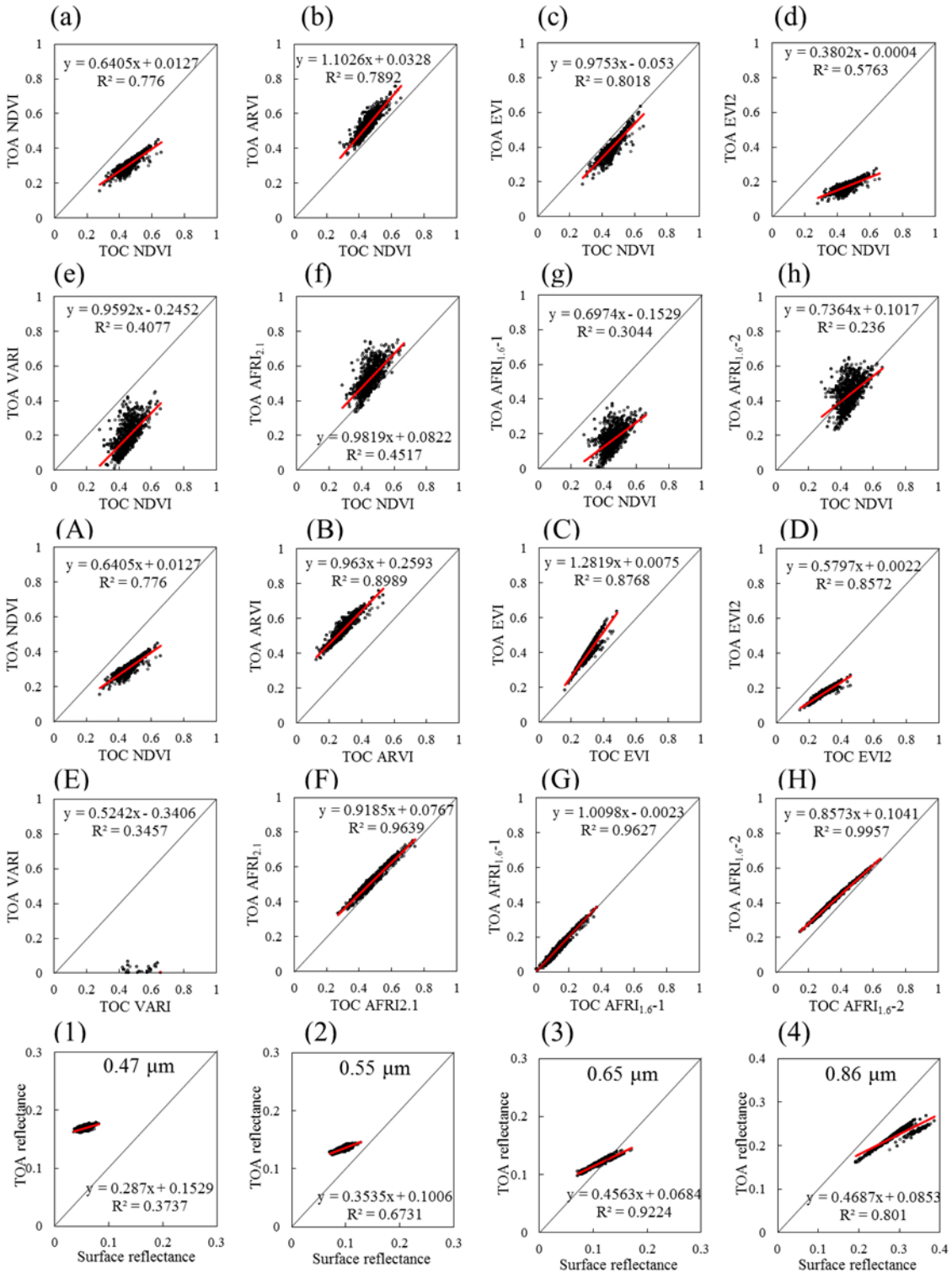

Figure 3.4 Experimental results for the Ubon_Ratchathani site (Julian calendar day 055 in 2011) with an AOD at 0.55 µm of 0.87). (**a**) TOA NDVI, (**b**) TOA ARVI, (**c**) TOA EVI, (**d**) TOA EVI2, (**e**) TOA VARI, (**f**) TOA $AFRI_{2.1}$, (**g**) TOA $AFRI_{1.6}$-1 and (**h**) TOA $AFRI_{1.6}$-2 plotted against the TOC NDVI; (**A**) TOA NDVI, (**B**) TOA ARVI, (**C**) TOA EVI, (**D**) TOA EVI2, (**E**) TOA VARI, (**F**) TOA $AFRI_{2.1}$, (**G**) TOA $AFRI_{1.6}$-1 and (**H**) TOA $AFRI_{1.6}$-2 plotted against their TOC index values, respectively; (**1**) TOA reflectance in blue (0.47 µm), (**2**) TOA reflectance in green (0.55 µm), (**3**) TOA reflectance in red (0.65 µm) and (**4**) TOA reflectance in NIR (0.86 µm) plotted against their surface reflectance values, respectively.

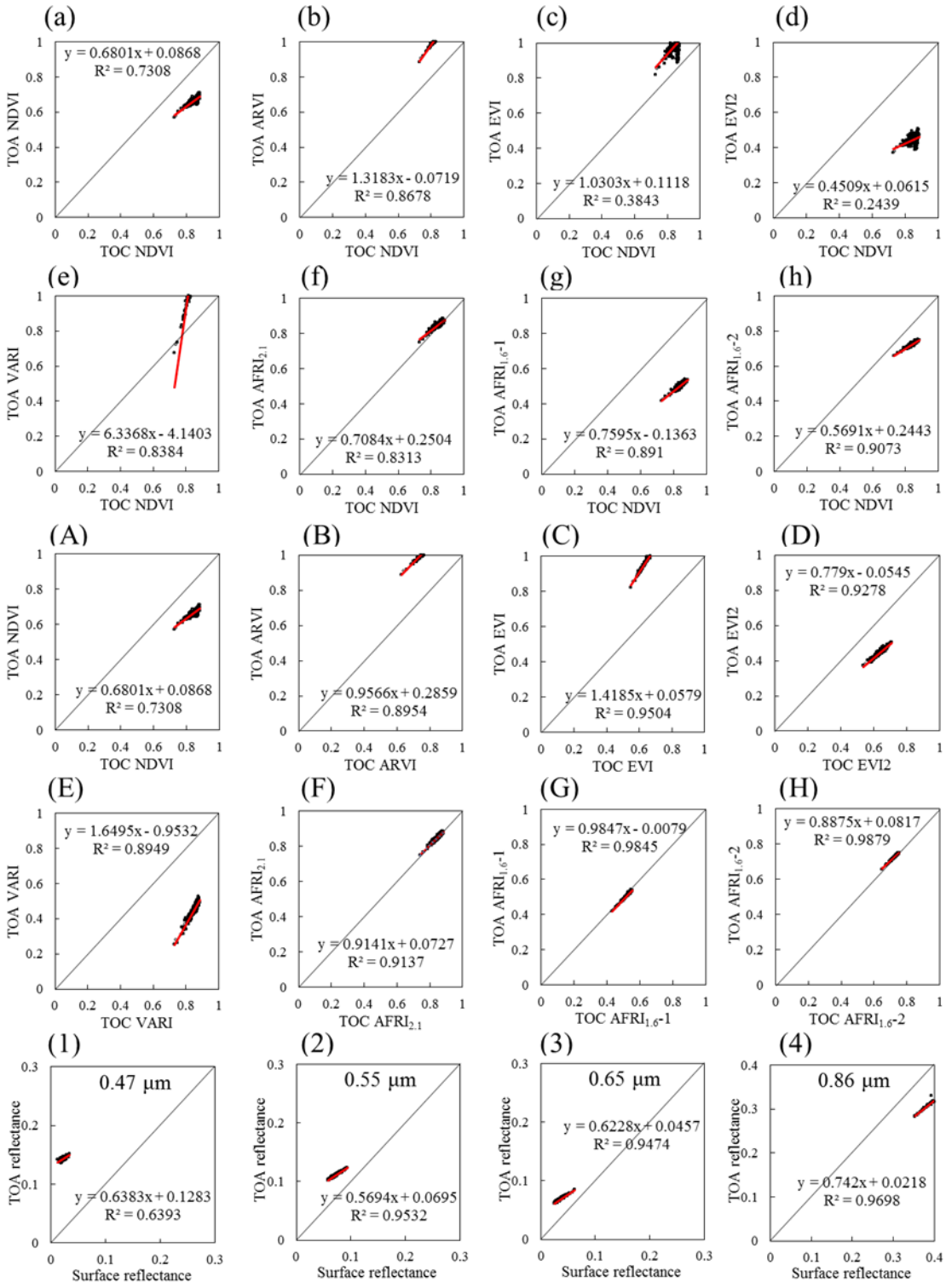

Figure 3.5 Experimental results for the Ussuriysk site (Julian calendar day 159 in 2008) with an AOD at 0.55 µm of 0.33). (**a**) TOA NDVI, (**b**) TOA ARVI, (**c**) TOA EVI, (**d**) TOA EVI2, (**e**) TOA VARI, (**f**) TOA $AFRI_{2.1}$, (**g**) TOA $AFRI_{1.6}$-1 and (**h**) TOA $AFRI_{1.6}$-2 plotted against the TOC NDVI; (**A**) TOA NDVI, (**B**) TOA ARVI, (**C**) TOA EVI, (**D**) TOA EVI2, (**E**) TOA VARI, (**F**) TOA $AFRI_{2.1}$, (**G**) TOA $AFRI_{1.6}$-1 and (**H**) TOA $AFRI_{1.6}$-2 plotted against their TOC index values, respectively; (**1**) TOA reflectance in blue (0.47 µm), (**2**) TOA reflectance in green (0.55 µm), (**3**) TOA reflectance in red (0.65 µm) and (**4**) TOA reflectance in NIR (0.86 µm) plotted against their surface reflectance values, respectively.

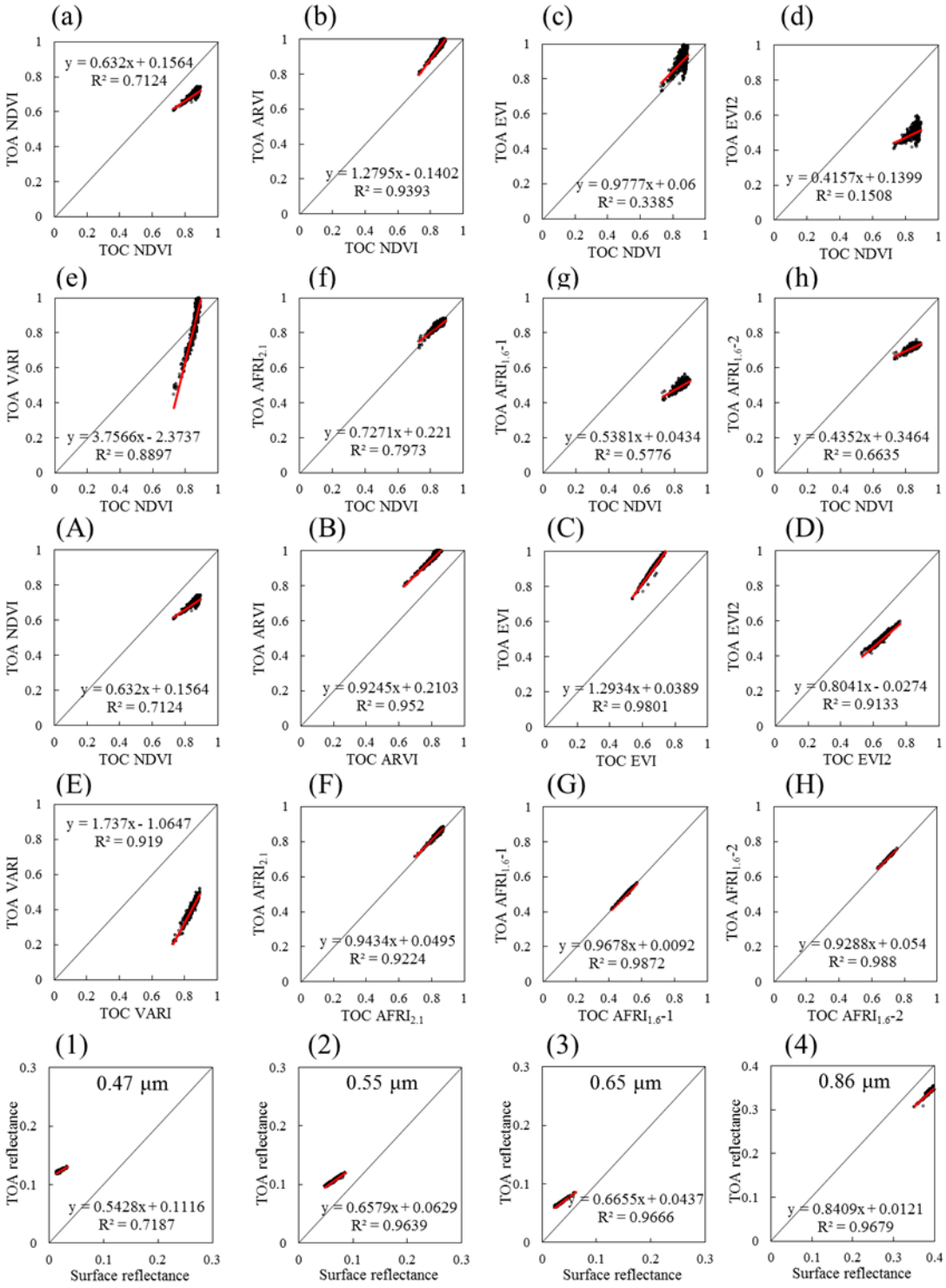

Figure 3.6 Experimental results for the Ussuriysk site (Julian calendar day 178 in 2008) with an AOD at 0.55 µm of 0.55). (**a**) TOA NDVI, (**b**) TOA ARVI, (**c**) TOA EVI, (**d**) TOA EVI2, (**e**) TOA VARI, (**f**) TOA $AFRI_{2.1}$, (**g**) TOA $AFRI_{1.6}$-1 and (**h**) TOA $AFRI_{1.6}$-2 plotted against the TOC NDVI; (**A**) TOA NDVI, (**B**) TOA ARVI, (**C**) TOA EVI, (**D**) TOA EVI2, (**E**) TOA VARI, (**F**) TOA $AFRI_{2.1}$, (**G**) TOA $AFRI_{1.6}$-1 and (**H**) TOA $AFRI_{1.6}$-2 plotted against their TOC index values, respectively; (**1**) TOA reflectance in blue (0.47 µm), (**2**) TOA reflectance in green (0.55 µm), (**3**) TOA reflectance in red (0.65 µm) and (**4**) TOA reflectance in NIR (0.86 µm) plotted against their surface reflectance values, respectively.

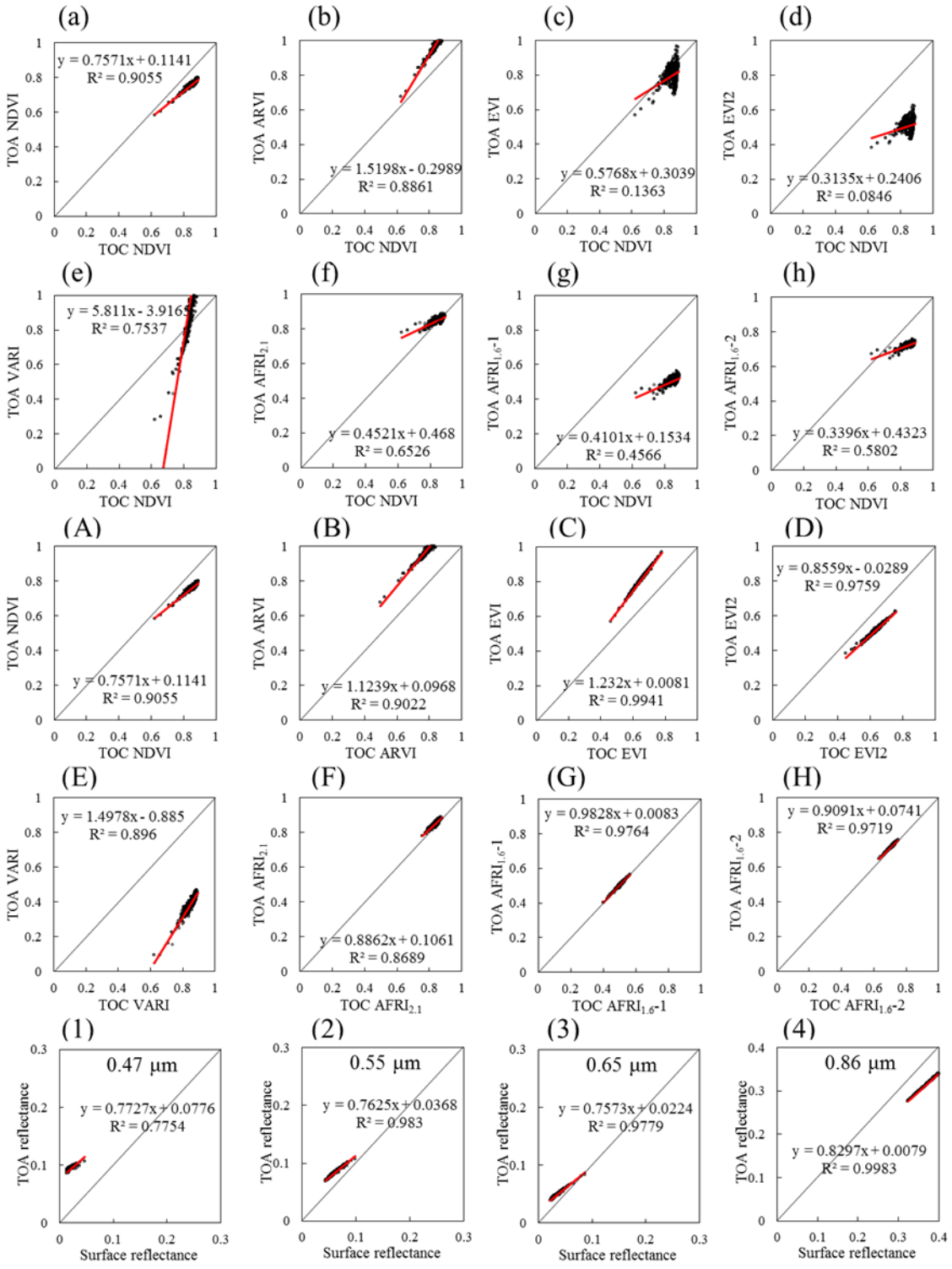

Figure 3.7 Experimental results for the Ussuriysk site (Julian calendar day 210 in 2008) with an AOD at 0.55 µm of 0.18). (**a**) TOA NDVI, (**b**) TOA ARVI, (**c**) TOA EVI, (**d**) TOA EVI2, (**e**) TOA VARI, (**f**) TOA $AFRI_{2.1}$, (**g**) TOA $AFRI_{1.6}$-1 and (**h**) TOA $AFRI_{1.6}$-2 plotted against the TOC NDVI; (**A**) TOA NDVI, (**B**) TOA ARVI, (**C**) TOA EVI, (**D**) TOA EVI2, (**E**) TOA VARI, (**F**) TOA $AFRI_{2.1}$, (**G**) TOA $AFRI_{1.6}$-1 and (**H**) TOA $AFRI_{1.6}$-2 plotted against their TOC index values, respectively; (**1**) TOA reflectance in blue (0.47 µm), (**2**) TOA reflectance in green (0.55 µm), (**3**) TOA reflectance in red (0.65 µm) and (**4**) TOA reflectance in NIR (0.86 µm) plotted against their surface reflectance values, respectively.

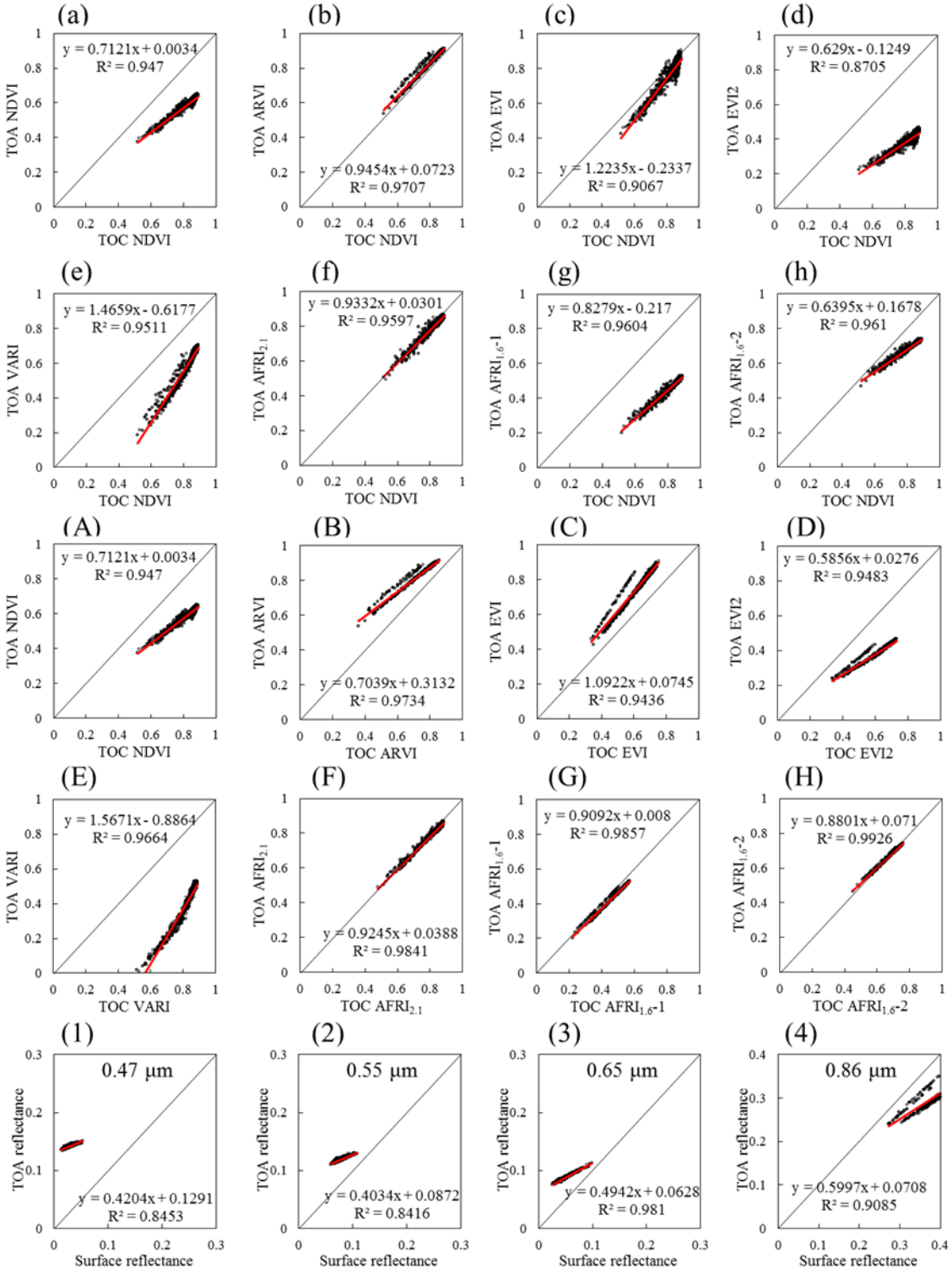

Figure 3.8 Experimental results for the Ussuriysk site (Julian calendar day 148 in 2009) with an AOD at 0.55 µm of 0.79). (**a**) TOA NDVI, (**b**) TOA ARVI, (**c**) TOA EVI, (**d**) TOA EVI2, (**e**) TOA VARI, (**f**) TOA $AFRI_{2.1}$, (**g**) TOA $AFRI_{1.6}$-1 and (**h**) TOA $AFRI_{1.6}$-2 plotted against the TOC NDVI; (**A**) TOA NDVI, (**B**) TOA ARVI, (**C**) TOA EVI, (**D**) TOA EVI2, (**E**) TOA VARI, (**F**) TOA $AFRI_{2.1}$, (**G**) TOA $AFRI_{1.6}$-1 and (**H**) TOA $AFRI_{1.6}$-2 plotted against their TOC index values, respectively; (**1**) TOA reflectance in blue (0.47 µm), (**2**) TOA reflectance in green (0.55 µm), (**3**) TOA reflectance in red (0.65 µm) and (**4**) TOA reflectance in NIR (0.86 µm) plotted against their surface reflectance values, respectively.

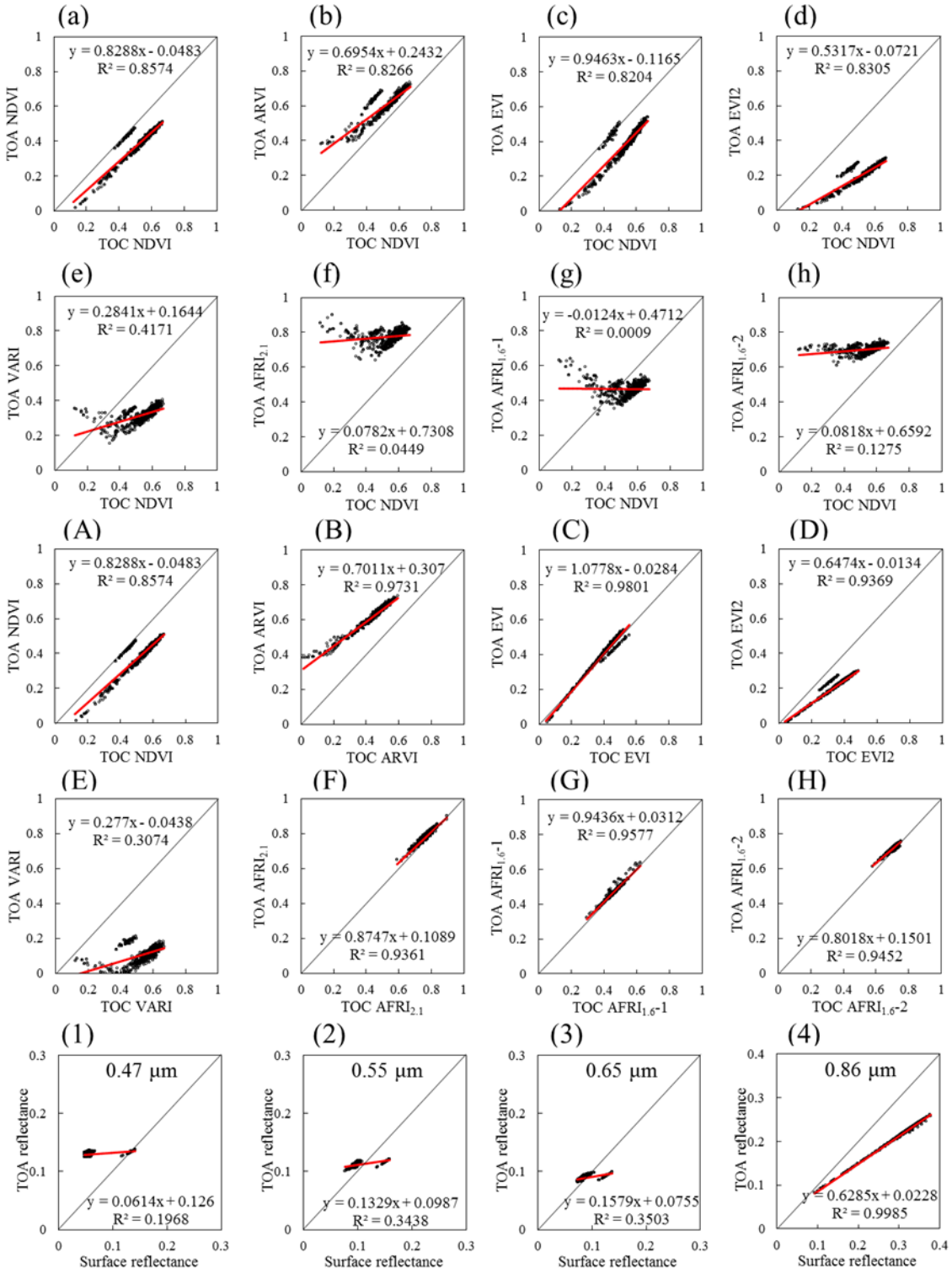

Figure 3.9 Experimental results for the Gandhi_College site (Julian calendar day 036 in 2012) with an AOD at 0.55 µm of 0.83). (**a**) TOA NDVI, (**b**) TOA ARVI, (**c**) TOA EVI, (**d**) TOA EVI2, (**e**) TOA VARI, (**f**) TOA $AFRI_{2.1}$, (**g**) TOA $AFRI_{1.6}$-1 and (**h**) TOA $AFRI_{1.6}$-2 plotted against the TOC NDVI; (**A**) TOA NDVI, (**B**) TOA ARVI, (**C**) TOA EVI, (**D**) TOA EVI2, (**E**) TOA VARI, (**F**) TOA $AFRI_{2.1}$, (**G**) TOA $AFRI_{1.6}$-1 and (**H**) TOA $AFRI_{1.6}$-2 plotted against their TOC index values, respectively; (**1**) TOA reflectance in blue (0.47 µm), (**2**) TOA reflectance in green (0.55 µm), (**3**) TOA reflectance in red (0.65 µm) and (**4**) TOA reflectance in NIR (0.86 µm) plotted against their surface reflectance values, respectively.

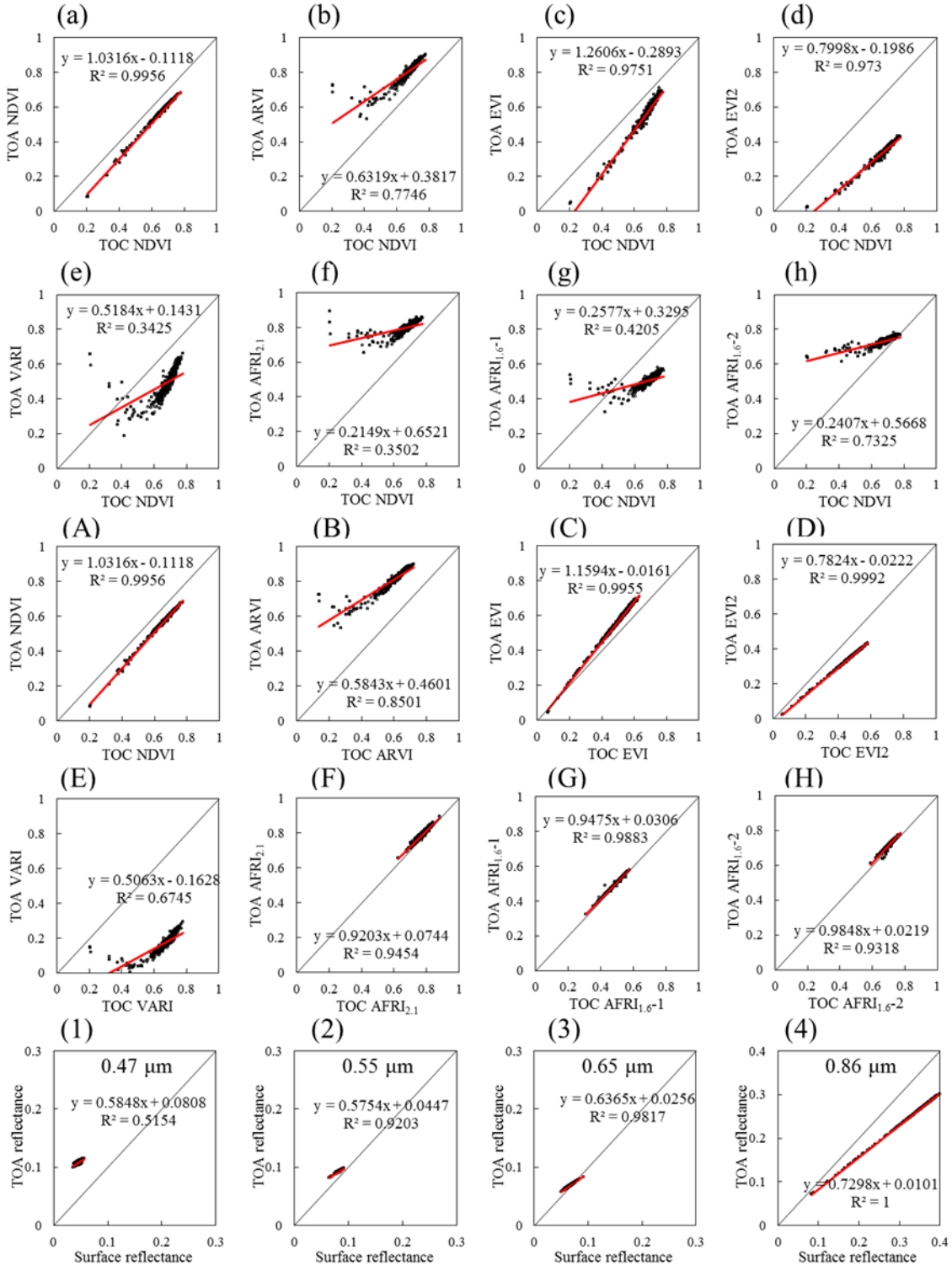

Figure 3.10 Experimental results for the Gandhi_College site (Julian calendar day 050 in 2012) with an AOD at 0.55 µm of 0.24). (**a**) TOA NDVI, (**b**) TOA ARVI, (**c**) TOA EVI, (**d**) TOA EVI2, (**e**) TOA VARI, (**f**) TOA $AFRI_{2.1}$, (**g**) TOA $AFRI_{1.6}$-1 and (**h**) TOA $AFRI_{1.6}$-2 plotted against the TOC NDVI; (**A**) TOA NDVI, (**B**) TOA ARVI, (**C**) TOA EVI, (**D**) TOA EVI2, (**E**) TOA VARI, (**F**) TOA $AFRI_{2.1}$, (**G**) TOA $AFRI_{1.6}$-1 and (**H**) TOA $AFRI_{1.6}$-2 plotted against their TOC index values, respectively; (**1**) TOA reflectance in blue (0.47 µm), (**2**) TOA reflectance in green (0.55 µm), (**3**) TOA reflectance in red (0.65 µm) and (**4**) TOA reflectance in NIR (0.86 µm) plotted against their surface reflectance values, respectively.

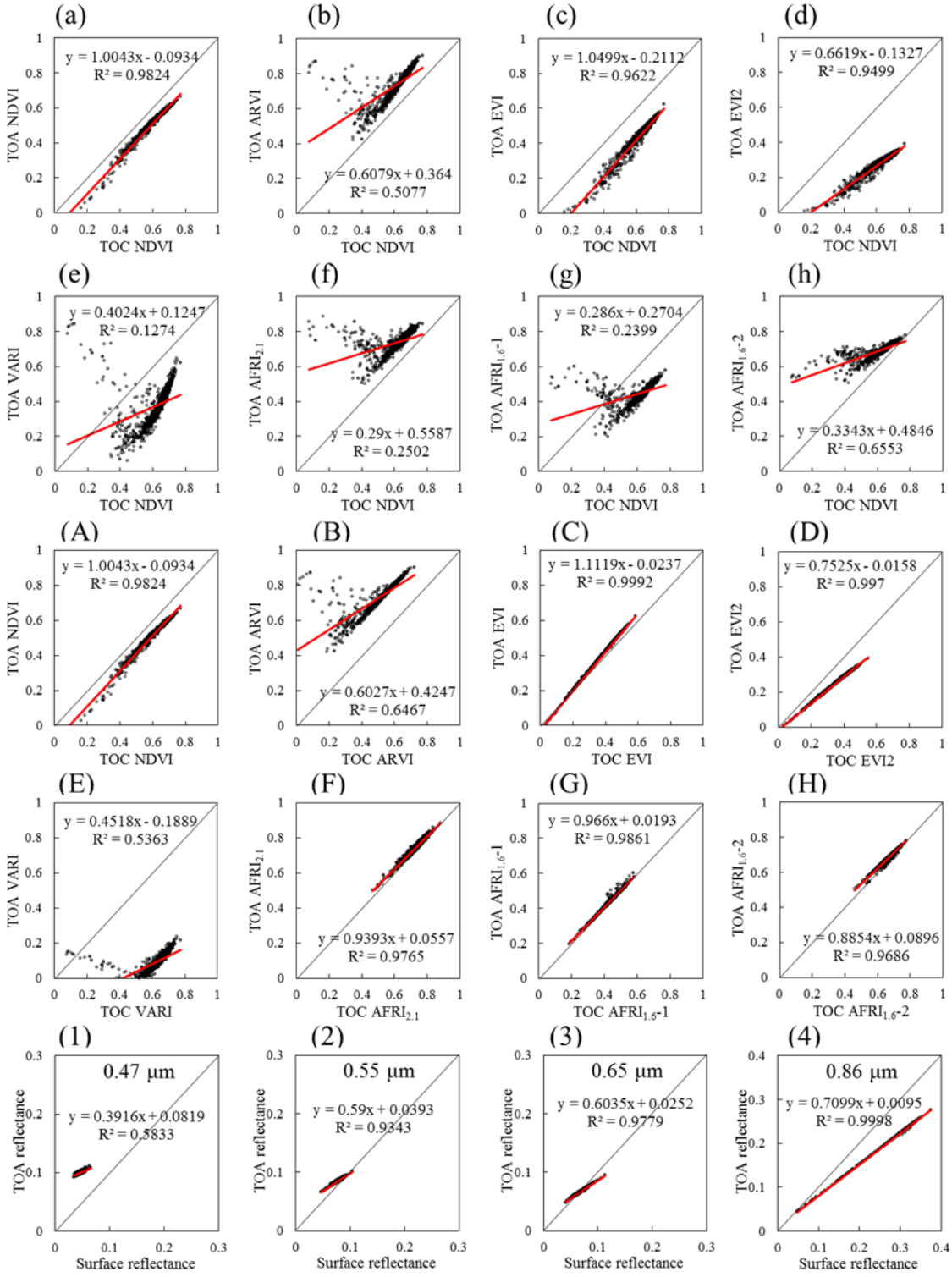

Figure 3.11 Experimental results for the Gandhi_College site (Julian calendar day 056 in 2012) with an AOD at 0.55 µm of 0.46). (**a**) TOA NDVI, (**b**) TOA ARVI, (**c**) TOA EVI, (**d**) TOA EVI2, (**e**) TOA VARI, (**f**) TOA $AFRI_{2.1}$, (**g**) TOA $AFRI_{1.6}$-1 and (**h**) TOA $AFRI_{1.6}$-2 plotted against the TOC NDVI; (**A**) TOA NDVI, (**B**) TOA ARVI, (**C**) TOA EVI, (**D**) TOA EVI2, (**E**) TOA VARI, (**F**) TOA $AFRI_{2.1}$, (**G**) TOA $AFRI_{1.6}$-1 and (**H**) TOA $AFRI_{1.6}$-2 plotted against their TOC index values, respectively; (**1**) TOA reflectance in blue (0.47 µm), (**2**) TOA reflectance in green (0.55 µm), (**3**) TOA reflectance in red (0.65 µm) and (**4**) TOA reflectance in NIR (0.86 µm) plotted against their surface reflectance values, respectively.

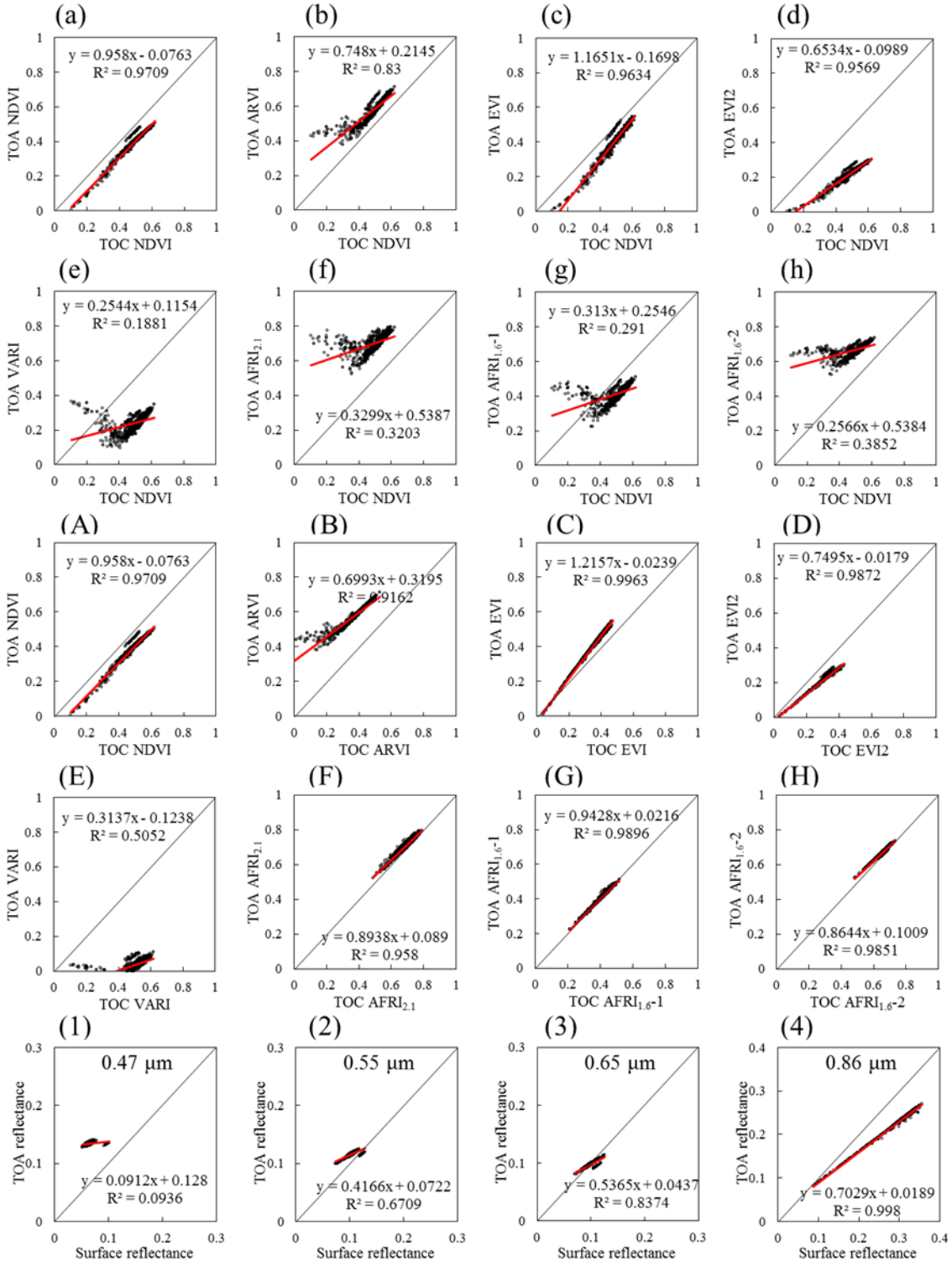

Figure 3.12 Experimental results for the Gandhi_College site (Julian calendar day 065 in 2012) with an AOD at 0.55 µm of 1.09). (**a**) TOA NDVI, (**b**) TOA ARVI, (**c**) TOA EVI, (**d**) TOA EVI2, (**e**) TOA VARI, (**f**) TOA $AFRI_{2.1}$, (**g**) TOA $AFRI_{1.6}$-1 and (**h**) TOA $AFRI_{1.6}$-2 plotted against the TOC NDVI; (**A**) TOA NDVI, (**B**) TOA ARVI, (**C**) TOA EVI, (**D**) TOA EVI2, (**E**) TOA VARI, (**F**) TOA $AFRI_{2.1}$, (**G**) TOA $AFRI_{1.6}$-1 and (**H**) TOA $AFRI_{1.6}$-2 plotted against their TOC index values, respectively; (**1**) TOA reflectance in blue (0.47 µm), (**2**) TOA reflectance in green (0.55 µm), (**3**) TOA reflectance in red (0.65 µm) and (**4**) TOA reflectance in NIR (0.86 µm) plotted against their surface reflectance values, respectively.

Table 3.2 The angle of observation and summarized statistics for the experimental data in the graphs (**a** to **h**) and (**1** to **4**) in Figures 3.1 to 3.4 (DOY is day of year, R_{red} is the reflectance at 0.65 μm, R_{NIR} is the reflectance at 0.86 μm, R_{blue} is the reflectance at 0.47 μm, and R_{green} is the reflectance at 0.55 μm).

Site_Name: Ubon_Ratchathani					
Year/DOY		**2010/047**	**2010/068**	**2010/324**	**2011/055**
AOD		**0.590**	**1.211**	**0.121**	**0.868**
NDVI	RMSE	0.203	0.225	0.083	0.153
	MBE	−0.202	−0.223	−0.079	−0.151
ARVI	RMSE	0.186	0.043	0.153	0.085
	MBE	0.184	0.040	0.127	0.080
EVI	RMSE	0.086	0.043	0.129	0.069
	MBE	0.081	−0.027	−0.118	−0.064
EVI2	RMSE	0.333	0.343	0.299	0.285
	MBE	−0.331	−0.341	−0.295	−0.283
VARI	RMSE	0.131	0.274	0.310	0.271
	MBE	−0.118	−0.271	−0.254	−0.264
$AFRI_{2.1}$	RMSE	0.100	0.052	0.168	0.092
	MBE	0.093	0.028	0.152	0.074
$AFRI_{1.6}$-1	RMSE	0.293	0.345	0.221	0.296
	MBE	−0.290	−0.341	−0.210	−0.291
$AFRI_{1.6}$-2	RMSE	0.049	0.101	0.087	0.073
	MBE	−0.013	−0.081	0.054	−0.019
R_{red}	RMSE	0.017	0.036	0.011	0.013
	MBE	0.016	0.035	−0.008	0.009
R_{NIR}	RMSE	0.094	0.064	0.084	0.073
	MBE	−0.093	−0.062	−0.082	−0.071
R_{blue}	RMSE	0.146	0.146	0.069	0.113
	MBE	0.146	0.146	0.069	0.113
R_{green}	RMSE	0.052	0.067	0.012	0.040
	MBE	0.052	0.067	0.010	0.040
Viewing Geometry (degree)	Solar zenith angle	43.360	34.315	41.122	38.038
	Sensor zenith angle	62.617	43.038	42.903	43.138
	Relative azimuth angle	31.700	25.720	50.030	31.725

Table 3.3 The angle of observation and summarized statistics for the experimental data in the graphs (**A** to **H**) and (**1** to **4**) in Figures 3.1 to 3.4 (DOY is day of year, R_{red} is the reflectance at 0.65 μm, R_{NIR} is the reflectance at 0.86 μm, R_{blue} is the reflectance at 0.47 μm, and R_{green} is the reflectance at 0.55 μm).

Site_Name: Ubon_Ratchathani					
Year/DOY		**2010/047**	**2010/068**	**2010/324**	**2011/055**
AOD		**0.590**	**1.211**	**0.121**	**0.868**
NDVI	RMSE	0.203	0.225	0.083	0.153
	MBE	−0.202	−0.223	−0.079	−0.151
ARVI	RMSE	0.344	0.198	0.283	0.250
	MBE	0.344	0.198	0.272	0.249
EVI	RMSE	0.241	0.150	0.069	0.095
	MBE	0.239	0.147	0.067	0.092
EVI2	RMSE	0.168	0.162	0.105	0.123
	MBE	−0.167	−0.161	−0.103	−0.122
VARI	RMSE	0.460	0.312	0.348	0.296
	MBE	0.458	0.311	0.316	0.294
$AFRI_{2.1}$	RMSE	0.040	0.035	0.034	0.040
	MBE	0.038	0.033	0.032	0.036
$AFRI_{1.6}$-1	RMSE	0.013	0.010	0.005	0.013
	MBE	0.011	0.000	0.003	−0.001
$AFRI_{1.6}$-2	RMSE	0.071	0.045	0.032	0.051
	MBE	0.070	0.042	0.029	0.049
R_{red}	RMSE	0.017	0.036	0.011	0.013
	MBE	0.016	0.035	−0.008	0.009
R_{NIR}	RMSE	0.094	0.064	0.084	0.073
	MBE	−0.093	−0.062	−0.082	−0.071
R_{blue}	RMSE	0.146	0.146	0.069	0.113
	MBE	0.146	0.146	0.069	0.113
R_{green}	RMSE	0.052	0.067	0.012	0.040
	MBE	0.052	0.067	0.010	0.040
Viewing Geometry (degree)	Solar zenith angle	43.360	34.315	41.122	38.038
	Sensor zenith angle	62.617	43.038	42.903	43.138
	Relative azimuth angle	31.700	25.720	50.030	31.725

Table 3.4 The angle of observation and summarized statistics for the experimental data in the graphs (**a** to **h**) and (**1** to **4**) in Figures 3.5 to 3.8 (DOY is day of year, R_{red} is the reflectance at 0.65 μm, R_{NIR} is the reflectance at 0.86 μm, R_{blue} is the reflectance at 0.47 μm, and R_{green} is the reflectance at 0.55 μm).

Site_Name: Ussuriysk					
Year/DOY		**2008/159**	**2008/178**	**2008/210**	**2009/148**
AOD		**0.328**	**0.554**	**0.183**	**0.792**
NDVI	RMSE	0.185	0.161	0.096	0.233
	MBE	−0.185	−0.161	−0.095	−0.231
ARVI	RMSE	0.199	0.101	0.150	0.031
	MBE	0.199	0.101	0.148	0.028
EVI	RMSE	0.142	0.055	0.075	0.062
	MBE	0.137	0.041	−0.060	−0.051
EVI2	RMSE	0.406	0.365	0.352	0.429
	MBE	−0.405	−0.363	−0.350	−0.427
VARI	RMSE	0.424	0.082	0.283	0.242
	MBE	0.392	0.001	0.224	−0.238
$AFRI_{2.1}$	RMSE	0.012	0.019	0.019	0.029
	MBE	0.003	−0.014	−0.004	−0.024
$AFRI_{1.6}$-1	RMSE	0.341	0.355	0.355	0.358
	MBE	−0.341	−0.355	−0.354	−0.357
$AFRI_{1.6}$-2	RMSE	0.122	0.141	0.138	0.130
	MBE	−0.122	−0.140	−0.136	−0.126
R_{red}	RMSE	0.033	0.033	0.015	0.043
	MBE	0.033	0.033	0.015	0.042
R_{NIR}	RMSE	0.087	0.056	0.061	0.097
	MBE	−0.086	−0.055	−0.061	−0.095
R_{blue}	RMSE	0.121	0.103	0.073	0.115
	MBE	0.121	0.103	0.073	0.115
R_{green}	RMSE	0.039	0.041	0.023	0.042
	MBE	0.039	0.041	0.023	0.042
Viewing Geometry (degree)	Solar zenith angle	29.136	25.124	29.400	26.085
	Sensor zenith angle	54.640	18.318	18.542	18.188
	Relative azimuth angle	33.361	38.002	41.358	42.940

Table 3.5 The angle of observation and summarized statistics for the experimental data in the graphs (**A** to **H**) and (**1** to **4**) in Figures 3.5 to 3.8 (DOY is day of year, R_{red} is the reflectance at 0.65 μm, R_{NIR} is the reflectance at 0.86 μm, R_{blue} is the reflectance at 0.47 μm, and R_{green} is the reflectance at 0.55 μm).

Site_Name: Ussuriysk					
Year/DOY		**2008/159**	**2008/178**	**2008/210**	**2009/148**
AOD		**0.328**	**0.554**	**0.183**	**0.792**
NDVI	RMSE	0.185	0.161	0.096	0.233
	MBE	−0.185	−0.161	−0.095	−0.231
ARVI	RMSE	0.252	0.149	0.198	0.096
	MBE	0.251	0.149	0.197	0.090
EVI	RMSE	0.332	0.235	0.158	0.135
	MBE	0.332	0.235	0.157	0.133
EVI2	RMSE	0.196	0.156	0.120	0.231
	MBE	−0.196	−0.155	−0.120	−0.228
VARI	RMSE	0.807	0.436	0.700	0.188
	MBE	0.794	0.431	0.680	0.186
$AFRI_{2.1}$	RMSE	0.006	0.006	0.012	0.025
	MBE	−0.001	0.002	0.010	−0.023
$AFRI_{1.6}$-1	RMSE	0.016	0.008	0.003	0.038
	MBE	−0.016	−0.007	0.000	−0.037
$AFRI_{1.6}$-2	RMSE	0.003	0.003	0.009	0.015
	MBE	0.000	0.003	0.009	−0.013
R_{red}	RMSE	0.033	0.033	0.015	0.043
	MBE	0.033	0.033	0.015	0.042
R_{NIR}	RMSE	0.087	0.056	0.061	0.097
	MBE	−0.086	−0.055	−0.061	−0.095
R_{blue}	RMSE	0.121	0.103	0.073	0.115
	MBE	0.121	0.103	0.073	0.115
R_{green}	RMSE	0.039	0.041	0.023	0.042
	MBE	0.039	0.041	0.023	0.042
Viewing Geometry (degree)	Solar zenith angle	29.136	25.124	29.400	26.085
	Sensor zenith angle	54.640	18.318	18.542	18.188
	Relative azimuth angle	33.361	38.002	41.358	42.940

Table 3.6 The angle of observation and summarized statistics for the experimental data in the graphs (**a** to **h**) and (**1** to **4**) in Figures 3.9 to 3.12 (DOY is day of year, R_{red} is the reflectance at 0.65 μm, R_{NIR} is the reflectance at 0.86 μm, R_{blue} is the reflectance at 0.47 μm, and R_{green} is the reflectance at 0.55 μm).

Site_Name: Gandhi_College					
Year/DOY		**2012/036**	**2012/050**	**2012/056**	**2012/065**
AOD		**0.829**	**0.236**	**0.456**	**1.086**
NDVI	RMSE	0.146	0.091	0.092	0.098
	MBE	−0.142	−0.091	−0.091	−0.097
ARVI	RMSE	0.085	0.145	0.141	0.093
	MBE	0.076	0.137	0.123	0.088
EVI	RMSE	0.151	0.120	0.182	0.089
	MBE	−0.146	−0.116	−0.181	−0.087
EVI2	RMSE	0.333	0.332	0.342	0.274
	MBE	−0.330	−0.331	−0.340	−0.273
VARI	RMSE	0.240	0.195	0.268	0.268
	MBE	−0.229	−0.177	−0.242	−0.259
$AFRI_{2.1}$	RMSE	0.241	0.153	0.148	0.211
	MBE	0.224	0.131	0.123	0.202
$AFRI_{1.6}$-1	RMSE	0.130	0.181	0.187	0.110
	MBE	−0.085	−0.163	−0.168	−0.090
$AFRI_{1.6}$-2	RMSE	0.176	0.097	0.102	0.176
	MBE	0.155	0.063	0.076	0.165
R_{red}	RMSE	0.010	0.003	0.004	0.004
	MBE	0.002	0.002	−0.001	−0.002
R_{NIR}	RMSE	0.093	0.083	0.077	0.072
	MBE	−0.091	−0.081	−0.075	−0.071
R_{blue}	RMSE	0.071	0.062	0.055	0.069
	MBE	0.068	0.062	0.055	0.069
R_{green}	RMSE	0.017	0.010	0.009	0.013
	MBE	0.011	0.010	0.008	0.012
Viewing Geometry (degree)	Solar zenith angle	45.043	39.647	41.513	39.248
	Sensor zenith angle	40.210	54.772	6.795	19.758
	Relative azimuth angle	124.292	123.934	44.702	41.717

Table 3.7 The angle of observation and summarized statistics for the experimental data in the graphs (**A** to **H**) and (**1** to **4**) in Figures 3.9 to 3.12 (DOY is day of year, R_{red} is the reflectance at 0.65 μm, R_{NIR} is the reflectance at 0.86 μm, R_{blue} is the reflectance at 0.47 μm, and R_{green} is the reflectance at 0.55 μm).

Site_Name: Gandhi_College					
Year/DOY		**2012/036**	**2012/050**	**2012/056**	**2012/065**
AOD		**0.829**	**0.236**	**0.456**	**1.086**
NDVI	RMSE	0.146	0.091	0.092	0.098
	MBE	−0.142	−0.091	−0.091	−0.097
ARVI	RMSE	0.171	0.217	0.219	0.203
	MBE	0.174	0.224	0.228	0.205
EVI	RMSE	0.003	0.061	0.022	0.054
	MBE	0.015	0.064	0.025	0.057
EVI2	RMSE	0.144	0.123	0.113	0.102
	MBE	−0.141	−0.121	−0.111	−0.100
VARI	RMSE	0.212	0.314	0.283	0.209
	MBE	0.213	0.316	0.290	0.211
$AFRI_{2.1}$	RMSE	0.014	0.012	0.012	0.016
	MBE	0.017	0.015	0.015	0.019
$AFRI_{1.6}$-1	RMSE	0.009	0.006	0.008	0.006
	MBE	0.005	0.005	0.004	−0.002
$AFRI_{1.6}$-2	RMSE	0.013	0.011	0.012	0.012
	MBE	0.015	0.013	0.015	0.014
R_{red}	RMSE	0.010	0.003	0.004	0.004
	MBE	0.002	0.002	−0.001	−0.002
R_{NIR}	RMSE	0.093	0.083	0.077	0.072
	MBE	−0.091	−0.081	−0.075	−0.071
R_{blue}	RMSE	0.071	0.062	0.055	0.069
	MBE	0.068	0.062	0.055	0.069
R_{green}	RMSE	0.017	0.010	0.009	0.013
	MBE	0.011	0.010	0.008	0.012
Viewing Geometry (degree)	Solar zenith angle	45.043	39.647	41.513	39.248
	Sensor zenith angle	40.210	54.772	6.795	19.758
	Relative azimuth angle	124.292	123.934	44.702	41.717

3.3.2 Comparison of TOA vegetation indices and individual TOC vegetation indices

To understand how much the atmospheric influences impact the mentioned VIs, we compared the TOA VIs with their respective TOC VIs, and the results are shown as graphs (A to H) in Figures 3.1 to 3.12. The larger differences between the TOA and TOC index values indicate that these VIs are more sensitive to atmospheric influences. For each VI, we can see that the TOA indices all showed very high correlations with their TOC indices. However, their TOA index values were increased or decreased by atmospheric influences. For example, the TOA ARVI is typically overestimated versus the TOC ARVI; conversely, the TOA EVI2 values were lower than the TOC values due to atmospheric effects. The RMSE and MBE of the TOA and TOC VIs are shown in Tables 3.3, 3.5, and 3.7, and Figures 3.13 to 3.15 show the comparisons of the RMSE values of the VIs over different experimental sites. Except for those of VARI, ARVI and EVI had the largest RMSE values. Because both ARVI and EVI rely on the blue band for the correction the atmospheric effects in the red band, the measurements of ARVI and EVI should utilize the atmospherically corrected or partially atmosphere-corrected (Rayleigh and ozone absorption) surface reflectances. The large errors in the ARVI and EVI simulations may be caused by the use of uncorrected TOA reflectances. The SWIR-derived AFRIs showed the best ability to “resist atmosphere influences” and have very low RMSE values even when the AOD value is very high.

3.3.3 Atmospheric influences in the MODIS red, NIR, blue, and green bands

The reduction in the precision of the remote sensing image interpretation for the detection of vegetation dynamics is essentially caused by the atmospheric effects in the bands that are used in VIs. Therefore, in Section 3.3.1 and 3.3.2, I analyzed those cases corresponding to the atmospheric influences in the MODIS red, NIR, blue, and green bands. The comparisons of the TOA and surface reflectances of these four bands are shown in the graphs (1 to 4) in Figures 3.1 to 3.12. I found that the TOA reflectances in the blue (graphs (1) in Figures 3.1 to 3.12) and green (graphs (2) in Figures 3.1 to 3.12) bands are obviously larger than the corresponding surface reflectances. This is because the blue and the green bands have shorter wavelengths than the red, making the former more easily affected by the atmospheric particles scattering, and the added path radiance intrinsic to the atmosphere, which has not been reflected by the Earth's surface, can increase the brightness of these bands [11,21]. For the red (graphs (3) in Figures 3.1 to 3.12) band, over the low reflectance area, the effect of the atmosphere is to create a bright surface. As the graphs (4) in Figures 3.1 to 3.12 shown, the TOA reflectance values in the NIR band dropped lower than the corresponding surface reflectance. The reduction in the NIR is caused by the atmospheric absorption. Figure 3.16 shows the standard deviations of the MBE for these four bands with different

AOD values. The lower standard deviation of the MBE values indicated a lower susceptibility to the influences of the atmosphere. Our results revealed that larger MBE values were derived from the shorter wavelength bands. Because of this, the uncorrected reflectance used in the blue band-based self-corrected ARVI and EVI led to unsatisfactory performances; in contrast to ARVI and EVI, the SWIR-based AFRIs were less affected by aerosol loading due to the ability of longer wavelength to penetrate the atmosphere, even in the presence of aerosols.

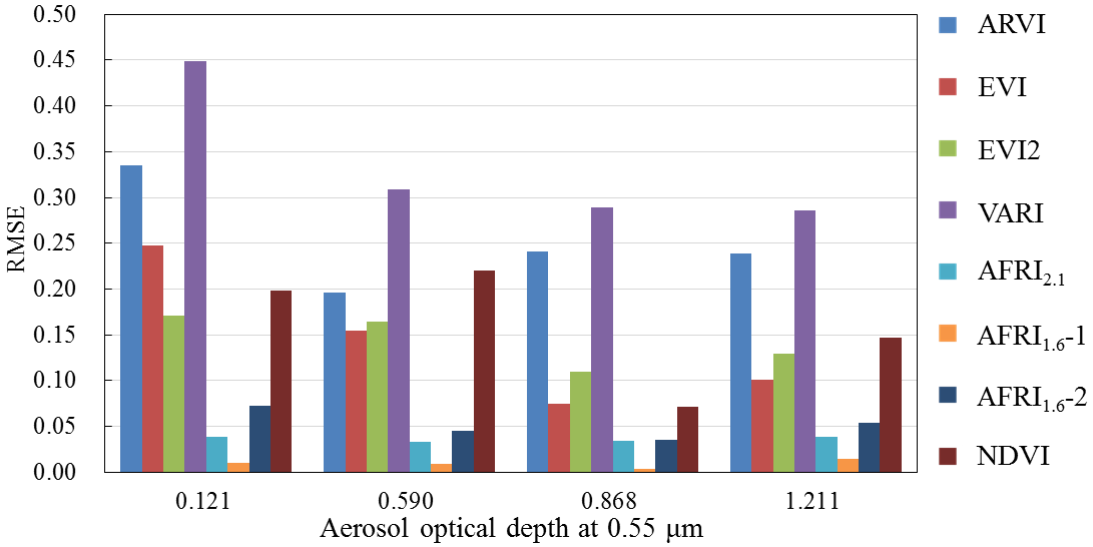

Figure 3.13 Experimental results over the Ubon Ratchathani site and the root mean square error (RMSE) between the TOA and TOC vegetation index values for different aerosol optical depths (AODs).

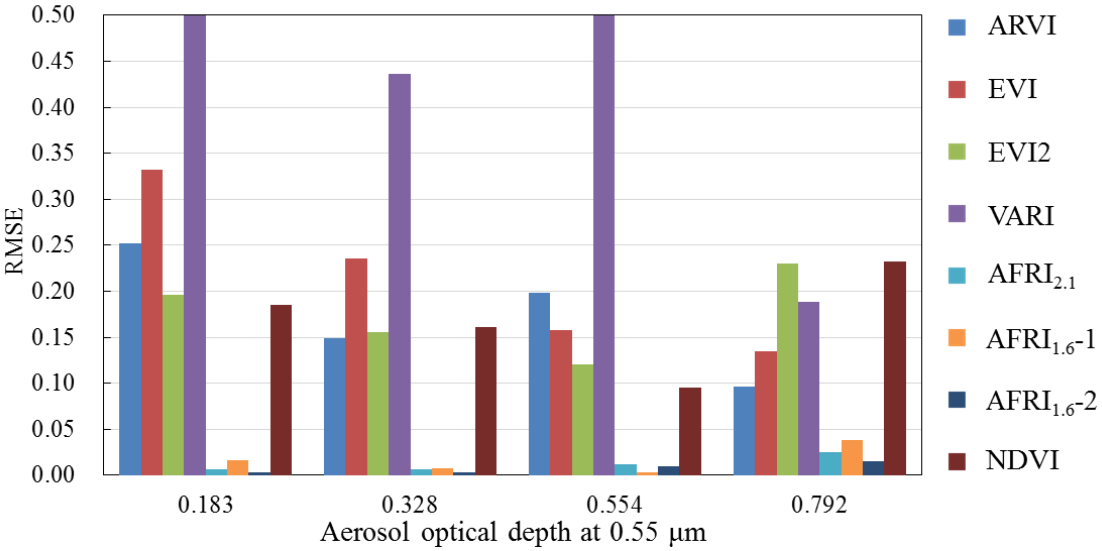

Figure 3.14 Experimental results over the Ussuriysk site and the RMSE between the TOA and TOC vegetation index values for different AODs.

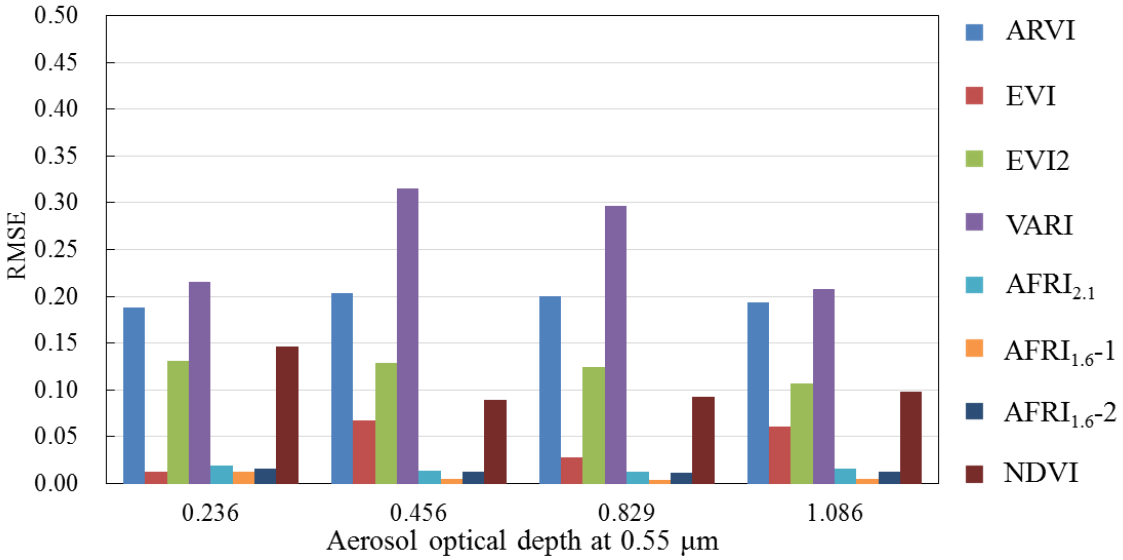

Figure 3.15 Experimental results over the Gandhi_College site and the RMSE between the TOA and TOC vegetation index values for different AODs.

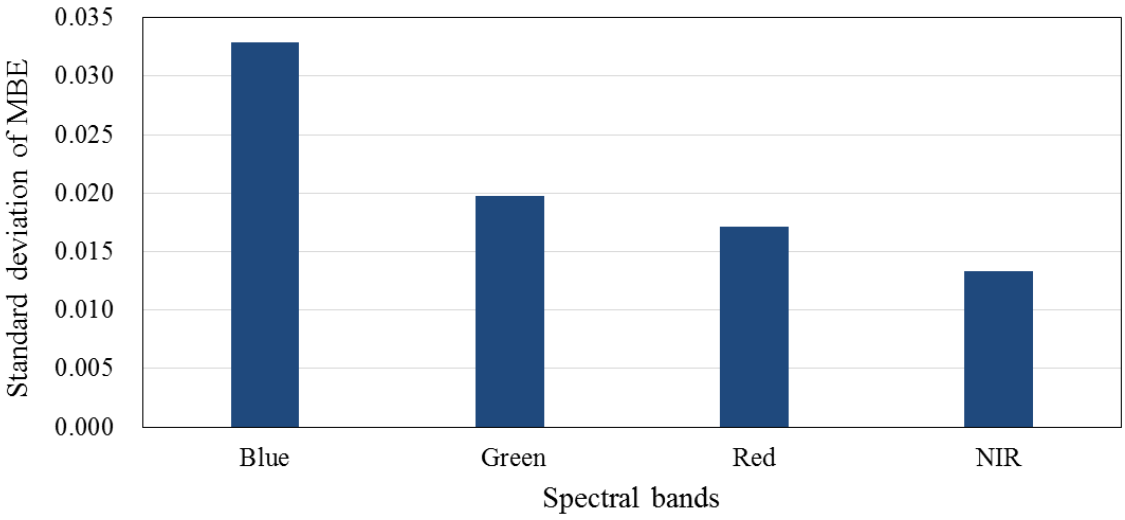

Figure 3.16 The standard deviation of the mean bias errors (MBEs) between the TOA and the surface reflectance in different spectral bands.

3.4 Conclusions

In this study, I evaluated the performances of ARVI, EVI, EVI2, VARI and AFRI for vegetation detection and monitoring with various AOD levels using the MODIS

and AERONET data.

The studies of Bowker et al. [24] showed that, without atmospheric effects, ARVI has the high correlation with NDVI. Our results revealed that, for different aerosol conditions, the TOA ARVI also showed high consistency with the TOC NDVI.

With the exception of that of ARVI, the TOA EVIs better agreed with the TOC NDVI than the other VIs. However, the poor agreement was observed over dense vegetated areas with low aerosols loadings, which is due to the non-linear behavior of NDVI leading to the saturation problem in areas with dense vegetation. It indicated that the atmospheric influences fade-out the differences between the EVI and NDVI caused by the saturation effect.

The success of the AFRIs is limited over vegetated area; the TOA AFRIs and the TOC NDVI are obviously more consistent over densely vegetated areas, and larger differences between the TOA AFRIs and the TOC NDVI may occur over low vegetation area.

Among the three different AFRIs, $AFRI_{2.1}$ and $AFRI_{1.6}$-2 have closer values to those of the TOC NDVI than those of $AFRI_{1.6}$.

The TOA and the TOC index values were compared for each VI, under different AOD levels. The SWIR-based VIs (e.g., AFRIs) showed smaller differences between their TOA and TOC index values than the other VIs. This demonstrated that the SWIR-based VIs are less affected by atmospheric influences.

For the application of the self-corrected VIs (e.g., ARVI and EVI), when using the TOA reflectance directly rather than the atmospherically corrected or partially atmosphere-corrected (Rayleigh and ozone absorption) surface reflectance, the TOA-derived values show extremely high correlations with the TOC values; however, the uncorrected reflectances can lead to the TOA-derived ARVI and EVI tending to overestimate the surface-derived values.

Conversely, the atmospheric effects reduced the TOA EVI2 and VARI values and led to the underestimation of vegetation conditions.

The experimental results verified that the effect of an atmosphere without clouds is to render a dark surface as bright in the visible region and to reduce the brightness in the NIR band. Among the visible bands, the blue band is most sensitive to the atmosphere; compared with the visible bands, the NIR band is less affected by atmospheric influences, but is sensitive to vegetation variations.

Miura et al. (1998) suggested that the effects of aerosols on the NIR band should

be corrected [16]; however, so far there have been relatively few published research papers on this topic. In this case, it is possible to correct the atmospheric effects in both the visible and NIR bands for VIs through a combination of the self-corrected and SWIR-based concepts in the advanced VIs (e.g., ARVI, EVI, AFRIs).

References

1. Jiang, Z.; Huete, A.R.; Chen, J.; Chen, Y.; Li, J.; Yan, G.; Zhang, X. Analysis of ndvi and scaled difference vegetation index retrievals of vegetation fraction. *Remote sensing of environment* **2006**, *101*, 366-378.
2. Jorgensen, S.E.; Svirezhev, Y.M. Towards a thermodynamic theory for ecological systems. Elsevier: 2004.
3. Huete, A.R. A soil-adjusted vegetation index (savi). *Remote sensing of environment* **1988**, *25*, 295-309.
4. Kaufman, Y.J.; Tanre, D. Atmospherically resistant vegetation index (arvi) for eos-modis. *IEEE transactions on Geoscience and Remote Sensing* **1992**, *30*, 261-270.
5. Liu, H.Q.; Huete, A. A feedback based modification of the ndvi to minimize canopy background and atmospheric noise. *IEEE Transactions on Geoscience and Remote Sensing* **1995**, *33*, 457-465.
6. Jiang, Z.; Huete, A.R.; Didan, K.; Miura, T. Development of a two-band enhanced vegetation index without a blue band. *Remote Sensing of Environment* **2008**, *112*, 3833-3845.
7. Hanan, N.; Prince, S.; Hiernaux, P. Spectral modelling of multicomponent landscapes in the sahel. *International Journal of Remote Sensing* **1991**, *12*, 1243-4258.
8. Huete, A.R.; Liu, H.Q. An error and sensitivity analysis of the atmospheric-and soil-correcting variants of the ndvi for the modis-eos. *IEEE Transactions on Geoscience and Remote Sensing* **1994**, *32*, 897-905.
9. Liu, G.-R.; Liang, C.-K.; Kuo, T.-H.; Lin, T.-H.; Huang, S. Comparison of the ndvi, arvi and afri vegetation index, along with their relations with the aod using spot 4 vegetation dat. *Terrestrial Atmospheric and Oceanic Sciences* **2004**, *15*, 15-32.
10. Gao, X.; Huete, A.R.; Ni, W.; Miura, T. Optical–biophysical relationships of vegetation spectra without background contamination. *Remote Sensing of Environment* **2000**, *74*, 609-620.
11. Didan, K.; Munoz, A.B.; Solano, R.; Huete, A. Modis vegetation index user's guide (mod13 series). *Vegetation Index and Phenology Lab, the University of Arizona, USA* **2015**.

12. Gitelson, A.A.; Kaufman, Y.J.; Stark, R.; Rundquist, D. Novel algorithms for remote estimation of vegetation fraction. *Remote sensing of Environment* **2002**, *80*, 76-87.
13. Schneider, P.; Roberts, D.; Kyriakidis, P. A vari-based relative greenness from modis data for computing the fire potential index. *Remote Sensing of Environment* **2008**, *112*, 1151-1167.
14. Stow, D.; Niphadkar, M.; Kaiser, J. Modis‐derived visible atmospherically resistant index for monitoring chaparral moisture content. *International Journal of Remote Sensing* **2005**, *26*, 3867-3873.
15. Kaufman, Y.J.; Remer, L.A. Detection of forests using mid-ir reflectance: An application for aerosol studies. *IEEE Transactions on Geoscience and Remote Sensing* **1994**, *32*, 672-683.
16. Miura, T.; Huete, A.; Leeuwen, W.v.; Didan, K. Vegetation detection through smoke‐filled aviris images: An assessment using modis band passes. *Journal of Geophysical Research: Atmospheres* **1998**, *103*, 32001-32011.
17. Karnieli, A.; Kaufman, Y.J.; Remer, L.; Wald, A. AFRI—aerosol free vegetation index. *Remote Sensing of Environment* **2001**, *77*, 10-21.
18. Bannari, A.; Morin, D.; Bonn, F.; Huete, A. A review of vegetation indices. *Remote sensing reviews* **1995**, *13*, 95-120.
19. NASA MODIS MODERATE RESOLUTION IMAGING SPECTRORADIOMETER, MODIS Design. Available online: https://modis.gsfc.nasa.gov/about/design.php (accessed on 28 March 2017).
20. Collection-6 Terra Product Descriptions: MOD02HKM. Available online: https://modaps.modaps.eosdis.nasa.gov/services/about/products/c6/MOD02HKM.html (accessed on 15 March 2017).
21. Vermote, E.; Kotchenova, S. Mod09 (surface reflectance) user's guide. https:// *modis-sr. ltdri. org/products/MOD09_UserGuide_v1_2. pdf S* **2008**.
22. Holben, B.N.; Eck, T.; Slutsker, I.; Tanre, D.; Buis, J.; Setzer, A.; Vermote, E.; Reagan, J.; Kaufman, Y.; Nakajima, T. AERONET—A Federated Instrument Network and Data Archive for Aerosol Characterization. *Remote sensing of environment* **1998**, *66*, 1-16.
23. Slutsker, I.; Kinne, S. Wavelength dependence of the optical depth of biomass burning, urban, and desert dust aerosols. *Journal of Geophysical Research: Atmospheres* **1999**, *104*.
24. Bowker, D.E.; Davis, R.E.; Myrick, D.L.; Stacy, K.; Jones, W.T. Spectral reflectances of natural targets for use in remote sensing studies. **1985**.

Chapter 4 A self-corrected method for correcting for atmospheric influences in vegetation indices

4.1 Introduction

Vegetation indices (VIs) are radiometric measures of vegetation or greenness and have been widely used for monitoring vegetation structure and function in remote sensing applications [1,2]. In recent decades, a large number of VIs have been developed by employing the sum, difference, ratio, or other linear combinations of two or more spectral bands in the visible to middle infrared spectrum that can provide key information for understanding the biosphere and its dynamics [3,4]. Among these, the Normalized Difference Vegetation Index (NDVI) [5] has been extensively used in many fields, including precision agriculture, rangeland management, and forest management [6]. NDVI is calculated using the difference in the reflectances of red (R_{red}) and near-infrared (NIR; R_{NIR}) radiation, as shown in Equation 1:

$$\mathrm{NDVI} = (\mathrm{R_{NIR}} - \mathrm{R_{red}})/(\mathrm{R_{NIR}} + \mathrm{R_{red}}) \quad (1)$$

The sensitivity of NDVI to the presence of vegetation is mainly based on the different behaviors between the red and NIR spectra over green vegetation: the chlorophyll of vegetation usually absorbs the energy in the red wavelength, while the mesophyll reflects in the NIR wavelength, and there is no such reflectance for areas with no vegetation [7,8]. However, NDVI also has several weaknesses, including its sensitivity to the effects of soil characteristics (type, brightness, color, wetness, etc.) [9], the saturation of the index value [10], and atmospheric influences [11]. Because the reflectance of the red and NIR bands observed by spaceborne sensors is disturbed by light-absorbing and scattering aerosols in the atmosphere, the observed NDVI is underestimated over vegetated surfaces [12,13].

To improve upon the NDVI by minimizing the soil influence, a number of new VIs have been proposed, such as the Soil-Adjusted Vegetation Index (SAVI) [14], the Transformed SAVI (TSAVI) [15], the Soil-Adjusted Ratio Vegetation Index (SAVI2) [16] and the Modified SAVI (MSAVI) [17]. Regarding the removal of aerosol influence on VIs, there are two main approaches: The first involves employing another band or parameter to correct the errors in the relevant band. For instance, the Atmospherically Resistant Vegetation Index (ARVI) was developed by incorporating the blue band that directly conducts atmospheric corrections on the red band [7]. In

addition, the Soil-adjusted and Atmospheric Resistant Vegetation Index (SARVI) and the Enhanced Vegetation Index (EVI), which evolved from NDVI, SAVI and ARVI, have the capacity to self-correct atmospheric influences by taking the soil properties and atmospheric interferences into account [18,19]. The second approach uses shortwave infrared (SWIR) spectral bands to construct VIs. Because the wavelength of the SWIR band is much larger than the radius of most common aerosols, the SWIR electromagnetic signal is able to penetrate atmospheric columns containing suspended aerosols [8,20]; however, the SWIR also remains the sensitive to vegetation [8]. Thus, several SWIR-based VIs have been developed. The usefulness of VIs based on the ratio of SWIR/NIR (1.6 μm/0.8 μm and 2.1 μm/0.8 μm) has been demonstrated in monitoring the state of forests, e.g., discriminating forest damage [21–23]. Miura et al. (1998) derived several 1.6- or 2.1-μm-based VIs (Equations 2a and 2b) and assessed their performance in a smoke-filled atmosphere [24]:

$$\mathrm{NDVI_{MIR}} = (\mathrm{R_{NIR}} - \mathrm{R_{MIR}})/(\mathrm{R_{NIR}} + \mathrm{R_{MIR}}) \quad (2a)$$

$$\mathrm{SAVI_{MIR}} = (\mathrm{R_{NIR}} - \mathrm{R_{MIR}})(1 + \mathrm{L})/(\mathrm{R_{NIR}} + \mathrm{R_{MIR}}) \quad (2b)$$

where MIR is either the 1.6- or 2.1-μm spectral band and L is a canopy background adjustment factor [14]. Subsequently, Karnieli et al. (2001) measured a variety of ground surfaces in Israel using a field spectrometer by aircraft and summarized the empirical linear relationship between the SWIR spectral band around 2.1 and 1.6 μm and the red band around 0.6 μm, where $R_{0.6} = 0.5R_{2.1}$ and $R_{0.6} = 0.66R_{1.6}$. Based on these relationships, the Aerosol FRee vegetation Index (AFRI) has been proposed, and the two versions of AFRI (Equations 3a and 3b) are formulated as follows [25]:

$$\mathrm{AFRI_{2.1}} = (\mathrm{R_{NIR}} - 0.5 * \mathrm{R_{2.1}})/(\mathrm{R_{NIR}} + 0.5 * \mathrm{R_{2.1}}) \quad (3a)$$

$$\mathrm{AFRI_{1.6}} = (\mathrm{R_{NIR}} - 0.66 * \mathrm{R_{1.6}})/(\mathrm{R_{NIR}} + 0.66 * \mathrm{R_{1.6}}) \quad (3b)$$

where $R_{2.1}$ and $R_{1.6}$ represent the reflectance of the 1.6- and 2.1-μm spectral bands, respectively. Under clear sky conditions, AFRI closely resembles NDVI, and they have almost identical values. The major application of AFRI is for assessing vegetation in the presence of smoke, anthropogenic pollution, or volcanic plumes [25]. Ben-ze'ev et al. (2001) assessed vegetation conditions in the presence of smoke from biomass burning using the AFRI and EVI, and the results showed that the AFRI is more effective than the EVI in observing vegetation conditions under biomass burning smoke conditions [18]. Although these studies were well performed, it should be noted that SWIR-based VIs only take the atmospheric influences in the visible band into consideration. However, the top-of-atmosphere (TOA) reflectance in the NIR band also suffers from the influence of aerosols. Figure 4.1 shows the TOA reflectance of the NIR band (0.86 μm) as a function of the aerosol optical depth (AOD) and surface

reflectance. We can see that there is a critical surface reflectance (approximately equal to 0.15 in Figure 4.1) almost not susceptible to aerosol change [13,26], and for the lower surface reflectance, aerosols decrease TOA reflectance values; in contrast, for the higher surface reflectance, aerosols decrease the TOA reflectance values. Therefore, by giving full consideration to the impact of aerosols on the NIR band, the VI accuracy can be improved, particularly for aerosol loading conditions. Nevertheless, the removal of the atmosphere contribution from TOA reflectance in NIR is a challenging task. Although the atmospheric correction approach can be used to derive precise surface reflectance, the complexity of the algorithm limits its applicability to VIs.

In this paper, I describe a self-corrected method for minimizing the atmospheric influences in the NIR and red bands. Section 4.2 describes the detailed development of the methodology. In Section 4.3, I assess the performance of our proposed method under different aerosol conditions (with different AOD values).

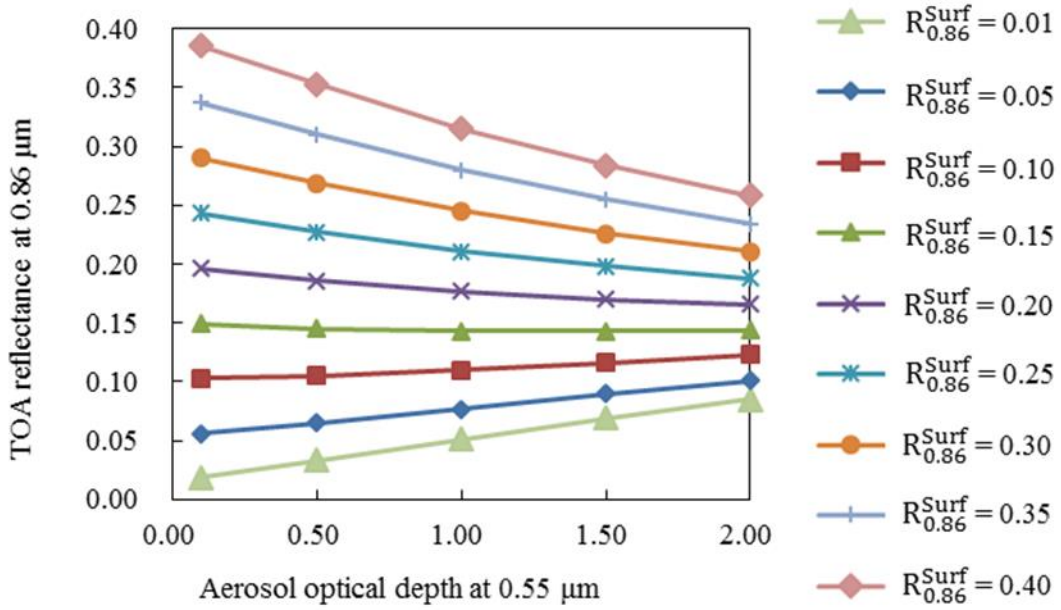

Figure 4.1 Moderate Resolution Imaging Spectroradiometer (MODIS) top-of-atmosphere (TOA) reflectance at 0.86 µm as a function of aerosol optical depth (AOD) at 0.55 µm and different surface reflectance values.

4.2 Materials and methods

4.2.1 Satellite data

The Moderate Resolution Imaging Spectroradiometer (MODIS) is the primary instrument onboard the Earth Observing System (EOS) Terra and Aqua satellites. As one of the most reliable data sources on the global scale, MODIS views the entire Earth's surface every 1 to 2 days, acquiring data in 36 spectral bands ranging in wavelength from 0.4 μm to 14.4 μm at a resolution of 250-1000 m and playing an important role in understanding global dynamics and processes occurring on the land, in the oceans, and in the lower atmosphere [27]. Because of its strengths, including its global coverage, high radiometric resolution and dynamic ranges and accurate calibration in the visible, NIR and thermal infrared bands [28], the satellite data provided from the MODIS platform can be considered as the ideal experimental data for our study.

MODIS/Terra Calibrated Radiances (MOD02HKM) in Collection 6 were used as the TOA reflectance data. The MOD02HKM product contains calibrated and geolocated at-aperture radiance data for 7 discrete bands located in the 0.45- to 2.20-micron region of the electromagnetic spectrum. Although MODIS bands 1 and 2 have 250-m resolution and bands 3 through 7 have 500-m resolution, the entire band dataset has been co-registered to the same spatial scale in the 500-m product [29].

The Geolocation Fields L1A dataset (MOD03) in Collection 6 records geodetic latitude, longitude, surface height above the geoid, solar zenith and azimuth angles, satellite zenith and azimuth angles and land/sea mask, some of which are important inputs in the atmospheric correction algorithm. Using these parameters in the MOD03 product, atmospherically corrected VIs can be generated, and the performance of the newly derived VIs can be assessed by comparing them with the atmospherically corrected VIs [30].

4.2.2 AERONET measurements

The Aerosol Robotic Network (AERONET) [31] is a worldwide network that provides ground-level AOD measurements with high quality. The AERONET Level 2.0 (cloud screened and quality-assured) data AOD measurements have very high accuracy, with uncertainty of only 0.01−0.02 (approximately 1/3−1/5 of satellite observations [32]). These data are usually considered as the “ground truth” and are widely used for various aerosol-related studies. In this study, to analyze the aerosol influence on VIs, I tested the performance of VIs under different aerosol loading conditions. The corresponding surface conditions can be derived by atmospheric correction. Since the quality of the atmospheric correction is strongly driven by

knowledge of the AOD, the selected experimental fields should be near the AERONET sites. According to the AOD values from the AERONET measurements, aerosol loading of experimental fields can be easily determined [33,34].

AERONET measures the direct sun and diffuse sky radiance in the 0.34−1.02-μm and 0.44−1.02-μm spectral ranges [35]; however, it does not measure AOD at the 0.55-μm wavelength, which is a vital input for the atmospheric correction processing. To obtain AOD at 0.55 μm, the AOD at other wavelengths can be interpolated to the 0.55-μm wavelength using the Angstrom Exponent α [36], defined as follows (Equation 4):

$$\alpha = -\frac{\ln\left(\frac{\tau_\lambda}{\tau_{0.55}}\right)}{\ln\left(\frac{\lambda}{0.55}\right)} \tag{4}$$

where $\boldsymbol{\tau_\lambda}$ represents the AOD at a given wavelength $\boldsymbol{\lambda}$ and α is the Angstrom exponent. The value of α is also provided by the AERONET measurement.

4.2.3 Methodology for minimizing atmospheric influences on the NIR and red bands

An overview of the strategy for correcting for the atmospheric influence on the NIR and red bands is shown in Figure 4.2. The fundamental processing steps mainly include (1) surface reflectance estimation using the relationship between the 0.65- and 2.1-μm bands ($R_{0.6} = 0.5R_{2.1}$) and prediction of atmospheric aerosol loading (AOD) according to TOA reflectance, surface reflectance, and the assumptions in atmospheric correction; (2) correcting TOA reflectance in the NIR and red bands using the proposed method and predicted AOD in the last step; (3) construction of VIs using the corrected NIR and red bands.

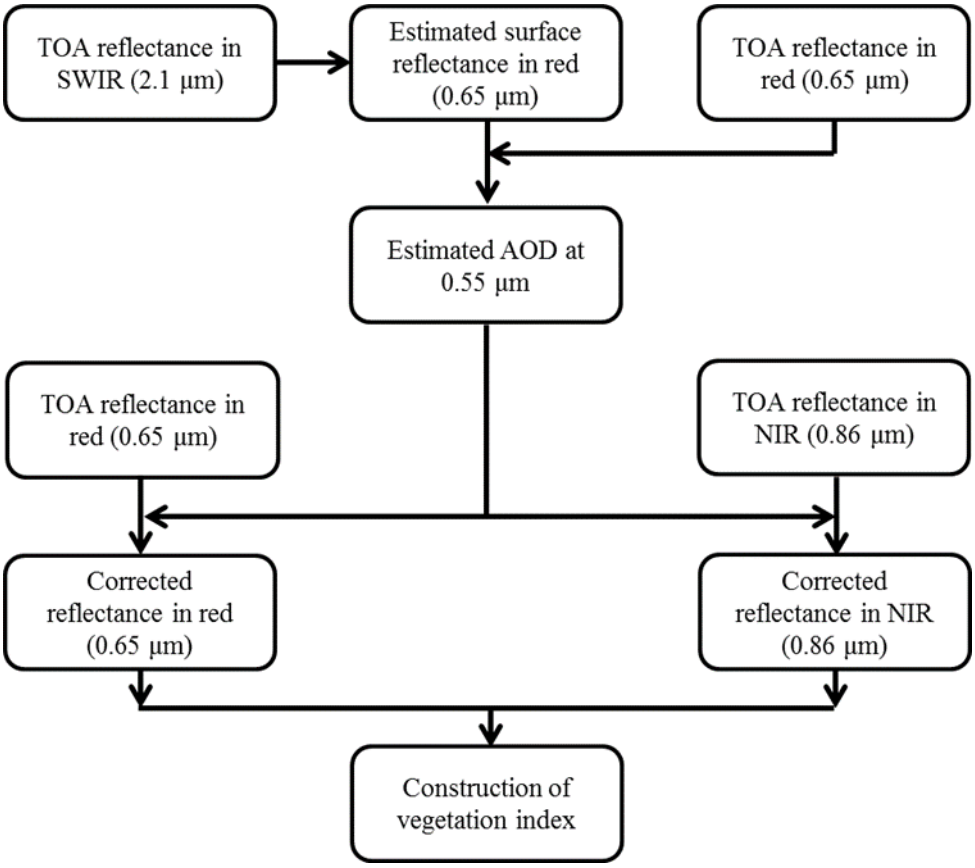

Figure 4.2 Flowchart of the self-correction method for removing the atmospheric influences in the MODIS near-infrared (NIR) and red bands along with the vegetation indices derived from the proposed method.

4.2.3.1 AOD prediction

The Dark Target (DT) algorithm is one of the common methods to determine the surface reflectance in the visible band, and it has been widely used in aerosol retrieval and atmospheric correction algorithms for different satellites. Because the SWIR band near the 2.1-μm wavelength is less affected by atmospheric aerosols and there are robust linear relationships between the TOA reflectance at 2.1 μm and the surface reflectance in the red or blue (0.47 and 0.65 μm for MODIS) bands, the MODIS DT algorithm uses these relationships to account for the surface signal in the red or blue channels [37–39].

In this study, the DT algorithm was used in the first step to estimate the surface reflectance at 0.65 μm, and the estimated surface reflectance at 0.65 μm is quantitatively equal to half of the TOA reflectance at 2.1 μm. According to the basic principle of the AOD retrieval algorithm, when the surface contribution is determined, and an appropriate aerosol model assumed, it is possible to retrieve the AOD values. The sensor that receives a signal at a certain wavelength is variable with respect to the

surface contribution, aerosol loading and observation geometry (solar zenith angle, satellite zenith angle and relative azimuth angle). The aerosol retrieval algorithm therefore takes the observation geometry into account. However, the observation geometry is generally not involved in the construction of VIs. Additionally, after the VI calculation (such as NDVI), the influences on the VI from observation geometry are greatly reduced [40]. In this study, I assumed a median viewing geometry with a solar zenith angle = 30°, satellite zenith angle = 30°, and relative azimuth angles = 90°, under which AOD prediction and correction processing for the NIR and red band would be conducted.

To quickly generate the AOD values from its TOA reflectance and the estimated surface reflectance, I used the Second Simulation of a Satellite Signal in the Solar Spectrum (6S) radiative transfer code to simulate the interactive changes among the AOD, TOA reflectance and the surface reflectance under the assumed observation geometry. In addition, the aerosol model employed the continental aerosol model that is a broadly used assumption over land retrieval. Figure 4.3 shows the AOD (with five given values of 0.1, 0.5, 1.0, 1.5, and 2.0) as a function of TOA reflectance and surface reflectance. As shown, for higher surface reflectance, the corresponding relationship between TOA reflectance and AOD displayed a larger slope. This pattern indicates that lower ground surface reflectance is more sensitive to the variation in AOD. The regression functions for different surface reflectance values in Figure 4.3 all have extremely high coefficients of determination values and can be formulated as follows (Equations 5a to 5c):

$$\mathrm{AOD} = \mathrm{Slope}_{\mathrm{red}} * \mathrm{R}_{0.65}^{\mathrm{TOA}} + \mathrm{Intercept}_{\mathrm{red}} \quad (5a)$$

where $\mathrm{R}_{0.65}^{\mathrm{TOA}}$ is the TOA reflectance at 0.65 μm and $\mathrm{Slope}_{\mathrm{red}}$ and $\mathrm{Intercept}_{\mathrm{red}}$ are the slope and intercept of the regression functions, respectively. The slope and intercept changes with varying surface reflectance were analyzed and are shown in Figure 4.4. Based on the generated fitting regression, the slope and intercept in Equation 3 can be determined using the empirical quadratic polynomial functions as follows (Equations 5b and 5c):

$$\mathrm{Slope}_{\mathrm{red}} = 2055.8 * \mathrm{R}_{0.65}^{\mathrm{surf}^2} - 28.436 * \mathrm{R}_{0.65}^{\mathrm{surf}} + 20.257 \quad (5b)$$

$$\mathrm{Intercept}_{\mathrm{red}} = -392.52 * \mathrm{R}_{0.65}^{\mathrm{surf}^2} + 6.7345 * \mathrm{R}_{0.65}^{\mathrm{surf}} - 0.7885 \quad (5c)$$

where $\mathrm{R}_{0.65}^{\mathrm{surf}}$ is the predicted surface reflectance at 0.65 μm from the SWIR band. Using Equations 5a to 5c, the AOD value under the assumed viewing geometry can be rapidly predicted with the TOA reflectance and surface reflectance at 0.65 μm.

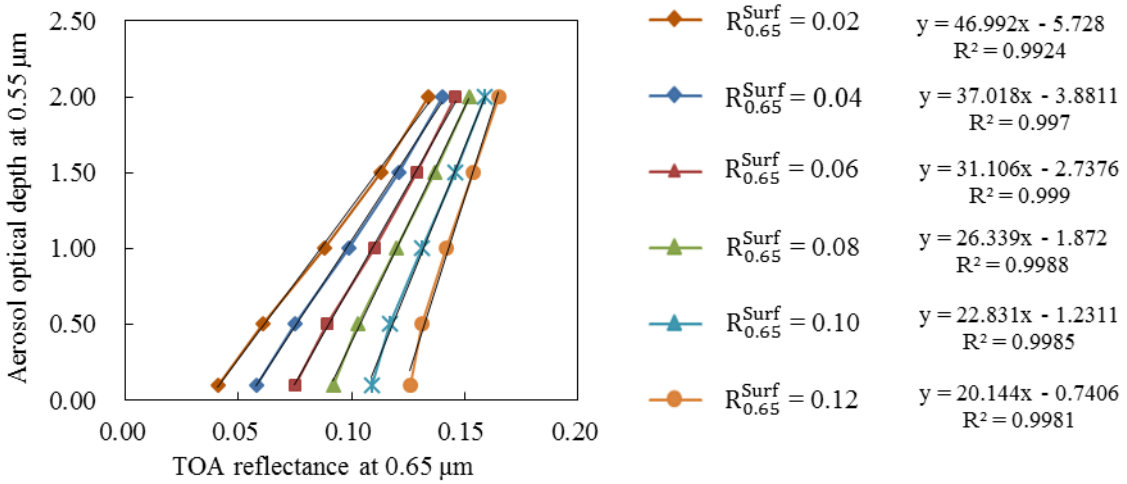

Figure 4.3 Changes in AOD at 0.55 µm varying with MODIS TOA reflectance and surface reflectance at 0.65 µm under the assumed viewing geometry.

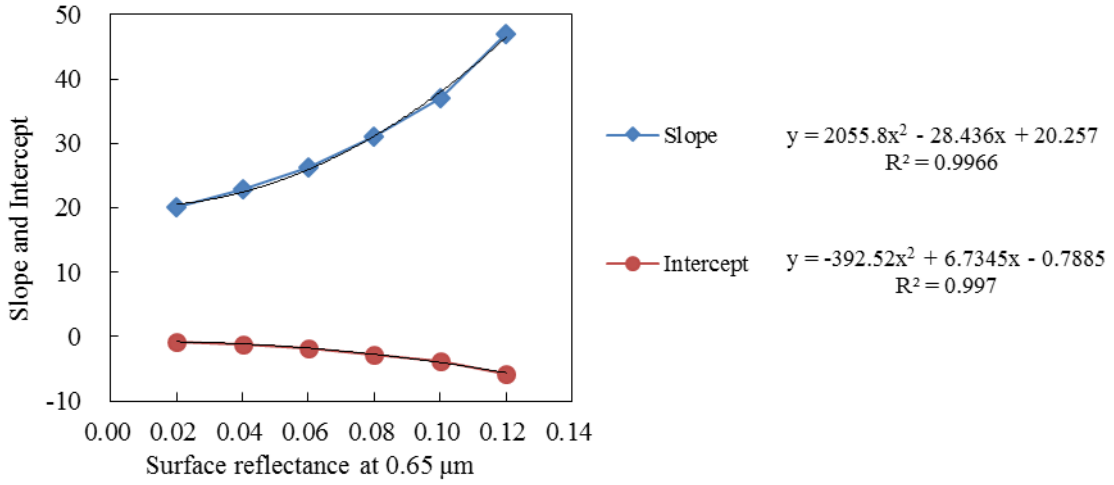

Figure 4.4 The coefficients (slope and intercept) of regression functions in Figure 4.3 as a function of surface reflectance at 0.65 µm.

4.2.3.2 Correction of the NIR band using estimated AOD

As explained in the overview of the strategy, the correction of atmospheric effects for the NIR band can be conducted based on the predicted AOD. Such a correction procedure is similar to atmospheric correction. When using the 6S radiative transfer code for the atmospheric correction, the following parameters are required as input: (1) geometric conditions, (2) atmospheric profile for the gaseous components, (3) the aerosol model (type and concentration), (4) the spectral condition, and (5) ground reflectance (type and spectral variation) [41]. Obviously, such sophisticated parameters and computation would hinder the application flexibility of the VI. Therefore, I followed the assumed observation geometry and aerosol model assumptions in the previous step to develop a simplified method to correct for the atmospheric effects for the NIR band.

In contrast to the previous step, I aimed to achieve the surface reflectance of the NIR band according to the estimated AOD. I pre-set a set of TOA reflectance values in the NIR band (with values of 0.01 and ranging from 0.05 to 0.4 with increments of 0.05) and used the 6S radiative transfer code to calculate the TOA reflectance corresponding surface reflectance for AOD values of 0.1, 0.5, 1.0, 1.5, and 2.0. The relationship between the surface reflectance in the NIR band and the AOD values for different TOA reflectance values is shown in Figure 4.5. All the relationships are well fitted by quadratic polynomial function curves, and therefore, I formulated the surface reflectance of the NIR band as a function of AOD and TOA reflectance as follows (Equations 6a to 6d):

$$R_{0.86}^{surf} = a * AOD^2 + b * AOD + c \quad (6a)$$

$$a = 0.156 * R_{0.86}^{TOA} - 0.03 \quad (6b)$$

$$b = 0.269 * R_{0.86}^{TOA} - 0.0259 \quad (6c)$$

$$c = 1.0405 * R_{0.86}^{TOA} - 0.0076 \quad (6d)$$

where $R_{0.86}^{surf}$ is the corrected reflectance in the NIR band. a, b, and c represent the coefficients of the regression functions in Figure 4.5. Because the values of these coefficients vary according to the different TOA reflectance values, I analyzed the relationships between these coefficients and the TOA reflectance. As shown in Figure 4.6, extremely strong linear relationships exist between these coefficients and the TOA reflectance. Therefore, the values of a, b, and c can be determined using Equations 6b to 6c, in which the coefficients are a function of the TOA reflectance in the NIR band.

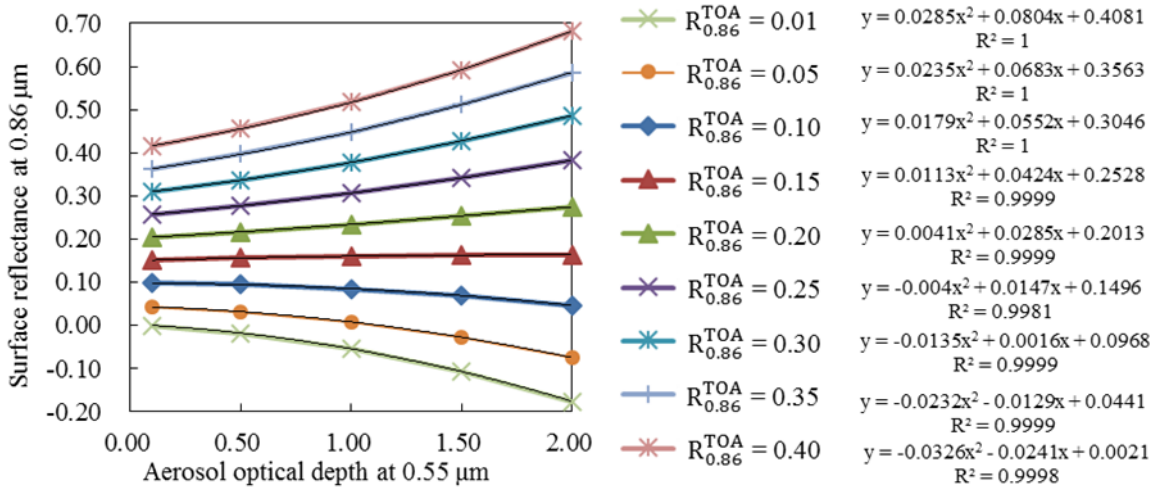

Figure 4.5 MODIS surface reflectance at 0.86 µm as a function of AOD at 0.55 µm under different TOA reflectance values.

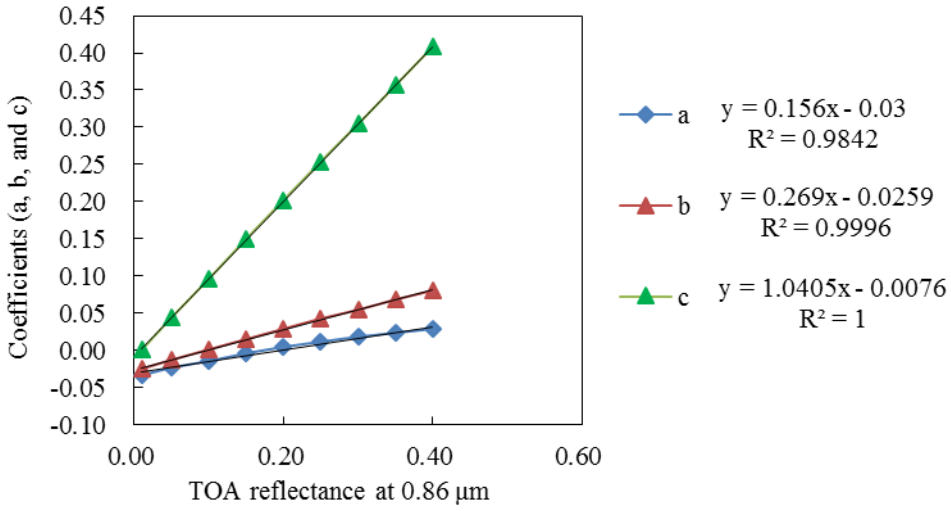

Figure 4.6 The coefficients (a, b, and c) of regression functions in Figure 4.5 as a function of TOA reflectance at 0.86 µm.

4.2.3.3 Correction of the red band using estimated AOD

The red band correction is similar to the NIR band correction method. Under the same assumptions, I ran the 6S radiative transfer code to simulate the atmospherically corrected reflectance in the red band with different TOA reflectance and AOD values. The surface reflectance of the red band can be computed according to the TOA reflectance and the estimated AOD using the following formulas (Equations 7):

$$R_{0.65}^{Surf} = a * AOD^2 + b * AOD + c \quad (7a)$$

$$a = 0.466 * R_{0.65}^{TOA} - 0.0922 \quad (7b)$$

$$b = 0.231 * R_{0.65}^{TOA} - 0.0257 \quad (7c)$$

$$c = 1.1682 * R_{0.65}^{TOA} - 0.0275 \quad (7d)$$

where $R_{0.65}^{Surf}$ is the corrected reflectance in the red band. As shown by the simulated results (Figure 4.7), the relationship between the corrected surface reflectance and AOD values for different observed TOA reflectance values can be well described using quadratic polynomial functions. In Equations 7, a, b, and c are the coefficients of the function, these coefficients are also a function of the TOA reflectance in the red band and can be determined according to the fitted regressions in Figure 4.8.

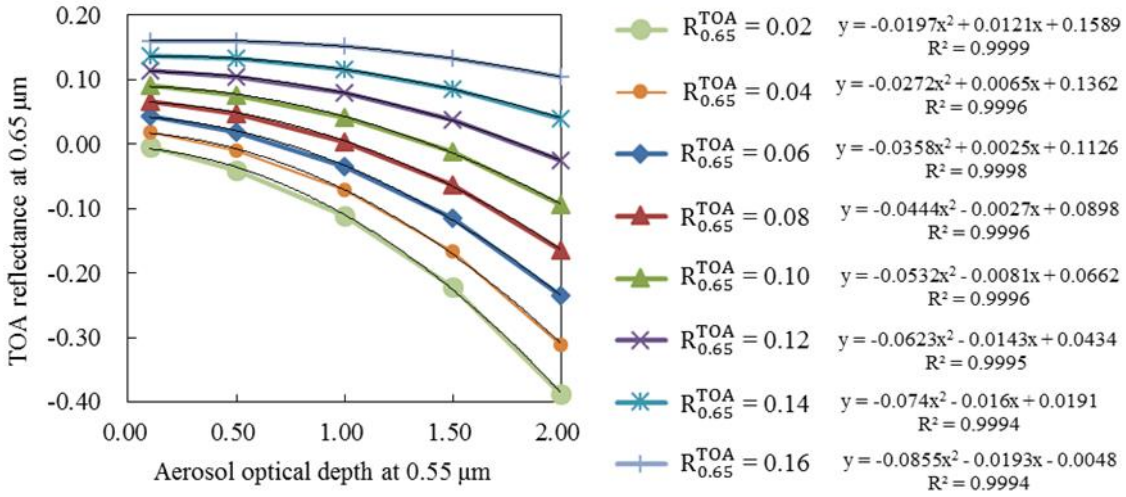

Figure 4.7 MODIS surface reflectance at 0.65 µm as a function of AOD at 0.55 µm under different TOA reflectance values.

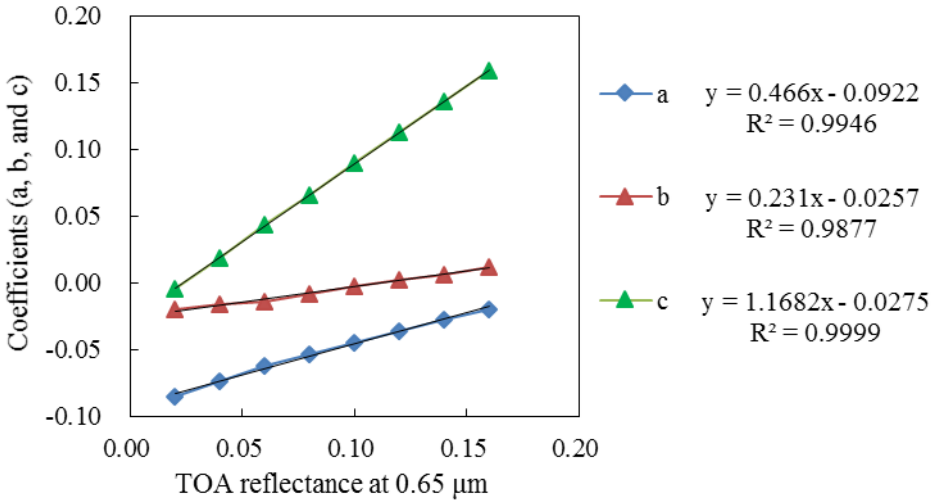

Figure 4.8 The coefficients (a, b, and c) of regression functions in Figure 4.7 as a function of TOA reflectance at 0.65 µm.

4.3 Results and discussion

4.3.1 Assessing the performance of the method with different aerosol loading conditions

The current approach was applied to correcting VIs under different aerosol conditions, and the performance was assessed through a comparison with the atmospherically corrected NDVI. Because the accuracy of atmospheric correction is strongly dependent on knowledge of the AOD [34], the spatially and temporally matched MODIS/AERONET collocated data were used as the experimental data for the accuracy assessment. The selection of MODIS/AERONET collocation data was based on the following criteria: the experimental MODIS MOD02HKM data should be located within a 10 km radius around the AERONET sites, and the AERONET measured must be within 30 minutes of MODIS overpassing.

To derive the atmospherically corrected NDVI, a pixel-by-pixel atmospheric correction was applied to the NIR and red bands using the 6S radiative transfer code. The key input parameters included the following: (1) the viewing geometry (solar zenith angle, satellite zenith angle and relative azimuth angle), which was obtained from the Geolocation Fields L1A dataset (MOD03); (2) mean AOD measurements within 30 minutes of MODIS overpassing; (3) the continental aerosol model, which is a common assumption for land retrieval; and (4) spectral conditions of the MODIS 0.86- and 0.65-µm bands. Using the 6S radiative transfer code enabled atmospheric correction working modality, and the surface reflectance at a certain wavelength could be computed according to input parameters.

4.3.1.1 Improvement of the corrected NIR-derived $AFRI_{2.1}$

Karnieli et al. (2001) showed that under clear sky conditions, $AFRI_{2.1}$ has almost identical values to NDVI. However, as the smoke conditions become heavy, the agreement between $AFRI_{2.1}$ and NDVI weakens [25]. Regarding this issue, I attempt to correct the NIR band of $AFRI_{2.1}$ using our approach to construct a corrected NIR-derived $AFRI_{2.1}$ (Equation 8).

$$AFRI_{2.1}^{Corrected} = \left(R_{NIR}^{Corrected} - 0.5 * R_{2.1}\right) / \left(R_{NIR}^{Corrected} + 0.5 * R_{2.1}\right) \quad (8)$$

where $R_{NIR}^{Corrected}$ and $AFRI_{2.1}^{Corrected}$ are the corrected NIR and the corrected NIR-derived $AFRI_{2.1}$, respectively. I compared the corrected NIR-derived $AFRI_{2.1}$ against the original $AFRI_{2.1}$ and the atmospherically corrected NDVI with different levels of aerosol loading to assess the performance of this method.

$AFRI_{2.1}$ was developed based on the linear relationship between surface reflectance at 0.65 μm and 2.1 μm and the rule of $R_{0.6} = 0.5R_{2.1}$, which is independent of the vegetation amounts [25]. Therefore, $AFRI_{2.1}$ works best over dark vegetated targets and cannot be applied effectively over water bodies or bright land surfaces [18]. In addition, the estimation of AOD, which is the first step of the current correction approach, used the rule of $R_{0.6} = 0.5R_{2.1}$. For quality control of the correction, the non-vegetated targets were eliminated by an empirical threshold based on the mechanism that NIR light is reflected by spongy mesophyll cells [8], since vegetated surfaces show relatively higher reflectance in the NIR than other surface types. I set an empirical threshold with an $R_{0.86}$ value of 0.225 to distinguish vegetated targets from others.

The experimental collocated MODIS/AERONET data from the Ubon_Ratchathani, Ussuriysk, and Gandhi_College sites were used for validation, and the experimental results are shown in Figures 4.9 to 4.11 and Tables 4.1 to 4.3. In Figures 4.9 to 4.11, the graphs in columns a to d have different AOD values; rows 1 and 2 show the comparisons of atmospherically corrected NDVI vs. $AFRI_{2.1}$ and atmospherically corrected NDVI vs. corrected NIR-derived $AFRI_{2.1}$; row 3 displays the comparisons of surface reflectance vs. TOA reflectance at 0.86 μm (black scatter plots) and the surface reflectance vs. corrected reflectance at 0.86 μm (green scatter plots). The statistical root mean square error (RMSE) and mean bias error (MBE) were used to investigate errors. Compared with the performance of $AFRI_{2.1}$ and the corrected NIR-derived $AFRI_{2.1}$, except for the case of Figures 4.9a, the corrected NIR-derived $AFRI_{2.1}$ are closer to the one-to-one line than the original $AFRI_{2.1}$, and the corrected NIR-derived $AFRI_{2.1}$ also exhibits lower RMSE and MBE (in absolute terms) values.

The performance of our method in the case of Figure 4.9a was poor due to system

error of the algorithm. The experimental data in Figure 4.9a are under very low aerosol conditions with an AOD value of 0.12, as shown in Figure 4.9(a-3), and the TOA reflectance of the NIR band is almost unaffected by atmospheric influences and has very similar values with the surface reflectance. Under such conditions, when the viewing geometry differed from our assumption, the errors caused by differences in viewing geometry would easily overwhelm the influences from the atmosphere and become the major error source.

As the graphs of row 3 in Figures 4.9 to 4.11 show, the NIR band is also affected by atmospheric aerosols: as the AOD values increase, the TOA reflectance of the NIR band shows an obviously larger degree of difference with the surface reflectance (black scatter plots), and their corresponding RMSE values are also higher. Additionally, all the statistical MBEs have negative values, which is because the vegetated surface radiance in NIR is reduced by the absorption of atmospheric aerosols. By comparing the corrected NIR reflectance with the uncorrected reflectance, we can observe that our method is effective for removing the atmospheric influences in the NIR. Except for the cases in Figures 4.9(a-3) and 4.9(b-3), the corrected NIR reflectance values (green scatter plots) are all very close to the one-to-one line, and the derived low RMSE and MBE (in absolute terms) values indicate that the corrected NIR reflectance values are almost identical to the surface reflectance values. Consequently, the performance of $AFRI_{2.1}$ has been improved by correcting for the atmospheric influences in the NIR band. The poor performance of the experimental data in Figure 4.9b is not the same as in Figure 4.9a. The measured AOD in Figure 4.9b is high, with a value of 0.59, whereas the corrected $AFRI_{2.1}$ only shows slight improvement because the observation was taken with an extremely high satellite zenith angle of 62.6°, which is markedly different from our geometric assumption, leading to large errors in the spectral band correction. However, the errors would largely degrade after construction of the vegetation index (such as the NDVI) [40].

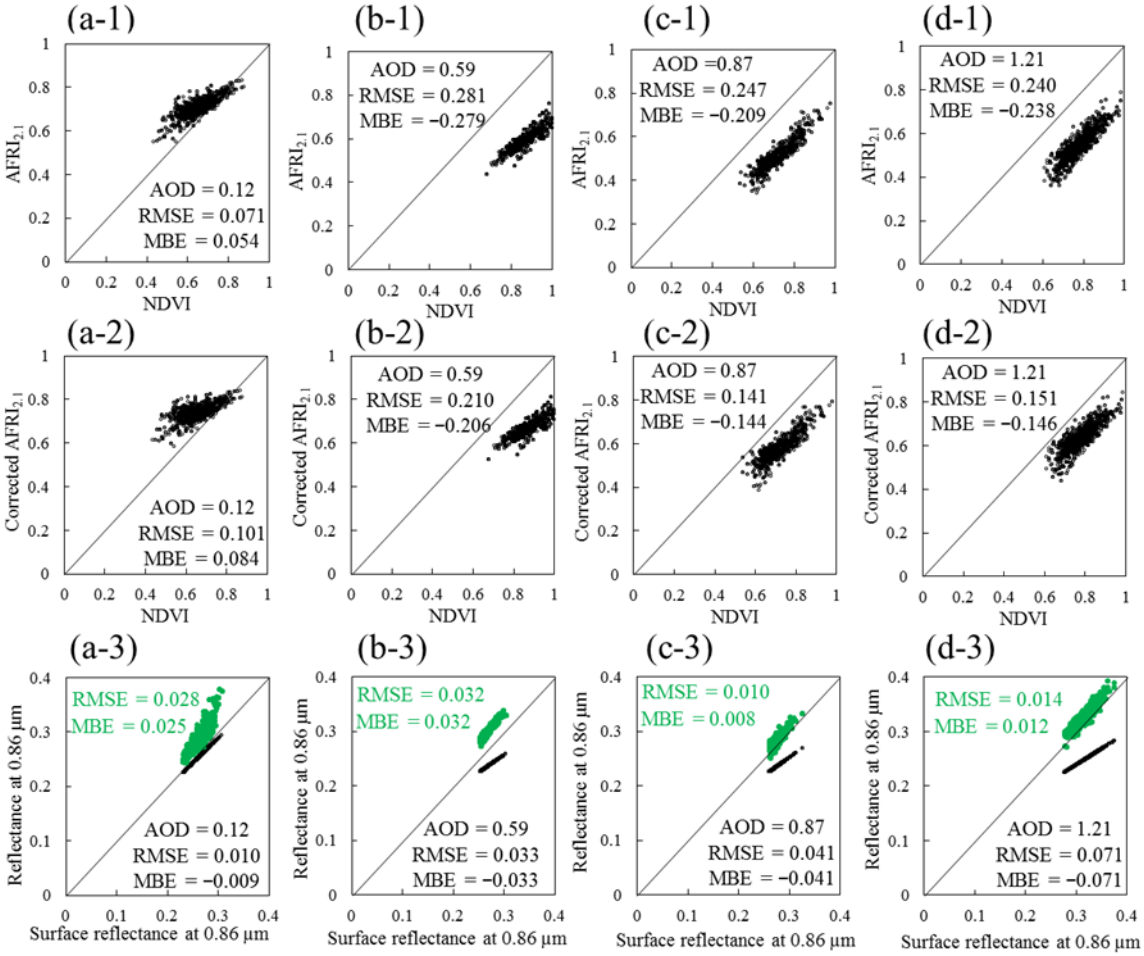

Figure 4.9 Experimental results of the Ubon_Ratchathani site. Aerosol-free vegetation ($AFRI_{2.1}$) (**Row 1**) and corrected NIR-derived $AFRI_{2.1}$ (**Row 2**) plotted against the atmospherically corrected Normalized Difference Vegetation Index (NDVI); the TOA reflectance at NIR (black plots) and corrected reflectance at NIR (green plots) against the surface reflectance at NIR (**Row 3**) for different aerosol loading conditions (AOD at 0.55 µm).

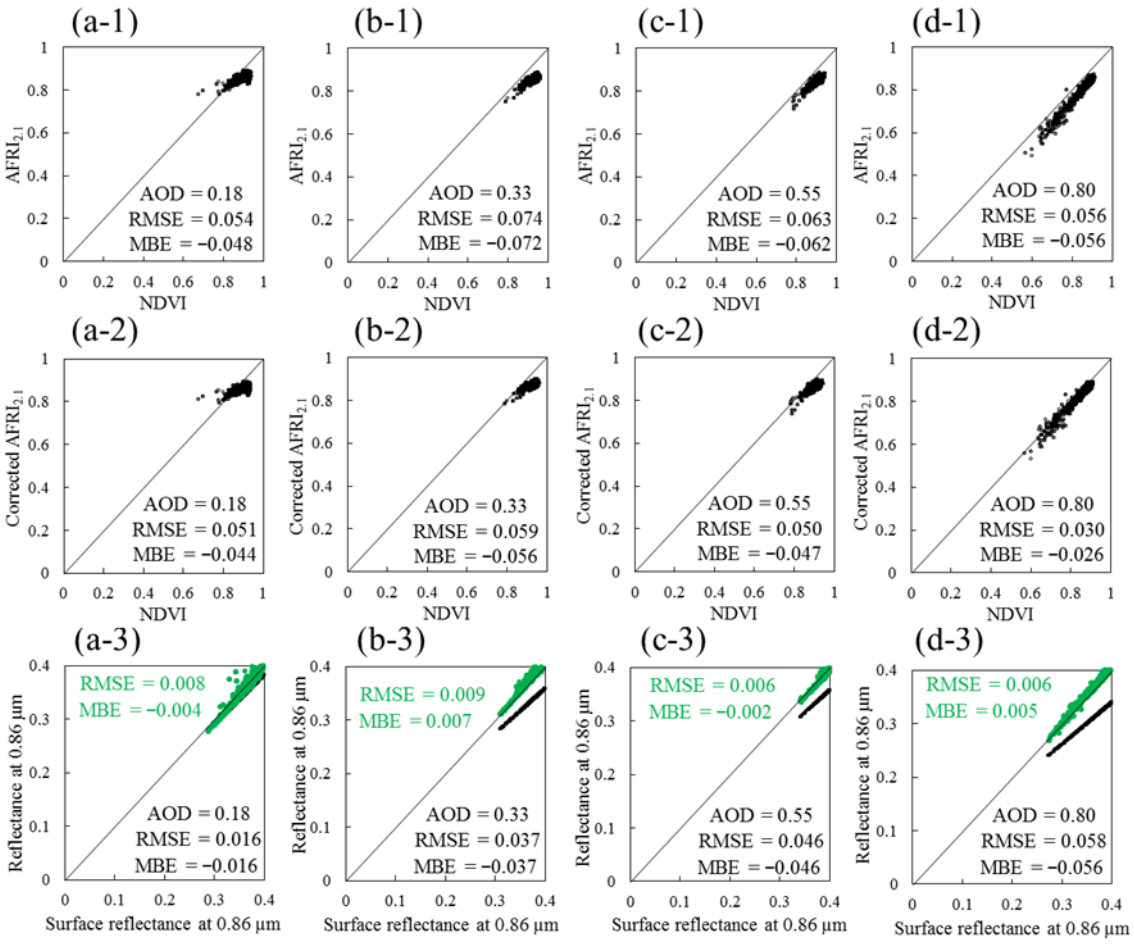

Figure 4.10 Experimental results of the Ussuriysk site. $AFRI_{2.1}$ (**Row 1**) and corrected NIR-derived $AFRI_{2.1}$ (**Row 2**) plotted against the atmospherically corrected NDVI; the TOA reflectance at NIR (black plots) and corrected reflectance at NIR (green plots) against the surface reflectance at NIR (**Row 3**) for different aerosol loading conditions (AOD at 0.55 μm).

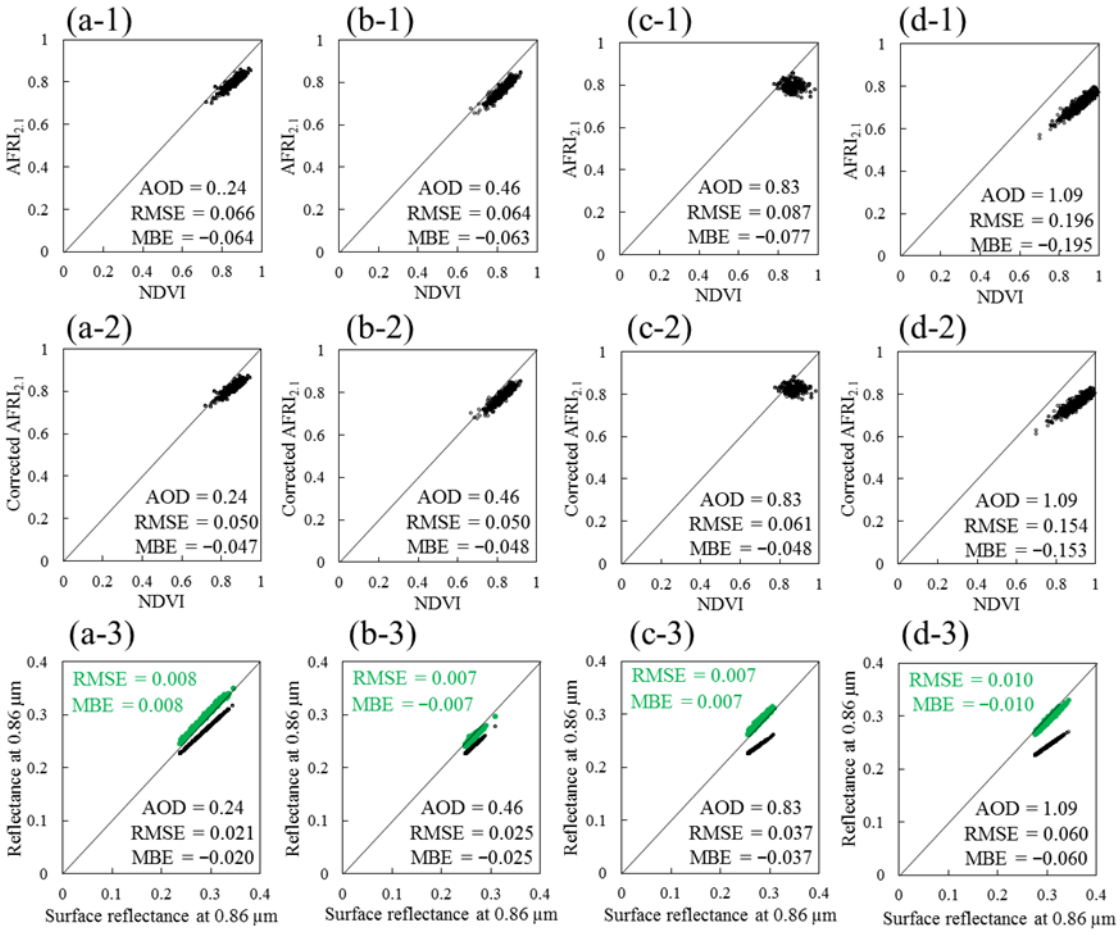

Figure 4.11 Experimental results of the Gandhi_College site. $AFRI_{2.1}$ (**Row 1**) and corrected NIR-derived $AFRI_{2.1}$ (**Row 2**) plotted against the atmospherically corrected NDVI; the TOA reflectance at NIR (black plots) and corrected reflectance at NIR (green plots) against the surface reflectance at NIR (**Row 3**) for different aerosol loading conditions (AOD at 0.55 µm).

4.3.1.2 Validation of the corrected NDVI by the current algorithm

The corrected NDVI is constructed using the corrected red and NIR bands based on our proposed strategy (Equation 9).

$$\mathrm{NDVI}^{\mathrm{Corrected}} = \left(\mathrm{R}_{\mathrm{NIR}}^{\mathrm{Corrected}} - \mathrm{R}_{\mathrm{red}}^{\mathrm{Corrected}}\right)/\left(\mathrm{R}_{\mathrm{NIR}}^{\mathrm{Corrected}} + \mathrm{R}_{\mathrm{red}}^{\mathrm{Corrected}}\right) \qquad (9)$$

I also validated our method by comparing the corrected NDVI against the atmospherically corrected NDVI using the same experimental collocated MODIS/AERONET data described in Section 4.3.1.1. The experimental results are shown Tables 4.1 to 4.3. In Figures 4.12 to 4.14, the graphs in columns a to d show different AOD values; rows 1 and 2 display the TOA reflectance-derived NDVI (uncorrected NDVI) vs. the atmospherically corrected NDVI and the corrected NDVI vs. atmospherically corrected NDVI, respectively; row 3 shows TOA reflectance at 0.65 μm (black scatter plots) vs. the surface reflectance and the corrected reflectance at 0.65 μm (green scatter plots) vs. the surface reflectance.

As shown in the graphs of row 1 in Figures 4.12 to 4.14, uncorrected NDVI is evidently susceptible to influences of atmospheric aerosols, and the uncorrected NDVI values typically decrease with increasing AOD. In addition to the influences in the NIR band (Section 4.3.1.1), atmospheric influences affect vegetation indices through increasing the ascending radiance over vegetation in the red portion of the spectrum [1].

The removal of atmospheric influences in VI is conducted in the NIR and red bands. The correction of effects in the NIR band is presented in Section 4.3.1.1. The graphs of row 3 in Figures 4.12 to 4.14 also indicate that the higher AOD values render higher TOA reflectance in the red band (at 0.65 μm) than surface reflectance (black scatter plots). Compared with the TOA reflectance, the reflectance values of the corrected data are all much closer to surface reflectance values (green scatter plots), and the much better RMSE and MBE values suggest that our algorithm is also effective in correction of the red band. Consequently, the corrected red and NIR band-derived NDVI has the capacity to measure vegetation conditions when aerosols are present in the atmosphere. The performances of the corrected NDVI with different AOD values are shown in the graphs of row 2 in Figures 4.12 to 4.14. Obviously, a majority of the errors in TOA NDVI from atmospheric influences were rectified in the corrected NDVI.

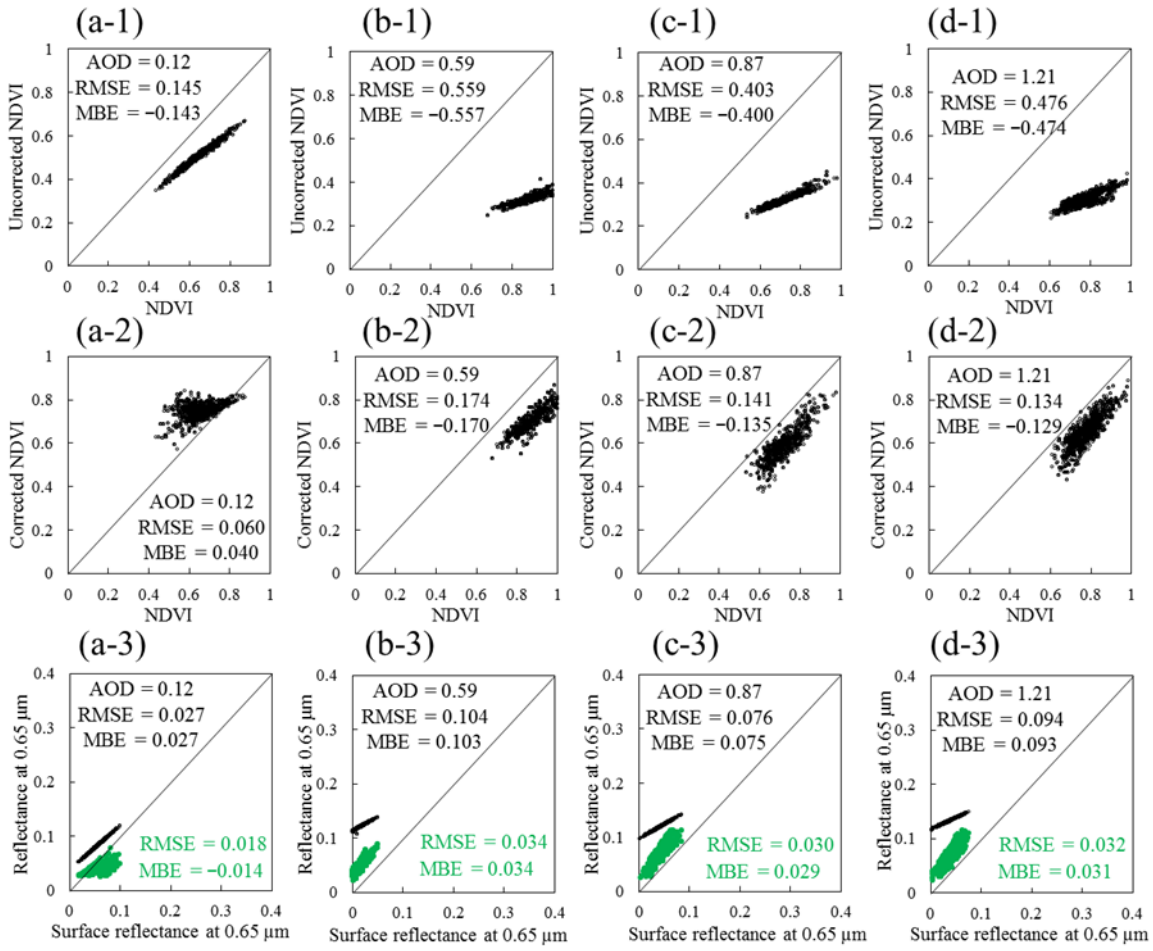

Figure 4.12 Experimental results for the Ubon_Ratchathani site. Uncorrected NDVI (**Row 1**) and corrected NDVI (**Row 2**) plotted against the atmospherically corrected NDVI; the TOA reflectance at the red band (black plots) and corrected reflectance at the red band (green plots) against the surface reflectance at the red band (**Row 3**) for different aerosol loading conditions (AOD at 0.55 µm).

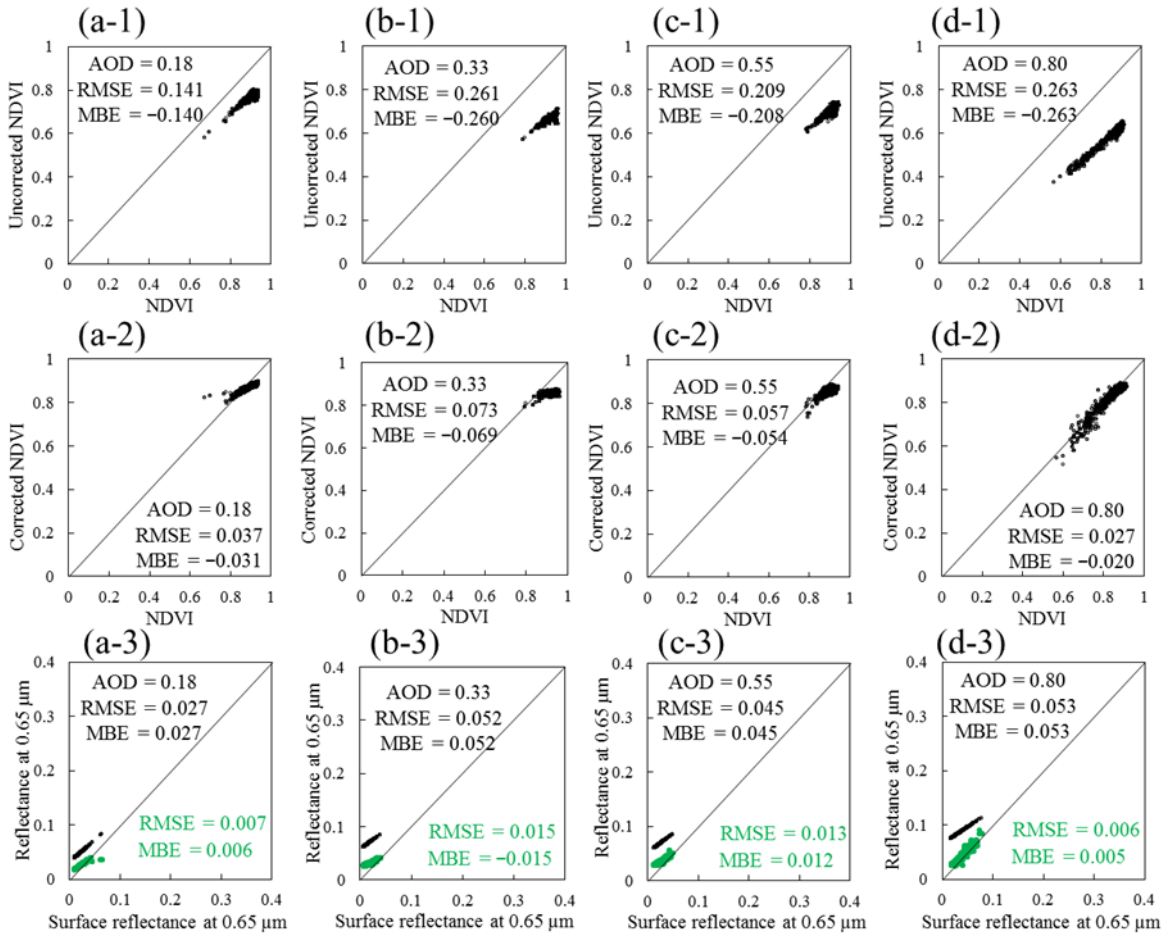

Figure 4.13 Experimental results for the Ussuriysk site. Uncorrected NDVI (**Row 1**) and corrected NDVI (**Row 2**) plotted against the atmospherically corrected NDVI; the TOA reflectance at the red band (black plots) and corrected reflectance at the red band (green plots) against the surface reflectance at the red band (**Row 3**) for different aerosol loading conditions (AOD at 0.55 µm).

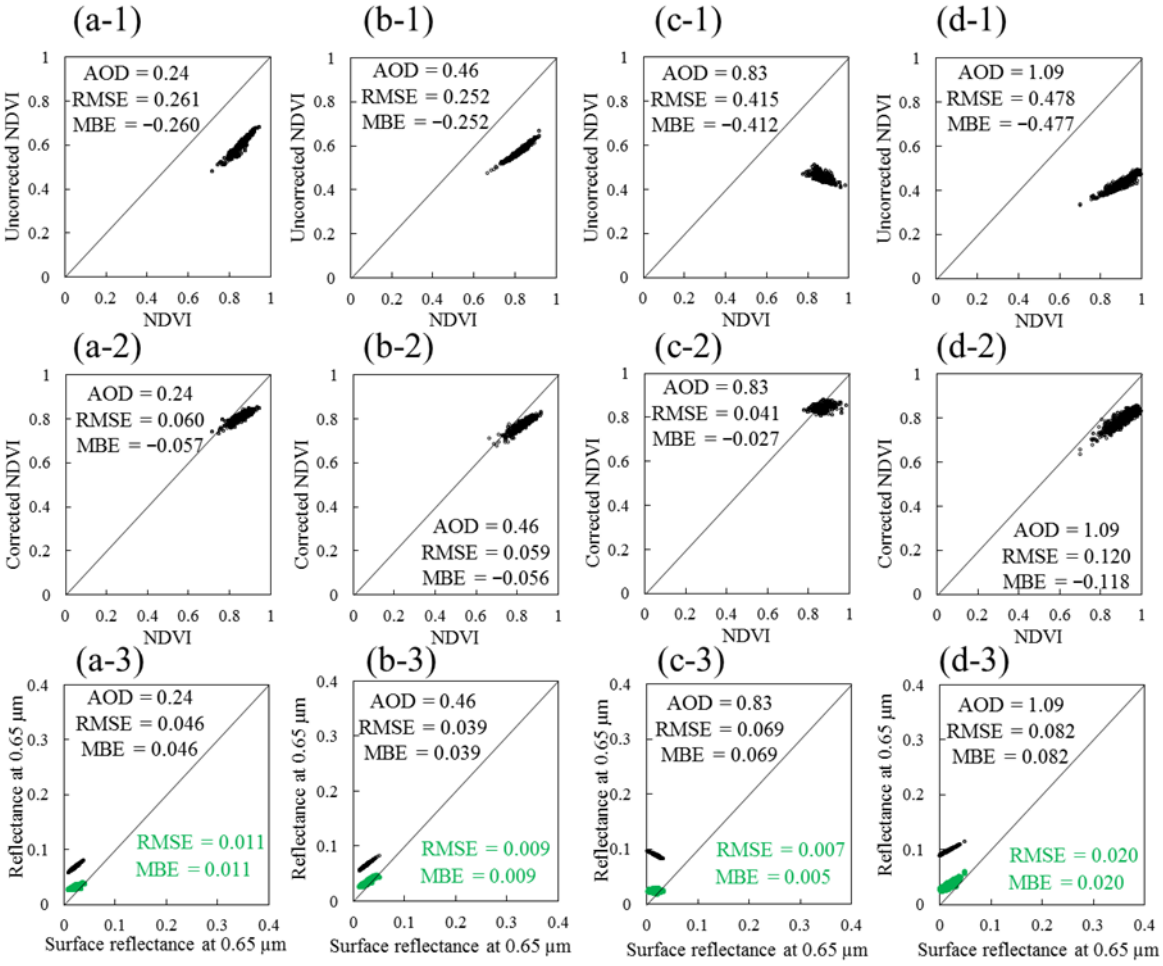

Figure 4.14 Experimental results for the Gandhi_College site. Uncorrected NDVI (**Row 1**) and corrected NDVI (**Row 2**) plotted against the atmospherically corrected NDVI; the TOA reflectance at the red band (black plots) and corrected reflectance at the red band (green plots) against the surface reflectance at the red band (**Row 3**) for different aerosol loading conditions (AOD at 0.55 µm).

Table 4. 1 The angle of observation and summary statistics for the experimental data near the Ubon_Ratchathani site (DOY is day of year, $NDVI^{U}$ is the uncorrected NDVI, $NDVI^{C}$ is the corrected NDVI using our method, and $AFRI_{2.1}{}^{C}$ is the corrected NIR-derived $AFRI_{2.1}$).

Site_Name: Ubon_Ratchathani					
Year/DOY		**2010/047**	**2010/068**	**2010/324**	**2011/055**
AOD		**0.590**	**1.211**	**0.121**	**0.868**
$NDVI^{U}$	RMSE	0.559	0.476	0.145	0.403
	MBE	−0.557	−0.474	−0.143	−0.400
$NDVI^{C}$	RMSE	0.174	0.134	0.113	0.141
	MBE	−0.170	−0.129	0.093	−0.135
$AFRI_{2.1}$	RMSE	0.281	0.240	0.071	0.247
	MBE	−0.279	−0.238	0.054	-0.209
$AFRI_{2.1}{}^{C}$	RMSE	0.210	0.151	0.101	0.141
	MBE	−0.206	−0.146	0.084	−0.144
$R_{0.65}^{TOA}$	RMSE	0.104	0.094	0.027	0.076
	MBE	0.103	0.093	0.027	0.075
$R_{0.65}^{Corrected}$	RMSE	0.034	0.032	0.018	0.030
	MBE	0.034	0.031	−0.014	0.029
$R_{0.86}^{TOA}$	RMSE	0.032	0.014	0.028	0.010
	MBE	−0.033	−0.071	−0.009	−0.041
$R_{0.86}^{Corrected}$	RMSE	0.033	0.071	0.010	0.041
	MBE	0.032	0.012	0.025	0.008
Viewing Geometry (degree)	Solar zenith angle	43.360	34.315	41.122	38.038
	Sensor zenith angle	62.617	43.038	42.903	43.138
	Relative azimuth angle	31.700	25.720	50.030	31.725

Table 4. 2 The angle of observation and summary statistics for the experimental data near the Ussuriysk site (DOY is day of year, $NDVI^{U}$ is the uncorrected NDVI, $NDVI^{C}$ is the corrected NDVI using our method, and $AFRI_{2.1}{}^{C}$ is the corrected NIR-derived $AFRI_{2.1}$).

Site_Name: Ussuriysk					
Year/DOY		**2008/159**	**2008/178**	**2008/210**	**2009/148**
AOD		**0.328**	**0.554**	**0.183**	**0.792**
$NDVI^{U}$	RMSE	0.261	0.209	0.141	0.263
	MBE	−0.260	−0.208	−0.140	−0.263
$NDVI^{C}$	RMSE	0.073	0.057	0.037	0.027
	MBE	−0.069	−0.054	−0.031	−0.020
$AFRI_{2.1}$	RMSE	0.074	0.063	0.054	0.056
	MBE	−0.072	−0.062	−0.048	−0.056
$AFRI_{2.1}{}^{C}$	RMSE	0.059	0.050	0.051	0.030
	MBE	−0.056	−0.047	−0.044	−0.026
$R_{0.65}^{TOA}$	RMSE	0.052	0.045	0.027	0.053
	MBE	0.052	0.045	0.027	0.053
$R_{0.65}^{Corrected}$	RMSE	0.015	0.013	0.007	0.006
	MBE	−0.015	0.012	0.006	0.005
$R_{0.86}^{TOA}$	RMSE	0.009	0.006	0.008	0.006
	MBE	−0.037	−0.046	−0.016	−0.056
$R_{0.86}^{Corrected}$	RMSE	0.037	0.046	0.016	0.058
	MBE	0.007	−0.002	−0.004	0.005
Viewing Geometry (degree)	Solar zenith angle	29.136	25.124	29.400	26.085
	Sensor zenith angle	54.640	18.318	18.542	18.188
	Relative azimuth angle	33.361	38.002	41.358	42.940

Table 4. 3 The angle of observation and summary statistics for the experimental data near the Gandhi_College site (DOY is day of year, $NDVI^{U}$ is the uncorrected NDVI, $NDVI^{C}$ is the corrected NDVI using our method, and $AFRI_{2.1}{}^{C}$ is the corrected NIR-derived $AFRI_{2.1}$).

Site_Name: Gandhi_College					
Year/DOY		**2012/036**	**2012/050**	**2012/056**	**2012/065**
AOD		**0.829**	**0.236**	**0.456**	**1.086**
$NDVI^{U}$	RMSE	0.415	0.261	0.252	0.478
	MBE	−0.412	−0.260	−0.252	−0.477
$NDVI^{C}$	RMSE	0.041	0.060	0.059	0.120
	MBE	−0.027	−0.057	−0.056	−0.118
$AFRI_{2.1}$	RMSE	0.087	0.066	0.064	0.196
	MBE	−0.077	−0.064	−0.063	−0.195
$AFRI_{2.1}{}^{C}$	RMSE	0.061	0.050	0.050	0.154
	MBE	−0.048	−0.047	−0.048	−0.153
$R_{0.65}^{TOA}$	RMSE	0.069	0.046	0.039	0.082
	MBE	0.069	0.046	0.039	0.082
$R_{0.65}^{Corrected}$	RMSE	0.007	0.011	0.009	0.020
	MBE	0.005	0.011	0.008	0.020
$R_{0.86}^{TOA}$	RMSE	0.007	0.008	0.007	0.010
	MBE	−0.037	−0.020	−0.025	−0.060
$R_{0.86}^{Corrected}$	RMSE	0.037	0.021	0.025	0.060
	MBE	0.007	0.008	−0.007	−0.010
Viewing Geometry (degree)	Solar zenith angle	45.043	39.647	41.513	39.248
	Sensor zenith angle	40.210	54.772	6.795	19.758
	Relative azimuth angle	124.292	123.934	44.702	41.717

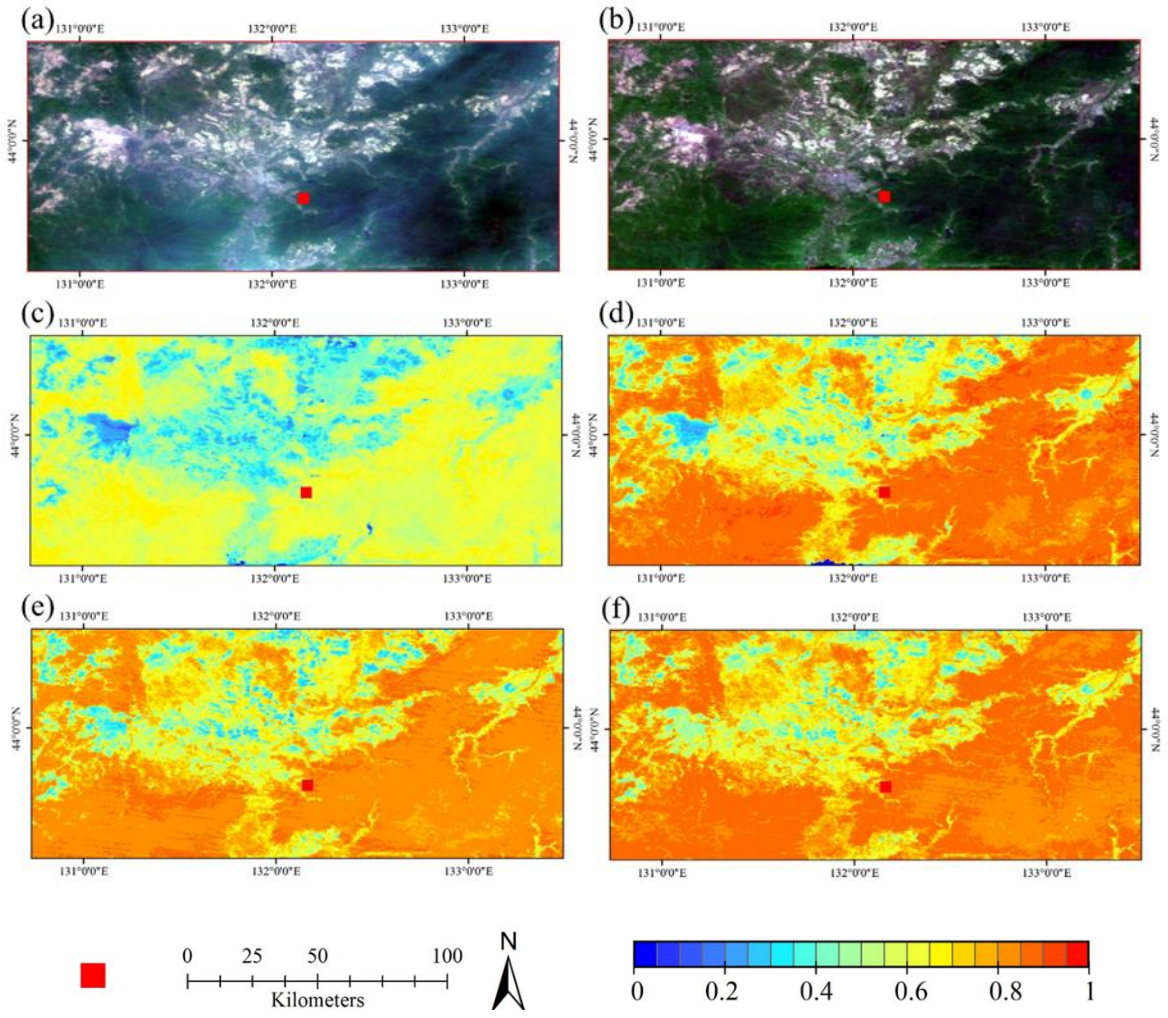

Figure 4.15 MODIS images of the case studies around the Aerosol Robotic Network (AERONET) Ussuriysk site: (**a**) True color composite (RGB = 0.65 µm, 0.56 µm, 0.47 µm) from the TOA reflectance; (**b**) true color composite from the surface reflectance; (**c**) NDVI derived from the TOA reflectance product; (**d**) NDVI derived from the MODIS surface reflectance product; (**e**) $AFRI_{2.1}$; (**f**) NDVI corrected by the proposed method. The red point is the location of the AERONET Ussuriysk site, and the corresponding AOD at 0.55 µm is 0.792.

Figure 4.15 displays the performances of TOA NDVI, $AFRI_{2.1}$ and the corrected NDVI over the area with the measured AOD of 0.792. Figure 4.15a is the true color composite using the MODIS TOA reflectance bands, and Figure 4.15b shows the true color composite using the MODIS surface reflectance product. Figure 4.15d shows the NDVI map that was calculated using the MODIS surface reflectance product; the mean NDVI value is 0.751. Compared with the surface reflectance calculated NDVI map, the TOA NDVI map (Figure 4.15c) shows a much lower NDVI value. Due to aerosol scattering and absorption, the observed NDVI was reduced at the satellite level, and the mean TOA NDVI value is equal to 0.539. Both $AFRI_{2.1}$ (Figure 4.15e) and the NDVI corrected by our method (Figure 4.15f) exhibited the ability of resist the aerosol influences; they have similar measurements in terms of the distribution with the surface reflectance-derived NDVI, and the mean vegetation indices values of 0.766 (for $AFRI_{2.1}$) and 0.769 (for corrected NDVI by our method) are similar to the surface reflectance-derived NDVI.

4.3.2 Errors from the observation conditions

The correction of atmospheric influences for our algorithm is performed under a given set of observation conditions (solar zenith angle of 30°, satellite zenith angle of 30°, and relative azimuth angles of 90°). For the same vegetation type and phenological stage, the changes in observation conditions can result in reflectance differences, thereby impacting the vegetation index determination. Therefore, I estimated the errors caused by other viewing geometries that differed from our assumption. The estimation of errors was conducted with fifteen varieties of geometrical condition combinations (shown in Table 4.4) and different AOD values (ranging from 0 to 2.0). Under the different observation geometric cases, the errors of the corrected reflectance for the 0.65 μm and 0.86 μm bands are shown in Figures 4.16 and 4.17, respectively. The color bar shows the error values that are the differences between the theoretical surface reflectance and the corrected reflectance using our approach. Based on the analysis, the observation geometries affect the accuracy of the reflectance correction in our algorithm, which could be concluded in the following manner: when the observation geometry is closer to our assumption conditions, the corrected reflectance is closer to the theoretical surface reflectance; when the solar zenith angle or satellite zenith angle is higher than the assumed angles, a relatively larger error can occur and vice versa. It should be noted that the errors in the NIR or red band from the observation conditions are greatly reduced after the construction in the NDVI calculation [40]. Therefore, the geometric errors of the new NDVI are much lower than those of the NIR or red band.

Table 4.4 Description of the different geometrical conditions set used in the simulation of the relationship between TANSO-CAI TOA reflectance and AOD with different surface conditions.

Case name	Solar zenith (degree)	Satellite zenith (degree)	Relative azimuth (degree)
a	0	0	0
b	0	30	0
c	0	30	180
d	0	60	0
e	0	60	180
f	30	0	0
g	30	30	0
h	30	30	180
i	30	60	0
j	30	60	180
k	60	0	0
l	60	30	0
m	60	30	180
n	60	60	0
o	60	60	180

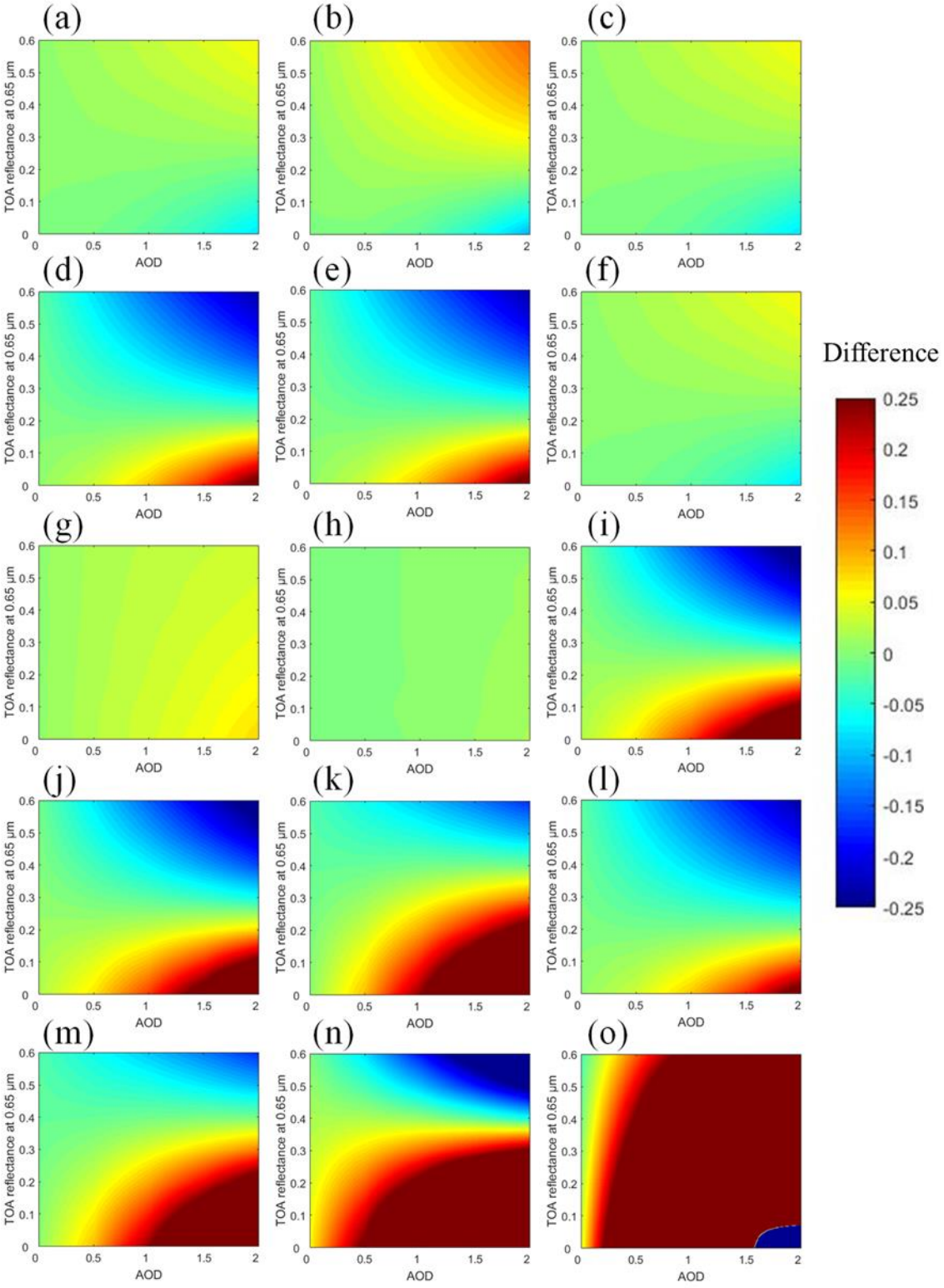

Figure 4.16 The simulated difference in the estimation of surface reflectance at 0.65 µm caused by different viewing geometries varying with AOD and TOA reflectance; (**a** to o) are the viewing geometries cases of (a to o) shown in Table 4.4.

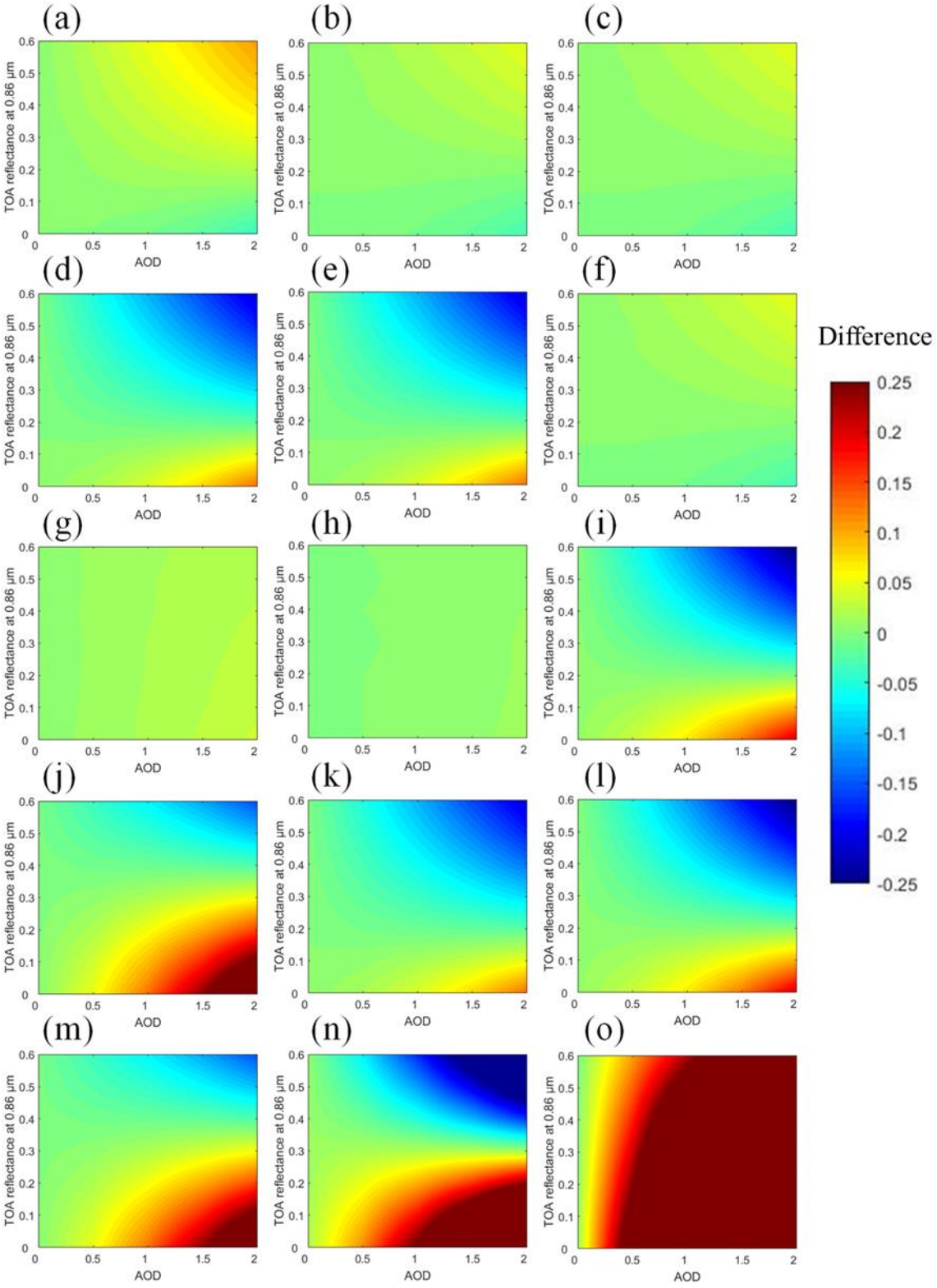

Figure 4.17 The simulated difference in the estimation of surface reflectance at 0.86 µm caused by different viewing geometries varying with AOD and TOA reflectance; (**a** to **o**) are the viewing geometries cases of (a to o) shown in Table 4.4.

4.4 Conclusions

In this study, I proposed a self-corrected approach to remove the atmospheric influence on vegetation indices based on predicted AOD values. Under a viewing geometric assumption with a relatively moderate solar zenith angle of 30°, satellite zenith angle of 30°, and relative azimuth angles of 90°, I used the 6S radiative transfer code to analyze the changes in surface reflectance of the MODIS red and NIR bands values along with different AOD and TOA reflectance values. Surface reflectance can be considered as a function of AOD and TOA reflectance. The surface reflectance estimation can be actualized based on the robust relationship between the surface reflectance at 0.65 μm and 2.1 μm, which is used in MODIS aerosol retrieval and surface reflectance algorithms. According to the changes in surface reflectance with varying AOD and TOA reflectances, I summarized three empirical functions to predict AOD and to correct the TOA reflectance in the NIR and red bands using the predicted AOD values.

The presented method has the capacity to correct for the atmospheric influences on the NIR and red bands. As a result, the corrected NIR and red bands can be directly used in the construction of vegetation indices (e.g., NDVI, RVI); additionally, a single corrected band can be used to improve the accuracy of the SWIR-derived vegetation indices (e.g., AFRI, $NDVI_{MIR}$).

The corrected NDVI has been investigated with different levels of aerosol loading. Compared with the TOA NDVI, the corrected NDVI generated near-true values, and the atmospheric influences on the NIR and red bands were largely removed. With the correction in the NIR band, the corrected NIR-derived $AFRI_{2.1}$ also showed improvement in vegetation condition measurement when aerosols are present in the atmosphere.

In the step of AOD prediction, the surface reflectance estimation is based on the rule of $R_{0.6} = 0.5R_{2.1}$. TOA reflectance at 2.1 μm is not sensitive to fine-mode aerosol particles and can be assumed as surface reflectance. However, this is not the case for dust aerosols, under which condition the atmosphere is no longer transparent [39]. In addition, a linear relationship of $R_{0.6} = 0.5R_{2.1}$ can be used over dark vegetation or brighter sparse vegetation surface conditions [25]. Thus, limited success of the method is expected in the case of dust or non-vegetated surface conditions.

Because the development of this method was under an assumed viewing geometry, the errors caused by the differences between actual and assumed viewing geometry can impact the correction in the NIR and red bands.

References

1. Bannari, A.; Morin, D.; Bonn, F.; Huete, A. A review of vegetation indices. *Remote sensing reviews* **1995**, *13*, 95-120.
2. Xiao, X.; Braswell, B.; Zhang, Q.; Boles, S.; Frolking, S.; Moore, B. Sensitivity of vegetation indices to atmospheric aerosols: Continental-scale observations in Northern Asia. *Remote Sensing of Environment* **2003**, *84*, 385-392.
3. Vermote, E.F.; El Saleous, N.Z.; Justice, C.O. Atmospheric correction of MODIS data in the visible to middle infrared: First results. *Remote Sensing of Environment* **2002**, *83*, 97-111.
4. Fletcher, R.S.; Escobar, D.E.; Skaria, M. Evaluating Airborne Normalized Difference Vegetation Index Imagery for Citrus Orchard Surveys. *HortTechnology* **2004**, *14*, 91-94.
5. NASA Earth Observatory. Available online: http://earthobservatory.nasa.gov/Features/MeasuringVegetation/measuring_vegetation_2.php (accessed on 28 October 2016).
6. Miura, T.; Huete, A.R.; Yoshioka, H.; Holben, B.N. An error and sensitivity analysis of atmospheric resistant vegetation indices derived from dark target-based atmospheric correction. *Remote sensing of Environment* **2001**, *78*, 284-298.
7. Kaufman, Y.J.; Tanre, D. Atmospherically Resistant Vegetation Index (ARVI) for EOS-MODIS. *IEEE transactions on Geoscience and Remote Sensing* **1992**, *30*, 261-270.
8. Liu, G.-R.; Liang, C.-K.; Kuo, T.-H.; Lin, T.-H.; Huang, S. Comparison of the NDVI, ARVI and AFRI vegetation index, along with their relations with the AOD using SPOT 4 vegetation data. *Terrestrial Atmospheric and Oceanic Sciences* **2004**, *15*, 15-32.
9. Huete, A.; Jackson, R. Suitability of Spectral Indices for Evaluating Vegetation Characteristics on Arid Rangelands. *Remote sensing of environment* **1987**, *23*, 213IN211-232IN218.
10. Lillesaeter, O. Spectral Reflectance of Partly Transmitting Leaves: Laboratory Measurements and Mathematical Modeling. *Remote Sensing of Environment* **1982**, *12*, 247-254.
11. Holben, B.N. Characteristics of maximum-value composite images from temporal AVHRR data. *International journal of remote sensing* **1986**, *7*, 1417-1434.
12. Fraser, R.S.; Kaufman, Y.J. Relative importance of aerosol scattering and absorption in remote sensing. *IEEE transactions on geoscience and remote sensing* **1985**, *23*, 625-633.
13. Wang, D.; Chen, Y.; Wang, M.; Quan, J.; Jiang, T. A new neighboring pixels

method for reducing aerosol effects on the NDVI images. *Remote Sens-Basel* **2016**, *8*, 489.

14. Huete, A.R. A Soil-Adjusted Vegetation Index (SAVI). *Remote sensing of environment* **1988**, *25*, 295-309.
15. Baret, F.; Guyot, G.; Major, D. In *TSAVI: A vegetation index which minimizes soil brightness effects on LAI and APAR estimation*, Geoscience and Remote Sensing Symposium, 1989. IGARSS'89. 12th Canadian Symposium on Remote Sensing, 1989 International, 1989; IEEE: pp 1355-1358.
16. Major, D.; Baret, F.; Guyot, G. A ratio vegetation index adjusted for soil brightness. *International Journal of Remote Sensing* **1990**, *11*, 727-740.
17. Qi, J.; Chehbouni, A.; Huete, A.; Kerr, Y.; Sorooshian, S. A Modified Soil Adjusted Vegetation Index. *Remote sensing of environment* **1994**, *48*, 119-126.
18. Ben‐Ze'ev, E.; Karnieli, A.; Agam, N.; Kaufman, Y.; Holben, B. Assessing vegetation condition in the presence of biomass burning smoke by applying the Aerosol‐Free Vegetation Index (AFRI) on MODIS images. *International Journal of Remote Sensing* **2006**, *27*, 3203-3221.
19. Huete, A.R.; Liu, H.Q. An Error and Sensitivity Analysis of the Atmospheric-and Soil-correcting Variants of the NDVI for the MODIS-EOS. *IEEE Transactions on Geoscience and Remote Sensing* **1994**, *32*, 897-905.
20. Kaufman, Y.J.; Remer, L.A. Detection of Forests Using Mid-IR Reflectance: An Application for Aerosol Studies. *IEEE Transactions on Geoscience and Remote Sensing* **1994**, *32*, 672-683.
21. Vogelmann, J. Comparison between two vegetation indices for measuring different types of forest damage in the north-eastern United States. *International Journal of Remote Sensing* **1990**, *11*, 2281-2297.
22. Vogelmann, J.E.; Rock, B.N. Assessing Forest Damage in High-Elevation Coniferous Forests in Vermont and New Hampshire Using Thematic Mapper Data. *Remote Sensing of Environment* **1988**, *24*, 227-246.
23. Vogelmann, J.E.; Rock, B.N. Use of Thematic Mapper Data for the Detection of Forest Damage Caused by the Pear Thrips. *Remote Sensing of Environment* **1989**, *30*, 217-225.
24. Miura, T.; Huete, A.R.; Yoshioka, H.; Holben, B.N. An error and sensitivity analysis of atmospheric resistant vegetation indices derived from dark target-based atmospheric correction. *Remote sensing of Environment* **2001**, *78*, 284-298.
25. Karnieli, A.; Kaufman, Y.J.; Remer, L.; Wald, A. AFRI—aerosol free vegetation index. *Remote Sensing of Environment* **2001**, *77*, 10-21.
26. Kaufman, Y.J. Satellite sensing of aerosol absorption. *Journal of Geophysical Research: Atmospheres* **1987**, *92*, 4307-4317.

27. NASA MODIS MODERATE RESOLUTION IMAGING SPECTRORADIOMETER. Available online: https://modis.gsfc.nasa.gov/about/ (accessed on 11 March 2017).
28. Guo, M.; Wang, X.; Li, J.; Yi, K.; Zhong, G.; Tani, H. Assessment of Global Carbon Dioxide Concentration Using MODIS and GOSAT data. *Sensors* **2012**, *12*, 16368-16389.
29. NASA Global Change Master Directory. Available online: https://gcmd.nasa.gov/KeywordSearch/Metadata.do?Portal=GCMD&EntryId=MOD02HKM&MetadataView=Full (accessed on 8 March 2017).
30. NASA A Global Change Master Directory Portal for EOSDIS. Available online: https://gcmd.nasa.gov/KeywordSearch/Metadata.do?Portal=daacs&KeywordPath=Parameters%7CSPECTRAL%2FENGINEERING%7CPLATFORM+CHARACTERISTICS%7CVIEWING+GEOMETRY&OrigMetadataNode=GCMD&EntryId=MOD03&MetadataView=Full&MetadataType=0&lbnode=mdlb4 (accessed on 10 March 2017).
31. AEROSOL ROBOTIC NETWORK. Available online: https://aeronet.gsfc.nasa.gov/new_web/index.html (accessed on 12 March 2017).
32. Chin, M. *Atmospheric aerosol properties and climate impacts*. DIANE Publishing: 2009.
33. Vermote, E.; El Saleous, N.; Justice, C.; Kaufman, Y.; Privette, J.; Remer, L.; Roger, J.; Tanre, D. Atmospheric correction of visible to middle‐infrared EOS‐MODIS data over land surfaces: Background, operational algorithm and validation. *Journal of Geophysical Research: Atmospheres* **1997**, *102*, 17131-17141.
34. MODIS LAND SURFACE REFLECTANCE SCIENCE COMPUTING FACILITY, Validation. Available online: http://modis-sr.ltdri.org/pages/validation.html (accessed on 2 March 2017).
35. Chen, H.; Cheng, T.; Gu, X.; Li, Z.; Wu, Y. Evaluation of Polarized Remote Sensing of Aerosol Optical Thickness Retrieval over China. *Remote Sens-Basel* **2015**, *7*, 13711-13728.
36. Ångström, A. The parameters of atmospheric turbidity. *Tellus* **1964**, *16*, 64-75.
37. Kaufman, Y.; Tanré, D.; Remer, L.A.; Vermote, E.; Chu, A.; Holben, B. Operational remote sensing of tropospheric aerosol over land from EOS moderate resolution imaging spectroradiometer. *Journal of Geophysical Research: Atmospheres* **1997**, *102*, 17051-17067.
38. Kaufman, Y.; Tanré, D.; Gordon, H.; Nakajima, T.; Lenoble, J.; Frouin, R.; Grassl, H.; Herman, B.; King, M.; Teillet, P. Passive remote sensing of tropospheric aerosol and atmospheric correction for the aerosol effect. *Journal of Geophysical Research: Atmospheres* **1997**, *102*, 16815-16830.

39. Kaufman, Y.; Wald, A.; Remer, L.; Gao, B.; Li, R.; Flynn, L. The MODIS 2.1 μm Channel-Correlation with Visible Reflectance for Use in Remote Sensing of Aerosol, *IEEE transactions on Geoscience and Remote Sensing* 35, 1286-1298. 1997.
40. Breunig, F.M.; Galvão, L.S.; Formaggio, A.R.; Epiphanio, J.C. Variation of modis reflectance and vegetation indices with viewing geometry and soybean development. *Anais da Academia Brasileira de Ciências* **2012**, *84*, 263-274.
41. Zhao, W.; Tamura, M.; Takahashi, H. Atmospheric and spectral corrections for estimating surface albedo from satellite data using 6S code. *Remote sensing of Environment* **2001**, *76*, 202-212.

Chapter 5 A 1.6-μm band-based self-corrected method for correcting the atmospheric influences in vegetation indices

5.1 Introduction

Vegetation indices (VIs) has been considered precise optical measures of vegetation canopy "greenness", a composite property of leaf chlorophyll, leaf area, canopy cover and structure, and are effectively used in the monitoring of the Earth's vegetation coverage from regional to global scales [1–3]. VIs can provide meaningful information for studies of plant health, water content, environmental stresses, and other important characteristics. Vegetation interacts with solar radiation differently than other natural materials, and the different plant materials, water contents, pigments, carbon contents, nitrogen contents, and other properties cause further variations across the observed spectrum [4]. Therefore, VIs can distinguish different vegetative covers according to their unique spectral behaviors [5,6]. The Normalized Difference Vegetation Index (NDVI) is the most well-known and widely used VI. NDVI is computed from the spectral differences between the near-infrared (NIR) and red bands, since the green vegetation strongly reflects radiation in the NIR, while chlorophyll absorbs radiation in the red wavelengths [7,8]. The usefulness of NDVI has been demonstrated in phonological studies of vegetation growing seasons, land cover classifications and global climate models [9–12].

However, when using NDVI to detect vegetation dynamics from satellite or airborne sensors, the spectral ground response is considerably affected by the spatiotemporal variations of the atmosphere, subsequently leading to increased errors in the qualitative and quantitative evaluations of the vegetation [6]. Several advanced VIs have been developed to enhance the vegetation response and minimize the effects of the atmosphere (absorption and scattering). The Atmospherically Resistant Vegetation Index (ARVI) and Enhanced Vegetation Index (EVI) were created by employing the blue band to correct the red band [13,14]. The middle-infrared NDVI ($NDVI_{MIR}$) used the 1.6 μm and 2.1 μm bands that have sensitivities to the vegetation and can replace the red band in the NDVI. Because 1.6 μm and 2.1 μm are longer wavelengths than those in the red band, they can penetrate atmospheric columns even when aerosols such as smoke or sulfates exist [12]. The Aerosol FRee vegetation Index (AFRI) that evolved from NDVI and $NDVI_{MIR}$ was developed based on the linear relationships between the visible and 2.1 μm (or 1.6 μm) bands. Under clear sky

conditions, AFRI closely resembles NDVI, and their values are almost identical. Since AFRI is less affected by atmospheric effects, its major application is in assessing vegetation in the presence of smoke, anthropogenic pollution, or volcanic plumes [15].

The atmospheric influences in the easily affected red band have been corrected or modified by different approaches in these VIs. One concern is that the NIR band remains sensitive to aerosols, which cause drops of radiance in the NIR band and thus the vegetation index [6,12,16]. Particularly, for cases of heavy aerosol loading (e.g., smoke), these VIs may not be applicable for interpreting the surface conditions at high accuracies. As Figure 5.1 shows, $AFRI_{2.1}$ is much less affected by atmospheric influences than NDVI, however, as the AOD values increase, the $AFRI_{2.1}$ values decrease and are lower than the true values.

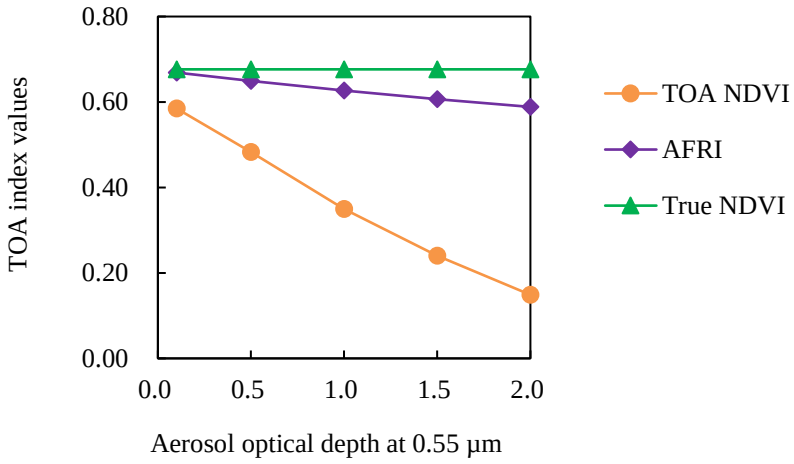

Figure 5.1 The top-of-atmosphere (TOA) vegetation indices: Normalized Difference Vegetation Index (NDVI) and Aerosol FRee vegetation Index (AFRI), with varying AOD values.

To overcoming this issue, in the Chapter 4, I introduced a self-corrected method, using a predicted AOD to correct the atmospheric influences in the red and NIR bands. It has been demonstrated that, through correcting the red and NIR bands, our method successfully improved the accuracy of the measuring of vegetation under aerosol loading conditions using NDVI and AFRI.

In our corrected method, the predicted AOD is considered as the prior information correction. The prediction of the AOD is based on the relationship between the surface reflectance at the 0.65 µm and 2.1 µm bands, which is known as the “Dark Target” (DT) method. The DT method for estimating surface reflectance over "dark" surfaces

has been widely used in aerosol retrieval and atmospheric correction. By using aircraft images from the Landsat Thematic Mapper and the Airborne Visible/Infrared Imaging Spectrometer, and spectral data measured from the ground, Kaufman et al. (1997) summarized the linear relationship between surface reflectance in the blue (0.47 μm) and red (0.65 μm) bands, and reflectance in the 2.1-μm band, as follows [17,18]:

$$\begin{cases} R_{0.65} = R_{2.1}/2 \\ R_{0.47} = R_{2.1}/4 \end{cases} \quad (1)$$

where $R_{2.1}$ is the reflectance at 2.1 μm. The 2.1-μm band is barely affected by aerosol path radiance and can penetrate most atmospheric aerosols. Therefore, the surface reflectance in the blue (0.47 μm) and red (0.65 μm) bands can be determined using Equation 1. This method was used to create the Moderate Resolution Imaging Spectroradiometer (MODIS) aerosol product of Collection 4.

It should be noted that, in our method, the self-corrected process is based on the utilization of the 2.1 μm band. Therefore, the application of this method is limited to those sensors that observe near the shortwave infrared (SWIR) 2.1 μm wavelength. However, there are several satellite sensors that do not resolve the 2.1-μm band and only have the 1.6-μm SWIR band, such as the advanced along track scanning radiometer (AATSR), Satellite Pour l'Observation de la Terre 4 (SPOT 4), Indian Remote Sensing Satellites-1C/1D (IRS-1C/1D), and Thermal and Near-infrared Sensor for Carbon Observation-Cloud and Aerosol Imager (TANSO-CAI) [19–22].

Based on this background, this study aimed to adapt the correction method for applications using satellite sensors that resolve only the 1.6-μm SWIR band. I attempted to define a connection between the surface reflectance in the 1.6 μm and 2.1 μm bands by analyzing the relationship between these two bands. Using the correlation between the 1.6 μm and 2.1 μm (1.6 vs. 2.1) bands, it is possible to conduct a 2.1-μm-based self-correction method for the 1.6-μm sensors.

5.2 Materials and methods

5.2.1 Satellite data and ground-level data

MODIS data are a reliable global-scale data source that observes the 1.6 μm and 2.1 μm wavelengths, making it possible to expediently analyze the reflectance relationship of 1.6 vs. 2.1. In this study, the surface reflectance products from MODIS and the ground-level AOD data from the Aerosol Robotic Network (AERONET) were used.

5.2.1.1 MODIS surface reflectance product (MOD09)

Each MODIS surface reflectance data set (MOD09) is a seven-band product computed from MODIS-Terra Level 1B land bands 1 (0.620–0.670 μm), 2 (0.841–0.876 μm), 3 (0.459–0.479 μm), 4 (0.545–0.565 μm), 5 (1.230–1.250 μm), 6 (1.628–1.652 μm), and 7 (2.105–2.155 μm). After adjusting for the effects of atmospheric gases, aerosols and thin cirrus clouds, the surface reflectance of MOD09 is estimated as if it would have been measured at ground level [23–25]. Thus, MOD09 surface reflectance is the source for the generation of downstream land surface products, such as the Vegetation Index (VI), Leaf Area Index (LAI), Fraction of Photosynthetically Active Radiation (FPAR), Bidirectional Reflectance Distribution Function (BRDF)/Albedo, Land Cover Snow Cover and Thermal Anomalies [26,27]. MOD09 Collection 5 has been validated, and for good quality retrievals (QA: no cloud, cloud shadow or high aerosol), the accuracy of the 1.6 μm and 2.1 μm channels is such that 97.69% and 98.64% of the observations were within the theoretical error bars of ± (0.005+5%) for the responding reflectance band [27].

5.2.1.2 AERONET AOD data

The ground-level AOD data are from AERONET [28], a worldwide remote sensing aerosol network that provides information on various aerosol properties using direct sun measurements of spectral AOD and the use of multiangular and multispectral measurements of sun radiance [29]. Unlike satellite remote sensing, AERONET measurements are unaffected by the uncertainties associated with surface properties and aerosol type assumptions. AERONET AOD products have been validated with a low uncertainty of 0.01 at visible and NIR wavelengths [28,30]. Thus, AERONET level 2.0 (cloud screened and quality-assured) data were used in this study to validate AOD retrieval from the satellite. In addition, the AERONET data were utilized to assist in the selection of the experimental data. However, since the AOD retrievals in this study were at 0.55 μm, a wavelength that AERONET does not use to measure AOD, the AERONET AOD needs to be interpolated to 0.55 μm using the Angstrom exponent α [31], defined as,

$$\alpha = -\frac{\ln\left(\frac{\tau_\lambda}{\tau_{0.55}}\right)}{\ln\left(\frac{\lambda}{0.55}\right)} \quad (2)$$

5.2.2 The relationship between reflectances at 1.6 μm and 2.1 μm

To analyze the reflectance relationship of 1.6 vs. 2.1, the MODIS surface reflectance product was used as the experimental data. Knowledge of AOD is an important factor that can affect the accuracy of the surface reflectance product [32,33]. As such, the experimental data selection referenced ground-level AOD measurements

taken from close proximity to AERONET sites to ensure the data used in the analyses were highly accurate. The experimental surface reflectance data were selected from nine AERONET sites in different global regions according to the following criteria: the MOD09 data should be obtained under cloud-free conditions, and from locations within 25-kilometers from AERONET sites; the MODIS-Terra overpasses within ±30 min of AERONET measurements, and measured AOD values should be lower than 0.1 (in order to minimize the influence of multiple aerosol scattering).

The linear relationship of surface reflectances at 1.6 μm and 2.1 μm is shown in Fig. 1a, and has a correlation coefficient (r) value of 0.847. Despite the high r-value, the relationship of 1.6 vs. 2.1 shows considerable scatter. For example, when the surface reflectance value of the 1.6-μm channel is 0.2, the corresponding scatter plots show surface reflectance values of the 2.1-μm channel ranging from 0.055 to 0.175, obviously biased against the regression line. Such uncertainty could result in incorrect surface reflectance estimations, thereby leading to large errors in AOD retrieval [34].

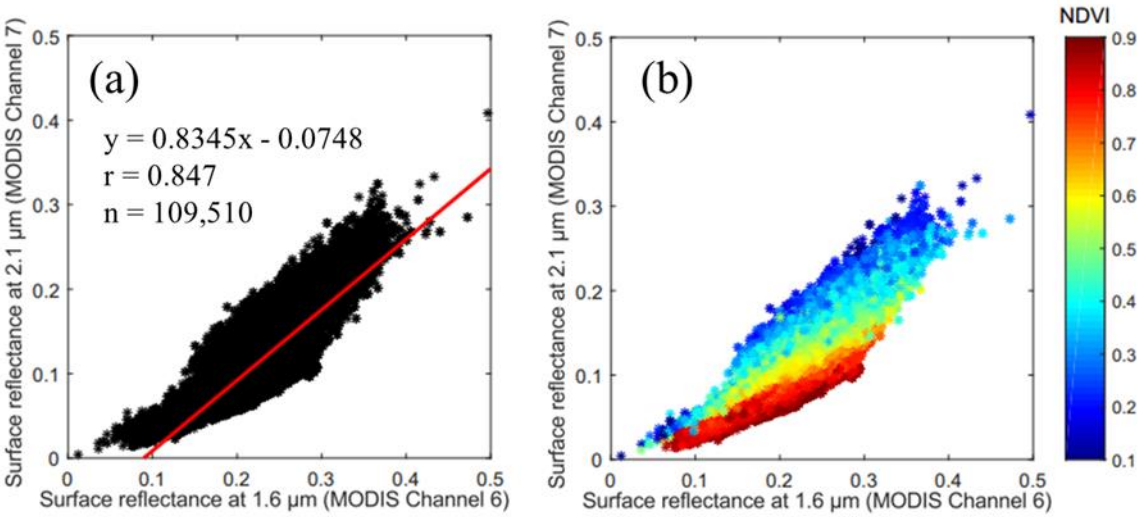

Figure 5.2 Scatter plots between Moderate Resolution Imaging Spectroradiometer (MODIS) surface reflectances at 1.6 μm and 2.1 μm. (**a**) The spectral linear relationship of surface reflectances at 1.6 μm and 2.1 μm. (**b**) Surface reflectances at 2.1 μm as a function of surface reflectance at 1.6 μm and NDVI. The color bar shows the NDVI values for each point.

In light of this, the relationship between surface reflectance at 0.6 μm and 2.1 μm is more robust, while the relationship between surface reflectance at 0.6 μm and 1.6 μm is very sensitive to the amount of surface vegetation [34–36]. It could be expected that the surface reflectance relationship of 1.6 vs. 2.1 may also be dependent on the

amount of vegetation. To confirm this conjecture and to develop a method for reducing scatter in the relationships of 1.6 vs. 2.1, I used the NDVI as a tuner to explore a new relationship. NDVI is a commonly applied numerical indicator used for evaluating vegetation conditions; it could be calculated with the reflectance of the red and NIR bands obtained from the space platform using Equation 3 [37]. NDVI values range from negative one to positive one; zero and negative values represent non-vegetated surfaces (such as soil, water, snow), and higher values indicate the higher possible densities of green vegetation.

$$\mathrm{NDVI} = (\mathrm{R_{NIR}} - \mathrm{R_{red}})/(\mathrm{R_{NIR}} + \mathrm{R_{red}}) \quad (3)$$

where R_{NIR} and R_{red} are the reflectances of the NIR and red bands respectively.

Figure 5.2b shows the relationship of surface reflectances at 1.6 μm and 2.1 μm. The colors of the points are their corresponding NDVI values, according to the color bar. As the figure shows, the NDVI is a significant factor in the relationship of 1.6 vs. 2.1. The exhibited evident regulation according to NDVI distribution is that the relationship of 1.6 vs. 2.1 seems to be vegetation dependent. As NDVI values vary from high to low, the slope of the corresponding linear relationship of 1.6 vs. 2.1 is continuously increasing. This verifies previous conjecture that the relationship of 1.6 vs. 2.1 is also sensitive to the amount of vegetation.

Compared with using the linear relationship of 1.6 vs. 2.1 directly, as shown in Figure 5.2a, it is possible to improve the accuracy of surface reflectance estimation through an NDVI-based correlation of 1.6 vs. 2.1. However, it is important to note that aerosols can influence NDVI with NDVI values typically decreasing as AOD increases, thus limiting its potential to evaluate surface conditions [35,38]. To overcome this drawback, other vegetation indices that are not sensitive to atmospheric aerosols could replace NDVI. In the MODIS DT algorithm Collection 5 and Collection 6, the $NDVI_{SWIR}$, a measure of vegetation "greenness" highly correlated with regular NDVI, was proposed. $NDVI_{SWIR}$ (shown as Equation 4) is defined as a function of the MODIS-measured reflectances of the 1.24 μm and 2.12 μm channels. Because longer wavelengths are much less affected by aerosols, consequently, $NDVI_{SWIR}$ is aerosol resistant [34,39].

$$\mathrm{NDVI_{SWIR}} = (\mathrm{R_{1.24}} - \mathrm{R_{2.12}})/(\mathrm{R_{1.24}} + \mathrm{R_{2.12}}) \quad (4)$$

where $R_{1.24}$ and $R_{2.12}$ are the MODIS-measured reflectances at 1.24 μm and 2.12 μm.

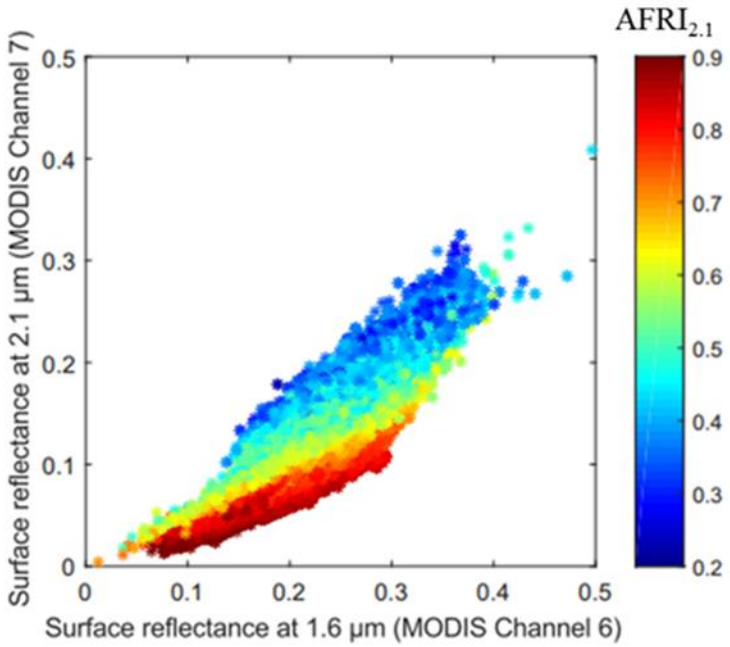

Figure 5.3 The MODIS surface reflectances at 2.1 μm as a function of surface reflectance at 1.6 μm and $AFRI_{2.1}$. The color bar shows the values of $AFRI_{2.1}$ for each point.

Similarly, I attempted to employ the $AFRI_{2.1}$ [15] to establish a new VI-based relationship for 1.6 vs. 2.1. $AFRI_{2.1}$ is calculated by using the NIR and SWIR bands as follows:

$$AFRI_{2.1} = (R_{NIR} - 0.5 * R_{2.1})/(R_{NIR} + 0.5 * R_{2.1}) \quad (5)$$

where R_{NIR} and $R_{2.1}$ are the reflectances of the NIR (MODIS channel 2) and 2.1 μm (MODIS channel 7) channels. In this equation, the coefficient 0.5 is determined based on the experiment results of Karnieli et al. (2001). They flew over a variety of ground surfaces in Israel, and performed measurements using a field spectrometer; under clear sky conditions. The empirical linear relationship between the SWIR spectral band around 2.1 μm and the red band around 0.6 μm was revealed as $R_{0.65} = 0.5R_{2.1}$ [15]. One key difference that emerges when comparing $AFRI_{2.1}$ (Equation 5) with the regular NDVI (Equation 3), is that the reflectance of the red band in NDVI has been replaced by the reflectance of the SWIR (2.1 μm) band, according to the mathematical relationship between the red and SWIR (2.1 μm) bands. Because the wavelength of SWIR is considered to have a much longer diameter than most aerosols, SWIR has the ability to penetrate atmospheric aerosols. In addition, SWIR is sensitive to vegetation. With these advantages, $AFRI_{2.1}$ is less susceptible to aerosol influence [15,40,41].

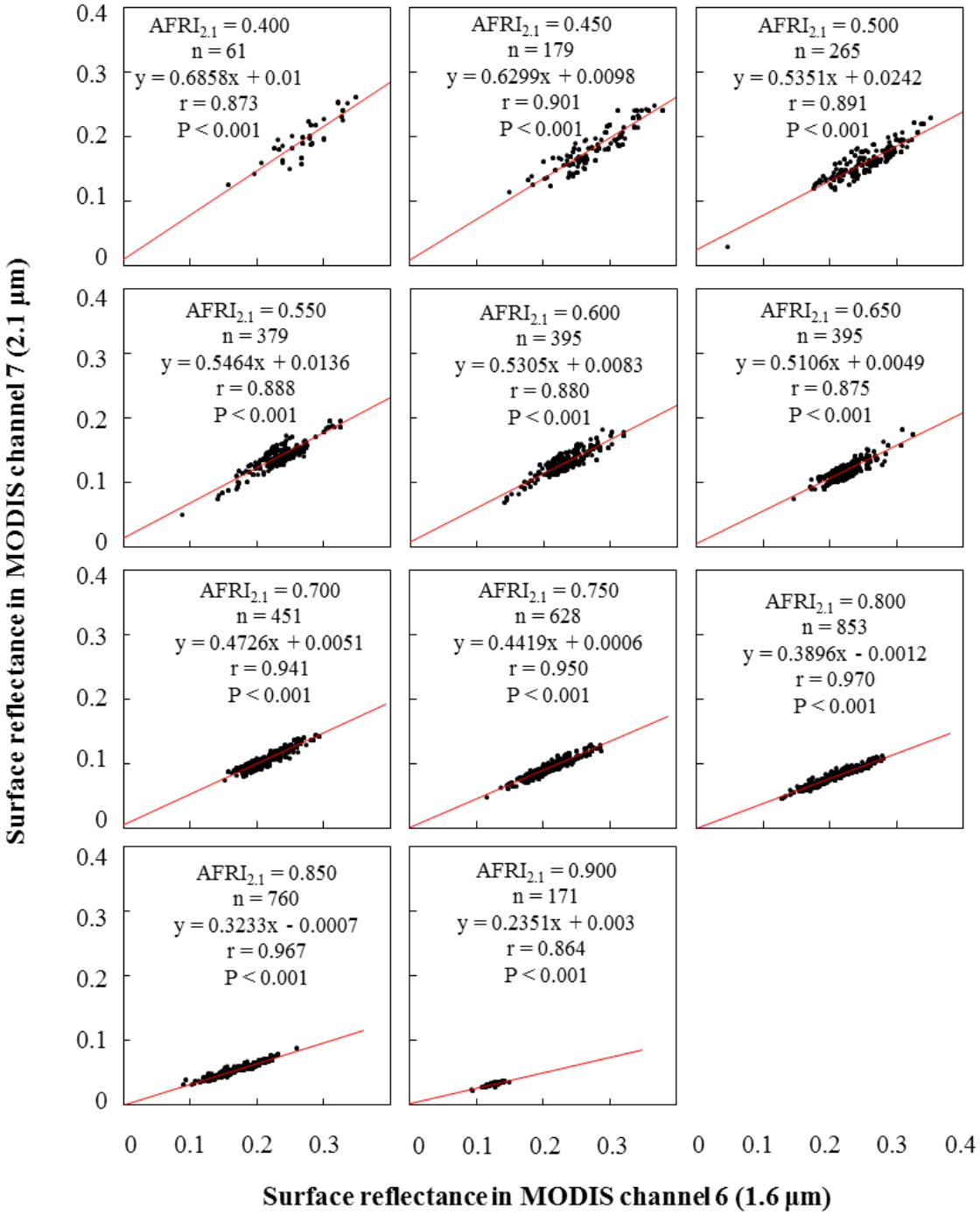

Figure 5.4 The relationship between surface reflectances at 2.1 µm and 1.6 µm vary with different $AFRI_{2.1}$ values (All data points in each graph fall within $AFRI_{2.1}$ value ± 0.001).

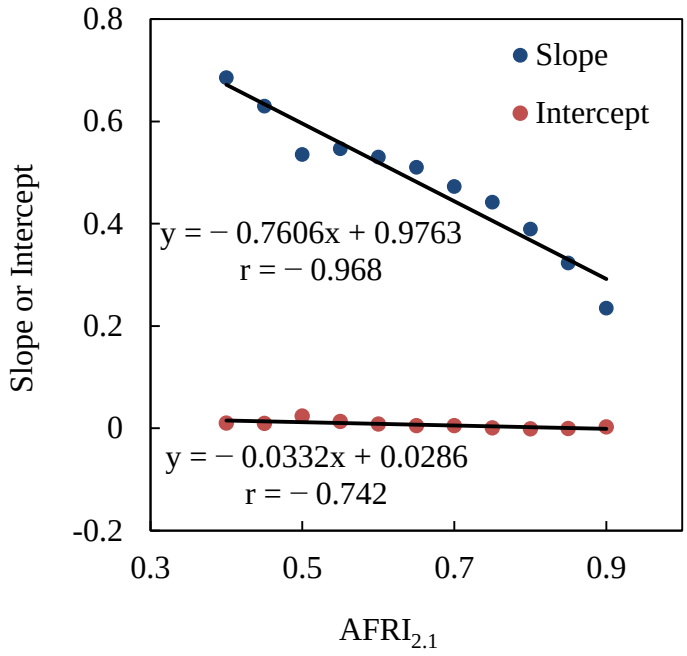

Figure 5.5 The slopes and intercepts of regression functions (for each graph in Figure 5.4) as a function of $AFRI_{2.1}$.

I used the $AFRI_{2.1}$ to interpret how the relationship of 1.6 vs. 2.1 changes with different surface conditions. The results are displayed in Figure 5.3, which also shows similarities to Figure 5.2b. To study in more quantitative detail how the relationship of 1.6 vs. 2.1 varies with $AFRI_{2.1}$, I picked out and grouped several experimental data from the sum of points in Figure 5.3, according to certain given $AFRI_{2.1}$ values. Each of the selected points groups is displayed in Figure 5.3, in which the surface reflectance of the 2.1 μm band is a function of the surface reflectance at 1.6 μm and the given $AFRI_{2.1}$ values. The given $AFRI_{2.1}$ values are all from 0.400 to 0.900, with intervals of 0.05. Compared with the linear correlation of 1.6 vs. 2.1 (in Figure 5.2a), all the scatter plots in Figure 5.4 have stronger correlations, and their corresponding r-values are seemingly higher than those in Figure 5.2a, implying that such an $AFRI_{2.1}$-based relationship has the potential capacity to describe the relationship of 1.6 vs. 2.1 with higher accuracy than to just using the general linear relationship (as shown in Figure 5.2a). Considering the regression functions of these scatter plots in Figure 5.4, the slopes of their regression lines become distinctly smaller as their $AFRI_{2.1}$ values increase. In order to understand the changes of these regression functions with varied $AFRI_{2.1}$, the slopes and intercepts of these regression lines were compared with their corresponding $AFRI_{2.1}$ values. Figure 5.5 shows that there is a very strong inverse relationship between the slope and $AFRI_{2.1}$, and its r-value is as high as −0.964. In addition, the relationship between intercepts and $AFRI_{2.1}$ has an r-value of −0.742. Based on these results, the slope and intercept for the relationship of 1.6 vs. 2.1 for

different $AFRI_{2.1}$ values can be determined, allowing an $AFRI_{2.1}$-based regression function (Equation 6) for estimating the reflectance in the 2.1 μm channel from 1.6 μm channel to be formulated as follows:

$$R_{2.1} = Slope_{1.6/2.1} * R_{1.6} + Intercept_{1.6/2.1}$$

with

$$Slope_{1.6/2.1} = a_1 * AFRI_{2.1} + b_1$$

$$Intercept_{1.6/2.1} = a_2 * AFRI_{2.1} + b_2 \quad (6)$$

where the $R_{2.1}$ and $R_{1.6}$ are the surface reflectances at 2.1 μm and 1.6 μm, and the $Slope_{1.6/2.1}$ and $Intercept_{1.6/2.1}$ are the function of $AFRI_{2.1}$, with the coefficients a_1 = −0.7606, b_1 = 0.9763, a_2 = −0.0332, and b_2 = 0.0286, which are decided according to the experiment results in Figure 5.5. I tested the performances of the linear regression function (as shown in Figure 5.2a) and the $AFRI_{2.1}$-based regression function derived by our team. The estimated results using the linear and the $AFRI_{2.1}$-based regression functions are compared with the true values, and results are shown in Figures 5.6a and 5.6b, respectively. It is obvious that the $AFRI_{2.1}$-based estimations correlate better with the true values. The comparisons in Figure 5.6b show much less scattering, and the r-value of the regression has clearly improved.

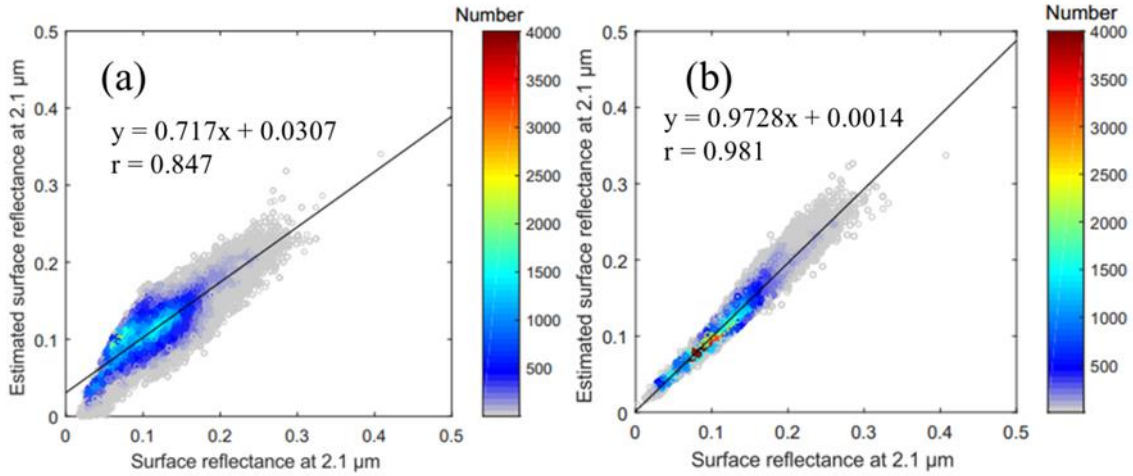

Figure 5.6 Comparisons of the estimated and the true surface reflectance at 2.1 μm. (**a**) The estimated surface reflectance is derived using the linear relationship shown in Figure 5.2a; (**b**) The estimated surface reflectance is derived from the known $AFRI_{2.1}$ using the $AFRI_{2.1}$-based regression function (Equation 5). The color bar shows the number for each point.

5.2.3 Estimation of aerosol free vegetation index ($AFRI_{2.1}$) using NIR and 1.6 μm bands

Although the $AFRI_{2.1}$-based approach performed well in testing, it is worth noting that the test results shown in Figure 5.6b are based on known $AFRI_{2.1}$. For sensors equipped with 2.1 μm and NIR bands, the $AFRI_{2.1}$ can easily be directly calculated using Equation 5. However, it is not feasible to derive the $AFRI_{2.1}$ from unequipped sensors. To resolve this difficulty, I developed a new method to estimate $AFRI_{2.1}$ using the 1.6 μm band. Equations 5 and (6) can be rewritten as Equations 7 and 8:

$$AFRI_{2.1} = (R_{0.8} - 0.5 * R_{2.1})/(R_{0.8} + 0.5 * R_{2.1}) \quad (7)$$

$$R_{2.1} = (a_1 * AFRI_{2.1} + b_1) * R_{1.6} + a_2 * AFRI_{2.1} + b_2 \quad (8)$$

where $R_{0.8}$ is the reflectance of the MODIS NIR channel, of which the center wavelength is at 0.86 μm. To substitute Equation 8 into Equation 7, the unknown term $R_{2.1}$ can be eliminated; after rearranging, a quadratic equation in $AFRI_{2.1}$ can be obtained (Equation 9). The solutions are presented as Equation 10:

$$AFRI_{2.1}{}^2 * 0.5 * (a_1 * R_{1.6} + a_2) + AFRI_{2.1} * (R_{0.8} + 0.5 * (a_1 + b_1) * R_{1.6} + 0.5 * (a_2 + b_2)) + (0.5 * b_1 * R_{1.6} + 0.5 * b_2 - R_{0.8}) = 0 \quad (9)$$

$$AFRI_{2.1} = \frac{-(R_{0.8}+0.5*(a_1+b_1)*R_{1.6}+0.5*(a_2+b_2))}{2*0.5*(a_1*R_{1.6}+a_2)} \pm \frac{\sqrt{(R_{0.8}+0.5*(a_1+b_1)*R_{1.6}+0.5*(a_2+b_2))^2-4*0.5*(a_1*R_{1.6}+a_2)*(0.5*b_1*R_{1.6}+0.5*b_2-R_{0.8})}}{2*0.5*(a_1*R_{1.6}+a_2)} \quad (10)$$

$AFRI_{2.1}$ in Equations 9 and 10 can be estimated using the 0.8 μm and 1.6 μm bands. In actual application, $AFRI_{2.1}$ solutions have two roots, because the $AFRI_{2.1}$ values should all be within the range of –1 to 1 (similar to the NDVI); thus there would be one reasonable root falling inside this range, with another unreasonable root falling outside of it. Using the estimated $AFRI_{2.1}$ and Equation 8, the $R_{2.1}$ can be calculated. The performances of the $AFRI_{2.1}$ and $R_{2.1}$ values estimated using the 1.6 μm-based approach were also tested by comparing them with their corresponding true values. Figure 5.7a shows the scatter plot of the estimated $AFRI_{2.1}$ versus true $AFRI_{2.1}$, and Figure 5.6b shows the scatter plot of the estimated $R_{2.1}$ versus the true $R_{2.1}$. All estimations show very good agreement with the true values, and the derived r-values are all above 0.92. The regression slope value is near to 1, and the intercept is close to 0.

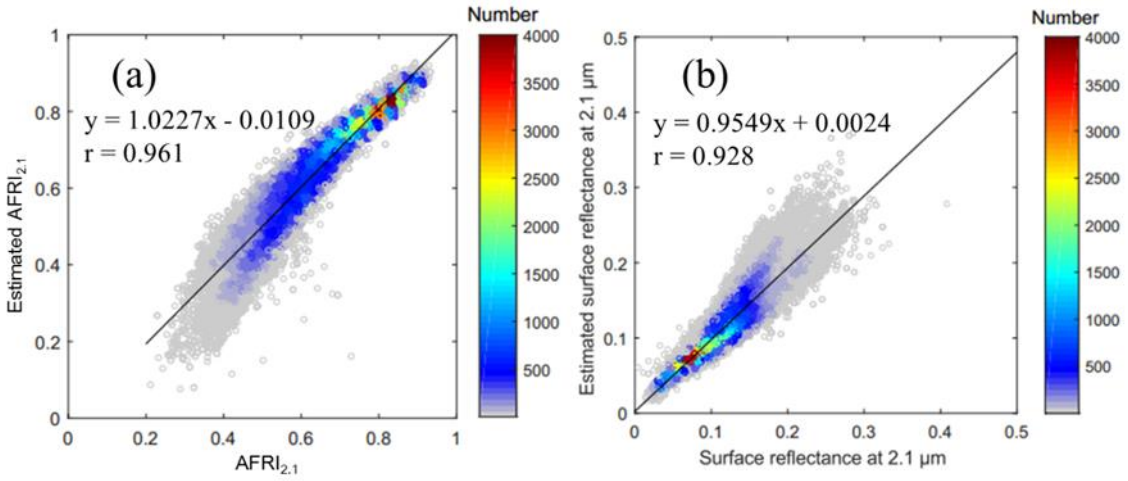

Figure 5.7 Comparisons of the estimated results and the true values. (**a**) Comparisons of the estimated $AFRI_{2.1}$ and the true $AFRI_{2.1}$. (**b**) Comparisons of the estimated and the true surface reflectance at 2.1 μm. The estimated surface reflectance at 2.1 μm is from the $AFRI_{2.1}$ estimated using the proposed method (Equations 7 to 10). The color bars show the number for each point.

5.2.4 A 1.6-μm band-based method for minimizing atmospheric influences in the NIR and red bands

An overview of the strategy for correcting the atmospheric influence on the NIR and red bands, using the 1.6-μm band, is shown in Figure 5.8. The fundamental processing steps shown by the dashed line were introduced in the Chapter 4. Using the method mentioned in this chapter, I can estimate the reflectance at the 2.1 μm from that of the 1.6 μm band, and then accomplish the self-correction process in the red and NIR bands. The corrected bands can be used in the construction of VIs.

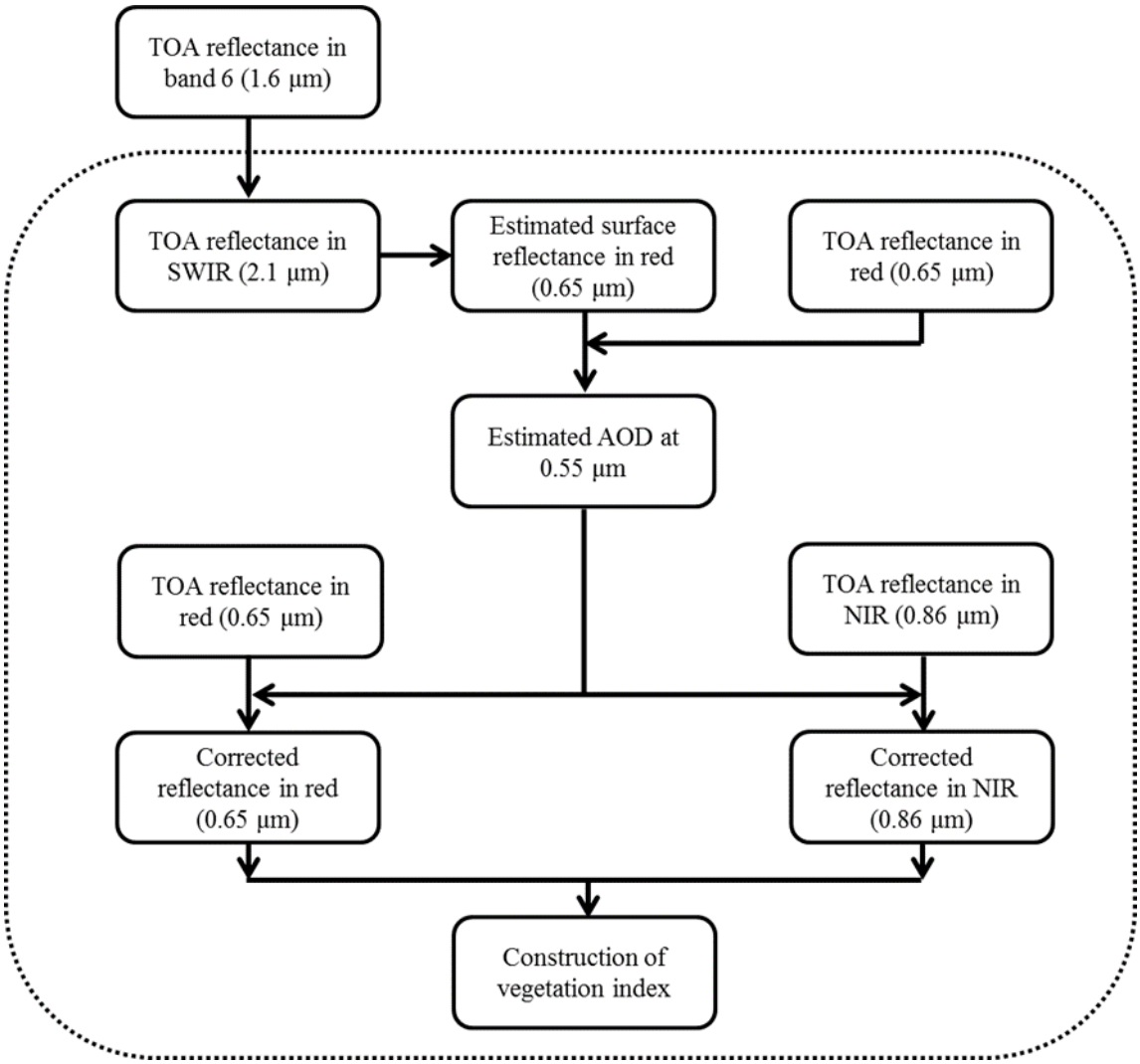

Figure 5.8 Flowchart of the 1.6-μm band-based self-correction method for removing the atmospheric influences in the MODIS near-infrared (NIR) and red bands, along with a newly derived method of vegetation indices construction.

5.3 Results and discussion

5.3.1 Accuracy assessment of the 1.6-μm band-based self-correction method

The major applications of our correction method include correcting the atmospheric influences in the NIR and red bands; the corrected NIR band can be used alone to improve the accuracy of the aerosol resist vegetation indices (e.g., the AFRI, $NDVI_{MIR}$); the corrected NIR and red bands can be used to calculate VIs (e.g., NDVI) and assess vegetation in the presence of aerosols. The performance of the 1.6-μm band-based self-correction method under different aerosol loadings (AOD) is assessed using the atmospherically corrected VIs. The selected spatially and temporally matched MODIS/AERONET collocated data in the Chapter 4 were used as the experimental

data in this work. The uncorrected VIs (top-of-atmosphere (TOA) VIs) were calculated using the reflectance data from the 6 collection of the MODIS/Terra calibrated radiances (MOD02HKM) products. According to the ground-level AOD measurements from AERONET, a pixel-by-pixel atmospheric correction was conducted using a second simulation of a satellite signal in the solar spectrum (6S) radiative transfer code, and the corrected VIs were calculated using the atmospherically corrected reflectances at the corresponding wavelengths.

5.3.1.1 Application of 1.6-μm band-based correction method for AFRI

Using the method introduced in Sections 5.2.2 and 5.2.3, the estimated $AFRI_{2.1}$ (Est-$AFRI_{2.1}$) and estimated 2.1-μm reflectance can be obtained from the 1.6-μm reflectance. The main advantage of $AFRI_{2.1}$ is in assessing vegetation in the presence of smoke, anthropogenic pollution, or volcanic plumes. The estimated 2.1-μm reflectance can help to adapt the self-correction method (in Chapter 4) to the sensors that possess only the 1.6 μm SWIR bands. Consequently, the correction of the NIR band can be accomplished by the implementation of the 1.6-μm band-based correction method, and the corrected NIR used in the AFRI was expected to outperform the original AFRI. There are two methods to calculate the corrected NIR-derived $AFRI_{2.1}$. The first one ($AFRI_{2.1}^{C1}$) is to replace the TOA NIR in Equation 10 with the corrected NIR, as shown in Equation 11:

$$AFRI_{2.1}^{C1} = \frac{-\left(R_{NIR}^{Corrected} + 0.5*(a_1+b_1)*R_{1.6} + 0.5*(a_2+b_2)\right)}{2*0.5*(a_1*R_{1.6}+a_2)} \pm \frac{\sqrt{\left(R_{NIR}^{Corrected} + 0.5*(a_1+b_1)*R_{1.6} + 0.5*(a_2+b_2)\right)^2 - 4*0.5*(a_1*R_{1.6}+a_2)*(0.5*b_1*R_{1.6}+0.5*b_2-R_{NIR}^{Corrected}}}{2*0.5*(a_1*R_{1.6}+a_2)} \quad (11)$$

where $R_{NIR}^{Corrected}$ is the corrected NIR, and $AFRI_{2.1}^{C1}$ is the corrected NIR-derived $AFRI_{2.1}$. There is another corrected NIR-derived $AFRI_{2.1,}$ proposed based on Equation 7, which is written as Equation 12:

$$AFRI_{2.1}^{C2} = \left(R_{NIR}^{Corrected} - 0.5 * R_{2.1}^{Estimated}\right)/\left(R_{NIR}^{Corrected} + 0.5 * R_{2.1}^{Estimated}\right) \quad (12)$$

where $R_{2.1}^{Estimated}$ is the estimated reflectance at 2.1 μm using the 1.6 μm band, and $AFRI_{2.1}^{C2}$ is the second version of the corrected NIR-derived $AFRI_{2.1}$.

Figures 5.9 to 5.11 show the experimental data from the Ubon Ratchathani, Ussuriysk, and Gandhi College sites, respectively; the graphs in the columns a-d have different AOD values.

The comparisons of $AFRI_{2.1}$ versus the atmospherically corrected NDVI, and the estimated $AFRI_{2.1}$ (Est-$AFRI_{2.1}$) versus the atmospherically corrected NDVI are shown in row 1 and row 2 in the Figures 5.9 to 5.11, respectively. It could be found that the

comparisons of $AFRI_{2.1}$ and Est-$AFRI_{2.1}$ show very strong similarities.

The comparisons of $AFRI_{2.1}^{C1}$ versus the atmospherically corrected NDVI, and $AFRI_{2.1}^{C2}$ versus the atmospherically corrected NDVI are shown in row 3 and row 4 of Figures 5.9 to 5.11, respectively. The comparisons of the TOA versus surface reflectances in NIR band (black scatter plots), and the corrected versus surface reflectances (green scatter plots) in the NIR band are shown in row 5 in Figures 5.9 to 5.11. The statistical root mean square error (RMSE) and mean bias error (MBE) were used to evaluate the errors between the TOA reflectance-derived values and the atmospherically corrected values, and the results for each graph in Figures 5.9 to 5.11 are summarized in Tables 5.1 to 5.3.

As the graphs of row 5 in Figures 5.9 to 5.11 show, except for one case (a-5 in Figure 5.9), all the corrected NIR band (green scatter plots) values had smaller RMSE and MBE (in absolute terms) values than the uncorrected NIR band (black scatter plots) values. Given higher AOD value conditions, larger improvements in accuracy were observed. This indicates that the 1.6-μm band-based correction method is effective for correcting the NIR band, even for high AOD levels. However, for light aerosol loadings, such as that in a-5 in Figure 5.9, which had an AOD value of 0.12, the atmospheric influences in the NIR band are easily overwhelmed by system errors from the correction process.

Compared with the performance of the uncorrected Est-$AFRI_{2.1}$, in most cases, the corrected $AFRI_{2.1}$ ($AFRI_{2.1}^{C1}$ and $AFRI_{2.1}^{C2}$) is closer to the atmospherically corrected values. Only in two cases (a-5 in Figure 5.9 and b-5 in Figure 5.11) were poorer RMSE and MBE values observed for the corrected $AFRI_{2.1}$ ($AFRI_{2.1}^{C1}$ and $AFRI_{2.1}^{C2}$). After further analysis, I found that the worst performance of case a-5 in Figure 5.9 was mainly due to errors in the correction of the NIR band, but the corrected NIR band in the case of b-5 in Figure 5.11 was much closer to the atmospherically corrected values. Therefore, the unsatisfactory performance in case b-5 in Figure 5.11 may have been caused by errors in the estimation of the reflectance at 2.1 μm.

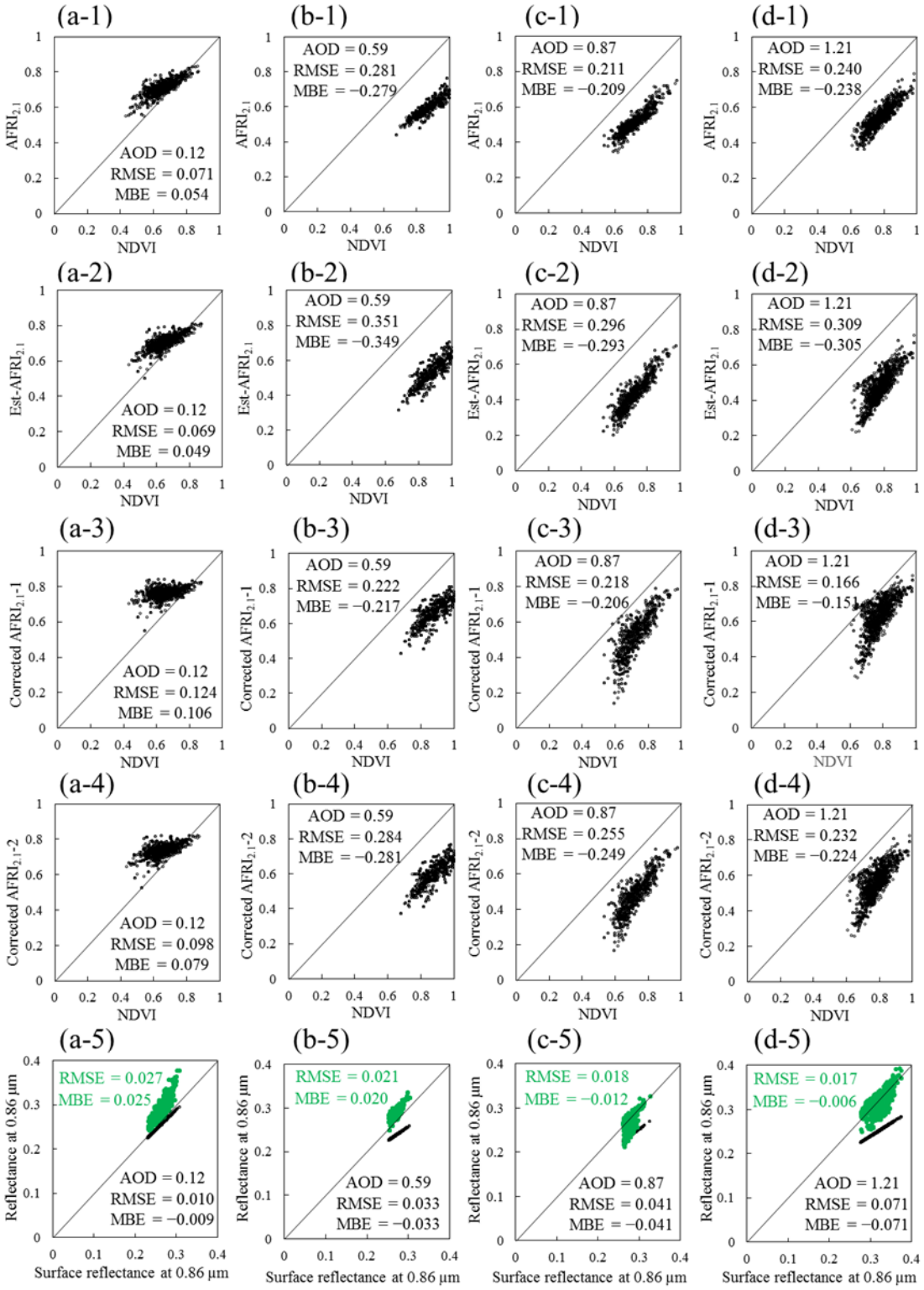

Figure 5.9 Experimental results of the Ubon_Ratchathani site. $AFRI_{2.1}$ (**Row 1**), estimated $AFRI_{2.1}$ (Est-$AFRI_{2.1}$) (**Row 2**), corrected NIR-derived $AFRI_{2.1}$ based on Equation 11 (Corrected $AFRI_{2.1}$-1) (**Row 3**), and corrected NIR-derived $AFRI_{2.1}$ based on Equation 12 (Corrected $AFRI_{2.1}$-2) (**Row 4**) plotted against the atmospherically corrected NDVI; the TOA reflectance at NIR (black plots) and corrected reflectance at NIR (green plots) against the surface reflectance at NIR (**Row 5**) for different aerosol loading conditions (AOD at 0.55 µm).

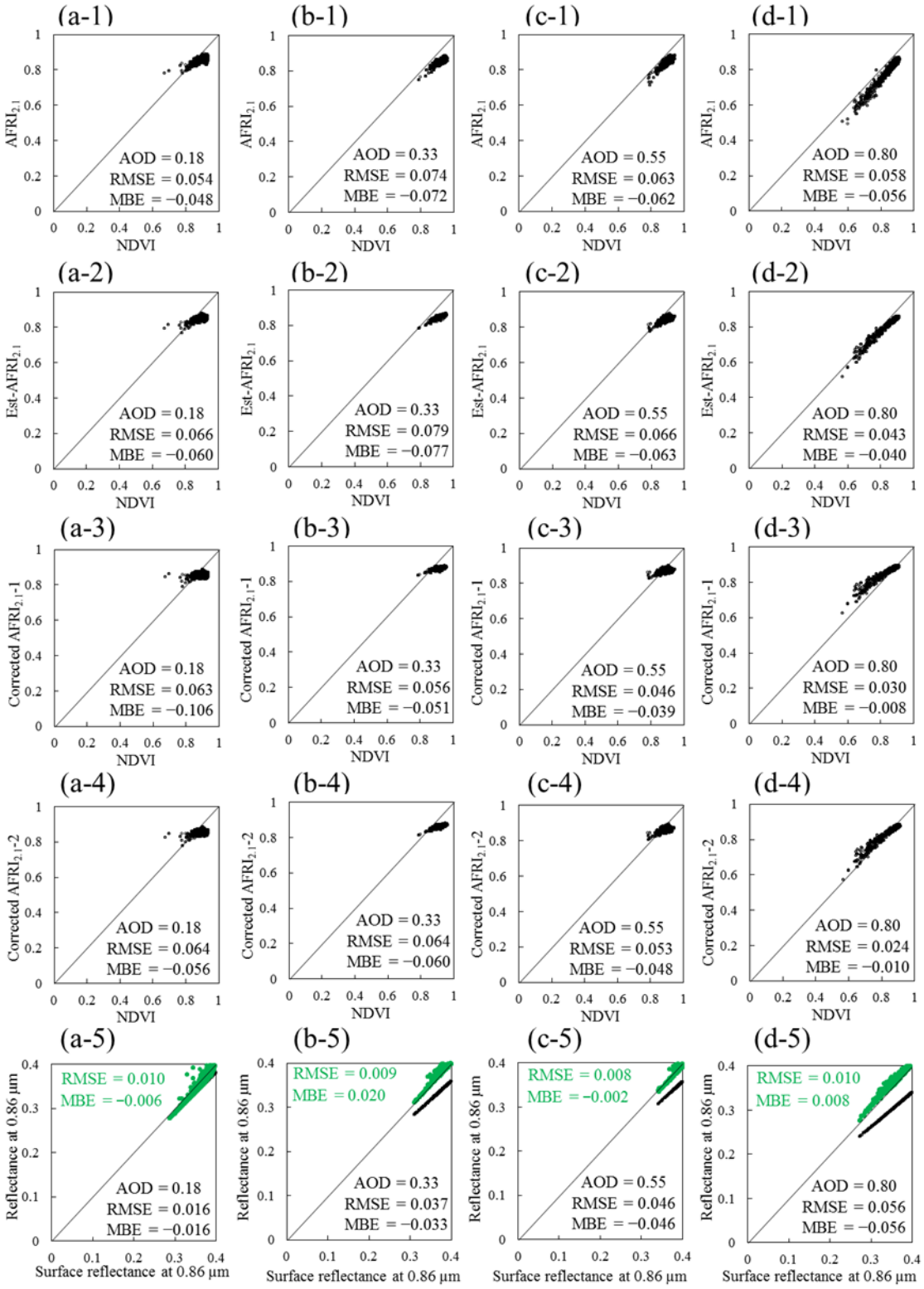

Figure 5.10 Experimental results of the Ussuriysk site. $AFRI_{2.1}$ (**Row 1**), estimated $AFRI_{2.1}$ (Est-$AFRI_{2.1}$) (**Row 2**), corrected NIR-derived $AFRI_{2.1}$ based on Equation 11 (Corrected $AFRI_{2.1}$-1) (**Row 3**), and corrected NIR-derived $AFRI_{2.1}$ based on Equation 12 (Corrected $AFRI_{2.1}$-2) (**Row 4**) plotted against the atmospherically corrected NDVI; the TOA reflectance at NIR (black plots) and corrected reflectance at NIR (green plots) against the surface reflectance at NIR (**Row 5**) for different aerosol loading conditions (AOD at 0.55 µm).

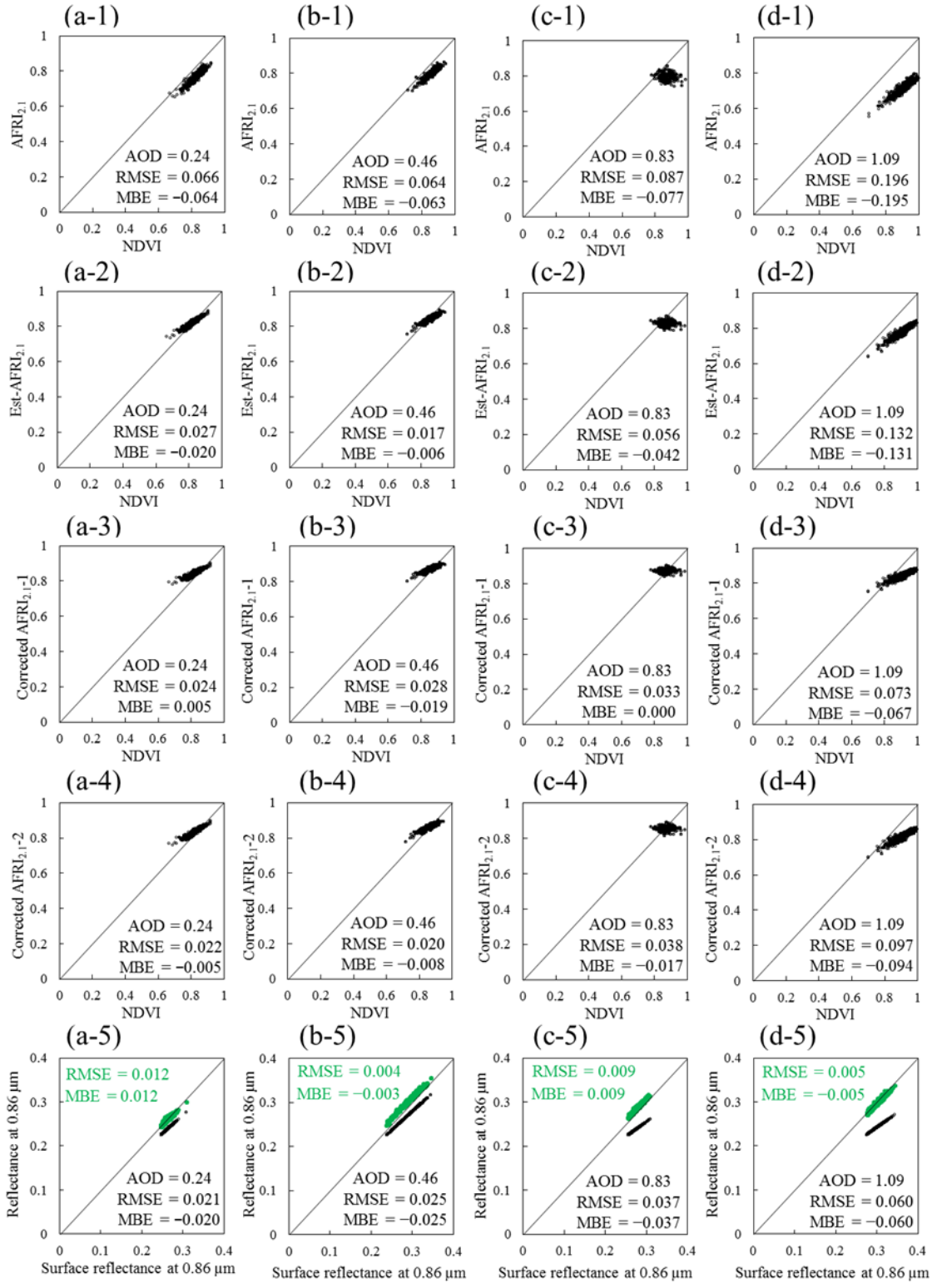

Figure 5.11 Experimental results of the Gandhi_College site. $AFRI_{2.1}$ (**Row 1**), estimated $AFRI_{2.1}$ (Est-$AFRI_{2.1}$) (**Row 2**), corrected NIR-derived $AFRI_{2.1}$ based on Equation 11 (Corrected $AFRI_{2.1}$-1) (**Row 3**), and corrected NIR-derived $AFRI_{2.1}$ based on Equation 12 (Corrected $AFRI_{2.1}$-2) (**Row 4**) plotted against the atmospherically corrected NDVI; the TOA reflectance at NIR (black plots) and corrected reflectance at NIR (green plots) against the surface reflectance at NIR (**Row 5**) for different aerosol loading conditions (AOD at 0.55 µm).

5.3.1.2 Corrected NIR and red bands-derived NDVI

Through correcting the TOA reflectances in red and NIR bands, atmospheric influences in NDVI would be corrected or reduced. The corrected NDVI was calculated from the corrected red and NIR bands, as follows (Equation 13):

$$\mathrm{NDVI}^{\mathrm{Corrected}} = \left(\mathrm{R}_{\mathrm{NIR}}^{\mathrm{Corrected}} - \mathrm{R}_{\mathrm{red}}^{\mathrm{Corrected}}\right)/\left(\mathrm{R}_{\mathrm{NIR}}^{\mathrm{Corrected}} + \mathrm{R}_{\mathrm{red}}^{\mathrm{Corrected}}\right) \qquad (13)$$

where $\mathrm{NDVI}^{\mathrm{Corrected}}$ stands for the corrected NDVI and $\mathrm{R}_{\mathrm{red}}^{\mathrm{Corrected}}$ stands for corrected NIR bands. The performance of our proposed correction method was evaluated by comparing the corrected NDVI against the atmospherically corrected NDVI under different AOD levels. The experimental results for Ubon_Ratchathani, Ussuriysk, and Gandhi_College sites are shown in Figures 5.12 to 5.14. The graphs in columns of a to d are with different AOD values. Rows 1 and 2 display the comparisons of TOA reflectance-derived NDVI vs. atmospherically corrected NDVI, and the corrected NDVI vs. atmospherically corrected NDVI. Row 3 shows the comparisons of surface reflectance vs. TOA reflectance at 0.65 μm (black scatter plots), and the surface reflectance vs. corrected reflectance at 0.65 μm (green scatter plots). Their statistical results are summarized in the Tables 5.1 to 5.3.

In Figures 5.12 to 5.14, the green scatter plots in row 3 show that the corrected red reflectance is closer to the one-to-one line than uncorrected red reflectance. Much better statistical RMSE and MBE values derived for the corrected red reflectance means that the correction method removed most of atmospheric influences in the red band. In addition, graphs in row 1 show that TOA NDVI values are lower than the surface NDVI values, and the larger bias were observed for higher AOD. Finally, graphs in row 2 demonstrate that the corrected NDVI show lower RMSE and MBE (in absolute terms) values, which revealed that our correction method used in the application of NDVI is effective, after correction, the errors in NDVI caused by atmospheric effects have been obviously improved.

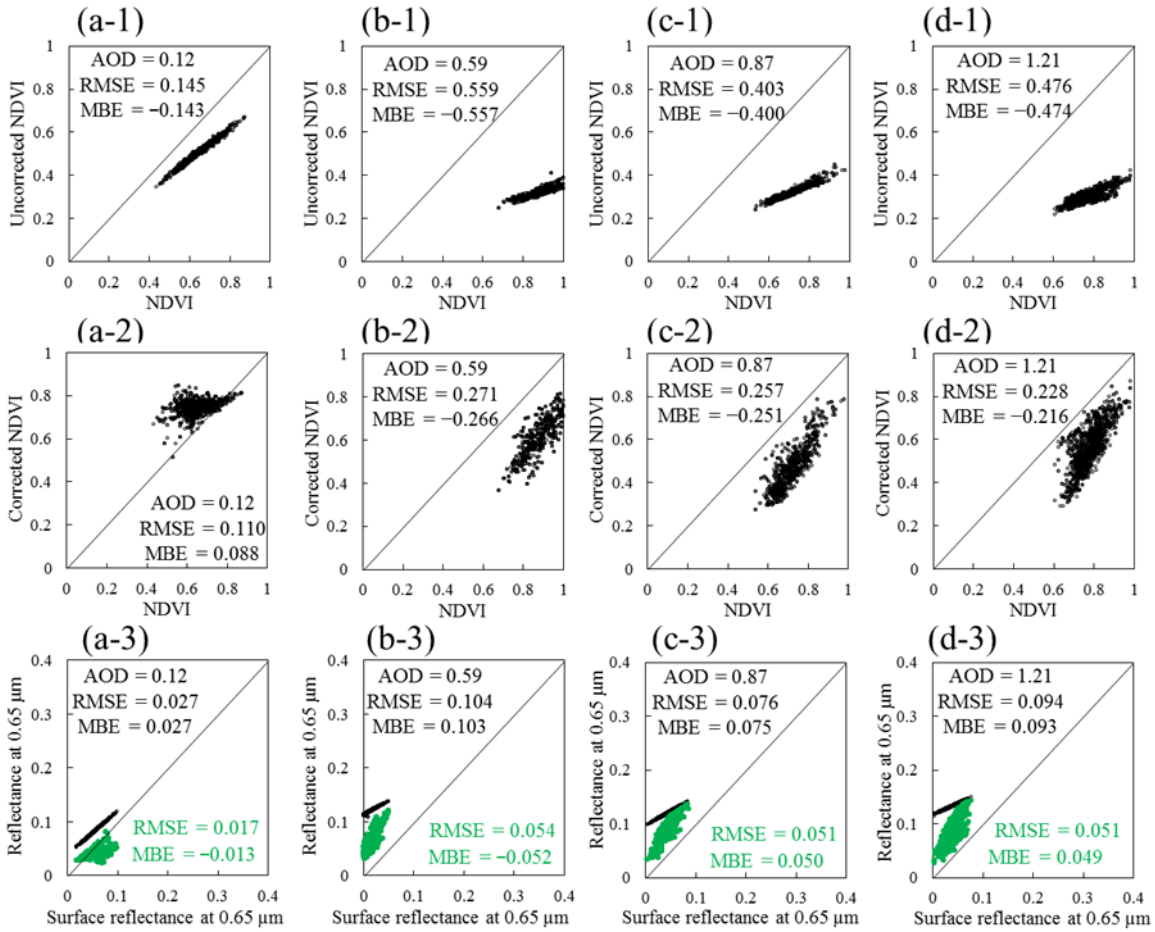

Figure 5.12 Experimental results for the Ubon Ratchathani site. Uncorrected NDVI (**Row 1**) and corrected NDVI (**Row 2**) plotted against the atmospherically corrected NDVI; the TOA reflectance at the red band (black plots) and corrected reflectance at the red band (green plots) against the surface reflectance at the red band (**Row 3**) for different aerosol loading conditions (AOD at 0.55 μm).

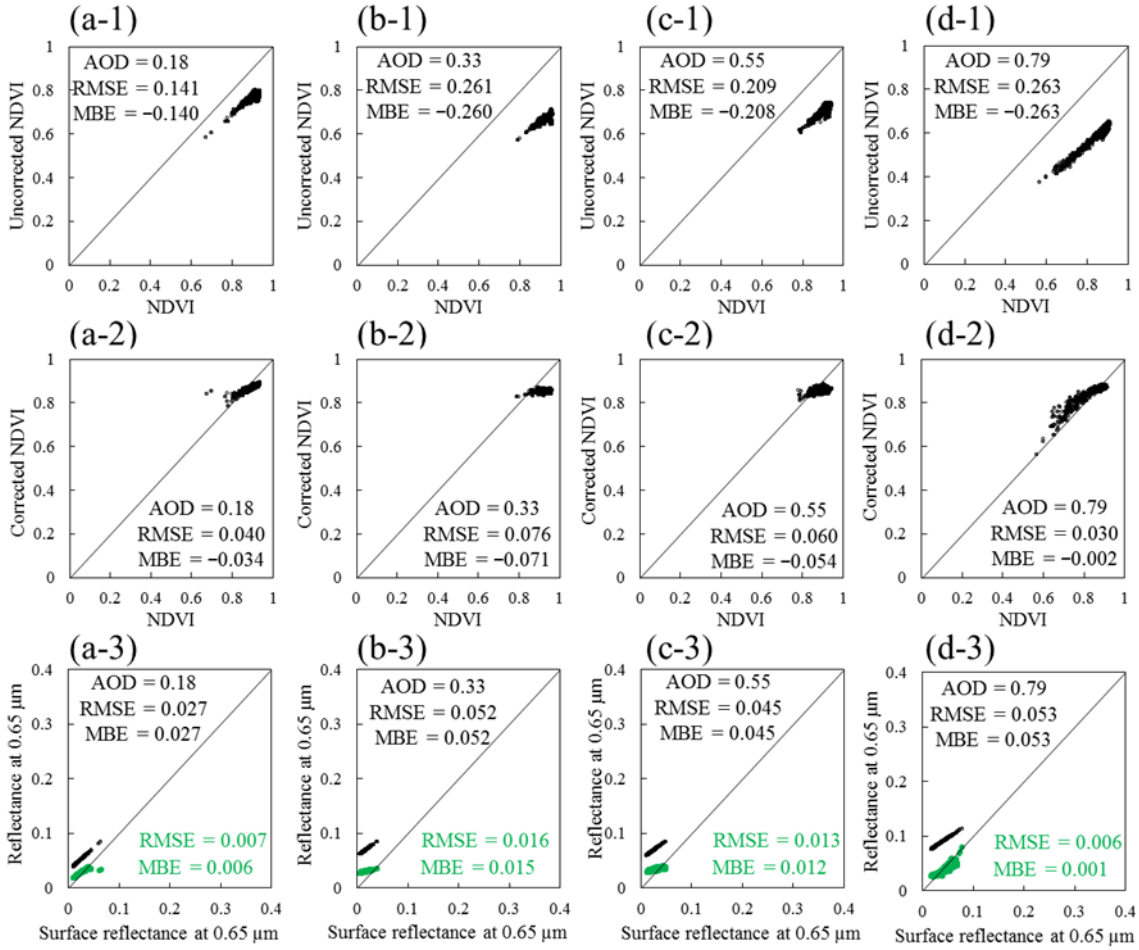

Figure 5.13 Experimental results for the Ussuriysk site. Uncorrected NDVI (**Row 1**) and corrected NDVI (**Row 2**) plotted against the atmospherically corrected NDVI; the TOA reflectance at the red band (black plots) and corrected reflectance at the red band (green plots) against the surface reflectance at the red band (**Row 3**) for different aerosol loading conditions (AOD at 0.55 µm).

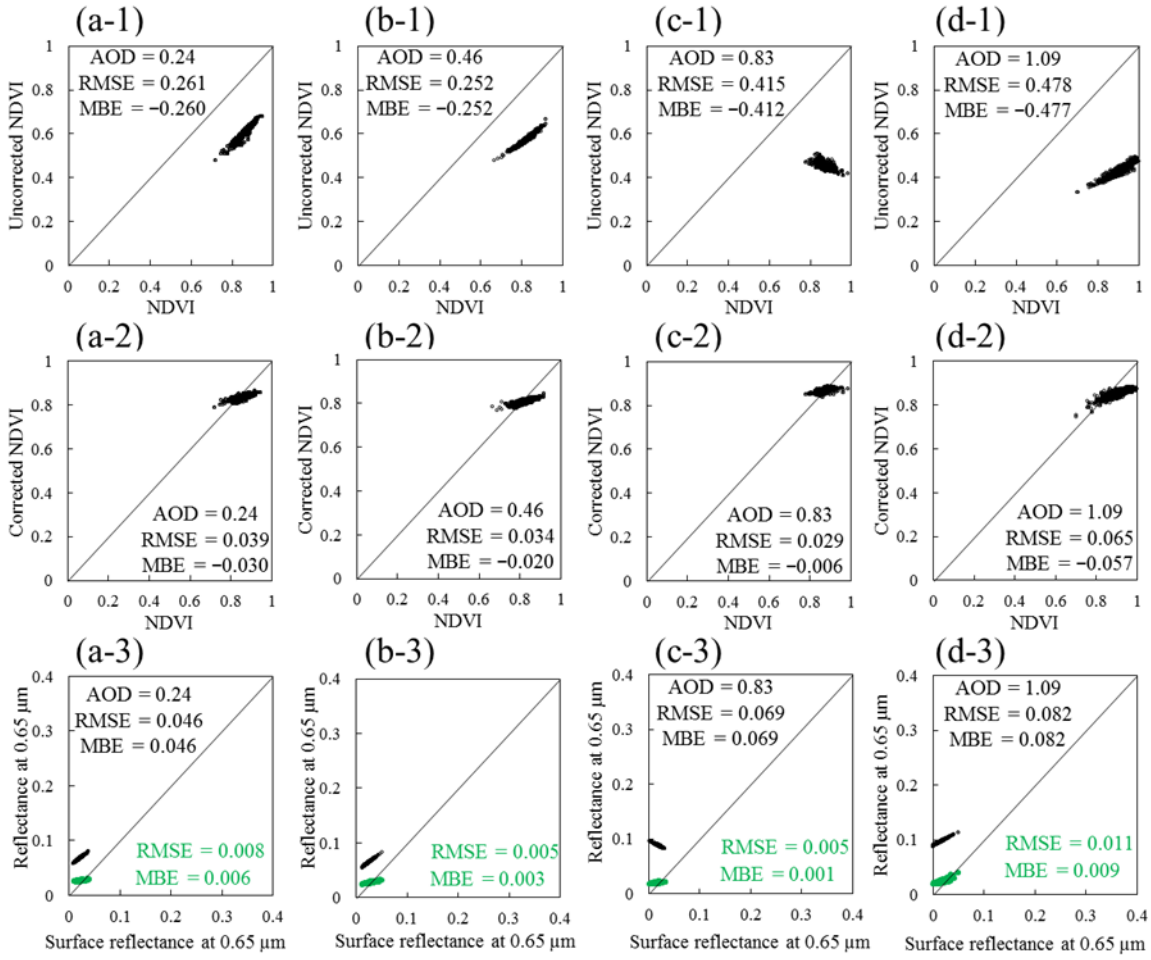

Figure 5.14 Experimental results for the Gandhi_College site. Uncorrected NDVI (**Row 1**) and corrected NDVI (**Row 2**) plotted against the atmospherically corrected NDVI; the TOA reflectance at the red band (black plots) and corrected reflectance at the red band (green plots) against the surface reflectance at the red band (**Row 3**) for different aerosol loading conditions (AOD at 0.55 µm).

Table 5.1 The angle of observation and summarized statistics for the experimental data in Figures 5.9 and 5.12 (DOY is day of year, $NDVI^{U}$ is the uncorrected NDVI, $NDVI^{C}$ is the corrected NDVI, $AFRI_{2.1}^{Est}$ is the estimated $AFRI_{2.1}$, $AFRI_{2.1}^{C1}$ is the corrected $AFRI_{2.1}$-1, $AFRI_{2.1}^{C2}$ is the corrected $AFRI_{2.1}$-2, $R_{0.65}^{TOA}$ and $R_{0.65}^{Corrected}$ are the TOA and surface reflectance at 0.65 μm, and $R_{0.86}^{TOA}$ and $R_{0.86}^{Corrected}$ are the TOA and surface reflectance at 0.86 μm).

Site_Name: Ubon_Ratchathani					
Year/DOY		**2010/047**	**2010/068**	**2010/324**	**2011/055**
AOD		**0.590**	**1.211**	**0.121**	**0.868**
$NDVI^{U}$	RMSE	0.559	0.476	0.145	0.403
	MBE	−0.557	−0.474	−0.143	−0.400
$NDVI^{C}$	RMSE	0.271	0.228	0.110	0.257
	MBE	−0.266	−0.216	0.088	−0.251
$AFRI_{2.1}$	RMSE	0.281	0.240	0.071	0.211
	MBE	−0.279	-0.238	0.054	−0.209
$AFRI_{2.1}^{Est}$	RMSE	0.351	0.309	0.069	0.296
	MBE	−0.349	−0.305	0.049	−0.293
$AFRI_{2.1}^{C1}$	RMSE	0.222	0.166	0.124	0.218
	MBE	−0.217	−0.151	0.106	−0.206
$AFRI_{2.1}^{C2}$	RMSE	0.284	0.232	0.098	0.255
	MBE	−0.281	−0.224	0.079	−0.249
$R_{0.65}^{TOA}$	RMSE	0.104	0.094	0.027	0.076
	MBE	0.103	0.093	0.027	0.075
$R_{0.65}^{Corrected}$	RMSE	0.054	0.051	0.017	0.051
	MBE	0.052	0.049	−0.013	0.050
$R_{0.86}^{TOA}$	RMSE	0.033	0.071	0.010	0.041
	MBE	−0.033	−0.071	−0.009	−0.041
$R_{0.86}^{Corrected}$	RMSE	0.021	0.017	0.027	0.018
	MBE	0.020	−0.006	0.025	−0.012
Viewing Geometry	Solar zenith angle	43.360	34.315	41.122	38.038
	Sensor zenith angle	62.617	43.038	42.903	43.138
	Relative azimuth angle	31.700	25.720	50.030	31.725

Table 5.2 The angle of observation and summarized statistics for the experimental data in Figures 5.10 and 5.13 (DOY is day of year, $NDVI^{U}$ is the uncorrected NDVI, $NDVI^{C}$ is the corrected NDVI, $AFRI_{2.1}^{Est}$ is the estimated $AFRI_{2.1}$, $AFRI_{2.1}^{C1}$ is the corrected $AFRI_{2.1}$-1, $AFRI_{2.1}^{C2}$ is the corrected $AFRI_{2.1}$-2, $R_{0.65}^{TOA}$ and $R_{0.65}^{Corrected}$ are the TOA and surface reflectance at 0.65 μm, and $R_{0.86}^{TOA}$ and $R_{0.86}^{Corrected}$ are the TOA and surface reflectance at 0.86 μm).

Site_Name: Ussuriysk					
Year/DOY		**2008/159**	**2008/178**	**2008/210**	**2009/148**
AOD		**0.328**	**0.554**	**0.183**	**0.792**
$NDVI^{U}$	RMSE	0.261	0.209	0.141	0.263
	MBE	−0.260	−0.208	−0.140	−0.263
$NDVI^{C}$	RMSE	0.076	0.060	0.040	0.030
	MBE	−0.071	−0.054	−0.034	−0.002
$AFRI_{2.1}$	RMSE	0.074	0.063	0.054	0.058
	MBE	−0.072	−0.062	−0.048	−0.056
$AFRI_{2.1}^{Est}$	RMSE	0.079	0.066	0.066	0.043
	MBE	−0.077	−0.063	−0.060	−0.040
$AFRI_{2.1}^{C1}$	RMSE	0.056	0.046	0.063	0.030
	MBE	−0.051	−0.039	−0.053	0.008
$AFRI_{2.1}^{C2}$	RMSE	0.064	0.053	0.064	0.024
	MBE	−0.060	−0.048	−0.056	−0.010
$R_{0.65}^{TOA}$	RMSE	0.052	0.045	0.027	0.053
	MBE	0.052	0.045	0.027	0.053
$R_{0.65}^{Corrected}$	RMSE	0.016	0.013	0.007	0.006
	MBE	0.015	0.012	0.006	0.001
$R_{0.86}^{TOA}$	RMSE	0.037	0.046	0.016	0.056
	MBE	−0.037	−0.046	−0.016	−0.056
$R_{0.86}^{Corrected}$	RMSE	0.009	0.008	0.010	0.010
	MBE	0.007	−0.002	−0.006	0.008
Viewing Geometry	Solar zenith angle	29.136	25.124	29.400	26.085
	Sensor zenith angle	54.640	18.318	18.542	18.188
	Relative azimuth angle	33.361	38.002	41.358	42.940

Table 5.3 The angle of observation and summarized statistics for the experimental data in Figures 5.11 and 5.14 (DOY is day of year, $NDVI^{U}$ is the uncorrected NDVI, $NDVI^{C}$ is the corrected NDVI, $AFRI_{2.1}^{Est}$ is the estimated $AFRI_{2.1}$, $AFRI_{2.1}^{C1}$ is the corrected $AFRI_{2.1}$-1, $AFRI_{2.1}^{C2}$ is the corrected $AFRI_{2.1}$-2, $R_{0.65}^{TOA}$ and $R_{0.65}^{Corrected}$ are the TOA and surface reflectance at 0.65 μm, and $R_{0.86}^{TOA}$ and $R_{0.86}^{Corrected}$ are the TOA and surface reflectance at 0.86 μm).

Site_Name: Gandhi_College					
Year/DOY		**2012/036**	**2012/050**	**2012/056**	**2012/065**
AOD		**0.829**	**0.236**	**0.456**	**1.086**
$NDVI^{U}$	RMSE	0.415	0.261	0.252	0.478
	MBE	−0.412	−0.260	−0.252	−0.477
$NDVI^{C}$	RMSE	0.029	0.039	0.034	0.065
	MBE	−0.006	−0.030	−0.020	−0.057
$AFRI_{2.1}$	RMSE	0.087	0.066	0.064	0.196
	MBE	−0.077	−0.064	−0.063	−0.195
$AFRI_{2.1}^{Est}$	RMSE	0.056	0.027	0.017	0.132
	MBE	−0.042	−0.020	-0.006	−0.131
$AFRI_{2.1}^{C1}$	RMSE	0.033	0.024	0.028	0.073
	MBE	0.000	0.005	0.019	−0.067
$AFRI_{2.1}^{C2}$	RMSE	0.038	0.022	0.020	0.097
	MBE	−0.017	−0.005	0.008	−0.094
$R_{0.65}^{TOA}$	RMSE	0.069	0.046	0.039	0.082
	MBE	0.069	0.046	0.039	0.082
$R_{0.65}^{Corrected}$	RMSE	0.005	0.008	0.005	0.011
	MBE	0.001	0.006	0.003	0.009
$R_{0.86}^{TOA}$	RMSE	0.037	0.021	0.025	0.060
	MBE	−0.037	−0.020	−0.025	−0.060
$R_{0.86}^{Corrected}$	RMSE	0.009	0.012	0.004	0.005
	MBE	0.009	0.012	−0.003	−0.005
Viewing Geometry	Solar zenith angle	45.043	39.647	41.513	39.248
	Sensor zenith angle	40.210	54.772	6.795	19.758
	Relative azimuth angle	124.292	123.934	44.702	41.717

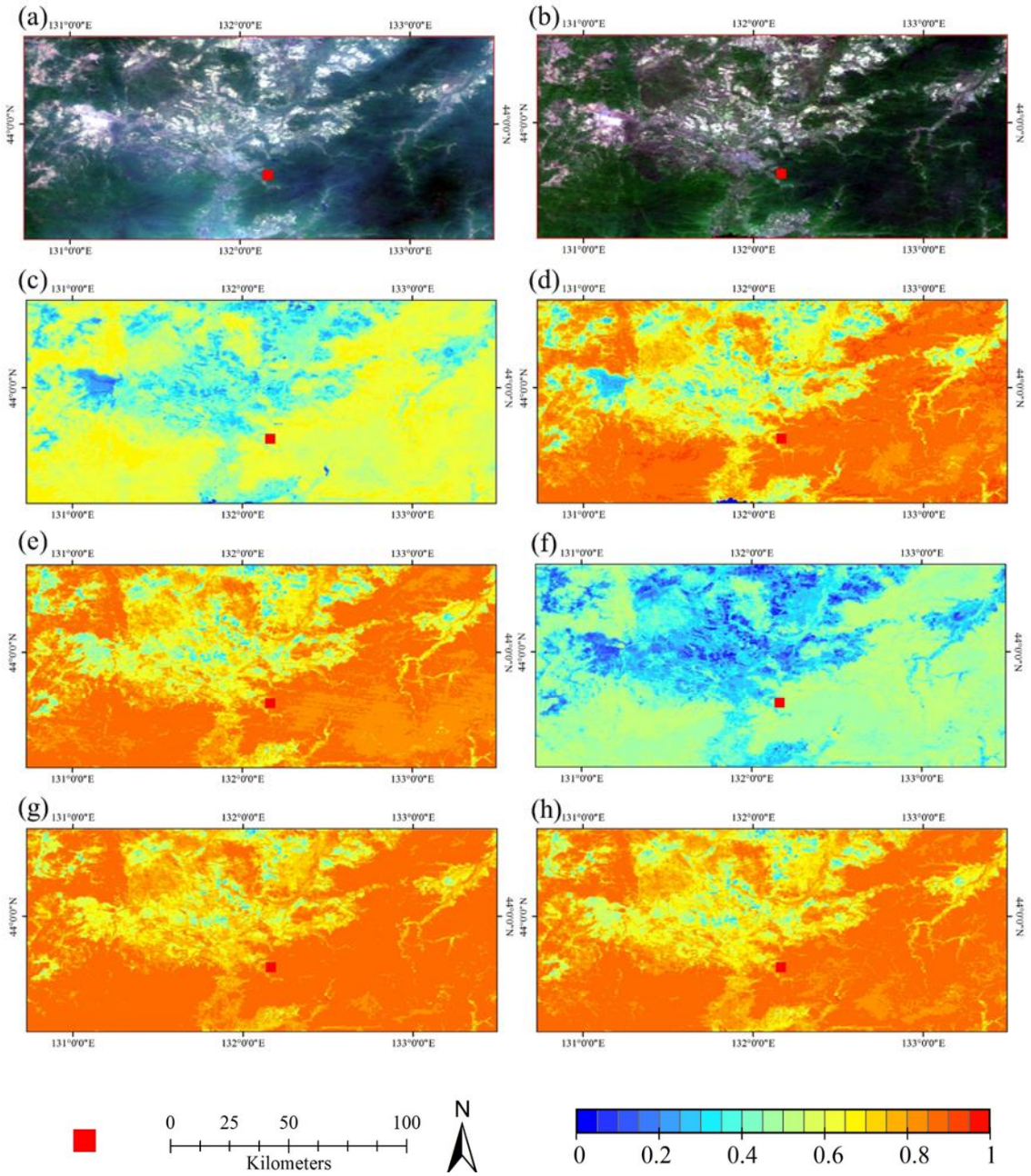

Figure 5.15 MODIS images of the case studies around the Aerosol Robotic Network (AERONET) Ussuriysk site: (**a**) True color composite (RGB = 0.65 µm, 0.56 µm, 0.47 µm) from the TOA reflectance; (**b**) true color composite from the surface reflectance; (**c**) NDVI derived from the TOA reflectance product; (**d**) NDVI derived from the MODIS surface reflectance product; (**e**) NDVI corrected by the proposed method; (**f**) $AFRI_{1.6}$; (**g**) $AFRI_{2.1}^{C1}$; and (**h**) $AFRI_{2.1}^{C2}$. The red point is the location of the AERONET Ussuriysk site, and the corresponding AOD at 0.55 µm is 0.792.

5.3.1.3 Case study

Figures 5.15a and b show two true color composites over the Ussuriysk sites using MODIS TOA reflectance bands, and MODIS surface reflectance bands respectively. The corresponding AERONET measurements is AOD at 0.55 μm with an interpolated value of 0.792. The MODIS TOA reflectance-derived NDVI and MODIS surface reflectance-derived NDVI maps are shown in Figures 5.15c and d. Because of heavy aerosol loading level, there are obviously differences between TOA NDVI and surface NDVI. The statistical results show that the MODIS surface reflectance-derived NDVI map has a mean NDVI value of 0.751, while the TOA NDVI map only has a mean NDVI value of 0.539. Figures 5.15e, g, and h illustrate the corrected NDVI, $AFRI_{2.1}^{C1}$ and $AFRI_{2.1}^{C2}$ maps, they all have much higher similarity with the surface NDVI map than the TOA NDVI. These three maps are closer to the surface NDVI with the mean VI values of 0.770, 0.810 and 0.786 respectively. Figure 5.15f illustrates the $AFRI_{1.6}$ map, which shows an underestimated interpretation for vegetation condition in this case, with lower VIs value even than TOA NDVI. Therefore, for the 1.6-μm sensors, the use of estimated $AFRI_{2.1}$ could perform better than directly using $AFRI_{1.6}$.

5.4 Conclusions

In this study, I proposed an approach to adapt the 2.1-μm based self-corrected method to the 1.6-μm sensors. Using the MODIS surface reflectance product, I analyzed the reflectance relationship between 1.6 μm and 2.1 μm, and found that the relationship varies according to the surface condition.

The vegetation index (NDVI or $AFRI_{2.1}$) can be a very accurate indicator of surface conditions, and the surface reflectance at 2.1 μm has been parameterized as an empirically derived function of the 1.6 μm surface reflectance and vegetation index. I grouped experimental data with given $AFRI_{2.1}$ values, and analyzed the changing characteristics of the regression functions (slope and intercept) obtained for the grouped data set. Our results show that the slopes of the regressions are extremely well correlated with $AFRI_{2.1}$, with an r-value of –0.968, and the relationship between regression intercepts and $AFRI_{2.1}$ is also high, with an r-value of –0.742. This means that the reflectance relationships at 1.6 μm and 2.1 μm are typically dependent on the amount of vegetation.

In terms of experimental results, an $AFRI_{2.1}$-based regression function for estimating reflectance at 2.1 μm from data observed at 1.6 μm was summarized. I tested and compared the performances in estimation with the linear regression function and the $AFRI_{2.1}$-based regression function. This comparison of results indicated that

the $AFRI_{2.1}$-based method has much better performance, and shows higher agreement with the true values.

As the $AFRI_{2.1}$ is calculated using the reflectance of the NIR and 2.1 μm bands, and because TANSO-CAI does not possess the 2.1 μm band, it is very difficult to directly use this $AFRI_{2.1}$-based method in the application of TANSO-CAI. As such, I initially developed a method to estimate $AFRI_{2.1}$ using the NIR and 1.6 μm bands. Then, using the estimated $AFRI_{2.1}$, a reflectance connection between the 1.6 μm and visible bands can be compiled via the estimated reflectance in the 2.1 μm band.

Based on the summarized relationship between the 1.6 and 2.1 μm bands, the 2.1-μm based self-corrected method has been successfully adapted to 1.6-μm based sensors.

The performance of the 1.6-μm based self-corrected method has been tested for different levels of AOD. For all experimental cases, the atmospheric influences in the red and NIR bands have been corrected by our correction method. Particularly with heavy aerosol loading conditions, most of errors caused by atmospheric effects have been reduced.

The corrected red and NIR bands were used in calculation of $AFRI_{2.1}$ and NDVI. Both corrected $AFRI_{2.1}$ and NDVI showed evident improvements in accuracy by comparison with their uncorrected VIs.

References

1. Shabanov, N.; Vargas, M.; Miura, T.; Sei, A.; Danial, A. Evaluation of the performance of Suomi NPP VIIRS top of canopy vegetation indices over AERONET sites. *Remote Sensing of Environment* **2015**, *162*, 29-44.
2. Huete, A.; Didan, K.; van Leeuwen, W.; Miura, T.; Glenn, E. MODIS vegetation indices. In *Land remote sensing and global environmental change*, Springer: 2010; pp 579-602.
3. Miura, T.; Huete, A.R.; Yoshioka, H.; Holben, B.N. An error and sensitivity analysis of atmospheric resistant vegetation indices derived from dark target-based atmospheric correction. *Remote sensing of Environment* **2001**, *78*, 284-298.
4. Kumar, L.; Schmidt, K.; Dury, S.; Skidmore, A. Imaging spectrometry and vegetation science. In *Imaging spectrometry*, Springer: 2002; pp 111-155.
5. Tucker, C.J. Red and photographic infrared linear combinations for monitoring vegetation. *Remote sensing of Environment* **1979**, *8*, 127-150.

6. Bannari, A.; Morin, D.; Bonn, F.; Huete, A. A review of vegetation indices. *Remote sensing reviews* **1995**, *13*, 95-120.
7. Tucker, C.J.; Townshend, J.R.; Goff, T.E. African land-cover classification using satellite data. *Science* **1985**, *227*, 369-375.
8. Tucker, C.J.; Vanpraet, C.L.; Sharman, M.; Van Ittersum, G. Satellite remote sensing of total herbaceous biomass production in the senegalese sahel: 1980-1984. *Remote sensing of environment* **1985**, *17*, 233-249.
9. Justice, C.O.; Townshend, J.; Holben, B.; Tucker, E.C. Analysis of the phenology of global vegetation using meteorological satellite data. International Journal of *Remote Sensing* **1985**, *6*, 1271-1318.
10. Townshend, J.; Justice, C.; Li, W.; Gurney, C.; McManus, J. Global land cover classification by remote sensing: Present capabilities and future possibilities. *Remote Sensing of Environment* **1991**, *35*, 243-255.
11. Sellers, P.; Tucker, C.; Collatz, G.; Los, S.; Justice, C.; Dazlich, D.; Randall, D. A global 1 by 1 NDVI data set for climate studies. Part 2: The generation of global fields of terrestrial biophysical parameters from the NDVI. *International Journal of remote sensing* **1994**, *15*, 3519-3545.
12. Miura, T.; Huete, A.; Leeuwen, W.V.; Didan, K. Vegetation detection through smoke‐filled AVIRIS images: An assessment using modis band passes. *Journal of Geophysical Research: Atmospheres* **1998**, *103*, 32001-32011.
13. Kaufman, Y.J.; Tanre, D. Atmospherically resistant vegetation index (ARVI) for eos-modis. *IEEE transactions on Geoscience and Remote Sensing* **1992**, *30*, 261-270.
14. Huete, A.; Justice, C.; Van Leeuwen, W. MODIS vegetation index (MOD13). *Algorithm theoretical basis document* **1999**, *3*, 213.
15. Karnieli, A.; Kaufman, Y.J.; Remer, L.; Wald, A. AFRI—aerosol free vegetation index. *Remote Sensing of Environment* **2001**, *77*, 10-21.
16. Fraser, R.S.; Kaufman, Y.J. Relative importance of aerosol scattering and absorption in remote sensing. *IEEE transactions on geoscience and remote sensing* **1985**, *23*, 625-633.
17. Kaufman, Y.; Tanré, D.; Remer, L.A.; Vermote, E.; Chu, A.; Holben, B. Operational remote sensing of tropospheric aerosol over land from EOS moderate resolution imaging spectroradiometer. *Journal of Geophysical Research: Atmospheres* **1997**, *102*, 17051-17067.
18. Hou, P.; Jiang, W.; Cao, G.; Li, J. Aerosol retrieval with satellite image and correlation analyses between aerosol distribution and urban underlaying surface. *International journal of remote sensing* **2012**, *33*, 3232-3251.
19. Llewellyn-Jones, D.; Edwards, M.; Mutlow, C.; Birks, A.; Barton, I.; Tait, H. Aatsr: Global-change and surface-temperature measurements from ENVISAT.

ESA bulletin **2001**, *105*, 25.
20. Arnaud, M.; Leroy, M. Spot 4: A new generation of spot satellites. *ISPRS journal of photogrammetry and remote sensing* **1991**, *46*, 205-215.
21. IRS-1C/1D (Indian Remote Sensing Satellites-1C/1D). Available online: https://directory.eoportal.org/web/eoportal/satellite-missions/i/irs-1c-1d (accessed on 3 May 2017).
22. GOSAT Instruments and Observational Methods. Available online: http://www.gosat.nies.go.jp/eng/gosat/page2.htm (accessed on 3 May 2017).
23. Vermote, E.F.; Kotchenova, R.; Ray, J. MODIS surface reflectance user's guide. Version 1.3. MODIS land surface reflectance science computing facility. *URL: http: modis-sr.ltdri.org/products/MOD09_UserGuide_v1_3. pdf* **2011**.
24. MODIS LAND SURFACE REFLECTANCE SCIENCE COMPUTING FACILITY homepage. Available online: https://modis-sr.ltdri.org/index.html (accessed on 25 December 2016).
25. Wang, S.; Yang, M.; Li, J.; Shen, Q.; Zhang, F. *MODIS surface reflectance product (MOD09) validation for typical inland waters in China*, SPIE Asia-Pacific Remote Sensing, 2014; International Society for Optics and Photonics: pp 92610F-92610F-92610.
26. Fan, L.; Berger, F.H.; Liu, H.; Bernhofer, C. Validating MODIS land surface reflectance products using ground-measured reflectance spectra - a case study in semi-arid grassland in Inner Mongolia, China. *International Journal of Remote Sensing* **2014**, *35*, 1715-1728.
27. Vermote, E.F.; Kotchenova, S. MODIS Meetings - MODIS Land Collection 5 Workshop Presentations. URL: https://modis.gsfc.nasa.gov/sci_team/meetings/c5meeting/pres/day1/vermote.pdf **2007**.
28. Holben, B.N.; Eck, T.; Slutsker, I.; Tanre, D.; Buis, J.; Setzer, A.; Vermote, E.; Reagan, J.; Kaufman, Y.; Nakajima, T. AERONET—A Federated Instrument Network and Data Archive for Aerosol Characterization. *Remote sensing of environment* **1998**, *66*, 1-16.
29. Choudhry, P.; Misra, A.; Tripathi, S. Study of MODIS derived AOD at three different locations in the Indo Gangetic Plain: Kanpur, Gandhi College and Nainital. *Annales Geophysicae* 2012, 1479-1493.
30. Slutsker, I.; Kinne, S. Wavelength dependence of the optical depth of biomass burning, urban, and desert dust aerosols. *Journal of Geophysical Research: Atmospheres* 1999, *104*.
31. Ångström, A. The parameters of atmospheric turbidity. *Tellus* **1964**, *16*, 64-75.
32. Vermote, E.; El Saleous, N.; Justice, C.; Kaufman, Y.; Privette, J.; Remer, L.;

Roger, J.; Tanre, D. Atmospheric correction of visible to middle‐infrared EOS‐MODIS data over land surfaces: Background, operational algorithm and validation. *Journal of Geophysical Research: Atmospheres* **1997**, *102*, 17131-17141.

33. MODIS LAND SURFACE REFLECTANCE SCIENCE COMPUTING FACILITY, Validation. Available online: http://modis-sr.ltdri.org/pages/validation.html (accessed on 21 December 2016).
34. Levy, R.C.; Remer, L.A.; Mattoo, S.; Vermote, E.F.; Kaufman, Y.J. Second‐generation operational algorithm: Retrieval of aerosol properties over land from inversion of Moderate Resolution Imaging Spectroradiometer spectral reflectance. *Journal of Geophysical Research: Atmospheres* **2007**, *112*.
35. Holzer-Popp, T.; Schroedter-Homscheidt, M.; Breitkreuz, H.; Martynenko, D.; Klüser, L. Improvements of synergetic aerosol retrieval for ENVISAT. *Atmospheric Chemistry & Physics* **2008**, *8*, 7651-7672.
36. Zhong, G.; Wang, X.; Tani, H.; Guo, M.; Chittenden, A.; Yin, S.; Sun, Z.; Matsumura, S. A modified aerosol free vegetation index algorithm for aerosol optical depth retrieval using GOSAT TANSO-CAI data. *Remote Sens-Basel* **2016**, *8*, 998.
37. Rouse Jr, J. Monitoring the vernal advancement and retrogradation (green wave effect) of natural vegetation. **1974**.
38. Sun, L.; Wei, J.; Bilal, M.; Tian, X.; Jia, C.; Guo, Y.; Mi, X. Aerosol Optical Depth Retrieval over Bright Areas Using Landsat 8 OLI Images. *Remote Sens-Basel* **2015**, *8*, 23.
39. Dark Target (MODIS Aerosol Retrieval Algorithm), Land Surface Reflectance. Available online: https://darktarget.gsfc.nasa.gov/algorithm/land/surface-reflectance (accessed on 25 December 2016).
40. Liu, G.-R.; Liang, C.-K.; Kuo, T.-H.; Lin, T.-H.; Huang, S. Comparison of the NDVI, ARVI and AFRI vegetation index, along with their relations with the AOD using SPOT 4 vegetation data. *Terrestrial Atmospheric and Oceanic Sciences* **2004**, *15*, 15-32.
41. Ben‐Ze'ev, E.; Karnieli, A.; Agam, N.; Kaufman, Y.; Holben, B. Assessing vegetation condition in the presence of biomass burning smoke by applying the Aerosol‐Free Vegetation Index (AFRI) on MODIS images. *International Journal of Remote Sensing* **2006**, *27*, 3203-3221.

Chapter 6 A dark target algorithm for the GOSAT TANSO-CAI sensor in aerosol optical depth retrieval over land

6.1 Introduction

Atmospheric aerosols are solid particles or liquid droplets suspended in the atmosphere with diameters ranging from 10^{-3} to 10^{2} micrometers [1]. Aerosol is a major component of the atmosphere and plays an important role in global environmental and climate change [2]. Aerosols can absorb or scatter the incoming solar radiation and affect the Earth's radiation budget, thus modulating the warming or cooling of the Earth [2,3]. Ground-level aerosols, also known as particulate matter (PM), are associated with human health and as such are regulated as a priority air quality pollutant [4,5]. Aerosol monitoring contributes significantly to the understanding of the Earth's environmental systems.

Satellites are increasingly being used to monitor the spatial and temporal distribution of aerosols from the local to a global scale, and to study their physical and chemical properties [6]. Spectral aerosol optical depth (AOD) is the most frequently used aerosol optical property. The main challenge of aerosol retrieval over land is to remove the surface contributions from the integrated reflectance signal at the satellite level [7–9].

The mature and well-defined Moderate Resolution Imaging Spectroradiometer (MODIS) Dark Target (DT) algorithm is used to retrieve aerosol properties over the land and ocean twice a day with near-global coverage [10]. In theory, the MODIS DT algorithm can be applied to any sensor that measures reflectance in wavelength bands that cover visible (e.g., red or blue bands) and shortwave infrared (SWIR, 2.1 μm band) [13]. The DT group has already adapted the MODIS DT algorithm to run operationally on the Visible Infrared Imaging Radiometer Suite (VIIRS) instrument aboard the Suomi-NPP polar orbiting satellite so as to create a long-term global AOD record [12,14]. However, it is worth noting that the operational MODIS DT algorithm is based on SWIR-visible surface relationships, with 2.1 μm being the key band for estimating surface reflectance. As such, adapting the MODIS DT algorithm to the sensors that do not have SWIR bands close the 2.1 μm band is difficult.

The Thermal and Near-Infrared Sensor for Carbon Observation Cloud and Aerosol Imager (TANSO-CAI) is one of the observation instruments onboard the

Greenhouse gases Observing SATellite (GOSAT). The GOSAT was designed to measure the total columns of carbon dioxide and methane, which are observed by the Fourier Transform Spectrometer (TANSO-FTS) [15,16]. The TANSO-CAI visualizes atmospheric and ground surface conditions during the daytime. One of its missions is to detect clouds and aerosols in the FTS's field of view to correct the obtained spectra with FTS [16]. However, because TANSO-CAI is a single-view sensor without any polarization information or SWIR bands near 2.1 μm, most of the conventional aerosol retrieval algorithms are not applicable [17]. For the time being, TANSO-CAI cannot provide any definitive aerosol data, so the aerosol-related information necessary for correcting TANSO-FTS data is derived from other platforms [18]. Although the challenges involved in developing an algorithm for retrieving AOD from GOSAT TANSO-CAI are considerable, such an algorithm is considered essential if precise aerosol information from the TANSO-CAI is ever to be obtained. It has the potential to reduce aerosol-related errors and improve the accuracy of TANSO-FTS data, and will also expand the scope of future aerosol-related research [19].

In this study, I aimed to adapt a MODIS-like DT algorithm to the GOSAT TANSO-CAI, which has only one 1.6 μm SWIR band. Due to the lack of a SWIR band near 2.1 μm, determining the surface reflectance in the visible band is comparatively difficult [20]. To resolve the difficulty in determining the surface reflectance I explored the reflectance relationship between the 1.6 μm and 2.1 μm bands (1.6 vs. 2.1), and attempted to develop an operational algorithm for aerosol retrieval.

6.2 Theoretical basis of AOD retrieval

Assuming that the land surface is Lambertian surface and that the atmospheric and aerosol loading are horizontally uniform, the relationship between top-of-atmosphere (TOA) reflectance (R_{TOA}), atmospheric contribution (R_{Atm}), and surface reflectance R_{Surf} can be described by Equation 1.

$$R_{TOA}(\lambda, \mu_0, \mu, \varphi) = R_{Atm}(\lambda, \mu_0, \mu, \varphi) + \frac{R_{Surf}(\lambda) T_d(\lambda, \mu_0) T_u(\lambda, \mu)}{1 - R_{Surf}(\lambda) S(\lambda)} \quad (1)$$

where λ is a given wavelength; μ_0, μ, and φ are the cosine of the solar zenith angle, the cosine of the satellite zenith angle, and the relative azimuth angle between the sun and the satellite, respectively; S is the atmospheric hemispherical albedo; T_d is the atmospheric transmittance from TOA to the surface; and T_u is the atmospheric transmission from the Earth's surface to a satellite receiver [8,21]. The terms of R_{Atm}, T_dT_u, and S are important atmospheric parameters that are functions of the AOD (τ) and can be extracted using the radiative transfer model. Therefore, as Equation 1 shows,

if the surface reflectance can be determined, then the AOD can be retrieved. Aerosol retrieval algorithms have been developed for many different satellite platforms based on this principle [22].

Kaufman et al. [8,23] summarized the linear relationship between surface reflectance in the blue (0.47 μm) and red (0.65 μm) bands, and reflectance in the 2.1 μm band. The 2.1 μm band can penetrate most aerosols. Therefore, the surface reflectance in the blue (0.47 μm) and red (0.65 μm) bands can be determined using the 2.1 μm band. This method was used to create the MODIS aerosol product of Collection 4. Additional information that allows better estimation of the surface reflectance has recently been introduced into the MODIS DT algorithm. After several studies suggested that the surface reflectance relationships in the visible and 2.1 μm bands were angle dependent [24–26], Levy et al. [11] found that different surface types display different ratios between the surface reflectance of the visible and 2.1 μm bands (the complete regression including slope and y-intercept). To reduce errors in the existing method, Levy et al. proposed a second-generation operational algorithm for MODIS data (Collection 5), which took the dependencies of angular variability and surface type into account, as in Equations 2:

$$\begin{cases} \mathrm{R}_{0.65} = \mathrm{R}_{2.1} * \mathrm{slope}_{0.65/2.1} + \mathrm{yint}_{0.65/2.1} \\ \mathrm{R}_{0.47} = \mathrm{R}_{0.65} * \mathrm{slope}_{0.47/0.65} + \mathrm{yint}_{0.47/0.65} \end{cases}$$

where

$$\begin{cases} \mathrm{slope}_{0.65/2.1} = \mathrm{slope}_{0.65/2.1}^{\mathrm{NDVI_{SWIR}}} + 0.002 * \Theta - 0.27 \\ \mathrm{yint}_{0.65/2.1} = -0.00025 * \Theta + 0.033 \end{cases}$$

$$\begin{cases} \mathrm{slope}_{0.47/0.65} = 0.49 \\ \mathrm{yint}_{0.47/0.65} = 0.005 \end{cases}$$

where in turn

$$\begin{cases} \mathrm{slope}_{0.65/2.1}^{\mathrm{NDVI_{SWIR}}} = 0.48;\ \mathrm{NDVI_{SWIR}} < 0.25, \\ \mathrm{slope}_{0.65/2.1}^{\mathrm{NDVI_{SWIR}}} = 0.58;\ \mathrm{NDVI_{SWIR}} > 0.75, \\ \mathrm{slope}_{0.65/2.1}^{\mathrm{NDVI_{SWIR}}} = 0.48 + 0.2 * (\mathrm{NDVI_{SWIR}} - 0.25); \\ \qquad 0.25 \le \mathrm{NDVI_{SWIR}} \le 0.75 \end{cases} \tag{2}$$

where $\mathrm{slope}_{0.65/2.1}$ and $\mathrm{yint}_{0.65/2.1}$ are the slope and the intercept for the relationship of surface reflectance in the 0.65 μm and 2.1 μm channels, and $\mathrm{slope}_{0.47/0.65}$ and $\mathrm{yint}_{0.47/0.65}$ are the slope and intercept for the relationship between surface reflectance in 0.47 μm and 0.65 μm channels. Θ is the scattering angle,

defined as Equation 3. $NDVI_{SWIR}$ is an aerosol resistant measure of vegetation "greenness", defined in Equation 4.

$$\Theta = \cos^{-1}(-\cos\theta_0 \cos\theta + \sin\theta_0 \sin\theta \cos\emptyset) \quad (3)$$

where θ_0, θ, and ϕ are the solar zenith angle, satellite zenith angle, and the relative azimuth angle between the sun and the satellite, respectively.

$$NDVI_{SWIR} = (R_{1.2} - R_{2.1})/(R_{1.2} + R_{2.1}) \quad (4)$$

where $R_{1.2}$ is the MODIS-measured reflectance at 1.2 μm. Surface reflectance estimations in both MODIS retrieval algorithm Collection 5 and the currently operational Collection 6 are based on this method.

Due to the lack of any 2.1 μm band on board GOSAT TANSO-CAI, the MODIS and TANSO-CAI all measure reflectance at 1.6 μm. Note that 1.6 μm and 2.1 μm belong to longer wavelengths that are much less affected by aerosols; thus, if there was a reliable relationship between the reflectance of the 1.6 μm and the 2.1 μm channels, then the potential exists to develop a MODIS-like DT algorithm that uses the 1.6 μm band to estimate visible surface reflectance.

6.3 Materials and methods

6.3.1 Satellite data and ground-level data

In this study, TANSO-CAI data from GOSAT, surface reflectance product and aerosol product data from MODIS, and ground-level AOD data from the Aerosol Robotic Network (AERONET) were used.

6.3.1.1 GOSAT TANSO-CAI Data

The GOSAT satellite is the world's first spacecraft to measure greenhouse gases. A joint project of the Japan Aerospace Exploration Agency (JAXA), the Ministry of the Environment of Japan (MOE), and the National Institute for Environmental Studies (NIES) of Japan, it was successfully launched on 23 January, 2009. TANSO-CAI is aboard GOSAT, conducting daytime observations of the atmosphere and ground surfaces in four spectral bands: 1 (0.370–0.390 μm), 2 (0.664–0.684 μm), 3 (0.860–0.880 μm), and 4 (1.560–1.650 μm). The spatial resolution at nadir is 500 m for bands 1–3, and 1500 m for band 4. GOSAT revisits the same point in space every 3 days [17].

GOSAT provides three processing-level products derived from TANSO-CAI observations: radiances, cloud flag, global radiance and reflectance distribution, as

well as Normalized Difference Vegetation Index (NDVI) products [16]. In our study, AOD retrieval uses CAI L1B+ radiance products, on which radiometric and geometric corrections (orthorectification, band-to-band registration, and resampling) are performed [27,28]. Before AOD retrieval, the radiance has to be converted to reflectance using Equation 5:

$$R_{TOA} = (\pi * L_\lambda * d^2)/(E_\lambda * \cos\theta_0) \quad (5)$$

where L is the radiation brightness of the corresponding TANSO-CAI band, d is the distance between the sun and the Earth, and E is the solar irradiance with weighting response function of the corresponding TANSO-CAI band. In addition, the CAI L1B+ radiance product provides detailed observational information (such as the solar zenith/azimuth angles and satellite zenith/azimuth angles) [29].

6.3.1.2 AERONET AOD data

The AERONET [30] AOD level 2.0 (cloud screened and quality-assured) data were used in this study to validate AOD retrieval from the satellite.

6.3.2 Estimation of aerosol free vegetation index ($AFRI_{2.1}$) using NIR and 1.6 μm bands

In Chapter 5, I analyzed the relationship between reflectance at 1.6 μm and at 2.1 μm using the MODIS surface reflectance product, and proposed a method to estimate Aerosol FRee vegetation Index ($AFRI_{2.1}$) and 2.1-μm reflectance from 1.6 μm band using Equations 6.

$$AFRI_{2.1}^{Est} = \frac{-(R_{0.8}+0.5*(a_1+b_1)*R_{1.6}+0.5*(a_2+b_2))}{2*0.5*(a_1*R_{1.6}+a_2)} \pm \frac{\sqrt{(R_{0.8}+0.5*(a_1+b_1)*R_{1.6}+0.5*(a_2+b_2))^2-4*0.5*(a_1*R_{1.6}+a_2)*(0.5*b_1*R_{1.6}+0.5*b_2-R_{0.8})}}{2*0.5*(a_1*R_{1.6}+a_2)} \quad (6a)$$

$$R_{2.1}^{Est} = (a_1 * AFRI_{2.1}^{Est} + b_1) * R_{1.6} + a_2 * AFRI_{2.1}^{Est} + b_2 \quad (6b)$$

where the $R_{0.8}$ and $R_{1.6}$ are the reflectances at MODIS 0.8 μm and 1.6 μm bands, and the $AFRI_{2.1}^{Est}$ and $R_{2.1}^{Est}$ are the estimated $AFRI_{2.1}$ and 2.1-μm reflectance. The coefficients values ($a_1 = -0.7606$, $b_1 = 0.9763$, $a_2 = -0.0332$, and $b_2 = 0.0286$) were are determined according to experiment results.

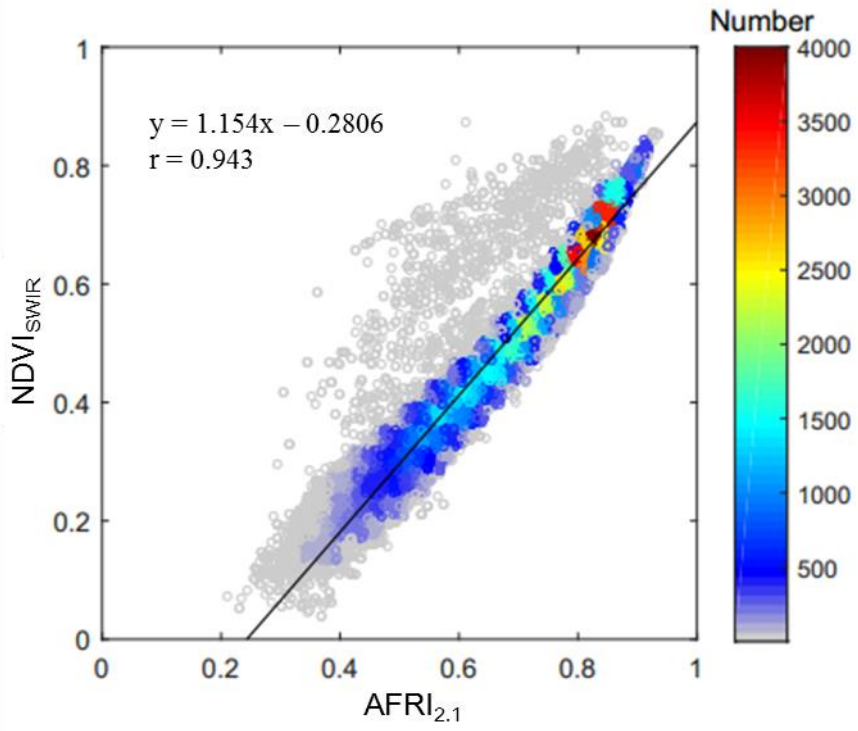

Figure 6.1 The relationship between shortwave infrared bands-derived vegetation index ($NDVI_{SWIR}$) and Aerosol FRee vegetation Index ($AFRI_{2.1}$). Both $NDVI_{SWIR}$ and $AFRI_{2.1}$ are calculated using Moderate Resolution Imaging Spectroradiometer (MODIS) surface reflectance products. The color bars show the number for each point.

An $AFRI_{2.1}$-based regression function used to describe the reflectance relationship of 1.6 vs. 2.1 was established through experimentation with MODIS surface reflectance products. Following the method used in the MODIS DT algorithm, the surface reflectance for the 0.6 μm band can be obtained from the 1.6 μm band by using the estimated reflectance at 2.1 μm. In the operational MODIS DT algorithms version of Collection 5 and the current Collection 6, the reflectance relationship of the 0.6 μm and 2.1 μm bands is adjusted according to geometry and vegetation amount. The geometry is based on the scattering angle (Equation 3), and the vegetation amount is estimated by $NDVI_{SWIR}$ (Equation 4), a variant of NDVI based on the SWIR bands [31]. When developing a MODIS-like AOD retrieval algorithm for TANSO-CAI, the scattering angle can be easily determined using observational information such as the solar zenith/azimuth angle and the satellite zenith/azimuth angle. $AFRI_{2.1}$ can also accurately predict the vegetation amount. The relationship between $NDVI_{SWIR}$ and $AFRI_{2.1}$ was calculated using experimental MODIS surface products, and is presented in Figure 6.1. It is evident that $AFRI_{2.1}$ correlates highly with $NDVI_{SWIR}$ ($r = 0.943$). According to this relationship, $AFRI_{2.1}$ can be considered an appropriate replacement for $NDVI_{SWIR}$ and suitable for practical use in the surface reflectance estimation

method. Based on the previous analysis, a 1.6 μm band based method that follows the MODIS DT algorithm (Equations 2) for estimating surface reflectance at 0.6 μm can be described as follows:

$$R_{0.6} = R_{2.1}^{Est} * slope_{0.6/2.1} + yint_{0.6/2.1}$$

where

$$\begin{cases} slope_{0.6/2.1} = slope_{0.6/2.1}^{AFRI_{2.1}} + 0.002 * \Theta - 0.27 \\ yint_{0.6/2.1} = -0.00025 * \Theta + 0.033 \end{cases}$$

where in turn

$$\begin{cases} slope_{0.6/2.1}^{AFRI_{2.1}} = 0.48;\ AFRI_{2.1} < 0.46, \\ slope_{0.6/2.1}^{AFRI_{2.1}} = 0.58;\ AFRI_{2.1} > 0.89, \\ slope_{0.6/2.1}^{AFRI_{2.1}} = 0.48 + 0.2 * (1.154 * AFRI_{2.1} - 0.281 - 0.25); \\ \qquad 0.46 \le AFRI_{2.1} \le 0.89 \end{cases} \quad (7)$$

where the $AFRI_{2.1}$ and the estimated reflectance at 2.1 μm, $R_{2.1}^{Est}$ can all be determined using the 1.6 μm band, according to the method described in Chapter 5.

Table 6.1 Parameters of the corresponding Greenhouse gases Observing SATellite Thermal and Near-Infrared Sensor for Carbon Observation Cloud and Aerosol Imager (GOSAT TANSO-CAI) and MODIS bands used in this study.

GOSAT TANSO-CAI				**MODIS**			
Band number	**Central wavelength (μm)**	**Bandwidth (μm)**	**Spatial resolution (m)**	**Band number**	**Central wavelength (μm)**	**Bandwidth (μm)**	**Spatial resolution (m)**
2	0.674	0.664−0.684	500	**1**	0.645	0.620−0.670	250
3	0.870	0.860−0.880	500	**2**	0.859	0.841−0.876	250
4	1.600	1.560−1.650	1500	**6**	1.640	1.628−1.652	500
				7	2.130	2.105−2.155	500

Table 6.1 summarizes the specifications of the MODIS and GOSAT TANSO-CAI bands associated with this study. Although both GOSAT TANSO-CAI and MODIS have bands near the 0.6 μm, 0.8 μm, and 1.6 μm wavelengths, differences exist in their center wavelengths and bandwidths, as well as in their spectral response functions. When applying Equations 7 to GOSAT TANSO-CAI data, the differences between the two platforms should first be determined and then corrected. Moreover, because the proposed method was developed based on MODIS experimental data, it should be noted that in actual application the surface reflectance of 0.6 μm would be estimated from the TOA reflectances of the 0.8 μm and 1.6 μm bands. In order to adapt the method (shown as Equations 7) that was developed based on the MODIS data to TANSO-CAI, I compared the uncorrected surface reflectance generated by directly applying Equations 7 to the TANSO-CAI data against the theoretical surface reflectance. An empirical function for correcting platform differences was summarized as:

$$\mathrm{R}_{0.67}^{\mathrm{Corrected}} = 1.2 * \mathrm{R}_{0.67}^{\mathrm{Uncorrected}} + 0.015 \quad (8)$$

where $\mathrm{R}_{0.67}^{\mathrm{Corrected}}$ is the corrected surface reflectance in the TANSO-CAI 0.67 μm band, and $R_{0.67}^{Uncorrected}$ is the uncorrected surface reflectance. Here, the theoretical surface reflectance is derived by the atmospheric correction with help from a Second Simulation of a Satellite Signal in the Solar Spectrum (6S) radiative transfer code [32], and the spatially and temporally matched AERONET data. Atmospheric correction is an important step to negate the atmospheric effects and derive surface reflectance values from satellite-observed data [11,33]. The 6S code is a physically based model and offers the atmospheric correction working modality to compute the surface reflectance [34]. For atmospheric correction, I selected spatially and temporally matched TANSO-CAI/AERONET collocated data according to the following criteria: AERONET sites measured within 30 min of the GOSAT overpasses; the selected TANSO-CAI data were located within a 25 kilometer radius around the AERONET sites. In addition, to ensure the accuracy of atmospheric correction and to avoid influence from multiple aerosol scattering, the selected collocated data for atmospheric correction should have a low AOD value ($\tau_{0.55} < 0.1$).

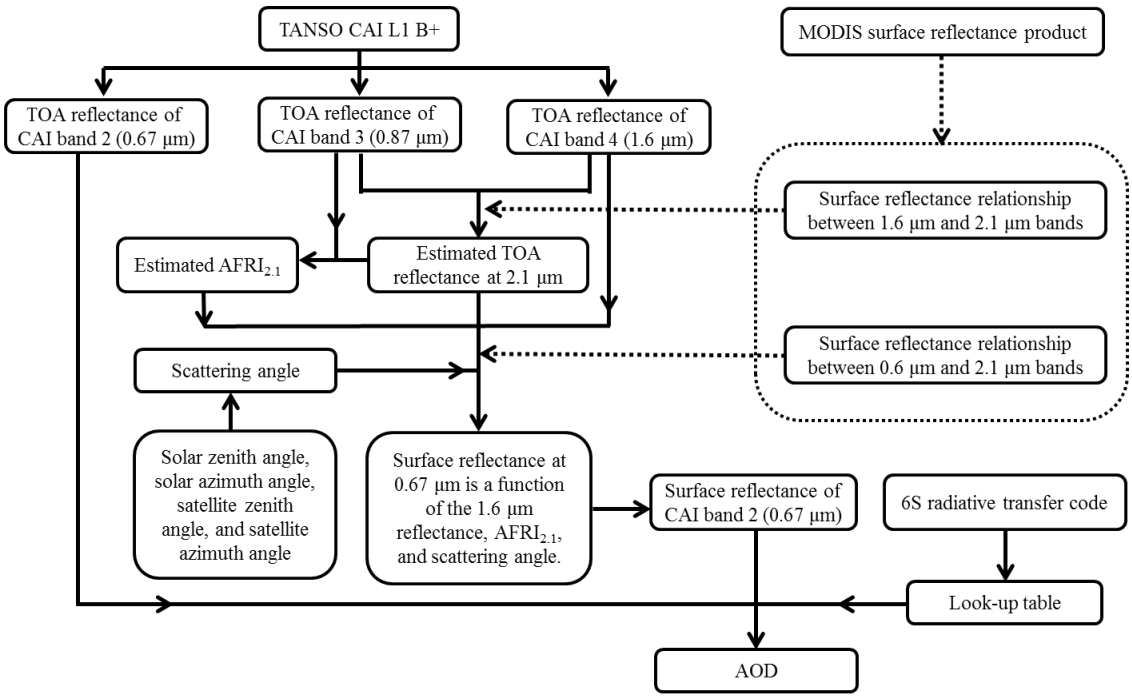

Figure 6.2 Flow chart of the GOSAT TANSO-CAI retrieval procedure. Dashed lines indicate the analysis of the relationship between associated bands using MODIS surface reflectance products.

6.3.3 AOD retrieval

The flowchart for GOSAT TANSO-CAI AOD retrieval is illustrated in Figure 6.2. The surface contributions can be determined using the methods mentioned previously. We can derive the AOD by solving the Equation 1 using the following atmospheric parameters (R_{Path}, T_dT_u, and S). As solving the equation is a time-consuming process, a look-up table method based on a large range of pre-computed atmospheric parameters using corresponding pre-set geometrical conditions (θ_0, θ, and ϕ) and AOD values was prepared to improve the efficiency of the AOD retrieval procedure. The atmospheric parameters (R_{Path}, T_dT_u, and S) can be pre-computed by repeatedly running the 6S radiative transfer code with different parameter combination inputs. The 6S radiative transfer code requires the following parameters as the input: spectral conditions, geometrical conditions, atmospheric model, aerosol model type, and AOD values. In the look-up table, the input parameters of the 6S radiative transfer code for pre-computing the atmospheric parameters (R_{Path}, T_dT_u, and S) are shown in Table 6.2. For the GOSAT TANSO-CAI band 2, 21 solar zenith angles, 6 satellite zenith angles, and 9 relative azimuth angles were pre-set to describe different geometrical conditions. Three different atmospheric models (Tropical, Midlatitude Summer, and Midlatitude Winter) were taken into account. The continental aerosol model, a broadly used assumption for over land retrieval, was selected as the aerosol model. AOD values

were set from 0.01 to 2.00, with intervals of 0.01, and the smallest value was set as 0.001.

Table 6.2 The input parameters of the Second Simulation of a Satellite Signal in the Solar Spectrum radiation transfer code for a pre-computing look-up table.

Parameters	Values
Spectral band	GOSAT TANSO-CAI band 2 (central wavelength at 0.67 μm)
Solar zenith angle	From 0° to 60°, with a step of 3°
Satellite zenith angle	From 0° to 60°, with a step of 12°
Relative azimuth angle	From 0° to 168°, with a step of 24°; and 180°
Atmospheric model	Midlatitude Summer, Midlatitude Winter and Tropical
Aerosol models	Continental aerosol model
AOD at 0.55 μm	Smallest with a value of 0.001, and from 0.01 to 2.00, with a step of 0.01

Table 6.3 Description of the set of different geometrical conditions used to simulate the relationship between TANSO-CAI TOA reflectance and aerosol optical depth (AOD) with different surface conditions.

Case name	Solar zenith (degree)	Satellite zenith (degree)	Relative azimuth (degree)
a	30	0	0
b	30	30	0
c	30	30	180
d	30	60	0
e	30	60	180
f	60	0	0
g	60	30	0
h	60	30	180
i	60	60	0
j	60	60	180

When using this look-up table to retrieve AOD for satellite data, the pre-set solar zenith angle, satellite zenith angle and relative azimuth angle combination closest to the actual satellite observation would be sought. Under the targeted geometrical condition, there are multiple corresponding sets of atmospheric parameters (R_{Path}, T_dT_u, and S) that have been pre-computed and recorded according to the different pre-set AOD values. Substituting every set of atmospheric parameters (R_{Path}, T_dT_u, and S) and the estimated surface reflectance into Equation 1 in sequence, allows the theoretical TOA reflectance for each sequence to be calculated. In the calculated multiple theoretical TOA reflectance, the value that is closest to the actual TOA reflectance would be selected, and the AOD value of this selected set considered as the retrieved AOD.

In the actual retrieval, however, not all the pixels meet the requirements of the retrieval algorithm; to ensure retrieval accuracy only the well-suited pixels should be taken into account during the retrieval. For example, it is possible to derive the AOD for pixels that have $AFRI_{2.1}$ values less than 0.4. Our algorithm however, works best when the $AFRI_{2.1}$ values are within the range of 0.4–0.9. Therefore, when the $AFRI_{2.1}$ values of pixels were outside this range, then errors in surface reflectance assumptions would increase, and the accuracy of the results would decrease. Additionally, regarding the limitations of the instrumentation, because the sensor receives TOA reflectance at certain wavelengths, values are variable with respect to the surface contributions, aerosol loading, and geometrical conditions (solar zenith angle, satellite zenith angle, and relative azimuth angle). In order to explore the application limitations of the TANSO-CAI band 2 in AOD retrieval, I simulated how TOA reflectance changes with different surface reflectances and different AOD values. The simulation was conducted with ten different geometrical condition combinations (shown in Table 6.3) and five different AOD values ($\tau_{0.55}$ = 0.1, 0.5, 1.0, 1.5, and 2.0). Figure 6.3a to j shows the simulation results according to the geometrical conditions cases of a to j in Table 6.3. Except for Figure 6.3j, which was simulated under extremely special geometrical conditions, all the other sub-figures demonstrated that lower surface reflectance has larger amplitudes of variation in TOA reflectance, with the AOD increasing. This indicated that when using TANSO-CAI band 2 in AOD retrieval, ground surfaces that have lower surface reflectance are more sensitive to AOD changes. Based on the experimental results, two thresholds have been set for selecting well-suited pixels in the retrieval scheme: the upper limit of surface reflectance in TANSO-CAI band 2 is set to 0.085, at the same time, the TOA reflectance of band 3 should be larger than 0.225.

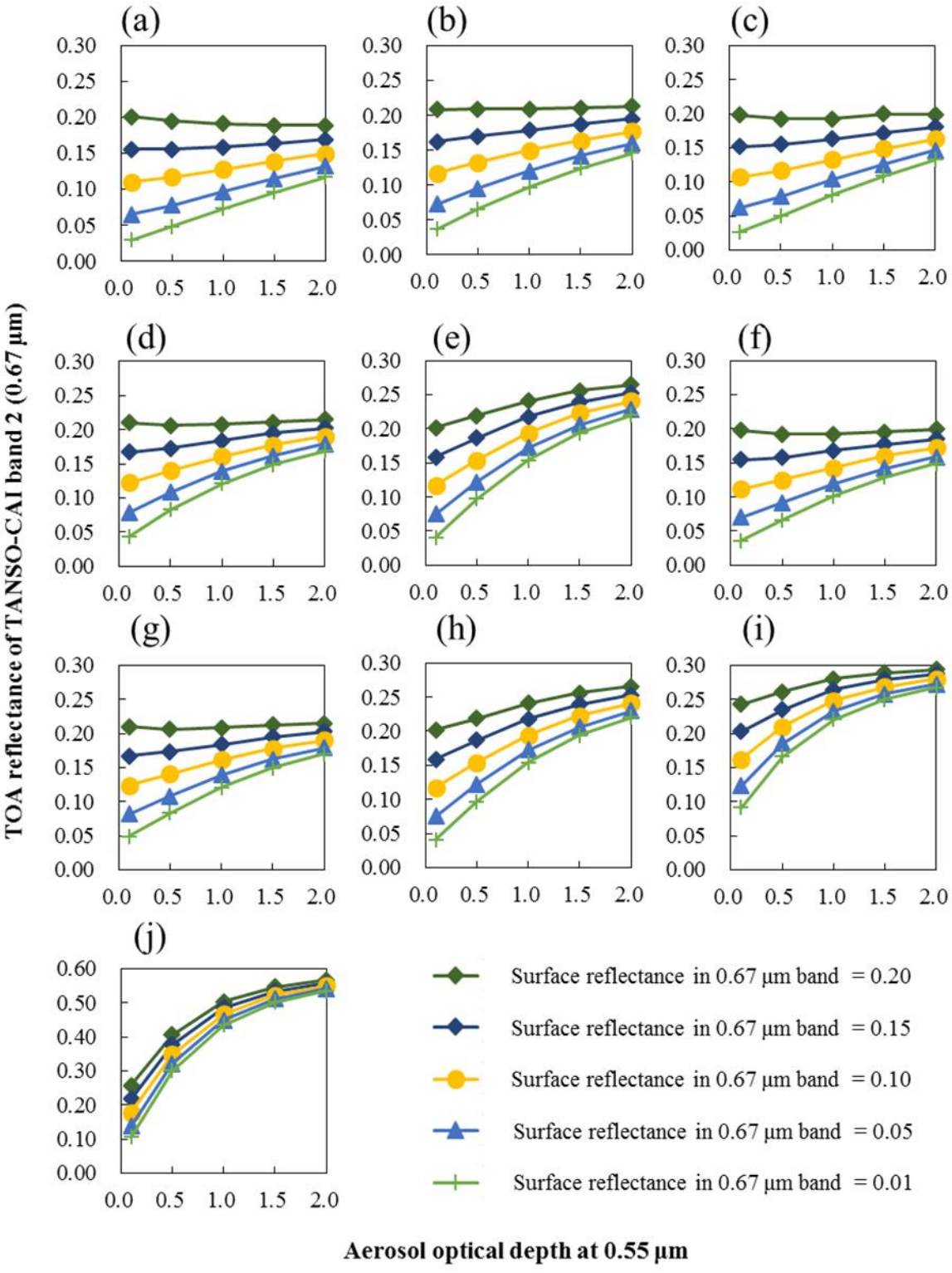

Figure 6.3 GOSAT TANSO-CAI TOA reflectance at 0.67 µm as a function of AOD under different surface reflectances; (**a** to **j**) are simulated under the corresponding observation geometric conditions cases of (a to j) shown in Table 6.3.

6.4 Results and discussion

The performance of TANSO-CAI retrieval AOD values at 0.55 μm with our algorithm has been evaluated by comparison with ground-level measurements from the collocated AERONET. As the AERONET AOD product has very high accuracy, it is usually considered as “ground truth” and is widely used for the quantitative validation of satellite-based retrievals [35]. To ensure comparability between the ground and satellite levels, spatially and temporally collocated TANSO-CAI and AERONET data were chosen based on the following criteria: the AERONET measurements are conducted within ±15 minutes of the GOSAT overpass time, and the TANSO-CAI data are collected within a 10 kilometer radius circular validation area around the AERONET site.

In this study, a total of 117 TANSO-CAI and AERONET collocated data were selected from five AERONET sites (Vientiane, Xinglong, Dhaka_University, Chiang_Mai_Met_Sta, and Ussuriysk) during the period from April 2009 to August 2014. The geographical information (longitude, latitude, and elevation) of these AERONET sites is shown in Table 6.4. Both the Vientiane and Chiang_Mai_Met_Sta sites are located in Southeast Asia, and the Dhaka_University, Xinglong, and Ussuriysk sites are located in South Asia, East Asia, and North Asia, respectively. Figure 6.4 illustrates the variations of matched TANSO-CAI and AERONET AODs, with observation dates for these five sites. Figure 6.5 shows the scatter plots between the TANSO-CAI AOD and AERONET AOD for individual and entire sites, and their corresponding summary statistics: the number of samples (N), mean AERONET AOD, root mean square error (RMSE), mean bias error (MBE), and expected error (EE) are shown in Table 6.4. As Figure 6.4 shows, the behavior of AODs from TANSO-CAI and AERONET is generally consistent for each site. In this regard, the retrievals are correlated with the overall AERONET sites, with r-values larger than 0.791. Even so, individual regions have their own particular characteristics. Apparently, the AODs retrieved from TANSO-CAI are slightly lower than the AERONET measurements over the Xinglong (Figure 6.4b) and Ussuriysk sites (Figure 6.4e), but conversely, the AODs retrieved over the Dhaka_University site (Figure 6.4c) are generally higher than the AERONET AODs. We could note that the AOD measurement data from the Xinglong and Ussuriysk sites are very low, with mean AOD values of 0.164 and 0.249, respectively. In addition, the dominant land cover type within a 10-kilometer radius around these two sites is tree cover (broadleaved and deciduous) [36]. Similarly, the studies of Xie et al. [37] show that, for vegetated sites under low aerosol AOD conditions, the MODIS DT tends to be underestimated. It could be due to an intrinsic system error in the algorithm or an instrument calibration issue. Alternately, the dominant land cover type around the Dhaka_University site is urban, with urban areas

comprising approximately 60% of the area within the 10 kilometer radius around the site [36]. Due to the complexity of urban type surfaces, this incorrect estimation of surface reflectance may impact the retrieval quality. On the other hand, the aerosol model assumption is also a critical factor closely associated with the retrieval results. The AOD over the Dhaka_University site is very high, with a mean value of 0.915. As Figure 6.4c shows, largely overestimated retrievals frequently occurred during the period from February to April for two consecutive years (2013 and 2014). This is possibly because the aerosol assumption cannot reflect the characteristics of atmospheric aerosols during this period. For these reasons, the retrievals over this site have the highest RMSE (0.328) and MBE (0.245). Very high correlation and low error rates are observed over the Vientiane (r-value = 0.921, RMSE = 0.141, and MBE = –0.059) and Chiang_Mai_Met_Sta (r-value = 0.974, RMSE = 0.140, and MBE = 0.099) sites, which are under a high level of aerosol loading and have a mean AERONET AOD of more than 0.7 and 0.5, respectively. The high quality of retrieval is possibly due to the rural vegetated land cover type around the sites [38].

The regression equations and lines of the TANSO-CAI versus AERONET AODs are displayed in Figure 6.5. In addition the dashed lines in the graphs are the EE lines. The EE is a confidence envelope that quotes the sum of the absolute and relative AOD errors, and is often used to estimate the uncertainty of aerosol products, such as the MODIS aerosol products. When 66% (one standard deviation) of the points fall within a bounding envelope of the EE as compared to AERONET, the products are considered "validated." For the MODIS DT product (Collection 5 and Collection 6), the EE for the land AOD product is ± (0.05 + 0.15τ), where τ is the true AOD value [39,40]. The envelope of the EE as described in Equation 9 shows:

$$\mathrm{AOD}_{(\mathrm{AERONET})} - |\mathrm{EE}| \leq \mathrm{AOD}_{(\mathrm{TANSO-CAI})} \leq \mathrm{AOD}_{(\mathrm{AERONET})} + |\mathrm{EE}|. \quad (9)$$

In Table 6.4, two different EEs (EE1: ± (0.05 + 0.15τ) and EE2: ± (0.1 + 0.15τ)) have been tentatively defined to estimate the uncertainty values of our algorithm. According to our statistical analysis, only the retrievals over Vientiane were "validated" by the EE1 criterion, with 78.6% of match-ups falling within the EE envelope of ± (0.05 + 0.15τ). For the total data, only 52.1% of points fell within the EE1 envelope. This means that the current algorithm cannot qualify the accuracy defined by EE1. However, the uncertainties of this algorithm were in good agreement within EE2. Except for Dhaka_University, more than 66% of match-ups fell within the EE2 envelope. For the overall data, 69.2% of the overall data fell within the EE2, and the retrievals highly agreed with the AERONET measurements with an r-value of 0.922.

Table 6.4 Geographical information and summary statistics for the entire data set and each individual site: longitude, latitude, elevation, number of samples (N), correlation coefficients (r), root mean square errors (RMSE), mean bias errors (MBE), and expected errors (EE).

Site name	Longitude (decimal degrees)	Latitude (decimal degrees)	Elevation (meters)	N	Mean AOD	r	RMSE	MBE	EE1	EE2
Vientiane	102.57	17.99	170	28	0.716	0.921	0.141	–0.059	78.6%	82.1%
Xinglong	117.58	40.40	970	19	0.164	0.791	0.136	–0.110	31.6%	73.7%
Dhaka_ University	90.40	23.73	34	31	0.915	0.855	0.328	0.245	41.9%	51.6%
Chiang_Mai_ Met_Sta	98.97	18.77	312	26	0.520	0.974	0.140	0.099	61.5%	73.1%
Ussuriysk	132.16	43.70	280	13	0.249	0.904	0.119	–0.089	38.5%	69.2%
Total				117	0.584	0.922	0.205	0.045	52.1%	69.2%

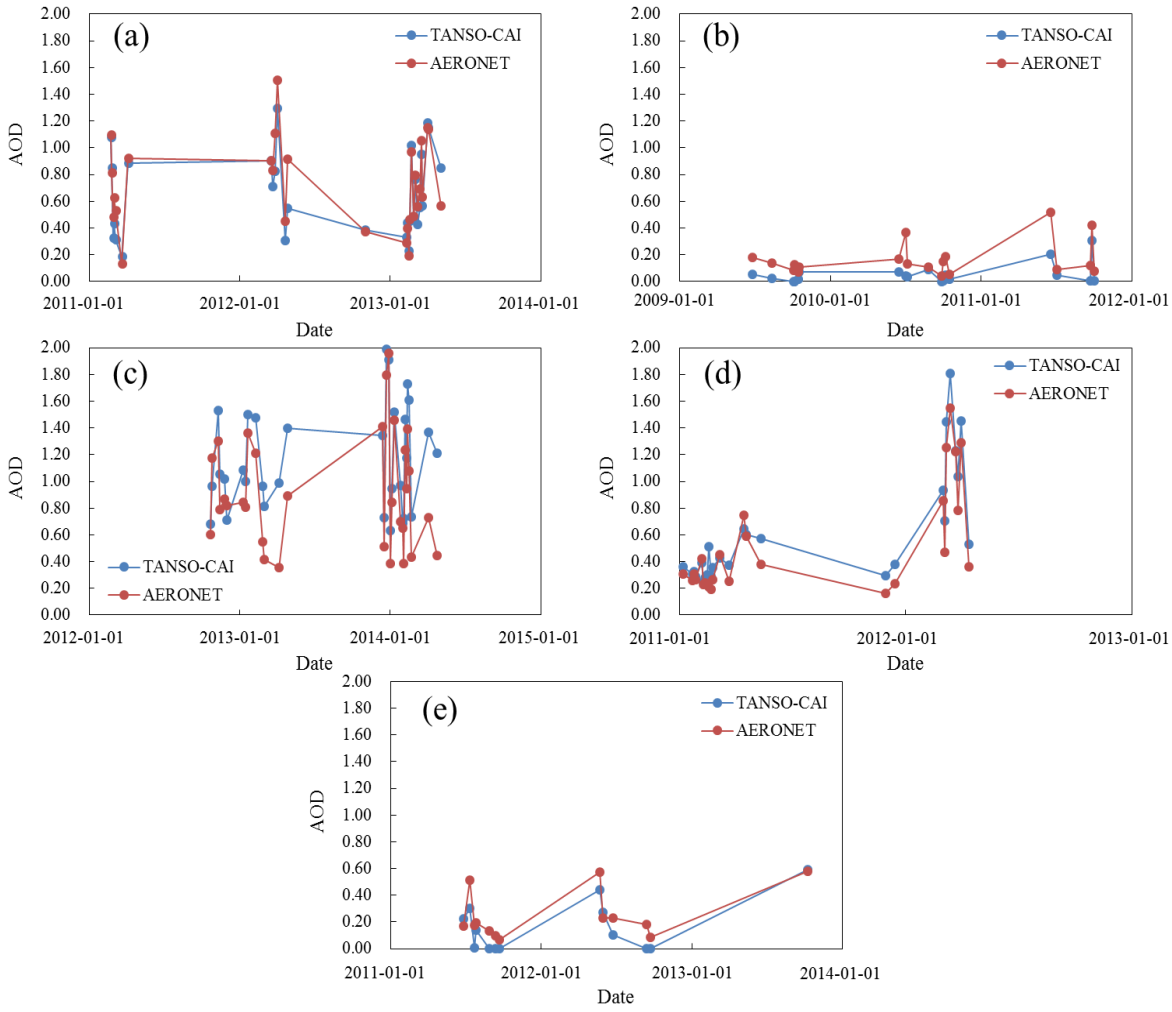

Figure 6.4 Variation curve of AODs from the spatially and temporally collocated TANSO-CAI and Aerosol Robotic Network (AERONET) data; (**a**) Vientiane site; (**b**) Xinglong site; (**c**) Dhaka_University site; (**d**) Chiang_Mai_Met_Sta site; and (**e**) Ussuriysk site.

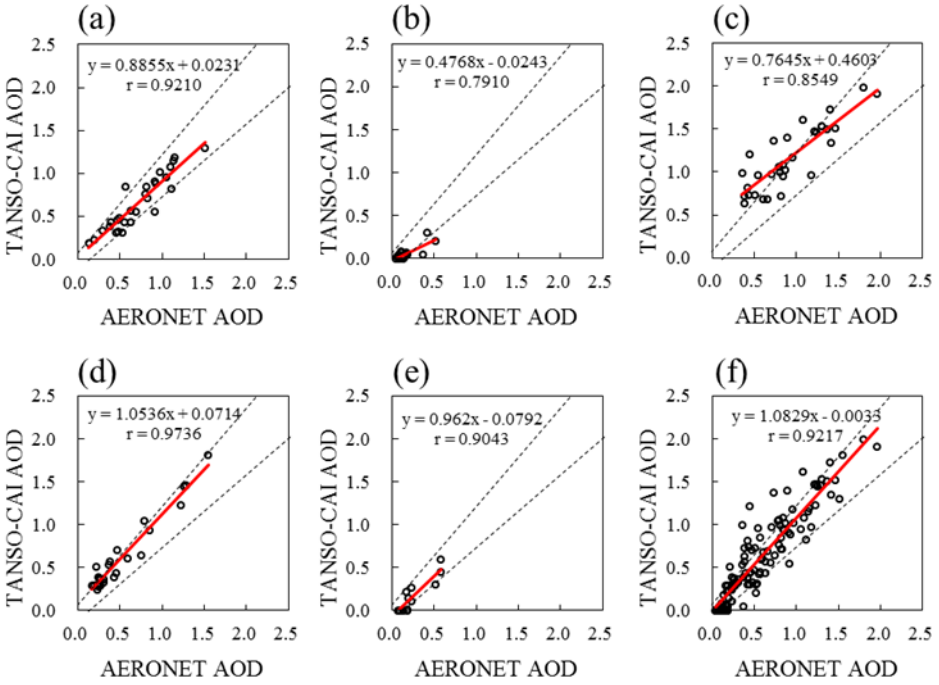

Figure 6.5 Validation of TANSO-CAI retrievals against AERONET measurements over different regions. (**a**) Vientiane site; (**b**) Xinglong site; (**c**) Dhaka_University site; (**d**) Chiang_Mai_Met_Sta site; (**e**) Ussuriysk site; and (**f**) for all sites. The red solid and dashed lines are the regression line, and the expected error (± (0.1 + 15% $AOD_{AERONET}$)) envelope line, respectively.

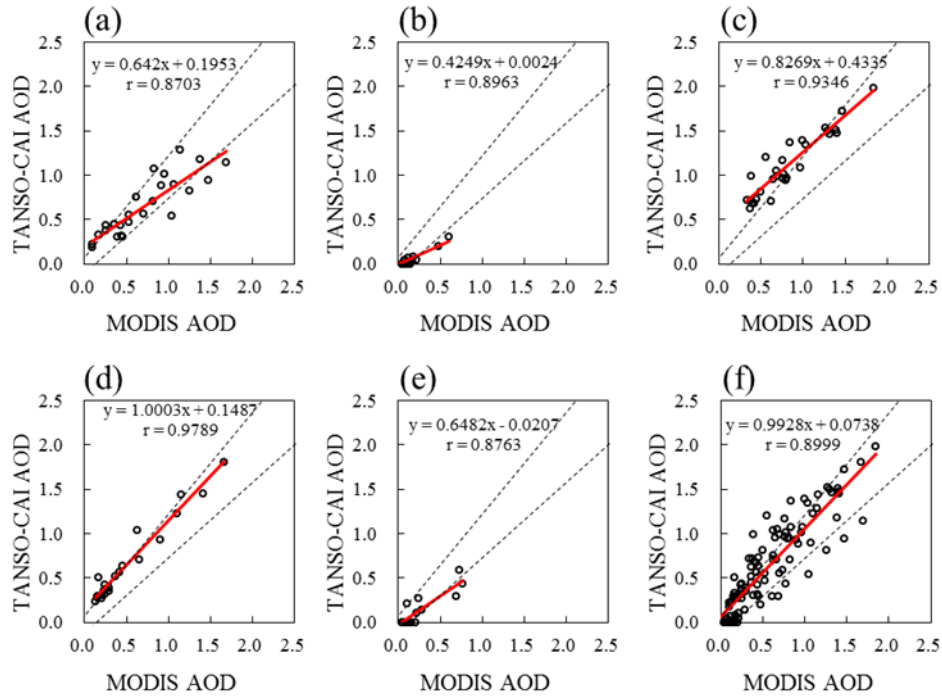

Figure 6.6 Comparison of TANSO-CAI retrievals against MYD04_3K AOD over different regions. (**a**) Vientiane site; (**b**) Xinglong site; (**c**) Dhaka_University site; (**d**) Chiang_Mai_Met_Sta site; (**e**) Ussuriysk site; and (**f**) for all sites. The red solid and dashed lines are the regression line, and the expected error (± (0.1 + 15% $AOD_{AERONET}$)) envelope line, respectively.

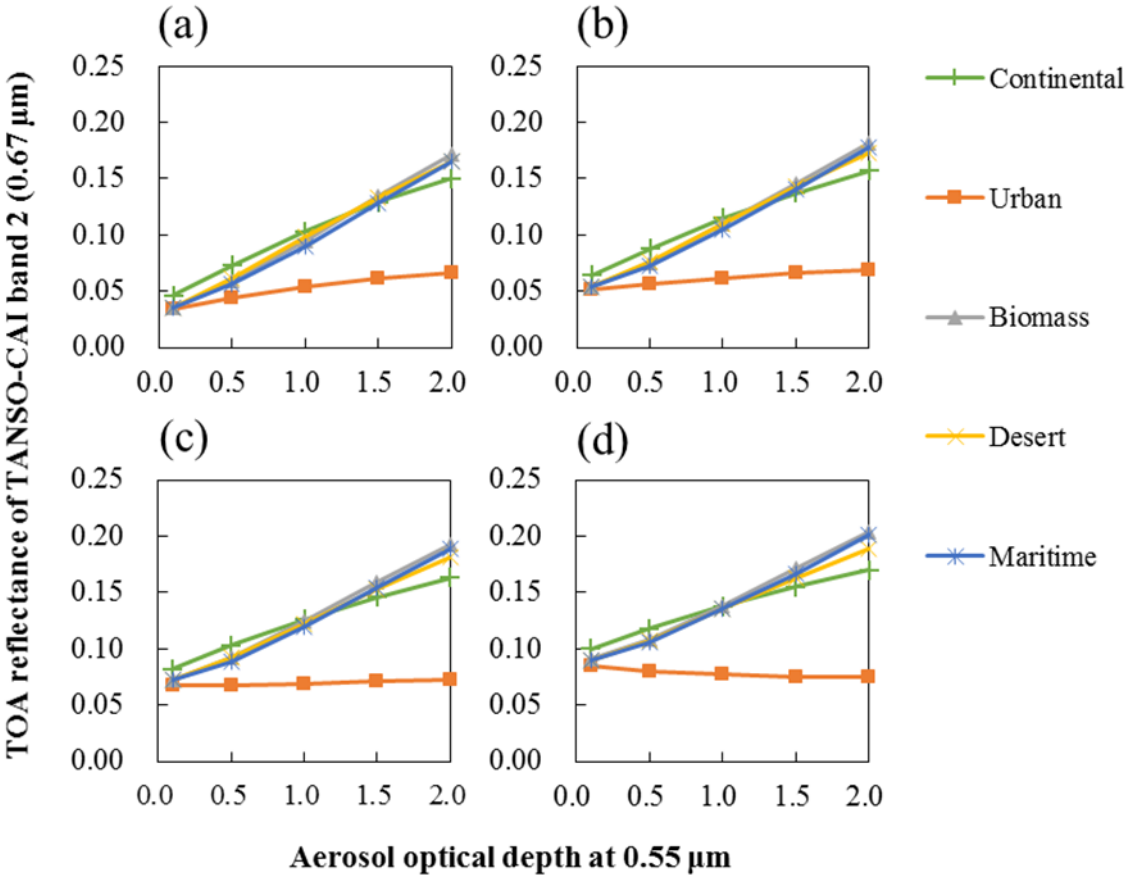

Figure 6.7 TANSO-CAI TOA reflectance as a function of AOD and surface reflectance at 0.67 µm under different aerosol models. The assumed surface reflectances are: (**a**) 0.02; (**b**) 0.04; (**c**) 0.06; and (**d**) 0.08. Simulation is performed under the observation geometric conditions with solar zenith angle = 30°, satellite zenith angle = 30°, and relative azimuth angles = 180°.

As part of this algorithm was developed based on several studies using the MODIS DT algorithm, the retrievals made using our algorithm were also compared with the MODIS standard aerosol products. Here, a MODIS DT Collection 6 AOD product at 3 km (MYD04_3K) from Aqua with a similar overpass time to GOSAT was used. Figure 6.6 compares the TANSO-CAI and MODIS retrievals made at comparable times and areas. The comparison results (Figure 6.5) show that the current algorithm performs reasonably well overall and also for individual sites. The correlations of TANSO-CAI and MODIS AODs are very strong, and the statistical r-values are all higher than 0.87. MODIS has 36 channels, and the DT algorithm uses the blue (at 0.47 µm), red (at 0.65 µm), and SWIR (at 2.1 µm) channels to account for the surface signals. Moreover, several additional aerosol models were also defined and used in AOD retrievals. However, compared with MODIS, the limitations of the TANSO-CAI spectral bands made aerosol retrieval very challenging. As GOSAT TANSO-CAI is not

equipped with the 2.1 μm band, the estimation of the surface reflectance has to rely on the relationship of 1.6 vs. 2.1. Although this relationship has proven to be extremely robust under low aerosol conditions, the associated uncertainty may in fact serve to increase actual AOD retrieval. Additionally, as MODIS DT is a multi-channel algorithm, the MODIS blue band is also employed in AOD retrieval. However, due to the lack of a blue band in TANSO-CAI, only one visible band is used for AOD retrieval. The single-band algorithm has no degree of freedom to select aerosol models [41].

I used the 6S radiative transfer code to simulate the relationships between TOA and surface reflectance in the TANSO-CAI 0.67 μm band under five different aerosol models: continental, urban, biomass, desert, and maritime [42]. Figure 6.7 shows the simulation results for the different models when surface reflectances were 0.02, 0.04, 0.06, and 0.08, respectively. We can see that under the urban aerosol model, the relationship between TOA and surface reflectance differs greatly from those of other aerosol models. With the exception of the urban aerosol model, there are only slight differences between each of the models. This implied that for the TANSO-CAI 0.67 μm band based algorithm, the continental aerosol model could potentially be used as the common assumption to describe aerosol scattering and absorption properties, but actually doing so would lead to large errors when the aerosol properties were in accordance with the urban aerosol type. Consequently, these deficiencies can restrict the performance of TANSO-CAI in its accuracy and range of application.

6.5 Conclusions

In this study, I proposed a GOSAT TANSO-CAI adapted DT algorithm for aerosol retrieval based on ideas from the MODIS DT algorithm. TANSO-CAI measures reflectance near the 1.6 μm wavelength. It does not measure the 2.1 μm wavelength. In the MODIS DT algorithm, relationships between the 2.1 μm and visible (red and blue) bands are used to account for the surface signals. In order to take full advantage of these relationships in the TANSO-CAI retrieval algorithm, I analyzed the reflectance relationship between 1.6 μm and 2.1 μm with the help of a MODIS surface reflectance product, and found that their relationship varies according to the surface condition.

In the MODIS DT algorithm, the estimation of visible surface reflectance is dependent on both geometry (scattering angle) and surface conditions ($NDVI_{SWIR}$). Our results show that $AFRI_{2.1}$ is highly correlated with the $NDVI_{SWIR}$ under low aerosol loading conditions (r-value of 0.943). Since both $NDVI_{SWIR}$ and $AFRI_{2.1}$ are defined by longer wavelengths that are much less influenced by aerosol than regular

NDVI, similar to the MODIS DT algorithm, I took the scattering angle and $AFRI_{2.1}$ into account to develop a method for estimating surface reflectance at 0.67 μm from the 1.6 μm band for TANSO-CAI.

AOD retrieval over land from TANSO-CAI was conducted based on estimated surface reflectance. These retrievals were validated by comparison against measurements from five different AERONET sites. The retrievals displayed very high consistency with the AERONET measurements (r-value of 0.922). The uncertainty values for this algorithm were assessed using the expected error envelope of ± (0.1 + 15% $AOD_{AERONET}$), and 69.2% of retrievals fell within this expected error lines. The mean bias error for the overall experimental data is 0.045.

The demonstrated approaches for GOSAT TANSO-CAI AOD retrieval can be used in conjunction with other sensors that measure reflectance in corresponding wavelength bands, especially sensors which have SWIR bands near the 1.6 μm wavelength but lack the 2.1 μm band. This study offers a new idea for estimating surface reflectance in the visible band from the SWIR band. However, like the MODIS DT algorithm, this algorithm is also unable to work over bright land surfaces. In addition, although the 1.6 μm and 2.1 μm SWIR bands are not sensitive to fine-mode aerosol particles, under the dust aerosol condition, the atmosphere is no longer transparent. Therefore, use of the current algorithm is restricted to dust aerosols [43,44].

References

1. Sun, L.; Wei, J.; Bilal, M.; Tian, X.; Jia, C.; Guo, Y.; Mi, X. Aerosol Optical Depth Retrieval over Bright Areas Using Landsat 8 OLI Images. *Remote Sens-Basel* **2015**, *8*, 23.
2. Choudhry, P.; Misra, A.; Tripathi, S. Study of MODIS derived AOD at three different locations in the Indo Gangetic Plain: Kanpur, Gandhi College and Nainital. *Annales Geophysicae* **2012**, 1479-1493.
3. Mateos, D.; Anton, M.; Toledano, C.; Cachorro, V.; Alados-Arboledas, L.; Sorribas, M.; Costa, M.J.; Baldasano, J. Aerosol radiative effects in the ultraviolet, visible, and near-infrared spectral ranges using long-term aerosol data series over the Iberian Peninsula. *Atmospheric Chemistry and Physics* **2014**, *14*, 13497-13514.
4. Jiang, X.; Liu, Y.; Yu, B.; Jiang, M. Comparison of MISR aerosol optical thickness with AERONET measurements in Beijing metropolitan area. *Remote Sensing of Environment* **2007**, *107*, 45-53.

5. Zhang, H.; Hoff, R.; Kondragunta, S.; Laszlo, I.; Lyapustin, A. Aerosol optical depth (AOD) retrieval using simultaneous GOES-East and GOES-West reflected radiances over the western United States. *Atmospheric Measurement Techniques* **2013**, *6*, 471-486.
6. Riffler, M.; Popp, C.; Hauser, A.; Fontana, F.; Wunderle, S. Validation of a modified AVHRR aerosol optical depth retrieval algorithm over Central Europe. *Atmospheric Measurement Techniques* **2010**, *3*, 1255-1270.
7. Kaufman, Y.; Tanré, D.; Gordon, H.; Nakajima, T.; Lenoble, J.; Frouin, R.; Grassl, H.; Herman, B.; King, M.; Teillet, P. Passive remote sensing of tropospheric aerosol and atmospheric correction for the aerosol effect. *Journal of Geophysical Research: Atmospheres* **1997**, *102*, 16815-16830.
8. Kaufman, Y.; Tanré, D.; Remer, L.A.; Vermote, E.; Chu, A.; Holben, B. Operational remote sensing of tropospheric aerosol over land from EOS moderate resolution imaging spectroradiometer. *Journal of Geophysical Research: Atmospheres* **1997**, *102*, 17051-17067.
9. Kokhanovsky, A.; Breon, F.-M.; Cacciari, A.; Carboni, E.; Diner, D.; Di Nicolantonio, W.; Grainger, R.; Grey, W.; Höller, R.; Lee, K.-H. Aerosol remote sensing over land: A comparison of satellite retrievals using different algorithms and instruments. *Atmospheric Research* **2007**, *85*, 372-394.
10. de Leeuw, G.; Holzer-Popp, T.; Bevan, S.; Davies, W.H.; Descloitres, J.; Grainger, R.G.; Griesfeller, J.; Heckel, A.; Kinne, S.; Klüser, L. Evaluation of seven European aerosol optical depth retrieval algorithms for climate analysis. *Remote Sensing of Environment* **2015**, *162*, 295-315.
11. Levy, R.C.; Remer, L.A.; Mattoo, S.; Vermote, E.F.; Kaufman, Y.J. Second‐generation operational algorithm: Retrieval of aerosol properties over land from inversion of Moderate Resolution Imaging Spectroradiometer spectral reflectance. *Journal of Geophysical Research: Atmospheres* **2007**, *112*.
12. Levy, R.; Munchak, L.; Mattoo, S.; Patadia, F.; Remer, L.; Holz, R. Towards a long-term global aerosol optical depth record: Applying a consistent aerosol retrieval algorithm to MODIS and VIIRS-observed reflectance. *Atmospheric Measurement Techniques* **2015**, *8*, 4083.
13. Dark Target (MODIS Aerosol Retrieval Algorithm), About the Algorithm. Available online: https://darktarget.gsfc.nasa.gov/algorithm (accessed on 26 December 2016).
14. Dark Target (MODIS Aerosol Retrieval Algorithm), Platforms, VIIRS. Available online: https://darktarget.gsfc.nasa.gov/platforms/viirs (accessed on 26 December 2016).
15. Fukuda, S.; Nakajima, T.; Takenaka, H.; Higurashi, A.; Kikuchi, N.; Nakajima, T.Y.; Ishida, H. New approaches to removing cloud shadows and evaluating the

380 nm surface reflectance for improved aerosol optical thickness retrievals from the GOSAT/TANSO‐Cloud and Aerosol Imager. *Journal of Geophysical Research: Atmospheres* **2013**, *118*.

16. GOSAT_pamphlet_en.pdf (7th Edition (July 2016)). Available online: http://www.gosat.nies.go.jp/eng/GOSAT_pamphlet_en.pdf (accessed on 26 December 2016).
17. Gao, L.; Li, J.; Chen, L.; Zhang, L.; Heidinger, A.K. Retrieval and validation of atmospheric aerosol optical depth from AVHRR over China. *IEEE Transactions on Geoscience and Remote Sensing* **2016**, *54*, 6280-6291.
18. Algorithm theoretical basis document (ATBD) for CO_2 and CH_4 columun amounts retrieval from GOSAT TANSO-FTS SWIR. Available online: http://data.gosat.nies.go.jp/GosatUserInterfaceGateway/guig/doc/documents/ATBD_FTSSWIRL2_V1.1_en.pdf (accessed on 26 December 2016).
19. Jung, Y.; Kim, J.; Kim, W.; Boesch, H.; Lee, H.; Cho, C.; Goo, T.-Y. Impact of aerosol property on the accuracy of a CO2 retrieval algorithm from satellite remote sensing. *Remote Sens-Basel* **2016**, *8*, 322.
20. Sun, L.; Sun, C.; Liu, Q.; Zhong, B. Aerosol optical depth retrieval by HJ-1/CCD supported by MODIS surface reflectance data. Science China Earth Sciences 2010, 53, 74-80.
21. Istomina, L.; von Hoyningen-Huene, W.; Kokhanovsky, A.; Schultz, E.; Burrows, J. Remote sensing of aerosols over snow using infrared AATSR observations. *Atmospheric Measurement Techniques* **2011**, *4*, 1133.
22. Zhang, Y.; Li, Z.; Qie, L.; Zhang, Y.; Liu, Z.; Chen, X.; Hou, W.; Li, K.; Li, D.; Xu, H. Retrieval of Aerosol Fine-Mode Fraction from Intensity and Polarization Measurements by PARASOL over East Asia. *Remote Sens-Basel* **2016**, *8*, 417.
23. Hou, P.; Jiang, W.; Cao, G.; Li, J. Aerosol retrieval with satellite image and correlation analyses between aerosol distribution and urban underlaying surface. *International journal of remote sensing* **2012**, *33*, 3232-3251.
24. Remer, L.A.; Wald, A.E.; Kaufman, Y.J. Angular and seasonal variation of spectral surface reflectance ratios: Implications for the remote sensing of aerosol over land. *IEEE Transactions on Geoscience and Remote Sensing* **2001**, *39*, 275-283.
25. Gatebe, C.K.; King, M.D.; Tsay, S.-C.; Ji, Q.; Arnold, G.T.; Li, J.Y. Sensitivity of off-nadir zenith angles to correlation between visible and near-infrared reflectance for use in remote sensing of aerosol over land. *IEEE Transactions on Geoscience and Remote Sensing* **2001**, *39*, 805-819.
26. Lyapustin, A.I. Three-dimensional effects in the remote sensing of surface albedo. *IEEE transactions on geoscience and remote sensing* **2001**, *39*, 254-263.
27. Algorithm theoretical basis document for TANSO-CAI L1B processing. Available online: https://data.gosat.nies.go.jp/GosatWebDds/productorder/distribution/user/

ATBD _CAIL1B_V1.0_en.pdf (accessed on 22 December 2016).
28. Algorithm theoretical basis document for TANSO-CAI L1B+ processing. Available online: https://data.gosat.nies.go.jp/GosatWebDds/productorder/distribution/user/ATBD_CAIL1BP_V1.01_en.pdf (accessed on 23 December 2016).
29. NIES GOSAT Product Format Descriptions. Available online: https://data.gosat.nies.go.jp/GosatWebDds/productorder/distribution/user/GOSAT_ProductDescription_V1.50_en.pdf (accessed on 24 December 2016).
30. Holben, B.N.; Eck, T.; Slutsker, I.; Tanre, D.; Buis, J.; Setzer, A.; Vermote, E.; Reagan, J.; Kaufman, Y.; Nakajima, T. AERONET—A Federated Instrument Network and Data Archive for Aerosol Characterization. *Remote sensing of environment* **1998**, *66*, 1-16.
31. Levy, R.C.; Remer, L.A.; Munchak, L.A. A surface reflectance scheme for retrieving aerosol optical depth over urban surfaces in MODIS dark target retrieval algorithm. *Atmospheric Measurement Techniques* **2016**, *9*, 3293.
32. Vermote, E.F.; Tanré, D.; Deuze, J.L.; Herman, M.; Morcette, J.-J. Second simulation of the satellite signal in the solar spectrum, 6S: An overview. *IEEE transactions on geoscience and remote sensing* **1997**, *35*, 675-686.
33. Vermote, E.F.; Kotchenova, S. Atmospheric correction for the monitoring of land surfaces. *Journal of Geophysical Research: Atmospheres* **2008**, *113*.
34. Vermote, E.F.; El Saleous, N.Z.; Justice, C.O. Atmospheric correction of MODIS data in the visible to middle infrared: *First results. Remote Sensing of Environment* **2002**, *83*, 97-111.
35. Le Treut, H. Greenhouse gases, aerosols and reducing future climate uncertainties. *Surveys in geophysics* **2012**, *33*, 723-731.
36. EUMETSAT Surface Albedo Validation Sites. Available online: http://savs.eumetsat.int (accessed on 18 October 2016).
37. Xie, Y.; Zhang, Y.; Xiong, X.; Qu, J.J.; Che, H. Validation of MODIS aerosol optical depth product over China using CARSNET measurements. *Atmospheric Environment* **2011**, *45*, 5970-5978.
38. Nichol, J.E.; Bilal, M. Validation of MODIS 3 km Resolution Aerosol Optical Depth Retrievals Over Asia. *Remote Sens-Basel* **2016**, *8*, 328.
39. Levy, R.C.; Remer, L.A.; Kleidman, R.G.; Mattoo, S.; Ichoku, C.; Kahn, R.; Eck, T. Global evaluation of the Collection 5 MODIS dark-target aerosol products over land. *Atmospheric Chemistry and Physics* **2010**, *10*, 10399-10420.
40. Dark Target (MODIS Aerosol Retrieval Algorithm), Validation Results. Available online: https://darktarget.gsfc.nasa.gov/validation/results (accessed on 26 December 2016).
41. Zhang, H.; Lyapustin, A.; Wang, Y.; Kondragunta, S.; Laszlo, I.; Ciren, P.; Hoff, R.

A multi-angle aerosol optical depth retrieval algorithm for geostationary satellite data over the United States. *Atmospheric Chemistry and Physics* **2011**, *11*, 11977.

42. Vermote, E.; Tanré, D.; Deuzé, J.; Herman, M.; Morcrette, J.; Kotchenova, S. Second simulation of a satellite signal in the solar spectrum-vector (6SV). *6S User Guide Version* **2006**, *3*, 1-55.
43. Kaufman, Y.J.; Tanré, D.; Boucher, O. A satellite view of aerosols in the climate system. *Nature* **2002**, *419*, 215-223.
44. Wang, J.; Xu, X.; Spurr, R.; Wang, Y.; Drury, E. Improved algorithm for MODIS satellite retrievals of aerosol optical thickness over land in dusty atmosphere: Implications for air quality monitoring in China. *Remote Sensing of Environment* **2010**, *114*, 2575-2583.

Chapter 7 Summary and conclusions

7.1 Summary of present work

Atmospheric aerosols have been recognized as the main source of uncertainty in evaluating the climate change. Aerosols near the surface effect on air quality and human health. In addition, atmospheric aerosols have also been well known to introduce large variations in remote sensing of dynamics over Earth's surface at satellite level. Aiming to derive atmospheric aerosols properties using satellite remote sensing technique, and to correct the atmospheric effects on the extracted information of Earth's surface at satellite-level, three main tasks have been undertaken: (1) Determination of surface contribution at satellite-level. (2) Establishment of aerosol retrieval algorithm (including assumptions of aerosol models, building of look-up table, and retrieval using look-up table). (3) Development of correction method for minimizing the atmospheric influences in spectral red and near-infrared (NIR) bands.

The aerosol retrieval was based on the observation from Greenhouse gases Observing SATellite Thermal and Near-infrared Sensor for Carbon Observation-Cloud and Aerosol Imager (GOSAT TANSO-CAI). The ground measured aerosol optical depth (AOD) from Aerosol Robotic Network (AERONET) were used to validate our retrievals. Moderate-Resolution Imaging Spectroradiometer (MODIS) and AERONET collocated data were used in analysis of atmospheric effects on the remote sensing of surface conditions (e.g., vegetation), and in validating the performance of the developed correction method. The satellite top-of-atmosphere (TOA) and surface radiance data, and ground-level and satellite-level AOD data used for these analyses are listed in Table 7.1.

Two new AOD retrieval algorithms for GOSAT TANSO-CAI were developed, and two new correction method for minimizing the atmospheric influences in spectral red and NIR bands were proposed in this thesis.

Table 7.1 Overview of data used in this thesis.

Chapter	Data category	Short name	Time scale	Cover areas
Chapter 2	Radiance data	TANSO CAI L1B+	2009–2014	Over 9 AERONET stations globally
	AOD data	AERONET Level 2.0	2009–2014	Over 16 AERONET stations globally
Chapter 3	Radiance data	MODIS MOD02HKM	2008–2014	Over 3 AERONET stations in Asia
		MODIS MOD09HKM	2008–2014	
	AOD data	AERONET Level 2.0	2008–2014	Over 3 AERONET stations in Asia
	Geolocation Fields	MODIS MOD03	2008–2014	Over 3 AERONET stations in Asia
Chapter 4	Radiance data	MODIS MOD09HKM	2008–2014	Over 3 AERONET stations in Asia
	AOD data	AERONET Level 2.0	2008–2014	Over 3 AERONET stations in Asia
	Geolocation Fields	MODIS MOD03	2008–2014	Over 3 AERONET stations in Asia
Chapter 5	Radiance data	MODIS MOD09HKM	2008–2014	Over 9 AERONET stations globally
	AOD data	AERONET Level 2.0	2008–2014	Over 3 AERONET stations in Asia
	Geolocation Fields	MODIS MOD03	2008–2014	Over 3 AERONET stations in Asia
Chapter 6	Radiance data	TANSO CAI L1B+	2009–2014	Over 9 AERONET stations globally
		MODIS MOD09HKM	2009–2014	
	AOD data	AERONET Level 2.0 MODIS MYD04_3K	2009–2014	Over 5 AERONET stations globally

7.2 Limitation of this study

7.2.1 Limitations in AOD retrieval algorithms

In Chapter 2 and Chapter 6, I introduced two new AOD retrieval algorithms for GOSAT TANSO-CAI sensor. Due to fewer spectral bands being available in GOSAT TANSO-CAI, only one visible band was used for aerosol retrieval, and its accuracy and ability has been limited. Because the single-band retrieval algorithm does not have the degree of freedom to choose aerosol type, the current algorithms used the continental aerosol model to describe the aerosol condition. Although the continental aerosol model is an often used assumption over land surfaces, it is obviously not satisfactory for all aerosols conditions. Improperly assuming aerosol type can lead to errors in retrieval.

In these two algorithms, the surface signal in the visible wavelength is estimated based on the shortwave infrared (SWIR) band at 1.6 um. TOA reflectance in 1.6 um is not sensitive to fine-mode aerosol particles and can be assumed as surface reflectance. However, under the dust aerosol condition, the atmosphere is no longer transparent. Therefore, use of the proposed algorithms are restricted to dust aerosols.

In addition, as typical vegetation-dependent algorithms (similar with MODIS Dark Target algorithm), these algorithms do not aim to work for bright surface (e.g., desert or urban).

In theory, these two AOD retrieval algorithms can be implemented for any satellite sensor if provide reflectances in the appropriate bands. For other sensors, however, because the specification (such as center wavelength, bandwidth and spectral responses) of corresponding bands may be different with TANSO-CAI, the difference in the specification of bands must be corrected when applying to other satellites.

7.2.2 Limitations in correction methods for atmospheric influences

In Chapter 4 and Chapter 5, two self-corrected methods to minimize the atmospheric influences on vegetation indices were introduces. In these methods, surface reflectance estimation is an important step, which is based on the reflectance relationship between red and SWIR 2.1 μm bands. The linear relationship of $R_{0.6} = 0.5R_{2.1}$ can be used for dark surface target. However, the 2.1 μm band also cannot penetrate the dust aerosols. Limited success of the methods are expected in the case of dust or non-vegetated surface conditions.

7.3 Further study

The proposed AOD algorithm is the first step towards the application of GOSAT data for the retrieval of AOD over land. I expect existing errors and the uncertainties in the algorithm to be improved in further studies by expanding experimental data, diversifying aerosol models in look-up tables, correcting elevated surface targets, and improving cloud detection algorithms.

Expectedly, Greenhouse gases Observing SATellite 2 (GOSAT-2), the successor to GOSAT, which is scheduled for launch in the Japanese fiscal year 2017, will carry a new observation instrument: Cloud and Aerosol Imager 2 (CAI-2). CAI-2 will have greatly improved observation capabilities over CAI; 10 bands in the ultraviolet, visible, NIR, and SWIR region, and capacity to observe in both the forward and backward directions (Table 7.2). Hence, the current algorithm could be adapted to operate on next-generation instruments, greatly ameliorating the existing problems caused by the single-band algorithm.

With regards to the second-generation sensor GOSAT CAI-2, this work could be a meaningful reference, and the existing deficiencies (e.g., the single-band based retrieval method) caused by current instrument limitations can be expected to improve in the future. Red and blue bands are used in the current MODIS DT algorithm, and GOSAT CAI-2 will provide new measurement capability in the blue band. According to Equation 2 in Chapter 6, an approach for estimating surface reflectance in the blue band from the 1.6 μm band could be developed, one which has the potential to modify the current algorithm for GOSAT CAI-2 by employing the blue band. Moreover, both CAI and CAI-2 possess the ultraviolet band, and the AOD at the ultraviolet band is an important parameter. The use of the ultraviolet band would be helpful for detecting absorbing aerosol, and offers a good opportunity for further studies to take the advantage of the GOSAT CAI ultraviolet band in aerosol retrieval.

Table 7.2 Specification of GOSAT TANSO-CAI-2.

+20 deg. (Forward viewing)			**–20 deg. (Backward viewing)**		
Band number	**Bandwidth (μm)**	**Spatial resolution (m)**	**Band number**	**Bandwidth (μm)**	**Spatial resolution (m)**
1	0.333−0.353	460	**6**	0.370−0.390	460
2	0.433−0.453	460	**7**	0.540−0.560	460
3	0.664−0.684	460	**8**	0.664−0.684	460
4	0.859−0.879	460	**9**	0.859−0.879	460
5	1.585−1.675	920	**10**	1.585−1.675	920

7.4 Final conclusion

The main objectives of this research are to develop an aerosol retrieval algorithm in order to retrieve aerosol properties from satellite observations, and to develop an atmospheric correction method for high-precision surface monitoring. For this, five main research tasks (from Chapter 2 to Chapter 6) have been undertaken:

(1) Chapter 2 introduced a new algorithm for retrieving AOD over land, from the CAI. The GOSAT and AERONET collocated data from different regions over the globe were used to analyze the relationship between the TOA reflectance in the SWIR (1.6 μm) band and the surface reflectance in the red (0.67 μm) band. Our results confirmed that the relationships between the surface reflectance at 0.67 μm and TOA reflectance at 1.6 μm are not constant for different surface conditions. I combined the advantages of the Aerosol FRee vegetation Index (AFRI), which is aerosol resistant and highly correlated with regular Normalized Difference Vegetation Index (NDVI), with our regression function, which can preserve the various correlations of 0.67 μm and 1.6 μm bands for different surface types, and developed a new surface reflectance and aerosol-free NDVI estimation algorithm, which I named the Modified $AFRI_{1.6}$ algorithm.

(2) Chapter 3 evaluated the performances of Atmospherically Resistant Vegetation Index (ARVI), Enhanced Vegetation Index (EVI), two-band-based EVI (EVI2), Visible Atmospherically Resistant Index (VARI) and AFRI for vegetation detection and monitoring with various AOD levels using the MODIS and AERONET data.

(3) Chapter 4 proposed a self-correction method for correcting the atmospheric influences in red and NIR bands. The corrected NIR band could be singly utilized to improve the measurement accuracy of SWIR-based vegetation indices. The corrected NIR and red band pair could also be directly used in the construction of vegetation indices, which would have the capability to assess vegetation and even aerosols that are present in the atmosphere. This method was applied in the construction of the corrected NIR-derived $AFRI_{2.1}$ and the corrected NDVI, the performances of which were investigated under different aerosol loading conditions. The results revealed that under different AOD values, the corrected NIR-derived $AFRI_{2.1}$ was generally closer to the atmospherically corrected NDVI than the original $AFRI_{2.1}$. Compared with the uncorrected NDVI, the NDVI corrected by our method exhibited an obviously better performance under aerosol loading conditions; the atmospheric influences on the NIR and red bands were largely removed, generating near-theoretical values.

(4) Chapter 5 analyzed the reflectance relationship between the 1.6 μm and 2.1

μm bands using the MODIS surface reflectance product, and attempted to adapt the 2.1-μm-based self-correction method to the 1.6-μm-based sensors, according to the reflectance relationship between the 1.6 μm and 2.1 μm bands. The analyzed results revealed that the reflectance relationship between the 1.6 μm and 2.1 μm bands is typically dependent on vegetation conditions. The performance of the 1.6-μm-based correction method has been tested with different levels of AOD by a comparison of the atmospherically corrected vegetation indices. The results showed that the atmospheric influences in the red and NIR bands were effectively corrected using the 1.6-μm-based correction method, and the corrected red and NIR band derived vegetation indices have obvious improvements in accuracy.

(5) Chapter 6 introduced a Dark Target algorithm for GOSAT CAI based on the strategy of MODIS DT algorithm. Similar to the current MODIS DT algorithms (Collection 5 and Collection 6), a TANSO-CAI-applicable approach that uses $AFRI_{2.1}$ and the scattering angle to account for the visible surface signals was proposed. Validations show that retrievals from the CAI have high agreement with the AERONET measurements, with an r-value of 0.922, and 69.2% of the AOD retrieved data falling within the expected error envelope of $\pm (0.1 + 15\% AOD_{AERONET})$.

Acknowledgements

First and foremost, I would like to give my deepest and sincerest gratitude to my venerable supervisor, Associate Prof. Wang Xiufeng, whose invaluable supervision, scholastic guidance, constant encouragement and extraordinary patience enable me to complete this research. Your intellectual suggestion, rigorous scientific attitude and far-sighted academic perspectives impact on all the stages of my study. Without your help, I would not be able to publish my papers and also would not have completed my Ph.D. thesis successfully. You are always concerned about my research progress, talk to me every week and give the valuable suggestions to my research. More importantly, you give meticulous care to my daily life. I learned a lot from you not only the academic knowledge, but also the correct way to deal with difficulties and things. Your goodness, generosity, selflessness are the guide and light of my further life. I just want to show my deeply appreciate that it's my great honor to be one of your students.

I am also grateful to Associate Prof. Tani Hiroshi for the meaningful advices in seminars, intermediate presentations and also advices for my Ph.D. thesis. Many thanks to Prof. Sameshima Ryoji, Prof. Noguchi Noboru and Prof. Hirota Tomoyoshi. I am grateful to yours critical comments and thoughtful suggestions.

I am greatly indebted to Assistant Prof. Anthony R. Chittenden. He helps me to check the English grammar in my thesis and research paper manuscript and also gives me useful advices to my research work. I also sincerely thank Dr. Guo Meng (Northeast Normal University, China) for his encouragement, helpful suggestions throughout my study.

Thanks also go to my lab mates Yin Shuai and Sun Zhongyi for their help and cooperation in making the laboratory atmosphere healthy. I feel happy and relaxed with them. Thank you for giving me a happy time. I also owe my sincere gratitude to my friends and my fellow classmates who gave me their help and time to find solutions to my problems during the difficult course of the thesis.

I also would like to thank the GOSAT Project of Japan and NASA for providing data for my study.

My Ph.D. Course was funded by Japanese Government Scholarship program. I am grateful to the Ministry of Education of Japan. With this support, I can focus all my attention on my research work.

I should finally like to express my gratitude to my beloved family who have always been helping me out of difficulties and supporting me consistently without a word of complaint.

Zhong Guosheng

Hokkaido University, Sapporo, Japan

Abbreviations

6S	Second Simulation of a Satellite Signal in the Solar Spectrum
AATSR	Advanced Along-Track Scanning Radiometer
ADEOS-1	Advanced Earth Observing Satellite 1
AERONET	Aerosol Robotic Network
AFRI	Aerosol FRee vegetation Index
AOD	Aerosol Optical Depth
ARVI	Atmospherically Resistant Vegetation Index
AVHRR	Advanced Very High Resolution Radiometer
BRDF	Bidirectional Reflectance Distribution Function
CAI	Cloud and Aerosol Imager
DT	Dark Target
EE	Expected Error
ENVISAT	Environmental Satellite
EOS	Earth Observing System
EVI	Enhanced Vegetation Index
EVI2	Modified 2-band EVI
FRAR	Fraction of Photosynthetically Active Radiation
FTS	Fourier Transform Spectrometer
GOSAT	Greenhouse gases Observing SATellite
IRS-1C/1D	Indian Remote Sensing Satellites-1C/1D
LAI	Leaf Area Index
MBE	Mean bias error
MIR	Middle infrared
MISR	Multi-angle Imaging SpectroRadiometer
MODIS	Moderate Resolution Imaging Spectroradiometer
MSAVI	Modified SAVI
NDVI	Normalized Difference Vegetation Index
NIR	Near-infrared
PM	Particulate Matter
PM2.5	Particulate matter with a diameter less than 2.5 μm
POLDER	Polarization and Directionality of Earth's Reflectance
RGB	Red, Green and Blue
RVI	Ratio Vegetation Index
RMSE	Root mean square error

SARVI	Soil-adjusted and Atmospheric Resistant Vegetation Index
SAVI	Soil-Adjusted Vegetation Index
SAVI2	Soil-Adjusted Ratio Vegetation Index
SCIAMACHY	Scanning Imaging Absorption Spectrometer for Atmospheric CHartographY
SPOT	Satellite Pour l'Observation de la Terre
SWIR	Shortwave infrared
SYNAER	SYNergetic Aerosol Retrieval
TANSO	Thermal and Near-Infrared Sensor for Carbon Observation
TOA	Top-of-atmosphere
TOC	Top-of-canopy
TSAVI	Transformed SAVI
UV	Ultraviolet
VARI	Visible Atmospherically Resistant Index
VI	Vegetation Index
VIIRS	Visible infrared Imaging Radiometer
XCO_2	Column-averaged dry-air mole fractions of CO_2